UNIVERSITY OF
MODENA AND REGGIO EMILIA

DOCTORAL DISSERTATION

A Study on the Electrification of Non-Road Vehicles: Powertrain Design and Charging Infrastructure Modeling

Author
Ciro ALOSA

Supervisor
Prof. Fabio IMMOVILLI

School Director
Prof. Franco ZAMBONELLI

A thesis submitted in fulfillment of the requirements for the degree of Doctor of Philosophy in the

Industrial Innovation Engineering (35^{th} cycle)

Department of Sciences and Methods for Engineering
Reggio Emilia

May 18th, 2023

"Nothing in life is to be feared, it is only to be understood. Now is the time to understand more, so that we may fear less."

Marie Curie

Dedicata a Diego

Acknowledgements

Now that my experience has come to an end, it's time to say goodbye and thank you to all the people who believed in me. I have not only expanded my knowledge, but above all I have had the opportunity to grow on a personal level.
My first thank you is for my tutor Profess Fabio Immovilli, who immediately believed in me, supporting me during these 4 years, in the happiest moments and in the most difficult ones. He represented a fundamental point of reference to which I was always able to turn, not only for the most demanding challenges, and with whom I had not only a working relationship but especially a friendship.
Thanks to my great family: my mom Olga, my dad Mario and my sister Stefania and my brother-in-law Daniel. I dedicate this work to my wonderful newborn nephew Diego. Thanks to my second family, Pino and Anna. Thanks to their support and their love it was easier for me to face this beautiful journey.
Thanks to my better half Isabella, her love gave me the strength to never give up and she was always there every time I needed her to support me during the most challenging moments.
I would also like to thank Professor Emilio Lorenzani, who not only helped me join the research group, but above all was a fundamental help during these years.
Last but not least, I thank my colleagues: Giovanni Migliazza, Emilio Carfagna, Fabio Bernardi and Dario Benatti. I was able to learn many things with them, but above all I was lucky enough to have spent wonderful moments of leisure and entertainment, having often made my working days lighter.

Contents

List of Figures

List of Tables

List of Symbols

f	current fundamental frequency	Hz
f_{sw}	switching frequency	Hz
T_{sw}	switching period	s
$\cos(\varphi)$	power factor	
v_{DC}	DC bus voltage	V
M_a	amplitude modulation index	
$\widetilde{M}_{\mathrm{A}}$	normalized amplitude modulation index	
i_{B}	battery current	A
p	pole-pairs number	
n	number of turns per slot	
q	number of slots per pole/phase	
p	number of pole-pairs	
N	number of turns per phase	
ω_m	angular mechanical speed	$\mathrm{rad\,s^{-1}}$
ω_e	angular electrical speed	$\mathrm{rad\,s^{-1}}$
$\omega_{e,b}$	machine electrical base speed	$\mathrm{rad\,s^{-1}}$
β_r	winding chording angle	
$K_{mag,\rho}$	magnets distribution factor	
$K_{d,\rho}$	ρ-th distribution factor	
$K_{p,\rho}$	ρ-th pitch factor	
$K_{w,\rho}$	ρ-th winding factor	
Φ_{M}	peak value of the flux-per-pole	Wb
Λ_{M}	magnets' flux linkage peak value	Wb
$E_{s0,\rho}$	ρ-th homopolar back-emf amplitude	V
$Z_{0,\rho}$	ρ-th homopolar impedance	Ω
k_{T}	PMSM torque constant	$\mathrm{N\,m\,A^{-1}}$
T_{EM}	electromagnetic torque	N m
P_{EM}	electromagnetic power	W
(m_a, m_b, m_c)	inverter duty-cycles	
(v_{pa}, v_{pb}, v_{pc})	inverter pole voltages	V
(v_{sa}, v_{sb}, v_{sc})	stator phase voltages	V
(i_{sa}, i_{sb}, i_{sc})	stator phase currents	A
$(\lambda_{sa}, \lambda_{sb}, \lambda_{sc})$	stator phase linked fluxes	Wb
(e_{sa}, e_{sb}, e_{sc})	stator phase back-EMFs	V
(i_{sd}, i_{sq}, i_{s0})	stator $dq0$ currents	A
(m_d, m_q, m_0)	inverter $dq0$ duty-cycles	
(v_{pd}, v_{pq}, v_{p0})	inverter $dq0$ pole voltages	V
(v_{sd}, v_{sq}, v_{s0})	stator $dq0$ voltages	V
(e_{sd}, e_{sq}, e_{s0})	stator $dq0$ back-EMFs	V

$(\lambda_{sd}, \lambda_{sq}, \lambda_{s0})$	stator $dq0$ linked fluxes	Wb
(L_d, L_q, L_0)	stator $dq0$ inductances	H
V_s	stator phase voltage peak	V
I_s	stator phase current peak	A
$I_{s,\mathrm{rms}}$	stator phase current rms	A
γ	FOC control angle	°
I_p	VSI phase current peak	A
i_o	half-bridge output current	A
β	diode conduction angle	°
$v_{Q\mathrm{on}}$	transistor on-voltage	V
$v_{D\mathrm{on}}$	diode on-voltage	V
$i_{Q\mathrm{on}}$	transistor on-current	A
$i_{D\mathrm{on}}$	diode on-current	A
$R_{D\mathrm{on}}$	diode on-resistance	Ω
$R_{Q\mathrm{on}}$	trans. on-resistance	Ω
V_{D0}	diode no-load voltage	V
V_{Q0}	trans. no-load voltage	V
$i_{Q,f}$	trans. on-current (forward phase)	A
$i_{Q,r}$	trans. on-current (reverse phase)	A
$i_{D,r}$	diode on-current (reverse phase)	A
$I_{Q\mathrm{rms}}$	IGBT trans. rms current	A
$I_{D\mathrm{rms}}$	IGBT diode rms current	A
$I_{Q\mathrm{avg}}$	IGBT trans. average current	A
$I_{D\mathrm{avg}}$	IGBT diode average current	A
$P_{\mathrm{sw}Q}$	trans. average switching losses	W
$P_{\mathrm{sw}D}$	diode average switching losses	W
$p_{\mathrm{c}Q,f}$	trans. instantaneous cond. loss. (forw. phase)	W
$p_{\mathrm{c}Q,r}$	trans. instantaneous cond. loss. (rev. phase)	W
$p_{\mathrm{c}D,r}$	diode instantaneous cond. loss. (rev. phase)	W
$P_{\mathrm{c}Q,f}$	trans. average cond. losses (forw. phase)	W
$P_{\mathrm{c}Q,r}$	trans. average cond. losses (rev. phase)	W
$P_{\mathrm{c}D,r}$	diode average cond. losses (rev. phase)	W
$\Theta_{\mathrm{J}Q}$	trans. junction temperature	°C
$\Theta_{\mathrm{J}D}$	diode junction temperature	°C
f_g	grid frequency	Hz
R_g	grid resistance	Ω
L_g	grid inductance	H
(v_{ga}, v_{gb}, v_{gc})	grid phase voltages	V
(i_{ga}, i_{gb}, i_{gc})	grid phase currents	A
(e_{ga}, e_{gb}, e_{gc})	grid phase EMFs	V
(i_{gd}, i_{gq})	grid dq currents	A
(v_{gd}, v_{gq})	grid dq voltages	V
(e_{gd}, e_{gq})	grid dq EMFs	V

Abstract

In the roadmap to decarbonization there is a trend in the electrification of new kinds of vehicles other than automotive ones. The latest European Commission Stage V standard provides even tighter emission limits of the so called Non-Road Mobile Machinery (NRMM), whose category includes railroad engines, industrial machinery, inland waterway vessels, offroad vehicles for recreational use, and so on. This work is intended to provide a general overview and discuss some challenges and solutions for the electrification of various non-road vehicles by focusing on the powertrain design, both at the electric machine level and the system level.

In this scenario, multi-three-phase drives are the subject of great interest for the transportation electrification given their modular construction with inherent redundant structure and the fault-tolerant capability. However, special attention must be given to the airgap radial force analysis under fault operation, but also to the machine design which must operate in harsh environments. Multi-three-phase drives can be also exploited to achieve reconfigurable architectures which has the ability to change the winding configuration to better match the machine speed to the vehicle operating point. The proposed architecture exhibits two main benefits at low speed operation: an increased efficiency and a reduced phase current ripple for a given switching frequency. The main advantage is the capability of reducing the number of active converters when the machine operates at low speed, thus reducing total converter power losses. However, the system complexity increases since reconfiguration cells are needed to interconnect the winding sets.

The employment of high voltage drives can limit the electrification of heavy-duty machinery due to the fact that most manufacturers do not have a specific know-how regarding the electric safety regulations. However, since many NRMM already feature ultra-low voltage systems onboard, the implementation of ultra-low voltage drives can support the widespread use of electric NRMM. Nevertheless, a low battery voltage reduces the machine performance and the powertrain dynamics. To overcome this limitations, Multi-Functional Converter Systems (MFCS) can be implemented in order to boost the battery voltage, by exploiting the electric motor winding and the three-phase inverter connected.

Inland waterway vessels are NRMM which can benefit from a battery electric propulsion system thanks to their short ranges and inherent close proximity to charging infrastructures on the shore. The present work details the design and numerical simulation of the electric machine for a rim-driven propeller thruster for naval applications. Thanks to the absence of the central hub, these thrusters have an increased efficiency and a more compact

structure when compared to the traditional ones, for this reason they are particularly suitable for lightweight boats.

The electrification of NRMMs and the consequent increasing number of battery vehicles require the development of a suitable and capillary charging infrastructure. The focus is towards solutions to reduce charging times while simultaneously taking into consideration the impact on the converters reliability. Indeed, the increasing power levels and the unpredictable usage pattern of charging stations users, along with the variation of ambient conditions, can cause a serious thermal stress to the power electronics switches in the converters, whose behavior must be carefully analyzed to schedule the maintenance periods accordingly. For this reason, a study carried out on the thermal modeling of a fast charging station converter is presented in this dissertation. The aim was to obtain a very fast, but accurate simulation of the converter thermal behavior in order to estimate the cumulative damage following different usage patterns and under various ambient conditions.

Publications

Journal papers

J1. C. Alosa, G. Migliazza, F. Immovilli and E. Lorenzani, "Reconfigurable Multi-Three-Phase Drive for Naval Rim-Driven Propulsion System," in IEEE Transactions on Industry Applications, vol. 58, no. 2, pp. 2075-2087, March-April 2022,
doi: 10.1109/TIA.2022.3142234.

Conference papers

C1. C. Alosa, F. Immovilli and E. Lorenzani, "Reconfigurable Multi-Three-Phase Propulsion System for Naval Rim-Driven Propeller," 2020 International Symposium on Power Electronics, Electrical Drives, Automation and Motion (SPEEDAM), 2020, pp. 442-447,
doi: 10.1109/SPEEDAM48782.2020.9161936.

C2. C. Alosa, F. Immovilli and E. Lorenzani, "Fault-Tolerant Multi-Three-Phase PMSM Machine for Offroad Vehicle Hybridization," 2020 International Symposium on Power Electronics, Electrical Drives, Automation and Motion (SPEEDAM), 2020, pp. 793-798,
doi: 10.1109/SPEEDAM48782.2020.9161914.

C3. C. Alosa, F. Immovilli and E. Lorenzani, "Multi-Three-Phase Propulsion System for Fault-Tolerant Naval Rim-Driven Propeller," 2020 International Conference on Electrical Machines (ICEM), 2020, pp. 2238-2244,
doi: 10.1109/ICEM49940.2020.9270680.

C4. D. Benatti, C. Alosa, E. Carfagna, F. Immovilli and E. Lorenzani, "Assessment of Master-Slave and Droop Control Strategies in Multi-Three-Phase Drives," 2021 IEEE Workshop on Electrical Machines Design, Control and Diagnosis (WEMDCD), 2021, pp. 163-168,
doi: 10.1109/WEMDCD51469.2021.9425685.

C5. C. Alosa, F. Immovilli and E. Lorenzani, "Assessment of a Multi-Functional Converter System for Traction Electric Drives," 2021 IEEE Energy Conversion Congress and Exposition (ECCE), 2021, pp. 2696-2703,
doi: 10.1109/ECCE47101.2021.9595626.

C6. C. Alosa, F. Immovilli and E. Lorenzani, "Design and Optimization of a Magnetic Gear for a Conveyor System Application," 2022 International Conference on Electrical Machines (ICEM), 2022, pp. 434-440,
doi: 10.1109/ICEM51905.2022.9910844.

C7. C. Alosa, F. Immovilli and E. Lorenzani, "Hairpin-Wound Rim-Driven Propeller for Electric Boats on Inland Waterways," 2022 International Conference on Electrical Machines (ICEM), 2022, pp. 1156-1162, doi: 10.1109/ICEM51905.2022.9910888.

Introduction

Motivation

Transportation electrification has become a recurrent topic both for scientific and industrial research since vehicles powered by internal combustion engines significantly contribute to the global air pollution with their massive emissions. The European Commission enforced stringent emission standards for non-road mobile machinery (NRMM), such as construction equipment, railroad engines, inland waterway vessels, and off-road recreational vehicles, [1]. Current Stage V standards tightened the restrictions on non-road engines and set stricter limits on emissions of particulate matter, with reductions greater than 95% compared to the initial Stage I standard, [2].

Unlike road vehicles, the electrification of heavy equipment is more complex due to many different factors and many difficulties must be faced in order to design a suitable electric drive according to the required application. One of the most challenging issue is to foresee a working cycle in order to properly size the electric machine given the torque and power demands of the equipment. Due to the large variability of the work conditions, the working cycle is often unknown or very poorly estimated and this brings a high level of uncertainty during the design phase.

Scope and Contribution

The work presented in this dissertation was conducted in order to analyze different case studies regarding the electrification of non-road mobile machinery (NRMM), by considering both the powertrain and the fast charging infrastructure. The studies were conducted in order to analyze different applications: first of all with a focus on the electrical machine design, by also considering the co-design approach with the power electronics, then by analyzing two different electric drives architectures, finally by developing a thermal model of 2-level voltage source inverters, intended for fast charging application, and which model can be extended also to traditional motor drive applications.

The integration of an electric drive on a mechanical transmission means that both the power converters and the electric machine must operate in harsh environments, usually characterized by high ambient temperatures and reduced heat exchange possibilities: thermal dissipation problems can arise especially when dealing with non-road vehicles, since the operating conditions are usually worse and they are not easily predictable. Moreover, the drive encumbrance should be limited as much as possible in order to improve the ease of integration withing the transmission. For this reason,

nowadays all major automotive manufacturers rely on the implementation of high-voltage batteries to obtain a high voltage DC bus stage for electric drives adopted in hybrid or full-electric vehicles. However, the employment of high voltage drives can limit the electrification of heavy-duty machinery due to the fact that most manufacturers do not have a specific know-how regarding the electric safety regulations. Nevertheless, since many NRMM already feature ultra-low voltage systems onboard, the implementation of ultra-low voltage drives can support the widespread use of electric NRMM. The main problem is that a low battery voltage can significantly reduce the machine performance and the powertrain dynamics. To overcome this limitations, Multi-Functional Converter Systems (MFCS) can be implemented in order to boost the battery voltage, by exploiting the electric motor winding and the three-phase inverter connected.

In this scenario, multi-three-phase drives are the subject of great interest for the transportation electrification given their inherent redundant structure and the fault-tolerant capability. A positive aspect is their inherent modular construction with the advantage of the reduction in complexity of both manufacturing and maintenance of the system. By exploiting the multi-three-phase architecture, reconfigurable drives can be obtained: when operating at reduced speed, reconfiguring the multi-three-phase machine in series results in the reduction of the number of active converters feeding the machine, with the ultimate goal of increasing system efficiency by reducing the converter losses. Among the benefits of this architecture, one is the ability to operate with a reduced base speed but with full torque and balanced electric machine operation, even in case of multiple converter failures. However, since the machine winding reconfiguration is achieved using bi-directional switches, additional conduction losses must be taken into account. Another one is in terms of efficiency which is related on the number of active converters, therefore it is independent on the power rating of the particular application. A secondary beneficial aspect is the reduction of the phase current ripple when the machine's windings are series connected, improving the harmonic distortion of the current and the associated losses.

The vicinity of inhabited centers to big inland waterways brings with it the necessity to reduce acoustic noise and the pollutant emissions of the vessels operating in these areas. For this reason, even if the electric mobility on water is in the early stage of development it has a great potential of growth. One of the great advantages is that inland waterway vessels operate on much shorter ranges, and are always relatively close to charging infrastructures. On the other hand, seafaring vessels are characterized by long range operation, requiring the additional burden of auxiliary generators/range extenders, adding complexity to the power-plant installation. Therefore In case of sailboats to be used on lakes, electric propulsion is clearly a winning choice: the propulsion engines are used for a very short time, on the order of minutes, usually only for maneuvering in or out of the marina. An internal combustion engine would not even reach the operating temperature, resulting in high pollutant emissions. For this reason, inland waterway vessels are the best candidate to benefit from a modular, self contained battery electric

propulsion system that can be easily incorporated in an existing boat design, completely substituting an internal combustion engine power-plant, without sacrificing performance.

The electrification of NRMMs and the consequent increasing number of battery vehicles require the development of a suitable and capillary charging infrastructure. The focus is towards solutions to reduce charging times while simultaneously taking into consideration the impact on the converters reliability. Indeed, the increasing power levels and the unpredictable usage pattern of charging stations users, along with the variation of ambient conditions, can cause a serious thermal stress in the converters, whose behavior must be carefully analyzed to schedule the maintenance periods accordingly. One important issue to be addressed is that the current power semiconductor thermal models have a high computational burden. This represents a clear challenge to be overcome since the resulting models can only be executed offline. In addition, and even representing a more important limitation of the thermal models applicability, long term damage estimations can be hardly achieved since the required simulation time is greater than the simulated operation time span of the converter. For example, if a long term damage estimation considering years of normal operation is required, the amount of data to be managed is huge and the required computational cost is so high that the estimations need a lot of time to get a result. At this purpose, an analytical thermal modeling approach is presented in this work, by also considering the temperature ripple due to the AC current fundamental frequency. The proposed model addresses the main limiting factor, that is the high computational burden, leading to extremely long computational time for the numerical simulations. The proposed model aims at reducing the computational cost and hence making possible to carry out long term damage estimations with affordable execution time. This fact opens the scenario of calculating the remaining useful lifetime of the device and hence allowing to modify the power converters operation in runtime, following the predictive maintenance directives.

Outline

This dissertation is organized in three chapters. In Chapter 1 the case study regarding the hybridization of a small hydraulic excavator is introduced and the multi-three-phase machine design specifications, requirements and constraints are presented, along with the case study of a trench digging test cycle. Finally the analysis of the radial pulling force on the rotor considering different stator fault cases is analyzed. Following this first case, a Multi-Functional Converter System (MFCS) is introduced and its electric circuit is analyzed, obtaining the fundamental relationship between the battery voltage and the DC bus voltage. Moreover the comparison between a traditional architecture, featuring a DC-DC boost converter between the battery and the inverter DC link, and the MFCS architecture is carried out.

In the first part of Chapter 2 an electric machine design for a rim-driven propeller is presented and some fundamental design considerations about

the design of the hairpin-wound machine are carried out. The FEA simulations results of the machine and the consequent thermal analysis are carried out to calculate the machine performance and temperatures following the specified operating conditions. In the second part of Chapter 2, the reconfigurable architecture is introduced and its performance is assessed by means of analytical calculation of the power electronics components losses and the analytic results are compared against the numerical simulations carried out in PLECS® environment. Finally the experimental results obtained with a double three-phase low voltage laboratory prototype are presented, demonstrating the mode of operation of the reconfigurable drive and its advantages in terms of current ripple and efficieny.

In Chapter 3 a thermal model of a power device employed in a 2-level voltage source inverter is presented. The analytical losses are calculated for two different modulation strategies and the temperature ripple at the grid frequency is also taken into account, by means of a Matlab script. The proposed model is characterized by a very high execution speed in comparison with a numerical simulation with PLECS® by providing a temperature profile with a very good accuracy. By exploiting the analytical model, a vehicle fast charger model is presented and different battery charging strategies are analyzed in order to evaluate their effect on the cumulative damage of the devices.

Chapter 1

Electrification of Industrial Machinery: Two Case Studies

The introduction of strict regulations in terms of air pollution is pushing automotive industry and heavy equipments vehicles manufacturers to integrate electric drives into the existing powertrain to downsize the internal combustion engine in order to reduce the emissions. In this scenario, multi-three-phase machines are gaining popularity primarily thanks to their fault-tolerant capability with respect to the classical three-phase machine: the possibility to segment the machine phase current into multiple three-phase inverter helps reducing the size of the converter and also build a redundant structure which improves the drive operation in case of fault. The present chapter reports the study of a multi-three-phase machine to be employed in the hybridization of a 5-ton bucket-excavator: the design of the machine was chosen to satisfy the constraints for the integration into the existing powertrain and to meet a reference trench digging test cycle. Detailed simulation of losses, including the effect of PWM modulation, was performed and then used as an input for the thermal analysis to assess the machine capability of operating in a harsh environment such as the under-the-hood intended application. Finally the fault operation capability by obtaining the airgap radial force under different fault scenarios was obtained. In the second part, a study was carried out on a Multi-Functional Converter System (MFCS), which was compared to a traditional architecture, featuring a DC-DC bidirectional boost converter stage between the battery and the inverter considering some figure of merits such as system efficiency, weight and machine performance. The DC-DC boost converter causes additional weight and encumbrance to the system, increasing the costs and having also an impact on the system efficiency. However, the circulation of the battery current in the machine of the MFCS can cause additional losses and can reduce the performance if the winding is not adequately designed. For this reason, the MFCS requires a different approach, in which the machine specifications and design must be developed together with the power electronics converter in order to take full advantage of the architecture's boost capability.

1.1 Introduction

The regulations about the air-polluting emissions in the automotive industry are becoming more and more stringent. Besides the automotive industry, the interest in the electric drives for transportation applications is growing among naval, aerospace and heavy machinery manufacturers for a ever more probable future electrification of their vehicles, [3]. New strict regulations are specifically targeting non-road machinery, e.g. the latest Stage V enforcing of [2], with limitations to operation and/or outright bans to be expected in the major cities. The main reason behind heavy equipment electrification is related to internal combustion engine (ICE) downsizing, since the peak power demand can be met by the combined power of the ICE and the electric machine. Given this fact, the implementation of a hybrid powertrain, in which the electric drive is integrated with the internal combustion engine, is nowadays almost mandatory. For this reason, electric drives are becoming a fundamental component for all kind of vehicles manufacturers, as the adoption of electric and hybrid vehicles in many fields in the next few years will be widespread. This fact has brought to the research and development of many kind of electrical machines and especially Permanent Magnet Synchronous Machines (PMSM), which feature many advantages among the electrical machines, such as high efficiency, high power density and ease of control. Many different PMSM topologies can be found in the literature and the common ground is to push forward the maximum speed, the torque (and power) density and the efficiency. Internal Permanent Magnet (IPM) machines are the most common synchronous machines in the automotive industry, thanks to their great flux-weakening capabilities, which allows to obtain a large constant power region, with a large ratio between the maximum speed and the nominal speed, but also featuring an additional term in the output torque, the so-called reluctance torque, which exploits the magnetic circuit anisotropy between the d and q axis in order to increase the machine torque. On the other hand, Surface Permanent Magnet (SPM) machines allow to reach higher torque densities, thanks to the stronger excitation flux given by the magnets placed on the surface of the rotor, but at the cost of a reduced flux-weakening capability, a higher risk of demagnetization and higher losses on the magnets due to the slotting effect.

In the framework of the transportation electrification, multi-phase and multi-three-phase machines are gaining popularity thanks to their inherent fault-tolerant capability and the possibility to obtain a modular architecture where independent three-phase modules can be introduced and treated as single units, separated from each other. However, a special attention must be given to the study of the mutual coupling between the three-phase sets, in consideration of different winding arrangements which can have a considerable impact in this matter. Not less important is the fault operation which can be problematic for the mechanical strength of the machine since the exclusion of one or more three-phase sets causes the arise of an unbalanced radial force on the rotor, which must be accounted for to avoid stator-rotor rubbing or

ultimately the destruction of the machine. Machine topology plays a distinctive role in the placement along the transmission when considering a Hybrid Electric Vehicle (HEV). Indeed, the machines specification change considerably based on the position within the powertrain. For example, if the electric machine is located between the internal combustion engine and the clutch they are mechanically coupled and rotate at the same mechanical speed, on the other hand if the machine is after the clutch its operation can be decoupled from the engine.

In battery powered applications a fundamental requirement is to maximize the efficiency in order to reduce the weight of the battery pack. Moreover it is important reduce the encumbrance of the electric machine and the associated power converters to simplify the powertrain layout and consequently ease the on-board integration. At this purpose, in order to reduce the machine volume and weight, the rated torque should be kept as low as possible and the machine speed should be maximized however, since the maximum reachable speed of a machine depends on the supply voltage, which in turn depends on the inverter's DC bus voltage level, for low voltage application it is not possible to reach high power ratings. As an example, mild-hybrid vehicles are characterized by an electric drive operating at a DC bus voltage of 48 V: given the high current ratings of the devices and the fact that the base speed cannot be pushed to high values as desired, the maximum achievable power in these applications is limited and it is usually in the range of some tens of kW. For all these reasons, nowadays all major automotive manufacturers rely on the implementation of high-voltage batteries to obtain a high voltage DC bus stage for electric drives adopted in hybrid or full-electric vehicles. However, a DC-DC converter is often interposed between the battery and the inverter in order to boost the battery voltage up to 600-800 V since there are practical limitations to the maximum design voltage of a battery pack, for safety and manufacturing considerations, but also to decouple the DC bus voltage from the battery state of charge. The major drawback of this solution is an additional component which increments the drive encumbrance and can have a negative impact on the vehicle efficiency, but resulting also in a more complex layout which hardens the drive integration in the vehicle. In this scenario, Multi-Functional Converter Systems (MFCS), [4]–[6], can be seen as a good opportunity to obtain an integrated three-phase DC-DC converter by exploiting the electric machine winding and allowing to boost the voltage of the battery connected to the star point of the machine winding, [7]. This solution however requires the oversizing of the electric machine winding, since the battery current flows through the machine. In addition, modulations issues arise since the inverter homopolar voltage is imposed by the battery potential, [8]–[10], producing a battery current ripple which causes additional stress in the battery and losses in the electric machine.

The integration of an electric drive on a mechanical transmission means that both the power converters and the electric machine must operate in harsh environments, usually characterized by high ambient temperatures and reduced heat exchange possibilities: thermal dissipation problems can

arise especially when dealing with non-road vehicles, since the operating conditions are usually worse and they are not easily predictable. The electrification of heavy equipment machinery, as for example excavators, unlike road vehicles is more complex due to many different factors and different kind difficulties must be faced in order to design a suitable electric drive according to the required application. One of the most challenging issue is to foresee a working cycle in order to properly size the electric machine given the torque and power demands of the equipment. Nevertheless, due to the large variability of the work conditions, the working cycle is often unknown or very poorly estimated and this brings a high level of uncertainty during the design phase. Furthermore, heavy equipment machinery can be subjected to high peak power demands during their operation leading to a very high electric machine overload which is however not predictable therefore a suitable margin must be taken during the design process in order to account for the abuse conditions.

In this chapter two case studies will be presented: the first one focuses on the design considerations and the operating limits of a multi-three-phase fault-tolerant machine intended for the hybridization of small hydraulic excavator, coupling the machine with the internal combustion engine. The machine consists of 4 three-phase sets with a single-layer fractional slot concentrated winding intended for the placement along the existing transmission to let the engine rotate at a fixed speed, maximizing its efficiency. The second study is aimed at the comparison of a traditional battery-fed electric drive, featuring a three-phase converter with a three-phase machine and a DC-DC converter between the battery and the inverter, against a Multi-Functional Converter System (MFCS) in order to assess the advantages and drawbacks of the MFCS in terms of weight, encumbrance and efficiency, implemented in a 3.5 ton forklift featuring a 48 V battery.

The chapter is organized as follows: in 1.2 the case study of a small hydraulic excavator is introduced and the main characteristics of the study are presented. Section 1.2.1 provides some considerations about the multi-three-phase machine winding while in 1.2.2 the multi-stator theory is briefly introduced and the mutual coupling between the sets is introduced. In 1.2.3 the machine design specifications, requirements and constraints are presented, along with the case study of a trench digging test cycle, while in 1.2.4 the numerical simulations, in terms of electromagnetic finite element analysis and thermal simulations on the test working cycle, carried out on the designed machine are presented. Finally in 1.2.5 the analysis of the radial pulling force on the rotor considering different stator fault cases is analyzed.

Following this first case study, in Section 1.3 a Multi-Functional Converter System (MFCS) is introduced and in Section 1.3.1 its electric circuit is analyzed, obtaining the fundamental relationship between the battery voltage and the DC bus voltage, Section 1.3.2. In Section 1.3.3 the battery current in the MFCS is analyzed: first of all the average battery current is calculated by means of a power balance of the system and afterwards the battery current ripple is calculated by considering in two different cases a regular-sampled sinusoidal PWM modulation and a Space Vector Modulation. In Section 1.3.4

some considerations about the choice of the poles/slots combination for an electric machine employed in a MFCS are detailed while in Section 1.3.5 the comparison between a traditional architecture, featuring a DC-DC boost converter between the battery and the inverter DC link, and the MFCS architecture is carried out by means of both finite element analysis and numerical 1-D simulations.

Finally, the findings of the studies detailed in this first chapter are summarized and discussed in Section 1.4.

1.2 Case Study of a Small Hydraulic Excavator Hybridization

Figure 1.1 shows the typical structure of a bucket excavator: commercial available small bucket excavators are characterized by a diesel internal combustion engine, which is responsible for the traction of the vehicle but also to supply all the hydraulic actuators available onboard.

In the proposed study, the aim is to design an electric machine to be coupled to the diesel ICE of a 5-Ton bucket excavator to create an hybrid powertrain, with the aim of increasing the efficiency and reducing the emissions. The main benefit obtained with the hybridization of a small excavator is the possibility to run the internal combustion engine at a fixed regime, in order to maximize its efficiency. Indeed, an example of a diesel ICE for a small excavator application with power-speed characteristic curve is presented in Figure 1.2 along with the specific consumption and the crankshaft torque curves evolution over the engine rotation regime. As the figure shows, the minimum specific consumption is achieved when the engine regime falls between 2000 min^{-1} and 3000 min^{-1} approximately. In a hybridization scenario, it would be preferable to choose the ICE speed falling within the minimum consumption speed range, allowing to produce a constant power and then manage the remaining share of power with a dedicated electric machine,

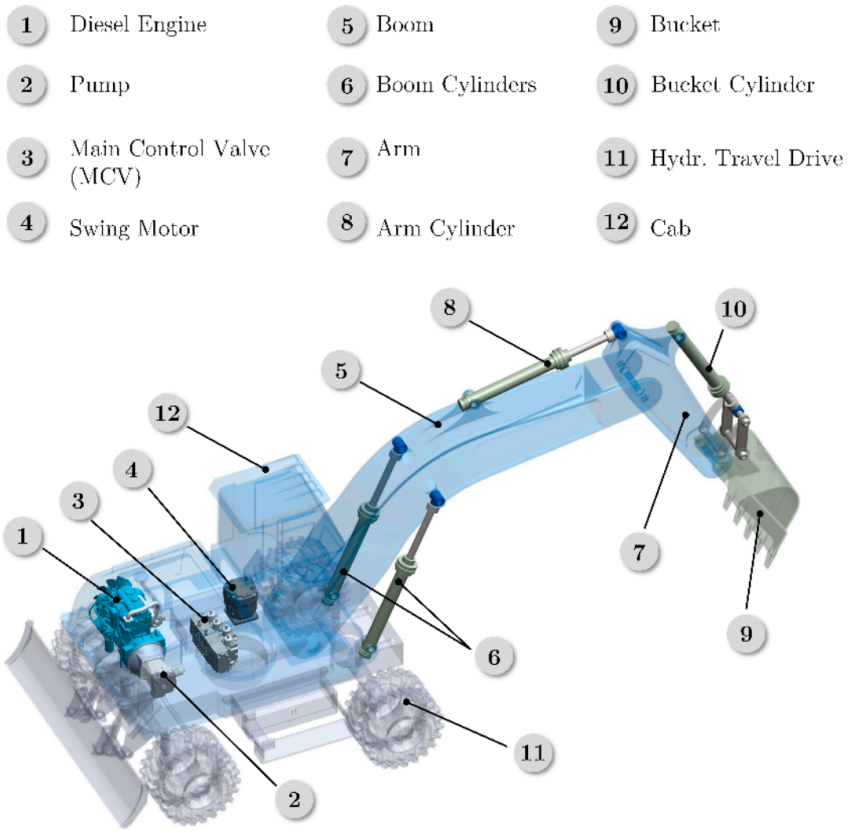

FIGURE 1.1: Example of a hydraulic excavator, from [11].

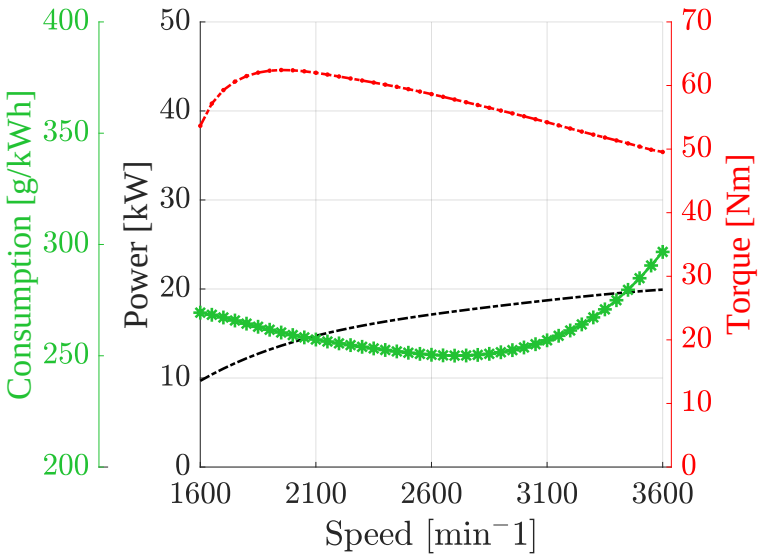

FIGURE 1.2: Lombardini LDW 1003 3 cylinder diesel internal combustion engine curves in terms of power, torque and specific consumption.

coupled on the same crankshaft of the internal combustion engine. This ideal scenario would allow to increase the powertrain efficiency and control the emission levels of the ICE by changing the rotation regime accordingly. The position of the electric machine along the powertrain transmission should be carefully chosen and depending on the location, the machine operating conditions can change considerably. According to the Figure 1.3, the electric machine can be placed in many different positions along the powertrain, [12]. The electric machine position is coded with a letter P and a number, from P0 to P4. For example, the position P0 is the location of the alternator, while the position P1 is before the clutch at the output of the ICE crankshaft. The exception is given by the code PS which represent a particular configuration of the powertrain, where two electric machines are coupled together with the ICE in a planetary gear to achieve a power split system. In this case, it was chosen to place the electric machine in the position P1 meaning that the machine and the internal combustion engine shafts are rigidly coupled and thus they rotate at the same regime. For a bucket excavator, the position P1 is the position between the ICE and the main hydraulic pumps. Given the application and positioning, the electric machine operating conditions are quite defined: for a given rotational speed of the ICE, the machine must provide the remaining share of the total requested power by changing the output torque accordingly. This means that the machine always operates at a given torque-speed point without the necessity of working in a constant power zone and for this reason a Surface Permanent Magnet (SPM) Synchronous Machine (SM) would be the best candidate. Moreover, in order to improve the reliability of the powertrain, the idea was to design a machine with a fault-tolerant capability, by implementing multiple three-phase modules thus allowing the possibility of the electric drive to work even in case of fault of one, or more, modules.

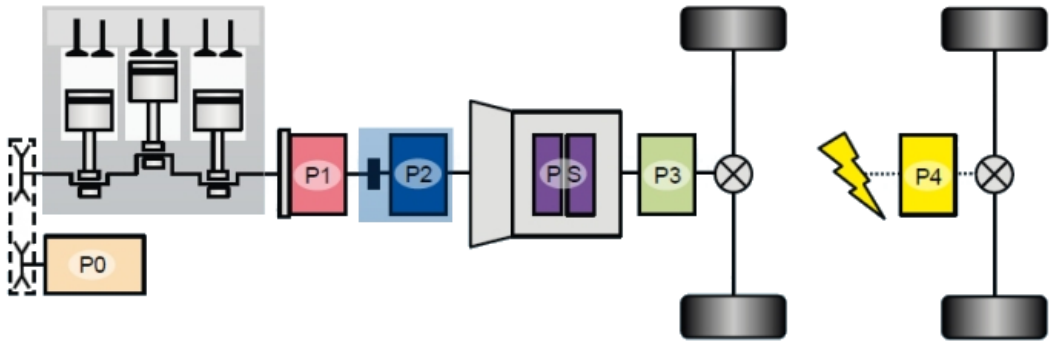

FIGURE 1.3: Possible integration position of an electric drive on a vehicle transmission, [13]. P0: front of the ICE; P1: before the clutch; P2: after the clutch (the ICE can be disconnected); PS: power split (e.g. Toyota hybrid system); P3: to the wheels before the differential; P4: full-electric transmission.

1.2.1 Machine Winding Considerations

In order to obtain an electric drive with a fault-tolerant operation capability, the work was aimed at the design of a multi-three-phase machine with a symmetric arrangement of the three-phase winding sets. In this work a symmetric quadruple three-phase machine was created starting from a three-phase machine with 4 parallel paths. A symmetric multi-phase machine consists of N three-phase sets, whose magnetic axis can be in phase or with a phase displacement of 180°. In Figure 1.4 the vector diagram of the symmetric quadruple three-phases machine is shown: the sets 1 and 3 are in phase while the sets 2 and 4 have a 180° phase. This kind of multi-phase machine is the most simple one, since it can be obtained from a traditional three-phase machine with multiple winding parallel paths. By supplying each parallel path with a three-phase inverter, a redundant drive is obtained: in case of fault of one of the inverters or one of the three-phase winding, the drive operation is still assured thanks to the remaining healthy three-phase modules. Symmetric multi-three-phase machines have the advantage of the redundancy, but they do not allow to control the higher order harmonics of the stator magnetomotive force (MMF) at the airgap, which would be otherwise possible with a multi-phase machine featuring an odd number of phases or a non symmetric displacement of the three-phase sets. Moreover, an important issue in multi-three-phase machines is the mutual coupling between the sets, which should be reduced as much as possible. The machine was designed by using a single-layer fractional slot concentrated winding (FSCW) with 4 turns per each phase. The reason behind this choice is to ease the manufacturing process and also physically isolate the phases of the different three-phase sets. Figure 1.5 shows two different winding arrangement which are possible. The first configuration, Figure 1.5(a), is supposed to be the best in terms of mutual coupling between the three-phase sets. Indeed, in this configuration each set is located within one sector of the machine (1/4 of the total stator circumference), and for this reason the magnetic interaction of one set with respect to

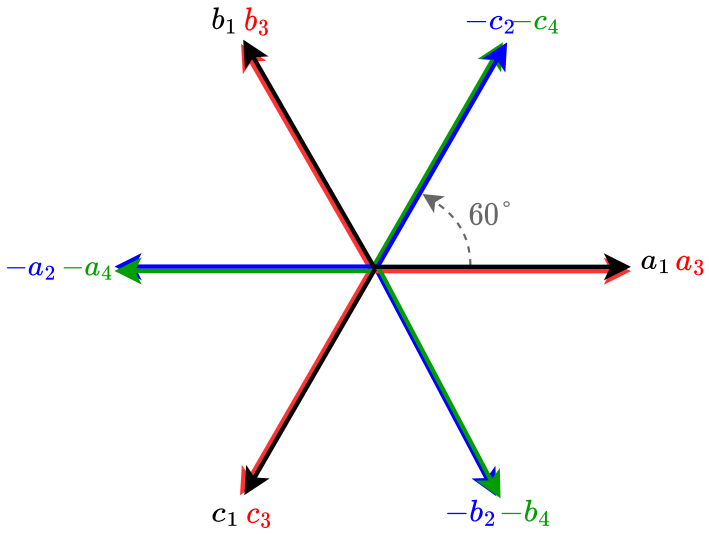

FIGURE 1.4: Vectorial diagram of the 12 phases symmetric machine.

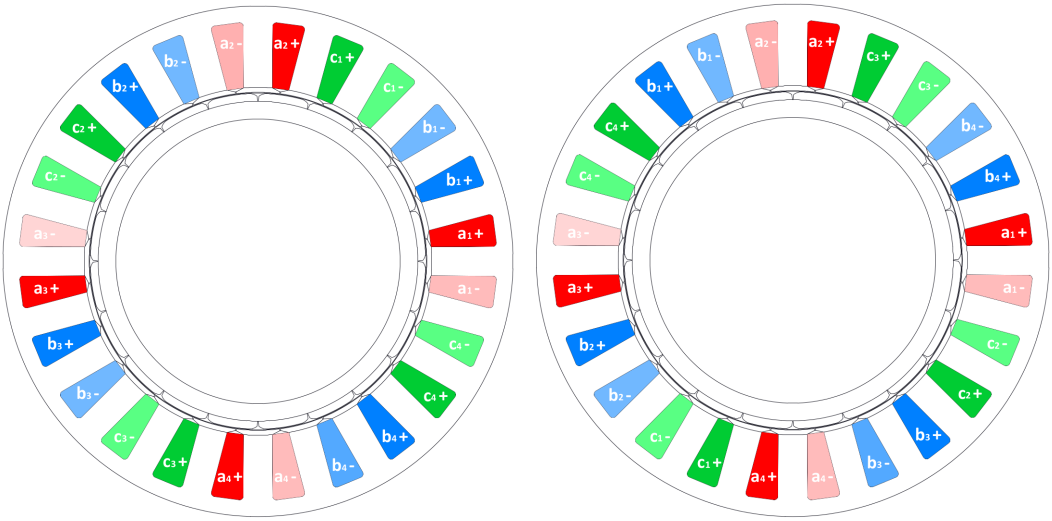

(a) (b)

FIGURE 1.5: Different single-layer winding arrangements of the machine: (a) each winding set is located into one-fourth of the machine (sectorized machine); (b) each winding set is equally distributed along the machine.

the others is low. For this reason, it could be possible to consider the multi-three-phase machine as it was composed of 4 three-phase "sub-machines" acting in parallel and mechanically coupled on the same shaft. On the contrary, in the second configuration, Figure 1.5(b), the mutual coupling between the three-phase set is higher, since the magneto-motive force (MMF) produced by one set is equally spatially distributed along the airgap circumference, causing the arise of a flux linkage on the others three-phase sets and the consequent mutual coupling. In this case, the machine should not be treated as the union of multiple three-phase "sub-machines" because the mutual inductance between two three-phase sets could be not negligible. However, both

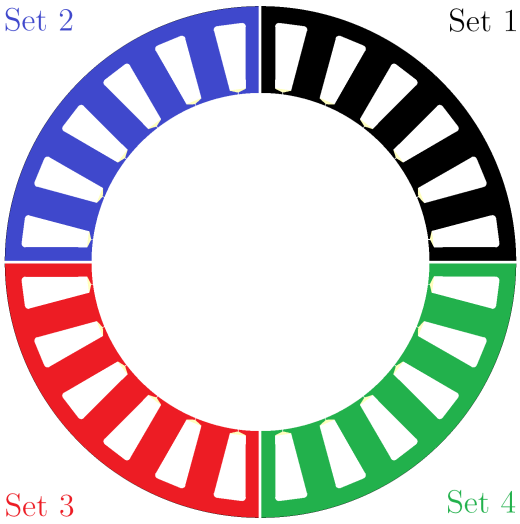

FIGURE 1.6: Schematic view of the sectorized quadruple three-phase machine. The three-phase sets are distributed along the stator circumference in anticlockwise direction.

the arrangements share some advantages and disadvantages in other aspect. For example, a big difference can be observed during the fault-operation in terms of radial force on the rotor, but also on the fault propagation. When all the sets are healthy, the the total MMF spatial distribution at the airgap is equally distributed and the total radial pulling forces acting on the rotor is balanced. On the other hand, considering the sectorized winding arrangement, in case of fault of one or more three-phase sets an unbalance can be observed in the total magneto-motive force spatial distribution. This unbalance causes an undesirable radial pulling force on the rotor which can be very stressful for the machine bearings if the total force reaches non-sustainable values. On the contrary, with the distributed winding arrangement the fault operation is always balanced, since the phases of each set are mechanically shifted of 120° and the airgap's MMF is equally distributed in the space. In the case of the machine under test for this work, a single-layer fractional slot concentrated winding with a sectorized arrangement was chosen. The reason is that, even with the issues given by the unbalanced force on the rotor, the a single-layer sectorized arragement features other advantages, as shown Figure 1.6. Firstly, since the phases of each set are located into one sector and not distributed around the stator, the connections to the dedicated power converter are shorter and thus the inverter integration with the machine can be easier. Secondly, thanks to the single-layer there is a physical separation between the sets and thus a failure on one winding set is less likely to propagate to the others. In addition, the low mutual coupling assured by the sectorized arrangement make sure the fault current circulating into the faulty set would not produce appreciable effects on the healthy ones. The advantage of adopting a single-layer winding is given primarily by the fact that in each slot there is only one phase of one three-phase set therefore a total physical separation between the phases of different sets is obtained. The redundant structure allows to intervene in case of fault of a three-phase converter: if one leg fails the

whole converter is excluded and the machine can still operate with a power derating (limp-mode operation). The same case can be applied if the fault is caused by a three-phase winding which is open-circuited or disconnected from the converter. The drawback of a single-layer winding is the higher harmonic content in the stator MMF with respect to a configuration with a double-layer winding. The higher harmonic distortion cause the circulation of harmonic eddy currents in the magnetic circuit and in the rotor magnets, resulting in higher iron and magnets losses along with the increment of the heat produced by the machine which can be difficult to dissipate and can be especially critical when the machine operates at high ambient temperatures. A fractional slot concentrated winding can be easily manufactured and it is suitable for a large scale production since it allows to assembly the stator by connecting the teeth which are manufactured and wound separately. This assembly strategy allows to achieve a full-automatic fabrication process of the stator bringing with it manufacturing advantages such as time and costs reduction. At the same time, the slot opening width can be minimized and therefore the airgap magnetic anisotropy is reduced, reducing the spatial harmonic content of the airgap magneto-motive force and the consequent magnets losses and cogging torque. In addition, a narrow slot opening helps in confining the faulty phases from the others and reduces the chance of a fault propagation. Employing a multi-three-phase segmented construction brings the additional benefits of the modular construction, while requiring the same overall switch count of the power converters. Indeed, since the machine is characterized by several three-phase sets and each of them is supplied by an independent three-phase converter, the per-phase current of each set is a fraction of the equivalent three-phase machine phase current. This means that a single three-phase converter in the multi-three-phase drive contains a lower number of paralleled solid-state devices with respect to a single three-phase converter which would fed the equivalent three-phase machine, with all the parallel paths connected together. For this reason, the total number of parallel devices does not change however the redundant structure is inherently more expensive since each three-phase set is fed by a whole independent three-phase converters, each of which features its own ancillary components.

1.2.2 Multi-Stator Modeling Approach

When dealing with multi-phase machines, there are two main modeling approaches that can be used. The Vector Space Decomposition (VSD) approach and the Multi Stator (MS) approach. The VSD approach is more suitable for asymmetric and proper multi-phase machines, when it is important to highlight the effect of the higher order spatial MMF's harmonics and it is possible to develop control algorithms to control these harmonics. On the other hand, the Multi Stator approach is more suitable to model symmetric multi-three-phase machines since it allows to treat each three-phase set separately, [14], [15], identifying the contribution given by each set and also by considering a mutual inductance to model the mutual coupling between the different

three-phase sets. As shown in [16], the mutual inductance between two different three-phase sets is mainly dependent on the winding arrangement of the machine. As discussed before, in a sectorized machine (i.e. when each set is located into one sector of the stator) the mutual coupling between the three-phase sets is minimized with respect to other kinds of arrangements. For a symmetric multi-three-phase machine with N three-phase sets, thanks to the Multi Stator modeling approach each k-th set is modeled in a dedicated dq reference frame. However, all the dq reference frames are in phase and rotate at the same electrical speed, synchronous with the rotor. More in detail, the machine equations can be written by considering a single three-phase set and then by introducing the self and mutual inductances to write the linked fluxes expressions. For the k-th three-phase winding set the stator equation is written as:

$$\mathbf{v}_s|_k = R_s \mathbf{i}_s|_k + \frac{d\boldsymbol{\lambda}_s|_k}{dt} \tag{1.1}$$

where:

$$\mathbf{v}_s|_k = \begin{bmatrix} v_{sa} \\ v_{sb} \\ v_{sc} \end{bmatrix}_k \qquad \mathbf{i}_s|_k = \begin{bmatrix} i_{sa} \\ i_{sb} \\ i_{sc} \end{bmatrix}_k \qquad \boldsymbol{\lambda}_s|_k = \begin{bmatrix} \lambda_{sa} \\ \lambda_{sb} \\ \lambda_{sc} \end{bmatrix}_k \tag{1.2}$$

are the k-th set phase voltage, phase currents and linked fluxes. Depending on the phase displacement γ_k of the k-th winding set magnetic axis with respect to the reference axis, the k-th transformation matrix from the three-phase reference frame to the dq reference frame can be written as:

$$\mathbf{P}|_k = \frac{2}{3} \begin{bmatrix} \cos(\theta_e + \gamma_k) & \cos(\theta_e + \gamma_k - \frac{2\pi}{3}) & \cos(\theta_e + \gamma_k + \frac{2\pi}{3}) \\ -\sin(\theta_e + \gamma_k) & -\sin(\theta_e + \gamma_k - \frac{2\pi}{3}) & -\sin(\theta_e + \gamma_k + \frac{2\pi}{3}) \\ \frac{1}{2} & \frac{1}{2} & \frac{1}{2} \end{bmatrix} \tag{1.3}$$

where $\theta_e = \int \omega_e t$ is the rotor electrical angle and ω_e is the rotor electrical speed. In this specific case, as depicted in Figure 1.4, for a symmetric three-phase machine the magnetic axis of all the three-phase sets are all in phase, $\gamma_1 = \gamma_2 = \gamma_3 = \gamma_4 = 0°$. By exploiting the transformation detailed in the matrix (1.3), the equations in the k-th dq reference frame become:

$$\begin{bmatrix} v_{sd} \\ v_{sq} \end{bmatrix}_k = R_s \begin{bmatrix} i_{sd} \\ i_{sq} \end{bmatrix}_k + \frac{d}{dt} \begin{bmatrix} \lambda_{sd} \\ \lambda_{sq} \end{bmatrix}_k + \begin{bmatrix} -\omega_e \lambda_{sq} \\ \omega_e \lambda_{sd} \end{bmatrix}_k \tag{1.4}$$

In general, the k-th set linked fluxes are a function of every dq current flowing through the machine three-phase sets. The linked fluxes for the k-th set can therefore be written as:

$$\begin{bmatrix} \lambda_{sd} \\ \lambda_{sq} \end{bmatrix}_k = \begin{bmatrix} L_d & 0 \\ 0 & L_q \end{bmatrix} \begin{bmatrix} i_{sd} \\ i_{sq} \end{bmatrix}_k + \sum_{\substack{h=1 \\ h \neq k}}^{N} \begin{bmatrix} M_d & 0 \\ 0 & M_q \end{bmatrix}_{kh} \begin{bmatrix} i_{sd} \\ i_{sq} \end{bmatrix}_h + \begin{bmatrix} \lambda_{\mathrm{M}} \\ 0 \end{bmatrix}_k \tag{1.5}$$

where $L_d(i_{sd}, i_{sq}, \theta_e), L_q(i_{isd}, i_{sq}, \theta_e)$ are the k-th set self inductances in the dq reference frame, $M_d(i_{sd}, i_{sq}, \theta_e), M_q(i_{sd}, i_{sq}, \theta_e)$ are the mutual inductances between the k-th and the h-th set, λ_M is the k-th set linked flux given by the

permanent magnets on the rotor and N is the total number of three-phase sets. Generally speaking, the self and mutual inductances are usually a function of the dq currents and the rotor position θ_e, since they depend on the saturation level of the machine magnetic circuit and on the reluctance of the magnetic circuit. The mutual inductances betweeen two sets depend on the mutual position of the sets and on the winding arrangement. In a sectorized machine the mutual inductances are lower with respect to a machine with a distributed winding and the mutual interaction between two adjacent sets is higher with respect to two opposite three-phase sets. Additional term could be introduced if the cross-coupling between the d axis and the q axis is considered, in this case a L_{dq} self and a M_{dq} mutual inductances should be added to the expression of the dq fluxes. In Figure 1.7, the inductances maps obtained with a finite element analysis are shown for the machine under test, the maps were obtained by supplying the three-phase set 1 and by keeping the currents of all the other sets equal to zero. Each map was calculated by averaging 4 different rotor positions and by using the following expressions:

$$\begin{aligned}
L_d|_k(i_{sd}|_k, i_{sq}|_k) &= \frac{1}{4}\sum_{n=1}^{4}\frac{\lambda_{sd}|_k(i_{sd}|_k, i_{sq}|_k, \theta_e|_n) - \lambda_{\mathrm{M}}|_k(\theta_e|_n)}{i_{sd}|_k} \\
L_q|_k(i_{sd}|_k, i_{sq}|_k) &= \frac{1}{4}\sum_{n=1}^{4}\frac{\lambda_{sq}|_k(i_{sd}|_k, i_{sq}|_k, \theta_e|_n)}{i_{sq}|_k} \\
M_d|_{kh}(i_{sd}|_k, i_{sq}|_k) &= \frac{1}{4}\sum_{n=1}^{4}\frac{\lambda_{sd}|_h(i_{sd}|_k, i_{sq}|_k, \theta_e|_n) - \lambda_{\mathrm{M}}|_h(\theta_e|_n)}{i_{sd}|_k} \\
M_q|_{kh}(i_{sd}|_k, i_{sq}|_k) &= \frac{1}{4}\sum_{n=1}^{4}\frac{\lambda_{sq}|_h(i_{sd}|_k, i_{sq}|_k, \theta_e|_n)}{i_{sq}|_k}
\end{aligned} \tag{1.6}$$

where $\lambda_{\mathrm{M}}|_k = \lambda_{sd}|_k(0,0)$ and $\lambda_{\mathrm{M}}|_h = \lambda_{sd}|_h(0,0)$, $\theta_e|_n$ is the rotor n-th electrical position. From the figures it is possible to observe that in general the mutual inductances between the set 1 and the others are at least one order of magnitude lower than the self inductances and the set 3 (which is in the opposite location with respect to the set 1) has the lowest mutual inductance. By introducing the (1.5), the (1.4) becomes:

$$\begin{aligned}
&\begin{bmatrix} v_{sd} \\ v_{sq} \end{bmatrix}_k \\
&= \begin{bmatrix} R_s & -\omega_e L_q \\ \omega_e L_d & R_s \end{bmatrix} \begin{bmatrix} i_{sd} \\ i_{sq} \end{bmatrix}_k + \begin{bmatrix} L_d & 0 \\ 0 & L_q \end{bmatrix} \frac{d}{dt} \begin{bmatrix} i_{sd} \\ i_{sq} \end{bmatrix}_k + \begin{bmatrix} 0 \\ \omega_e \lambda_{\mathrm{M}} \end{bmatrix}_k \\
&+ \sum_{\substack{h=1 \\ h\neq k}}^{N} \begin{bmatrix} M_d & 0 \\ 0 & M_q \end{bmatrix}_{kh} \frac{d}{dt} \begin{bmatrix} i_{sd} \\ i_{sq} \end{bmatrix}_h + \sum_{\substack{h=1 \\ h\neq k}}^{N} \begin{bmatrix} 0 & -M_q \\ M_d & 0 \end{bmatrix}_{kh} \begin{bmatrix} i_{sd} \\ i_{sq} \end{bmatrix}_h
\end{aligned} \tag{1.7}$$

The electromagnetic torque produced by the k-th three-phase set can be calculated as:

$$T_{\mathrm{EM}}|_k = 1.5p \begin{bmatrix} \lambda_{sd} \\ \lambda_{sq} \end{bmatrix}_k^T \begin{bmatrix} i_{sq} \\ -i_{sd} \end{bmatrix}_k \tag{1.8}$$

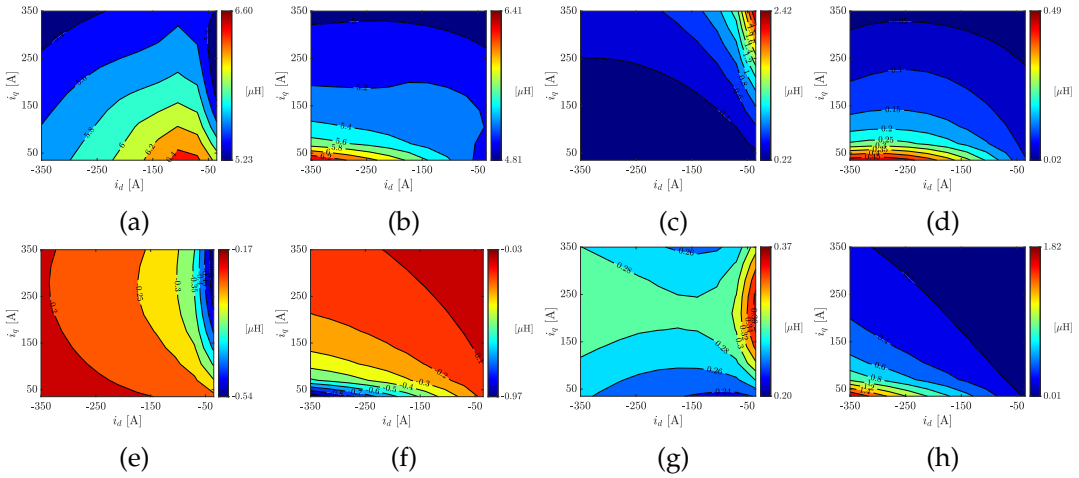

FIGURE 1.7: Inductances maps for the machine under test: (a) L_d (b) L_q (c) $M_{d,21}$ (d) $M_{q,21}$ (e) $M_{d,31}$ (h) $M_{q,31}$ (g) $M_{d,41}$ (h) $M_{q,41}$.

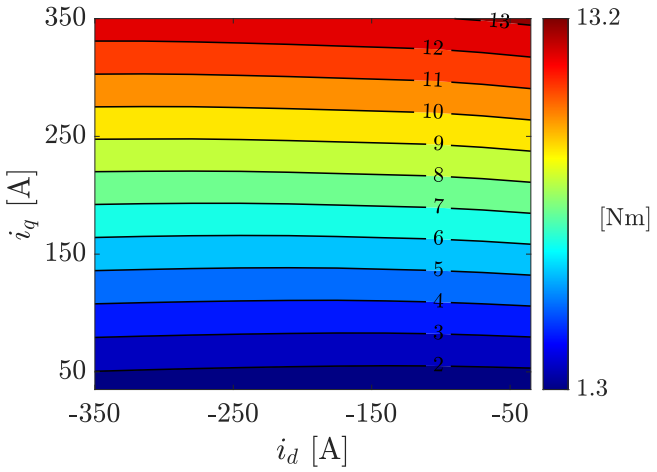

FIGURE 1.8: Torque map of one three-phase set in the dq reference frame taking into account only the self-producing torque component.

by substituting the (1.5), the torque expression becomes:

$$\begin{aligned} T_{\mathrm{EM}}|_k = 1.5p \begin{bmatrix} L_d & 0 \\ 0 & L_q \end{bmatrix} \begin{bmatrix} i_{sd} i_{sq} \\ -i_{sd} i_{sq} \end{bmatrix}_k + \begin{bmatrix} 1.5p\lambda_{\mathrm{M}} i_{sq} \\ 0 \end{bmatrix}_k \\ + 1.5p \sum_{\substack{h=1 \\ h \neq k}}^{N} \begin{bmatrix} M_d & 0 \\ 0 & M_q \end{bmatrix}_{kh} \begin{bmatrix} i_{sd} \\ i_{sq} \end{bmatrix}_h^T \begin{bmatrix} i_{sq} \\ -i_{sd} \end{bmatrix}_k \end{aligned} \tag{1.9}$$

the torque produced by one set is the sum of a self-producing torque component, $T_{\mathrm{EM}}|_{kk} = 1.5p(\lambda_{\mathrm{M}}|_k i_{sq}|_k + (L_d|_k - L_q|_k) i_{sd}|_k i_{sq}|_k)$ and an additional term given by the mutual inductances $T_{\mathrm{EM}}|_{kh} = 1.5p(M_d|_{kh} i_{sd}|_h i_{sq}|_k - M_q|_{kh} i_{sq}|_h i_{sd}|_h)$. In Figure 1.8 the torque map of the three-phase set 1 in the dq reference frame in shown. The torque map is referred only to the $T_{\mathrm{EM}}|_{kk}$ term, thus neglecting the effect of the mutual coupling: The total torque produced by the machine

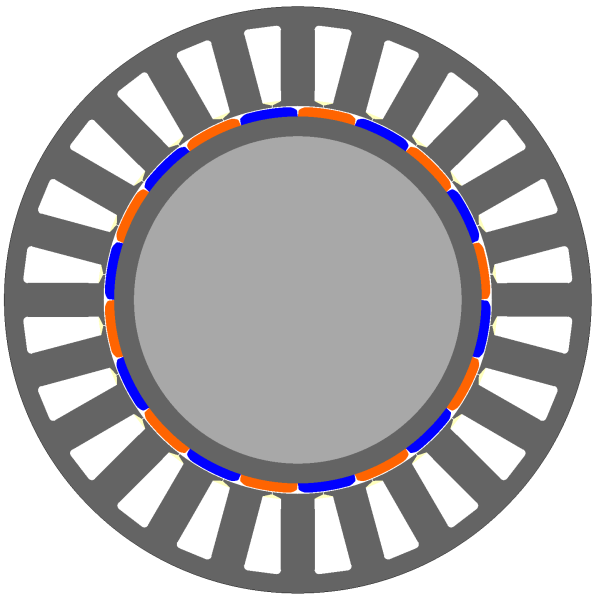

FIGURE 1.9: Machine 2D View from Altair®Flux®.

is given by the sum of the single torque components of each set:

$$\begin{aligned} T_{\mathrm{EM}} = \sum_{k=1}^{N} T_{\mathrm{EM}}|_k = 1.5p \sum_{k=1}^{N} (\lambda_{\mathrm{M}}|_k i_{sq}|_k + (L_d|_k - L_q|_k) i_{sd}|_k i_{sq}|_k) \\ + 1.5p \sum_{k=1}^{N} \sum_{\substack{h=1 \\ h \neq k}}^{N} (M_d|_{kh} i_{sd}|_h i_{sq}|_k - M_q|_{kh} i_{sq}|_h i_{sd}|_h) \end{aligned} \tag{1.10}$$

In [15] a decoupling method is presented in order to remove the magnetic coupling between the three-phase sets in the torque expression and, by considering that in a healthy machine all the three-phase sets are the same and they are supplied with the same phase currents, the total machine torque can be calculated as $T_{\mathrm{EM}} = N T_{\mathrm{EM}}|_k$, where N is the number of three-phase sets.

1.2.3 Definition of the Machine Specifications

In Table 1.1 the nameplate data of the Lombardini LDW 1003 engine chosen for this study is summarized, while in Figure 1.2 the characteristic curves are depicted. According to the manufacturer, this engine is suitable for a mini excavator application. The main task of the electric machine is to assist the internal combustion engine (ICE) during the machinery work cycles, particularly providing the peak torque demand in order to allow the ICE operation in a fixed speed regime. However, to design the best machine for the required application the excavator work cycle must be defined with a low grade of uncertainty. Generally, heavy-duty machinery work cycles are composed of different tasks that must be accomplished within a certain period, for the sake of productivity. The analysis of a 5-ton class bucket-excavator doing a trench digging test cycle was presented in [17]. According to the study of the trench digging test cycle, each task requires a specific amount of energy and power

TABLE 1.1: Lombardini LDW 1003 diesel internal combustion engine main specifications.

Number of cylinders	3
Displacement	1028 cm^3
Maximum speed	3600 min^{-1}
Maximum torque @ 2000 min^{-1}	67 N m
Maximum power	20 kW

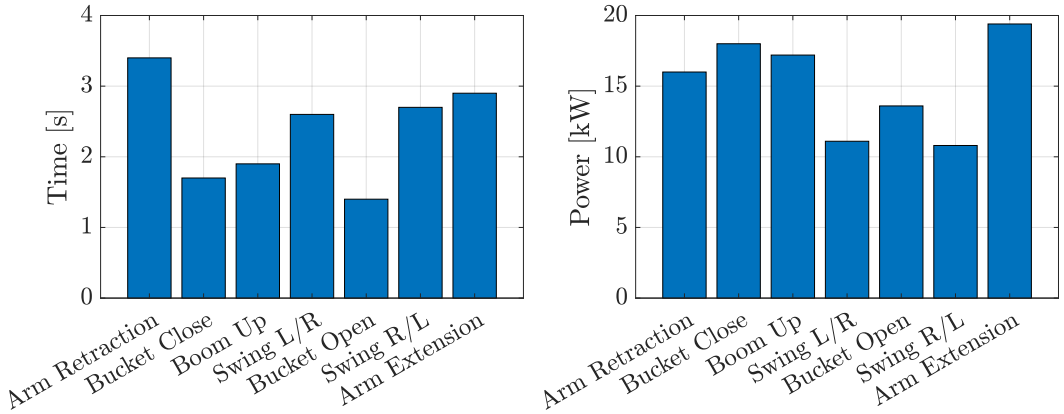

FIGURE 1.10: Trench digging test cycle (a) duration time and (b) power for the different tasks, [17].

and has a specific duration time, Figure 1.10. According to the reference, the test cycle complies with JCMAS (Japan Construction Mexhanization Association Standard) requirements for trench digging, where testing ground must be prepare with a trench of 1 m deep and execute the following tasks:

1. arm retraction;
2. bucket close
3. boom-up
4. swing left/right;
5. bucket open;
6. swing right/left;
7. arm extension.

In this work, the test cycle presented in [17] was used as a reference duty-cycle to design the electric machine for the hybridization of the excavator powertrain. Starting from the required energy needed to execute the work cycle, the average requested power for each work cycle task was calculated by dividing the energy by the task duration time. After that, the electric machine work cycle power was derived from the bucket excavator reference

TABLE 1.2: Digging trech test cycle specifications.

ICE speed	$2200\,\mathrm{min}^{-1}$
ICE power	14.5 kW
ICE torque	63 N m
Electric machine speed	$2200\,\mathrm{min}^{-1}$
Electric machine RMS torque	14 N m
Electric machine peak torque	21 N m
Electric machine peak power	5 kW

TABLE 1.3: Electric machine specifications and constraints.

DC bus voltage	48 V
Number of three-phase sets	4
Poles/Slots	20p/24s
Rated speed	$3600\,\mathrm{min}^{-1}$
Rated electric frequency	600 Hz
Rated torque	20 N m
Rated current density	$3.5\,\mathrm{A_{rms}/mm^2}$
Winding type	FSCW - Single Layer
Maximum active outer diameter	300 mm
Maximum active axial length	30 mm
Winding temperature	140 °C
Magnets temperature	100 °C

work cycle by subtracting the constant ICE output power contribution. As discussed at the beginning, it was chosen to let the ICE operate at a fixed operating point, as to maximize efficiency, Table 1.2. The ICE speed was chosen in order to fall in the range between $2000\,\mathrm{min}^{-1}$ and $3000\,\mathrm{min}^{-1}$ in order to reduce the specific consumption and the final choice fell on the value of $2200\,\mathrm{min}^{-1}$, considered to be a good compromise between efficiency and engine durability. Once the engine operating speed regime was defined, the constant power output was obtained from the power-speed characteristic of Figure 1.2 and the electric machine work cycle torque was obtained, Figure 1.11(a). The electric machine specifications were defined according to the RMS torque and the maximum ICE speed: the rated torque was chosen to be slightly higher than the work cycle RMS torque while the electric machine rated speed was imposed equal to the maximum ICE speed regime, Table 1.3. An important consideration when facing the electric machine design is given the following: earth-moving machinery like excavators can be subjected to unexpected heavy tasks and abuse due to sudden earth obstacles that anyway must be overcome. For this reason the hybrid powertrain must be designed in order to be able to face these unexpected torque tasks without any sort of problems and this is why it is very important to design the electric machine with a reasonable overload capability. An additional constraint was given by the DC bus operating voltage which was imposed equal to 48 V,

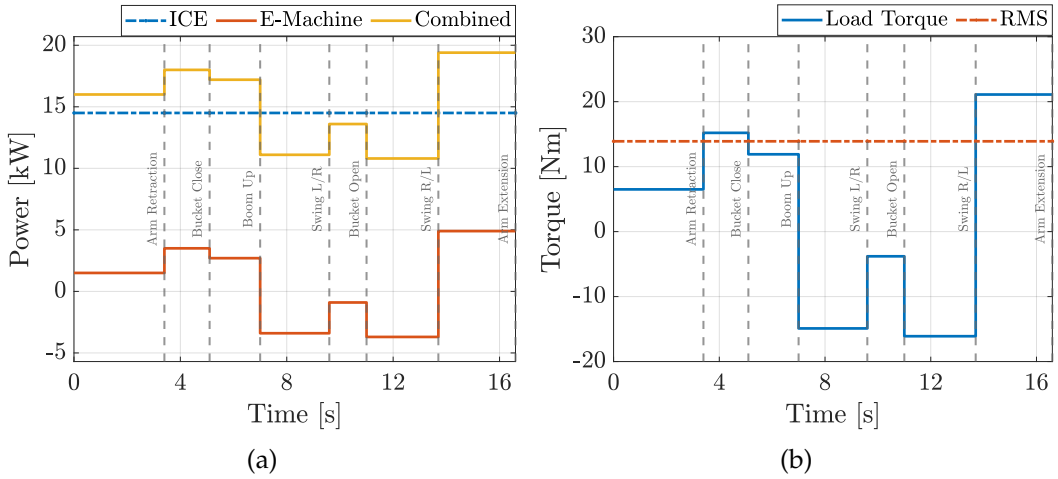

FIGURE 1.11: Electric machine power duty-cycle (a) and torque duty-cycle (b) for each task of the trench digging work cycle.

TABLE 1.4: Machine materials.

Stator lamination	Cogent NO20
Winding	Copper
Magnets	N45UH
Rotor back-iron	Stainless Steel (solid)
Shaft	Iron
Housing	Aluminium (Alloy 195 Cast)

which is the typical voltage of a mild-hybrid powertrain. The rationale behind this choice is primarily related to the fact that heavy machinery and diesel engine manufacturers have a limited know-how in the electrification field and therefore the aim is to avoid the complications associated with the high-voltages, in both the machine side and the human side as for example: electric shock hazard, machine winding insulation, electromagnetic compatibility. The major drawback of employing a low voltage drive is the high phase current which arise in case of a high power application: in this case, a high number of power devices in parallel must be employed for the three-phase converters feeding the machine. In this case, the use of a multi-three-phase machine can be useful to divide the phase current into multiple parallel paths, each of which connected to a three-phase converter. The chosen place of integration of the electric machine in the powertrain transmission consists in specific installation requirements, ambient operating temperature and machine size constraints which must be carefully taken into account in the design phase. Indeed, the P1 position between the internal combustion engine and the clutch, as shown in Figure 1.3, limits the volume available for the electric machine which translates into specific limits for the outer diameter, but especially for the maximum axial length.

TABLE 1.5: Machine geometric parameters.

Dimensions		**Masses**	
Housing outer diameter	300 mm	Stator lamination	4.8 kg
Active outer diameter	270 mm	Rotor lamination	1.1 kg
Active axial length	30.0 mm	Winding	2.5 kg
Stator bore	178.7 mm	Magnets	0.5 kg
Stator tooth	15.6 mm	Shaft	5.1 kg
Stator yoke	8.7 mm	Housing (air cooling)	0.7 kg
Opening slot	0.5 mm	Housing (liquid cooling)	1.6 kg
Slot height	37.0 mm	Total (air cooling)	18.6 kg
Slot Area	450 mm^2	Total (liquid cooling)	21.3 kg
Airgap	0.6 mm		
Magnets width	4.2 mm		
Shaft diameter	150.5 mm		

1.2.4 Numerical Validation

Provided the specifications and constraints summarized in Table 1.3, the design of the machine was first carried out by using an analytical approach in order to define the main parameters such as number of turns per phase, stator bore, magnets width and the other stator geometric parameters, resulting in the results of Table 1.5 while in Table 1.6 the electrical data of the machine is provided. In order to keep the iron losses low and given the high electric frequency, up to 600 Hz, it was chosen to use the *Cogent NO20*, with a lamination thickness of 0.2 mm, for the stator. On the other hand, given the high ambient temperature, the magnets were made with a NdFeB alloy and more specifically using the *N45UH* magnets. The rotor back-iron was assumed as a solid component made of a stainless steel, as summarized in Table 1.4. Thanks to the segmented stator structure permitted by the fractional-slot winding configuration, it was possible to adopt a quasi-closed slot geometry: this option gave the possibility to reduce the flux space modulation at the airgap and therefore to reduce the magnet losses. Another choice was to keep the rated current density small in order to limit the winding losses and reduce the heat produced in the stator. Following the analytical design phase, several finite element analysis (FEA) simulations were carried out to adjust the final geometry and analyze the machine performance. Finally, the thermal simulation of the machine was conducted in order to estimate the temperatures of the different parts. The FEA simulations were carried out by using Altair®Flux®and Altair®FluxMotor®, while the thermal simulations were made by using Ansys Motor-CAD. As the efficiency map depicted in Figure 1.12 shows, the machine features the maximum efficiency of 92 % when delivers the rated torque of 20 N m and rotating at a speed between 600 min^{-1} and 1200 min^{-1} approximately. Anyway, a large region is characterized by an efficiency above 90 %. The FEA simulations were carried out to analyze the machine behavior in the 7 different tasks of the trench digging test cycle and for each task the simulations were aimed at calculating the losses in the

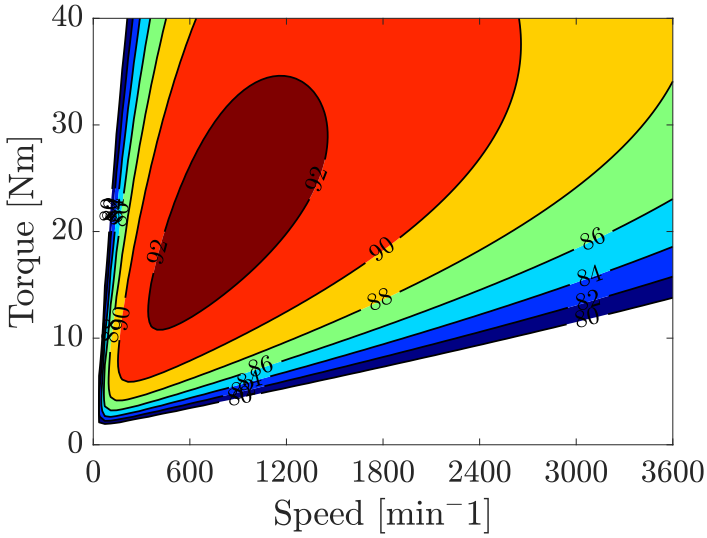

FIGURE 1.12: Machine efficiency map.

TABLE 1.6: Machine winding and electrical data.

Conductors per phase (one set)	8
Conductors per slot	4
Wire type	AWG 16
Parallel strands for each conductor	31
Conductor cross-section	40.6 mm^2
Gross fill-factor	36 %
Rated current (one set)	140 A_{rms}
Magnets remanence	1.21 T

stator iron, in the winding and in the magnets. Two different sets of FEA simulations were carried out: in the first one the currents were considered perfectly sinusoidal and a dq model was used to impose the desired current: the i_{sd} current of each three-phase set was set to zero while the i_{sq} currents were obtained by starting from the required torque for each task. The simulation conditions are summarized in Table 1.7. In this analysis, the machine

TABLE 1.7: FEA simulation parameters, with $i_{sd} = 0$.

Task	i_{sq} **(one set)**	**Speed**	**Temperatures**	
			Winding	**Magnets**
Arm Extension	36 A_{rms}			
Swing R/L	76 A_{rms}			
Bucket Open	61 A_{rms}			
Swing L/R	-63 A_{rms}	2200 min^{-1}	140 °C	100 °C
Boom Up	-12 A_{rms}			
Bucket Close	-69 A_{rms}			
Arm Retraction	103 A_{rms}			

TABLE 1.8: PLECS simulation parameters.

Machine		**Regulators**	
Phase resistance	0.54 m Ω	Current K_p (d, q)	(0.0104,0.0078)
Inductances (L_d, L_q)	1.66 µH, 1.25 µH	Current K_i	3.36
Magnets' linked flux	2.55 mWb	Speed K_p	143.5
Switching frequency	25 kHz	Speed K_i	3500
Shaft inertia	8.03 gm^2	Speed saturation	1000 A_{rms}
Friction constant	5.27 mN m s		

TABLE 1.9: PLECS simulation reference torque and speed for each task, with $i_{sd,ref} = 0$.

Task	**Load Torque Reference**	**Speed Reference**
Arm Extension	6.5 N m	
Swing R/L	15.2 N m	
Bucket Open	11.9 N m	
Swing L/R	−14.9 N m	2200 min^{-1}
Boom Up	−3.8 N m	
Bucket Close	−16.1 N m	
Arm Retraction	21.1 N m	

was supposed to work in a balanced condition, where all the three-phase sets are healthy therefore the same i_{sq} current was used for all the sets. In the second set of simulations the aim was to assess the impact of the PWM current ripple on the machine losses and on the torque ripple and consequently use analyze the thermal behavior of the machine with more realistic values. In order to do so, the three-phase currents with PWM were obtained by means of a 1-D numerical model built in Plexim PLECS® environment by using a field oriented control, the parameters used for the PLECS simulation are summarized in Table 1.8. For each task, the reference speed of 2200 min^{-1} was set for the speed controller, while at the machine shaft the load torque shown in Figure 1.11(b) and summarized in Table 1.9, was imposed. A balanced operation was supposed, meaning that all the three-phase sets were subjected to the same phase current. The comparison of the electromagnetic torque ripple with and without the PWM on the phase currents are shown in Figure 1.13 where it is clear that the PWM causes an appreciable increment on the torque ripple. In Figure 1.14 is shown the comparison of the losses and the efficiency calculated in the two cases: the PWM produces a considerable increment of the machine total losses, especially for the winding AC component an thus a reduction of the overall efficiency in all the tasks is observed.

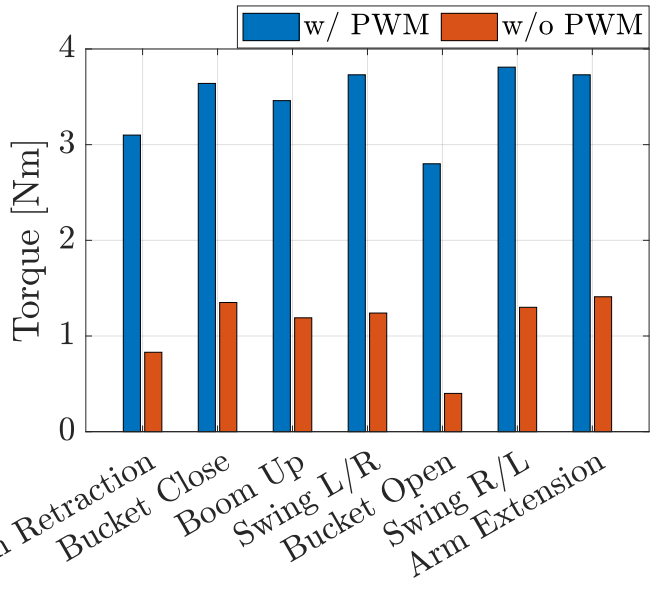

FIGURE 1.13: Electromagnetic torque ripple with and without PWM ripple on the machine phase currents.

1.2.4.1 Machine thermal behavior

The machine thermal simulation was carried out in order to validate the assumptions made during the design phase, where a winding temperature of 140 °C and a magnet temperature of 100 °C were considered. The temperature evolution of each machine part was obtained with simulations in Ansys Motor-CAD by using the average loss values for each work cycle, with and without the PWM on the phase currents, calculated by means of the FEA simulations shown before. The thermal simulation becomes particularly necessary when the machine operates in harsh environments as for example a under the hood application, where high ambient temperature arise quickly given the presence of the internal combustion engine: in this analysis the ambient temperature was assumed equal to 80 °C. In addition, the chosen position for the electric machine integration, which is between the internal combustion engine and the clutch, does not ensures an optimal heat exchange with the external ambient since a very little space is available for the machine, [18]. For this reasons, a potential torque derating could be introduced if some machine parts would reach non sustainable temperature: for example, the winding insulation class defines the maximum temperature the insulation can endure with a reasonable life span, for each 10 °C temperature increment the insulation life is approximately halved. Not less important are the magnets: NdFeB alloys can usually operate up to 180 °C, but their remanence at high temperature is highly reduced (usually every 100 °C a 40 % reduction is observed) while SmCo alloys are rated for higher temperatures, but they are more expensive and also fragile (i.e. particular care is required during the manufacturing and installation process) The idea of the design was to keep the cooling system as simple as possible and for this reason a forced air cooling was implemented. The air flow speed was assumed

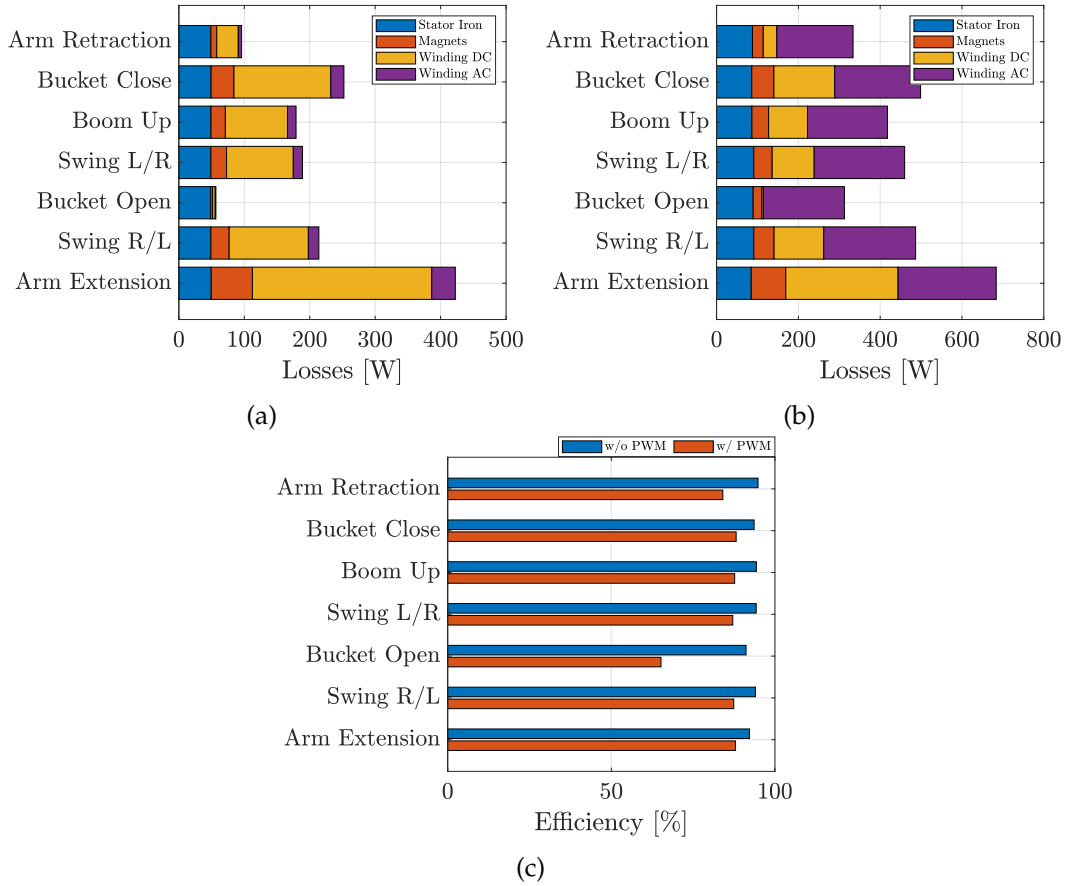

FIGURE 1.14: Machine losses in the work cycle (a) without PWM ripple and (b) with PWM ripple on the phase currents and efficiency comparison in the two cases (c) calculated at a winding temperature of 140 °C and a magnet temperature of 100 °C.

equal to $10\,\mathrm{m\,s^{-1}}$ and the machine housing was built by introducing a certain number of axial fins all over the circumference. The aim of the thermal simulations is to assess the machine steady-state temperature after repeating a certain number of the test cycle reported in Figure 1.16 to verify if the expected temperature limits are exceeded. The machine temperatures reach the steady-state condition after approximately 2 hours and, as expected, the hottest part is represented by the winding. Figure 1.17(c) shows the comparison of the maximum temperatures values, highlighting the effect the PWM ripple on the phase currents causes on the increment of the machine temperatures in all the different parts. Indeed, as Table 1.11 shows, there is a significant increase in the magnets and the winding temperatures because of the high-frequency PWM ripple. The maximum admissible temperature for a NdFeB alloy type magnet is usually up to approximately 180 °C therefore the obtained temperature value falls in the safe zone. On the other hand, the winding insulation must be chosen at least of class H type, which is rated for a maximum temperature of 180 °C. It should be noted that the winding and magnets temperature used for the FEA analysis considering the PWM on the phase currents were imposed equal to 140 °C and 100 °C respectively.

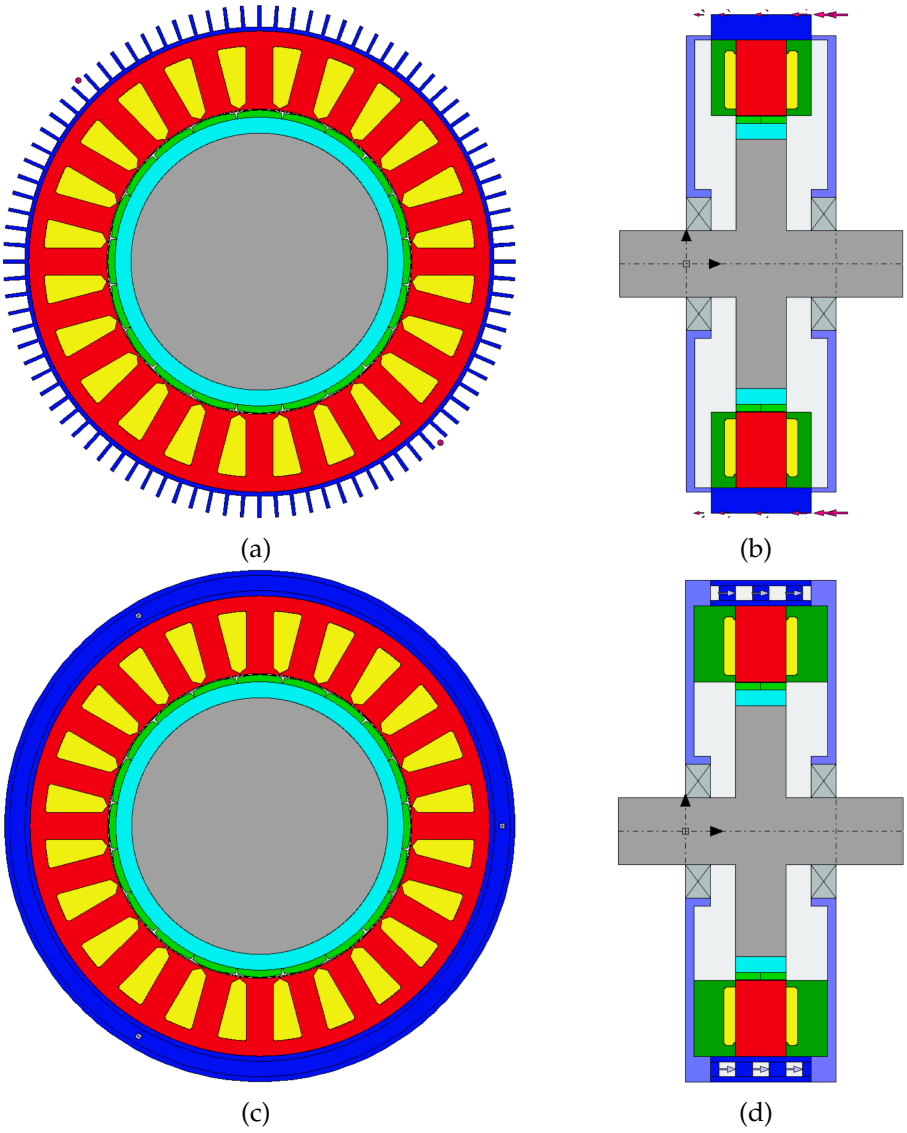

FIGURE 1.15: Front and axial view of the machine from Ansys MotorCAD: (a) air cooled front view; (b) air cooled axial view; (c) liquid cooled front view; (d) liquid cooled axial view. The same housing outer diameter was used for both the versions of the machine.

However, since the machine steady-state temperature with the PWM losses are higher, the actual losses are higher than the actual values used for the thermal analysis. This problem is due to different factors: firstly, the low fill-factor causes a reduction of the actual thermal dissipation capability of the winding since the slot impregnation material thermal conductivity is a lot lower than the copper one. Secondly, the adoption of standard impregnation and potting material does not ensures a proper thermal exchange with the machine housing and better materials (featuring better thermal characteristics) should be used. It is then expected that the actual machine temperature would be much higher and for this reason the cooling system was modified by adopting a liquid cooling method in place of the forced convection one.

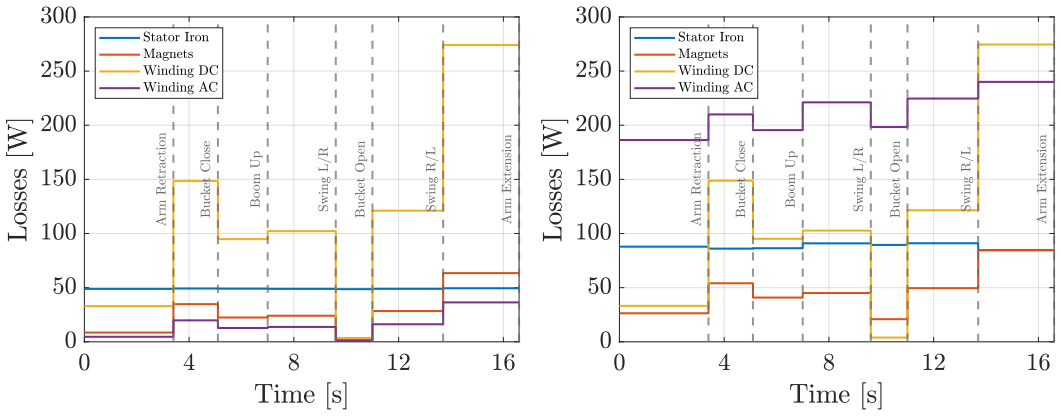

FIGURE 1.16: (a) losses without PWM and and (b) losses with PWM ripple for a trench digging test cycle calculated at a 140 °C winding temperature and a 100 °C magnet temperature.

TABLE 1.10: Motor-CAD simulation parameters.

Air Cooling		**Water Jacket**	
Ambient Temperature		80 °C	
Air flow speed	10 m s^{-1}	Coolant flow rate	4 L min^{-1}
		Coolant type	EGW 50/50
		Coolant temperature	60 °C
		WJ channel height	9 mm
		WJ channel width	10 mm
		WJ channel spacing	10 mm
Conductivity Coefficients [W m^{-1} K^{-1}]			
Winding		401	
Housing		168	
Stator lamination		27	
Shaft		52	
Rotor back-iron		25	
Winding impregnation		0.2	
Wire insulation		0.2	
Slot liner		0.2	
Rotor banding		0.2	
End-Winding potting		0.3	

For this purpose a spiral water jacket was implemented on the machine housing featuring a 50/50 water-glycol fluid with an inlet temperature of 60 °C. The thermal simulation was carried out by considering the same ambient temperature of 80 °C and a fluid volume rate equal to 4 L/min. As the Figure 1.18 shows the new cooling method ensures a sensible reduction on the maximum temperature on the winding hotspot, which falls under the design target of 140 °C, and also on the magnets, whose steady-state temperature is

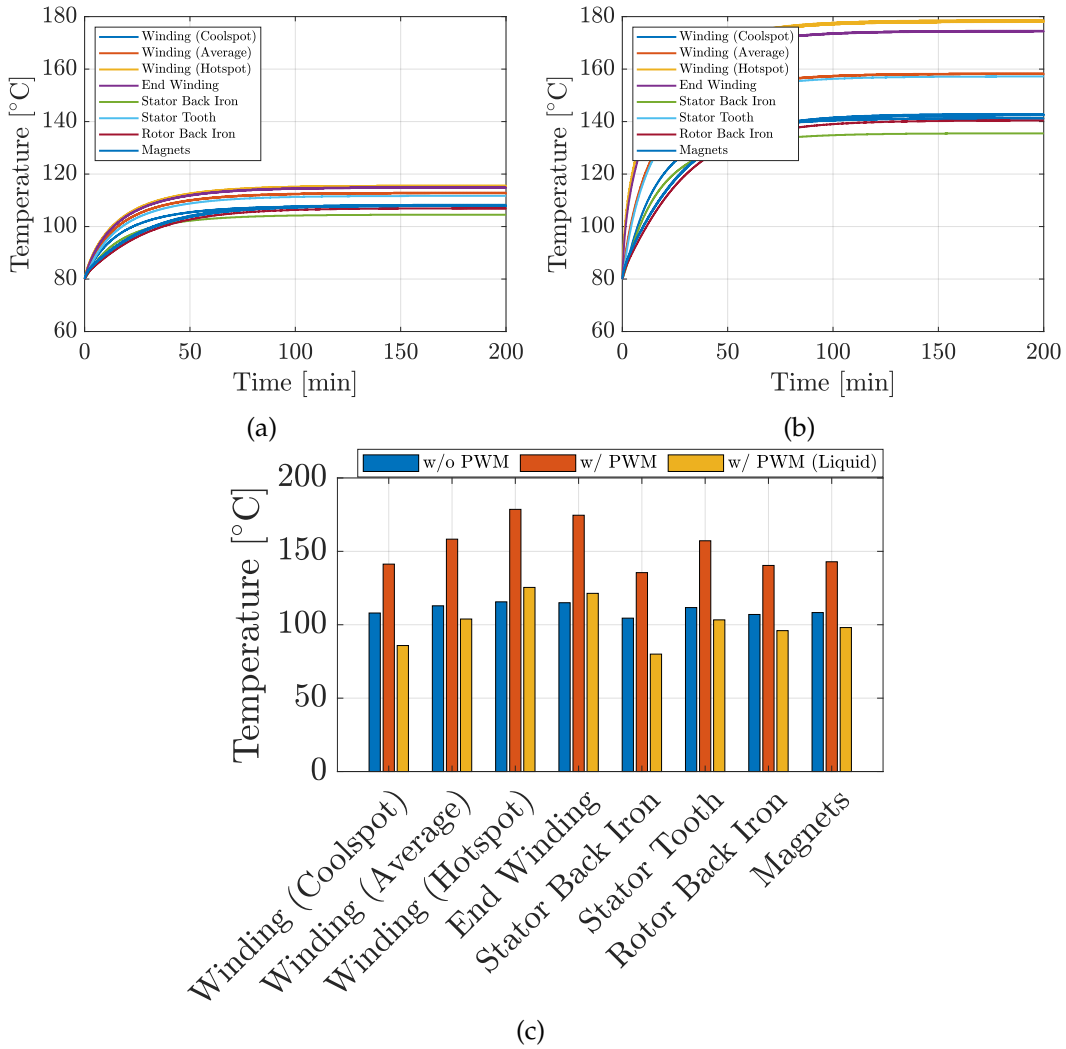

FIGURE 1.17: Machine temperatures after 800 work cycles (a) without PWM ripple and (b) with PWM ripple on the phase currents.

below the design value of 100 °C.

1.2.5 Airgap radial force analysis in fault conditions

The main advantage of a multi-three-phase electric drive is the inherent fault operation capability. Indeed, if one phase fails (in the machine winding or in the inverter) there is the possibility to exclude the corresponding three-phase set and allow the electric machine to operate with the remaining healthy sets, even though the output power rating is reduced. The fault-tolerance of a multi-three-phase machine is directly tied to the number of sets which compose the winding and thus on the number of three-phase converters supplying the machine. The higher is the number of three-phase modules (the union of a three-phase set and a three-phase converter), the lower is the torque derating and the higher is the number of faults the machine can

TABLE 1.11: Machine steady-state temperatures with and without superimposed PWM ripple on the phase currents.

	w/o PWM	**w/ PWM**	**w/PWM (Liquid)**
Winding (Coolspot)	108 °C	141 °C	86 °C
Winding (Average)	113 °C	158 °C	104 °C
Winding (Hotspot)	116 °C	179 °C	125 °C
End Winding	115 °C	175 °C	121 °C
Stator Back Iron	105 °C	136 °C	80 °C
Stator Tooth	112 °C	157 °C	103 °C
Rotor Back Iron	107 °C	140 °C	96 °C
Magnets	108 °C	143 °C	98 °C

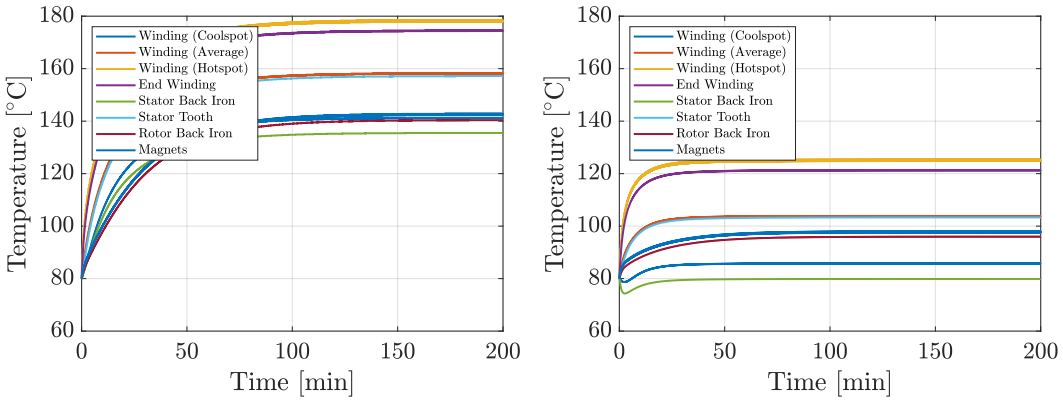

FIGURE 1.18: Machine temperatures after 800 work cycles considering the PWM on the phase currents: (a) with forced air blown cooling and (b) with liquid cooling.

sustain. However, as discussed earlier it is important to avoid the physical fault propagation from one set to another and this is made possible by adopting single-layer winding arrangements which avoid the coexistence of phases of different sets into the same slot. In addition, in order to reduce the mutual coupling between the sets it is important to adopt a fractional-slot concentrated winding with a sectorized distribution of the sets along the stator circumference. This allows to minimize the mutual inductance and thus the minimum interaction between the sets also in fault conditions, but at the cost of an unbalance in the magnetomotive force (MMF) at the airgap. The unbalance in the airgap's MMF produces a pulling force on the rotor which can be problematic for the bearings' mechanical resistance resulting also in a possible eccentricity of the rotor, which in turn causes vibration and noise issues. In the worst case, a bearings failure can occur with the consequent rotor-stator rubbing and ultimately the destruction of the electrical machine.

In order to analyze the behavior of the machine in case of fault, different finite element analysis were carried out with different fault scenarios. In Figure 1.19 the considered fault cases are shown, each case is characterized

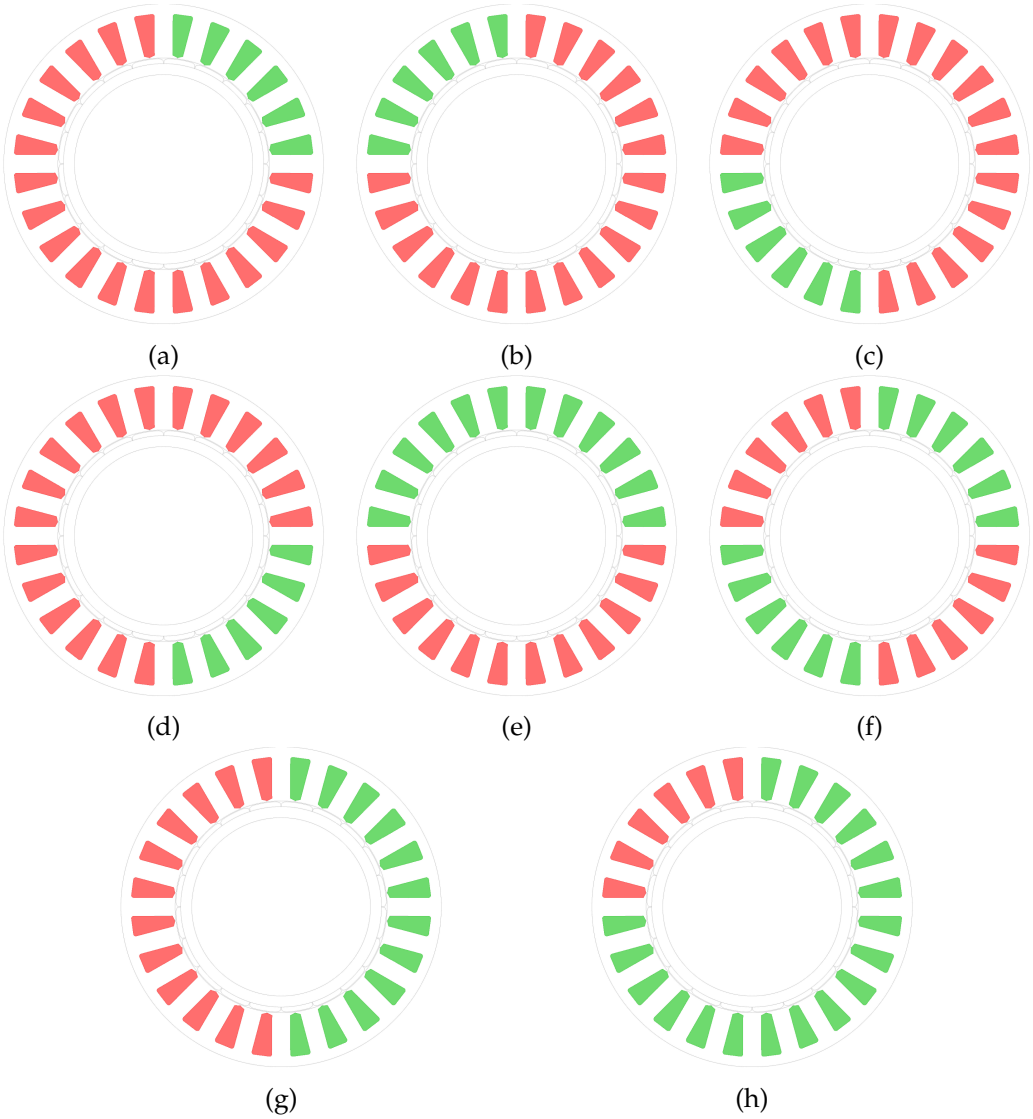

FIGURE 1.19: Fault cases: (a) HFFF (b) FHFF (c) FFHF (d) FFFH (e) HHFF (f) HFHF (g) HFFH (h) HFHH. The three-phase sets are ordered in the anti-clockwise direction.

by 4 letters and each position is correspondent to a three-phase set: one set can be healthy (H) or faulty (F). If the set is healthy then it is supplied with a constant i_{sq} current ($i_{sd} = 0$) while if the set is faulty then $i_{sq} = 0$. The sets are displaced along the stator circumference in anticlockwise direction, as presented in Figure 1.6. For example, the case HFHF correspond to the scenario where the sets 1 and 3 are healthy while the sets 2 and 4 are faulty. It is important to point out that only the radial force aspect was taken into account in this analysis and the effect of the mutual coupling between the sets in case of fault was not studied however, given the sectorized winding arrangement, it is expected that the mutual inductances between the three-phase sets would be very low. Figure 1.20 shows in the XY plane the resulting force acting on the rotor and in the different fault scenarios considered. In Figure 1.20(a) for example, only one set is healthy: the resulting force on

the rotor is 90° out of phase with respect to the active three-phase set. The Table 1.12 summarizes the results of the FEA simulations: for each fault case the maximum amplitude force, the average torque and the percentage torque ripple are summarized. As the table shows, the worst case scenario is represented by the cases HFFH and HHFF, i.e. when two adjacent sets are faulty, causing a total pulling force of 287 N on the rotor. On the contrary, when the two faulty sets are opposite, i.e. case HFHF, the radial force is zero however the resulting torque ripple is the highest among all the fault scenarios. On the other hand, the cases with only one set healthy are characterized by the same

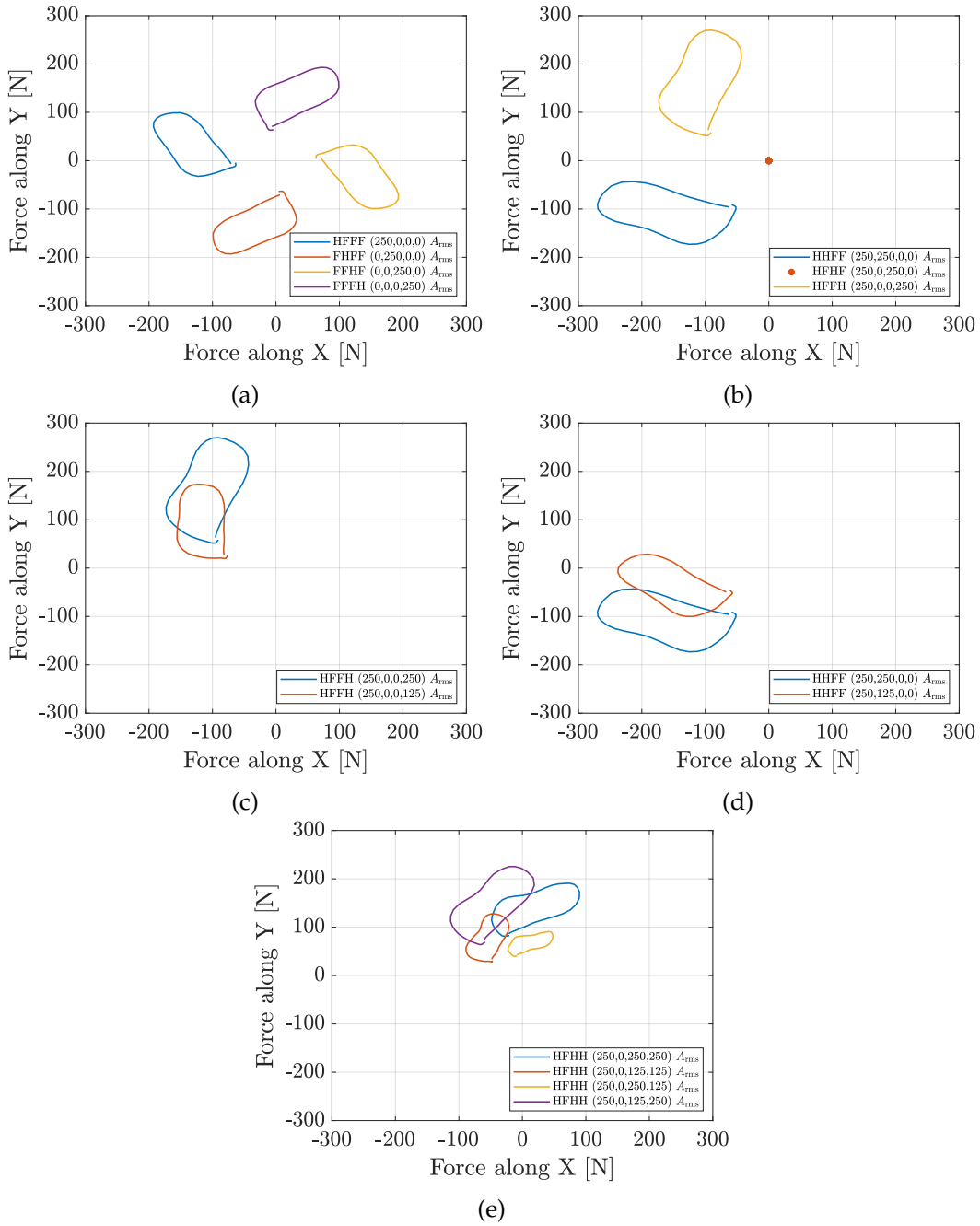

FIGURE 1.20: Airgap radial force amplitude versus rotor position in different fault conditions.

TABLE 1.12: Machine maximum airgap radial force amplitude and maximum electromagnetic torque in different fault conditions.

Case	i_{sq} [A_{rms}]				**Max F** [N]	**Torque**	
	Set 1	**Set 2**	**Set 3**	**Set 4**		**Avg.** [N m]	**Ripple** [%]
HFFF	250	0	0	0	208	12.6	5.7
FHFF	0	250	0	0	208	12.6	5.7
FFHF	0	0	250	0	208	12.6	5.7
FFFH	0	0	0	250	208	12.6	5.7
HFHF	250	0	250	0	0	25.3	7.0
HFFH	250	0	0	250	287	25.0	3.5
	250	0	0	125	218	19.0	2.4
HHFF	250	250	0	0	287	25.0	3.5
	250	125	0	0	234	19.0	3.3
HFHH	250	0	250	250	205	37.5	3.2
	250	0	125	125	137	25.5	3.3
	250	0	250	125	101	31.6	2.9
	250	0	125	250	226	31.5	2.9

force, as expected. As expected, the table also shows that the machine torque is proportional to the number of active sets, confirming the machine derating when it operates under faulty conditions. The HFHH scenario was analyzed by considering different combinations of the i_{sq} and it can be observed that if two of the three-remaining sets are fed with half of the current of the other one then the radial force is halved. On the other hand, feeding the opposite set with half of the current of two adjacent sets causes an increment of the pulling force. It is worth noticing that, in all the cases the percentage torque ripple does not change significantly.

1.3 A Multifunctional Converter System for an Electric Forklift

The Multi-Functional Converter System is a new kind of electric drive which allows to integrate a boost converter into a traditional electric drive composed of a battery, a DC link, a three-phase inverter and a three-phase machine. This topology exhibits an intrinsic three-phase DC-DC bi-directional boost converter which exploits the machine phase inductances to boost the battery voltage. As shown in Figure 1.21, the layout of the Multi-Functional Converter System (MFCS) is deeply different from a traditional drive, where the battery is connected directly to the DC link, in a MFCS the battery is connected to the star point of the machine winding hence the star point must be physically accessible. Since the battery is connected between the star point and the inverter ground, the voltage of the neutral point with respect to the ground is equal to the battery voltage: this causes the circulation of a homopolar current which contains triplen and switching harmonics components which increase the rms value of the phase currents and also their harmonic distortion. This fact can negatively affect the losses and the performance of both the machine the inverter, in which the homopolar current

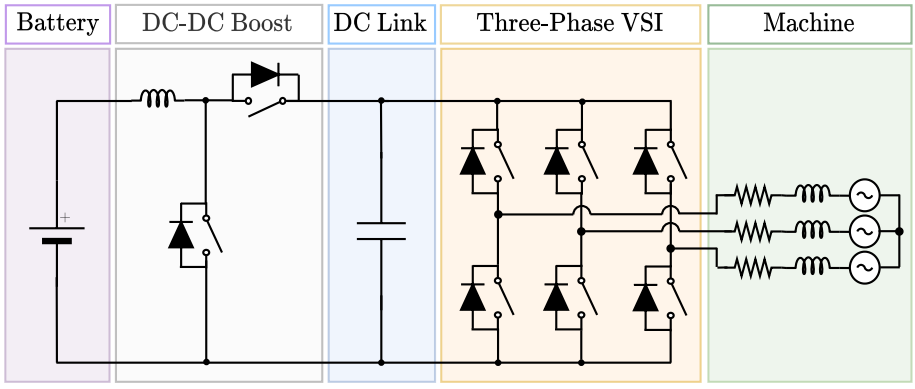

(a)

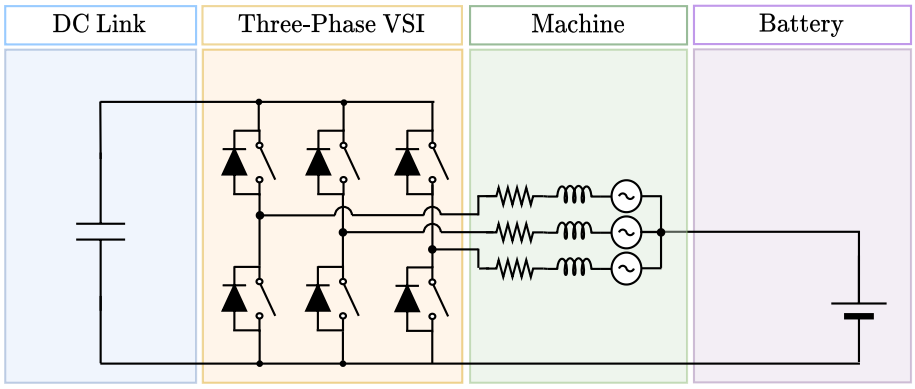

(b)

FIGURE 1.21: Electric scheme of: (a) traditional architecture with a DC-DC boost stage and (b) Multi-Functional Converter System.

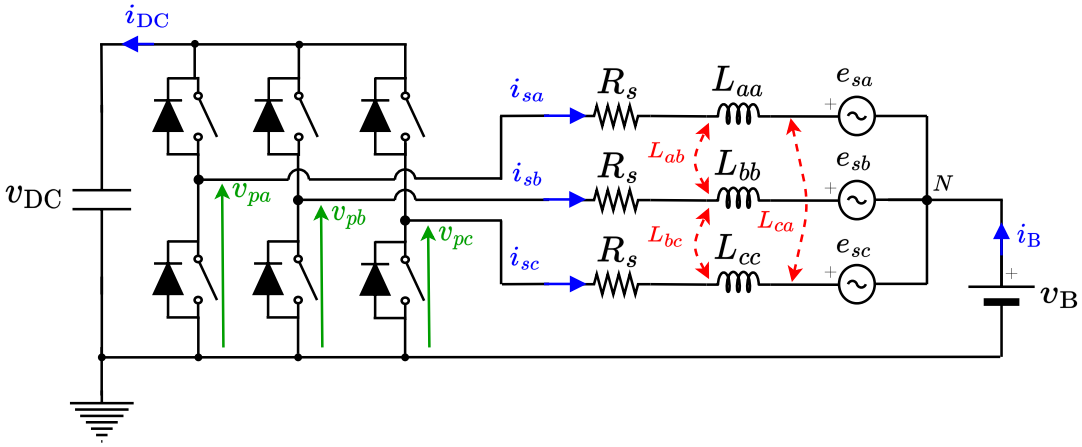

FIGURE 1.22: Electric scheme of a multi-functional converter system.

causes an unbalance in the losses distribution and the consequent increased damage in some of the solid-state devices.

The analysis of the MFCS was carried out with a first analytical insight of the machine equations to analyze the harmonic content of the machine phase and battery currents. Following the analytical examination, the requirements and specifications of the electrical machine were defined for the case study of a 5-ton hydraulic forklift electrification. The machine design was carried out in order to exploit the advantages of the MFCS architecture.

1.3.1 Machine Equations

Figure 1.22 shows the schematic of a Multi-Functional Converter System (MFCS) which will be analyzed in the following in order to find the relationship between the battery voltage and the DC bus voltage, but also the expression of the battery current i_B. The mathematical analysis of the MFCS starts by considering the single phases of the machines and the self and mutual coupling between them. In fact, since the sum of the phase currents is not zero, it cannot be defined a synchronous inductance for the phase voltage expressions. The machine phase voltages can be written as:

$$\begin{bmatrix} v_{sa} \\ v_{sb} \\ v_{sc} \end{bmatrix} = R_s \begin{bmatrix} i_{sa} \\ i_{sb} \\ i_{sc} \end{bmatrix} + \frac{d}{dt} \begin{bmatrix} \lambda_{sa} \\ \lambda_{sb} \\ \lambda_{sc} \end{bmatrix} \tag{1.11}$$

where $[v_{sa}\ v_{sb}\ v_{sc}]^T$ are the phase voltages, $[i_{sa}\ i_{sb}\ i_{sc}]^T$ are the phase currents, $[\lambda_{sa}\ \lambda_{sb}\ \lambda_{sc}]^T$ are the linked fluxes and R_s is the phase resistance. In addition, it is easy to see that:

$$i_{sa} + i_{sb} + i_{sc} = -i_B \tag{1.12}$$

where i_{B} is the battery current. The relationship between the phase voltages and the inverter's leg voltages $[v_{pa}\ v_{pb}\ v_{pc}]^T$ is given by:

$$\begin{bmatrix} v_{sa} \\ v_{sb} \\ v_{sc} \end{bmatrix} = \begin{bmatrix} v_{pa} \\ v_{pb} \\ v_{pc} \end{bmatrix} - \begin{bmatrix} v_{\mathrm{B}} \\ v_{\mathrm{B}} \\ v_{\mathrm{B}} \end{bmatrix} \tag{1.13}$$

where v_{B} is the neutral voltage, given by the battery, with respect to the inverter ground. By exploiting the (1.13), the (1.11) becomes:

$$\begin{bmatrix} v_{pa} \\ v_{pb} \\ v_{pc} \end{bmatrix} - \begin{bmatrix} v_{\mathrm{B}} \\ v_{\mathrm{B}} \\ v_{\mathrm{B}} \end{bmatrix} = R_s \begin{bmatrix} i_{sa} \\ i_{sb} \\ i_{sc} \end{bmatrix} + \frac{d}{dt} \begin{bmatrix} \lambda_{sa} \\ \lambda_{sb} \\ \lambda_{sc} \end{bmatrix} \tag{1.14}$$

At steady-state, considering a Field Oriented Control (FOC) the machine phase currents can be written as:

$$\begin{bmatrix} i_{sa} \\ i_{sb} \\ i_{sc} \end{bmatrix} = I_s \begin{bmatrix} -\sin(\theta_e + \gamma) \\ -\sin(\theta_e + \gamma - \frac{2\pi}{3}) \\ -\sin(\theta_e + \gamma + \frac{2\pi}{3}) \end{bmatrix} + \begin{bmatrix} -i_{\mathrm{B}}/3 \\ -i_{\mathrm{B}}/3 \\ -i_{\mathrm{B}}/3 \end{bmatrix} \tag{1.15}$$

where I_s is the amplitude of the fundamental component, responsible for the torque production and γ is the control angle. The angle $\theta_e = \omega_e t$ is the position of the rotor magnetic axis, ω_e is the electrical pulsation (or electrical speed of the rotor. The machine equations can be written in a compact form as:

$$\mathbf{v}_p - \mathbf{v}_{\mathrm{B}} = R_s \mathbf{i}_s + \frac{d\boldsymbol{\lambda}_s}{dt} \tag{1.16}$$

where:

$$\mathbf{v}_p = \begin{bmatrix} v_{pa} \\ v_{pb} \\ v_{pc} \end{bmatrix}, \quad \mathbf{v}_{\mathrm{B}} = \begin{bmatrix} v_{\mathrm{B}} \\ v_{\mathrm{B}} \\ v_{\mathrm{B}} \end{bmatrix}, \quad \mathbf{i}_s = \begin{bmatrix} i_{sa} \\ i_{sb} \\ i_{sc} \end{bmatrix}, \quad \boldsymbol{\lambda}_s = \begin{bmatrix} \lambda_{sa} \\ \lambda_{sb} \\ \lambda_{sc} \end{bmatrix} \tag{1.17}$$

are the phase voltages vector, the battery voltage vector, the phase currents vector and the linked fluxes vector. The linked fluxes can be expressed is the following way:

$$\begin{bmatrix} \lambda_{sa} \\ \lambda_{sb} \\ \lambda_{sc} \end{bmatrix} = \begin{bmatrix} L_{aa} & L_{ab} & L_{ca} \\ L_{ab} & L_{bb} & L_{bc} \\ L_{ca} & L_{bc} & L_{cc} \end{bmatrix} \begin{bmatrix} i_{sa} \\ i_{sb} \\ i_{sc} \end{bmatrix} + \begin{bmatrix} \lambda_{\mathrm{M}a} \\ \lambda_{\mathrm{M}b} \\ \lambda_{\mathrm{M}c} \end{bmatrix} \tag{1.18}$$

the phase back electromotive forces (back-EMFs) are equal to:

$$\begin{bmatrix} e_{sa} \\ e_{sb} \\ e_{sc} \end{bmatrix} = \frac{d}{dt} \begin{bmatrix} \lambda_{\mathrm{M}a} \\ \lambda_{\mathrm{M}b} \\ \lambda_{\mathrm{M}c} \end{bmatrix} \tag{1.19}$$

The linked fluxes can be written in a compact form as:

$$\boldsymbol{\lambda}_s = \mathbf{L}_s \mathbf{i}_s + \boldsymbol{\lambda}_{\mathrm{M}} \tag{1.20}$$

where:

$$\mathbf{L}_s = \begin{bmatrix} L_{aa} & L_{ab} & L_{ca} \\ L_{ab} & L_{bb} & L_{bc} \\ L_{ca} & L_{bc} & L_{cc} \end{bmatrix}, \quad \boldsymbol{\lambda}_{\mathrm{M}} = \begin{bmatrix} \lambda_{\mathrm{M}a} \\ \lambda_{\mathrm{M}b} \\ \lambda_{\mathrm{M}c} \end{bmatrix} \tag{1.21}$$

are the inductance matrix and the magnets' linked flux vector respectively. According to [19], the following expressions can be written for the self and mutual inductances:

$$\begin{aligned}
L_{aa}(\theta_e, i_{sa}) &= L_\sigma + L_{s0}(i_{sa}) + \sum_{\rho=2,4,\ldots}^{\infty} L_{s\rho}(i_{sa}) \cos(\rho\theta_e) \\
L_{bb}(\theta_e, i_{sb}) &= L_\sigma + L_{s0}(i_{sb}) + \sum_{\rho=2,4,\ldots}^{\infty} L_{s\rho}(i_{sb}) \cos(\rho\theta_e - \rho\frac{2\pi}{3}) \\
L_{cc}(\theta_e, i_{sc}) &= L_\sigma + L_{s0}(i_{sc}) + \sum_{\rho=2,4,\ldots}^{\infty} L_{s\rho}(i_{sc}) \cos(\rho\theta_e + \rho\frac{2\pi}{3}) \\
L_{ab}(\theta_e, i_{sa}) &= -L_{m0}(i_{sa}) + \sum_{\rho=2,4,\ldots}^{\infty} L_{m\rho}(i_{sa}) \cos(\rho\theta_e + \rho\frac{2\pi}{3}) \\
L_{bc}(\theta_e, i_{sb}) &= -L_{m0}(i_{sb}) + \sum_{\rho=2,4,\ldots}^{\infty} L_{m\rho}(i_{sb}) \cos(2\rho\theta_e) \\
L_{ca}(\theta_e, i_{sc}) &= -L_{m0}(i_{sc}) + \sum_{\rho=2,4,\ldots}^{\infty} L_{m\rho}(i_{sc}) \cos(\rho\theta_e - \rho\frac{2\pi}{3})
\end{aligned} \tag{1.22}$$

where L_σ is the stator leakage inductance, L_{s0} is the self-inductance average value, $L_{s\rho}$ is the amplitude of the ρ-th harmonic of the self-inductance, L_{m0} is the mutual-inductance average value and $L_{m\rho}$ is the amplitude of the ρ-th harmonic of the mutual inductance. The magnets' linked fluxes depend on the rotor position and they can be written as the sum of a fundamental component and other infinite harmonic components:

$$\begin{bmatrix} \lambda_{\mathrm{M}a} \\ \lambda_{\mathrm{M}b} \\ \lambda_{\mathrm{M}c} \end{bmatrix} = \Lambda_{\mathrm{M1}} \begin{bmatrix} \cos(\theta_e) \\ \cos(\theta_e + \frac{2\pi}{3}) \\ \cos(\theta_e - \frac{2\pi}{3}) \end{bmatrix} + \sum_{\rho=2}^{\infty} \Lambda_{\mathrm{M}\rho} \begin{bmatrix} \cos(\rho\theta_e) \\ \cos(\rho\theta_e + \rho\frac{2\pi}{3}) \\ \cos(\rho\theta_e - \rho\frac{2\pi}{3}) \end{bmatrix} \tag{1.23}$$

where $\Lambda_{\mathrm{M1}} = NK_{w1}K_{mag1}\Phi_{\mathrm{M1}}$ is the amplitude of the fundamental component and $\Lambda_{\mathrm{M}\rho} = NK_{w,\rho}K_{mag,\rho}\Phi_{\mathrm{M},\rho}$ is the amplitude of the ρ-th harmonic, N is the number of conductors per phase, $K_{w,\rho}$ is the ρ-th harmonic winding factor, $K_{mag,\rho}$ is the ρ-th harmonic magnets distribution factor and $\Phi_{\mathrm{M},\rho}$ is the ρ-th harmonic flux per pole.

In order to obtain the machine equations in the $dq0$ reference frame, the $abc \rightarrow dq0$ Park transform matrix is introduced:

$$\mathbf{P} = \frac{2}{3}\begin{bmatrix} \cos(\theta_e) & \cos(\theta_e - \frac{2\pi}{3}) & \cos(\theta_e + \frac{2\pi}{3}) \\ -\sin(\theta_e) & -\sin(\theta_e - \frac{2\pi}{3}) & -\sin(\theta_e + \frac{2\pi}{3}) \\ 1/2 & 1/2 & 1/2 \end{bmatrix} \tag{1.24}$$

By exploiting the (1.24), the following anti-transformations can be defined:

$$\begin{aligned} \mathbf{v}_p &= \mathbf{P}^{-1}\mathbf{v}_{pdq0} \\ \mathbf{v}_\mathrm{B} &= \mathbf{P}^{-1}\mathbf{v}_{\mathrm{B}dq0} \\ \mathbf{i}_s &= \mathbf{P}^{-1}\mathbf{i}_{sdq0} \\ \boldsymbol{\lambda}_s &= \mathbf{P}^{-1}\boldsymbol{\lambda}_{sdq0} \end{aligned} \tag{1.25}$$

where:

$$\mathbf{P} = \begin{bmatrix} \cos(\theta_e) & -\sin(\theta_e) & 1 \\ \cos(\theta_e - \frac{2\pi}{3}) & -\sin(\theta_e - \frac{2\pi}{3}) & 1 \\ \cos(\theta_e + \frac{2\pi}{3}) & -\sin(\theta_e + \frac{2\pi}{3}) & 1 \end{bmatrix} \tag{1.26}$$

and:

$$\mathbf{v}_{pdq0} = \begin{bmatrix} v_{pd} \\ v_{pq} \\ v_{p0} \end{bmatrix}, \mathbf{v}_{\mathrm{B}dq0} = \begin{bmatrix} 0 \\ 0 \\ v_\mathrm{B} \end{bmatrix}, \mathbf{i}_{sdq0} = \begin{bmatrix} i_{sd} \\ i_{sq} \\ i_{s0} \end{bmatrix}, \boldsymbol{\lambda}_{sdq0} = \begin{bmatrix} \lambda_{sd} \\ \lambda_{sq} \\ \lambda_{s0} \end{bmatrix} \tag{1.27}$$

Applying the Park transformation to the (1.20) yields to:

$$\boldsymbol{\lambda}_{sdq0} = \mathbf{L}_{dq0}\mathbf{i}_{sdq0} + \boldsymbol{\lambda}_{\mathrm{M}dq0} \tag{1.28}$$

The matrix $\mathbf{L}_{dq0} = \mathbf{P}\mathbf{L}_s\mathbf{P}^{-1}$ is the $dq0$ inductances while $\boldsymbol{\lambda}_{\mathrm{M}dq0}$ is the magnets' linked flux vector in the $dq0$ reference frame:

$$\mathbf{L}_{dq0} = \mathbf{P}\mathbf{L}_s\mathbf{P}^{-1} = \begin{bmatrix} L_d & 0 & 0 \\ 0 & L_q & 0 \\ 0 & 0 & L_0 \end{bmatrix}, \quad \boldsymbol{\lambda}_{\mathrm{M}dq0} = \begin{bmatrix} \lambda_{\mathrm{M}d} \\ \lambda_{\mathrm{M}q} \\ \lambda_{\mathrm{M}0} \end{bmatrix} \tag{1.29}$$

The $dq0$ inductances are a function of the rotor position θ_e and the $dq0$ currents and for the purpose of this work only the expression of the homopolar inductance is written hereafter, [19]:

$$L_0 = \frac{1}{3}(L_{aa} + L_{bb} + L_{cc}) + \frac{2}{3}(L_{ab} + L_{bc} + L_{ca}) \tag{1.30}$$

remembering the (1.22) yields to:

$$L_0 = L_\sigma + L_{s0} - 2L_{m0} \tag{1.31}$$

the expression above shows that the homopolar inductance does not depend on the rotor position. The linked fluxes in the expanded form are then equal

to:

$$\begin{bmatrix}\lambda_{sd}\\ \lambda_{sq}\\ \lambda_{s0}\end{bmatrix} = \begin{bmatrix}L_d & 0 & 0\\ 0 & L_q & 0\\ 0 & 0 & L_0\end{bmatrix}\begin{bmatrix}i_{sd}\\ i_{sq}\\ i_{s0}\end{bmatrix} + \begin{bmatrix}\lambda_{\mathrm{M}d}\\ \lambda_{\mathrm{M}q}\\ \lambda_{\mathrm{M}0}\end{bmatrix} \tag{1.32}$$

By applying the Park transformation to the (1.23), and by neglecting all the harmonics not multiple of 3, the magnets' linked flux vector in the $dq0$ reference frame can be written as:

$$\begin{bmatrix}\lambda_{\mathrm{M}d}\\ \lambda_{\mathrm{M}q}\\ \lambda_{\mathrm{M}0}\end{bmatrix} = \begin{bmatrix}\Lambda_{\mathrm{M}1}\\ 0\\ \sum_{\rho=3,6,\dots}^{\infty}\Lambda_{\mathrm{M}\rho}\cos(\rho\theta_e)\end{bmatrix} \tag{1.33}$$

by inserting the (1.33) into the (1.32) finally leads to:

$$\begin{bmatrix}\lambda_{sd}\\ \lambda_{sq}\\ \lambda_{s0}\end{bmatrix} = \begin{bmatrix}L_d i_{sd} + \Lambda_{\mathrm{M}1}\\ L_q i_{sq}\\ L_0 i_{s0} + \sum_{\rho=3,6,\dots}^{\infty}\Lambda_{\mathrm{M}\rho}\cos(\rho\theta_e)\end{bmatrix} \tag{1.34}$$

By applying the Park transformation matrix to the (1.16) the following expression is obtained:

$$\mathbf{v}_{pdq0} - \mathbf{v}_{Bdq0} = R_s\mathbf{i}_{sdq0} + \frac{d\boldsymbol{\lambda}_{sdq0}}{dt} + \mathbf{T}\boldsymbol{\lambda}_{sdq0} \tag{1.35}$$

where:

$$\mathbf{T} = \mathbf{P}\frac{d}{dt}[\mathbf{P}^{-1}] = \begin{bmatrix}0 & -\omega_e & 0\\ \omega_e & 0 & 0\\ 0 & 0 & 0\end{bmatrix} \tag{1.36}$$

The currents transformation from abc to $dq0$ is equal to:

$$\mathbf{i}_{sqd0} = \begin{bmatrix}i_{sd}\\ i_{sq}\\ i_{s0}\end{bmatrix} = \mathbf{P}\begin{bmatrix}i_{sa}\\ i_{sb}\\ i_{sc}\end{bmatrix} = \begin{bmatrix}-I_s\sin(\gamma)\\ I_s\cos(\gamma)\\ -i_{\mathrm{B}}/3\end{bmatrix} \tag{1.37}$$

which leads to:

$$i_{s0} = -\frac{i_{\mathrm{B}}}{3} \tag{1.38}$$

representing the relationship between the homopolar and the battery current.

1.3.2 "Embedded Boost" Input/Output Relation

As described in [20], in order to find the relationship between the neutral voltage and the DC bus voltage, the average relationship in the $dq0$ reference frame must be obtained. The average values are calculated within one switching period $T_{\mathrm{sw}} = 1/f_{\mathrm{sw}}$, the average pole voltages in the $dq0$ frame can be written as a function of the average DC bus voltage $\overline{v}_{\mathrm{DC}}$ as:

$$\overline{\mathbf{v}}_{pdq0} = \mathbf{m}_{dq0}\overline{v}_{\mathrm{DC}} \tag{1.39}$$

where $\mathbf{m}_{dq0} = \mathbf{P}\mathbf{m}_s = \begin{bmatrix} m_d & m_q & m_0 \end{bmatrix}^T$ is the average duty-cycle vector in the $dq0$ frame and $\mathbf{m}_s = \begin{bmatrix} m_a & m_b & m_c \end{bmatrix}^T$ is the average duty-cycle vector in the *abc* frame. By substituting the (1.39) into the (1.35), one can write:

$$\mathbf{m}_{dq0}\overline{v}_{\mathrm{DC}} - \overline{\mathbf{v}}_{\mathrm{B}dq0} = R_s\overline{\mathbf{i}}_{sdq0} + \frac{d\overline{\boldsymbol{\lambda}}_{sdq0}}{dt} + \mathbf{T}\overline{\boldsymbol{\lambda}}_{sdq0} \tag{1.40}$$

by considering only the homopolar equation yields to:

$$m_0\overline{v}_{\mathrm{DC}} - V_{\mathrm{B}} = R_s\bar{i}_{s0} + \frac{d\overline{\lambda}_{s0}}{dt} \tag{1.41}$$

where V_{B} is the average battery voltage. From the (1.32) the average homopolar flux can be written as:

$$\overline{\lambda}_{s0} = L_0\bar{i}_{s0} + \overline{\lambda}_{\mathrm{M}0} \tag{1.42}$$

where $\overline{\lambda}_{\mathrm{M}0} = \frac{1}{T_{\mathrm{sw}}}\int_{t-T_{\mathrm{sw}}}^{t} \lambda_{\mathrm{M}0}\, d\tau$. By introducing the (1.42) and the (1.38) into the (1.41) yields to:

$$m_0\overline{v}_{\mathrm{DC}} - V_{\mathrm{B}} = -\frac{1}{3}R_s\bar{i}_{\mathrm{B}} - \frac{1}{3}L_0\frac{d\bar{i}_{\mathrm{B}}}{dt} + \frac{d\overline{\lambda}_{\mathrm{M}0}}{dt} \tag{1.43}$$

As mentioned before, the homopolar component of the magnets linked flux must be canceled to avoid the arise of a braking torque into the machine, therefore the (1.43) becomes:

$$m_0\overline{v}_{\mathrm{DC}} - V_{\mathrm{B}} = -\frac{1}{3}R_s\bar{i}_{\mathrm{B}} - \frac{1}{3}L_0\frac{d\bar{i}_{\mathrm{B}}}{dt} \tag{1.44}$$

At steady-state, the expression above can be written as:

$$\overline{v}_{\mathrm{DC}} \approx \frac{V_{\mathrm{B}}}{m_0} \tag{1.45}$$

The (1.45) defines the input-output relationship of the "embedded boost" in the multi-functional converter system. This result shows that the Multi-Functional Converter System (MFCS) is capable of boosting the voltage of the battery connected to the machine neutral point. The DC bus voltage is controlled by modifying the value of the homopolar component of the inverter's duty-cycles m_0.

1.3.3 Battery Current Analysis

The analysis of the battery current is very important since it gives information about the behavior of the system. The battery current consists of the sum of two terms:

$$i_{\mathrm{B}} = I_{\mathrm{B}} + \tilde{i}_{\mathrm{B}} \tag{1.46}$$

where:

1. I_{B}: a constant component which depends on the power flow from/to the battery to the DC bus voltage (average current);
2. $\tilde{i}_{\mathrm{B}}$: a ripple component which depends on the machine's parameters and the inverter modulation strategy;

therefore the first one is the "useful" component of the battery current since it is due by the fact that the battery must provide the power to the machine: it can be calculated by means of a power balance. On the other hand the variable component, as it will be shown, is inherent in the system due to the fixed neutral point potential and it cannot be avoided. The circulation of this variable component is due to the hompolar phase voltage and it is possible because the neutral point is not isolated: this component does not produce active power and causes additional joule losses in the machine and additional stress on both the battery and the DC link capacitor, representing a negative effect of the MFCS architecture. The inverter's leg voltages are a function of the duty-cycles m_a, m_b, m_c:

$$\begin{bmatrix} v_{pa} \\ v_{pb} \\ v_{pc} \end{bmatrix} = v_{\mathrm{DC}} \begin{bmatrix} m_a \\ m_b \\ m_c \end{bmatrix} \tag{1.47}$$

from the (1.13), the following relationship is obtained:

$$\begin{bmatrix} v_{pa} \\ v_{pb} \\ v_{pc} \end{bmatrix} = \begin{bmatrix} v_{sa} \\ v_{sb} \\ v_{sc} \end{bmatrix} + \begin{bmatrix} V_{\mathrm{B}} \\ V_{\mathrm{B}} \\ V_{\mathrm{B}} \end{bmatrix} \tag{1.48}$$

At steady-state, the following reference phase voltages are imposed to the modulator:

$$\begin{bmatrix} v_{sa} \\ v_{sb} \\ v_{sc} \end{bmatrix} = V_s \begin{bmatrix} \cos(\theta_e + \phi') \\ \cos(\theta_e + \phi' - 2\pi/3) \\ \cos(\theta_e + \phi' + 2\pi/3) \end{bmatrix} \tag{1.49}$$

where $\phi' = \phi + \pi/2$ and ϕ is the voltages phase angle with respect to the reference axis. By substituting the (1.47) and the (1.49) into the (1.48), one obtains:

$$v_{\mathrm{DC}} \begin{bmatrix} m_a \\ m_b \\ m_c \end{bmatrix} = V_s \begin{bmatrix} \cos(\theta_e + \phi') \\ \cos(\theta_e + \phi' - 2\pi/3) \\ \cos(\theta_e + \phi' + 2\pi/3) \end{bmatrix} + \begin{bmatrix} V_{\mathrm{B}} \\ V_{\mathrm{B}} \\ V_{\mathrm{B}} \end{bmatrix} \tag{1.50}$$

therefore:

$$\mathbf{m} = M_{\mathrm{A}} \begin{bmatrix} \cos(\theta_e + \phi') \\ \cos(\theta_e + \phi' - 2\pi/3) \\ \cos(\theta_e + \phi' + 2\pi/3) \end{bmatrix} + \begin{bmatrix} V_{\mathrm{B}}/v_{\mathrm{DC}} \\ V_{\mathrm{B}}/v_{\mathrm{DC}} \\ V_{\mathrm{B}}/v_{\mathrm{DC}} \end{bmatrix} \tag{1.51}$$

where $\mathbf{m} = [m_a \; m_b \; m_c]^T$ and:

$$\mathbf{m}' = \begin{bmatrix} m'_a \\ m'_b \\ m'_c \end{bmatrix} = M_{\mathrm{A}} \begin{bmatrix} \cos(\theta_e + \phi') \\ \cos(\theta_e + \phi' - 2\pi/3) \\ \cos(\theta_e + \phi' + 2\pi/3) \end{bmatrix} \tag{1.52}$$

where $M_{\mathrm{A}} = V_s / v_{\mathrm{DC}}$ is the amplitude modulation index. From the (1.45) it results that $m_0 \approx \frac{V_{\mathrm{B}}}{v_{\mathrm{DC}}}$ therefore, m_0 represents a degree of freedom and it can be arbitrarily chosen in the interval $(0, 1)$: it imposes a vertical translation of m'_a, m'_b, m'_c. However, as the detailed analysis carried out in [20] shows, the variation of m_0 changes the maximum amplitude modulation index which can be obtained since each duty-cycle m_a, m_b, m_c must be strictly fall in the interval $[0, 1]$. For a sinusoidal PWM modulation strategy (SPWM) $m_0 = 0.5$ and the maximum modulation index is $M_{\mathrm{A}} = 0.5$, while in case of a Space Vector Modulation (SVM) the homopolar component m_0 is not constant, however its average value is 0.5 while the maximum modulation index is $M_{\mathrm{A}} = 1/\sqrt{3}$. The main problem of the SVM is that the homopolar component m_0 of the duty-cycles is a triangle signal whose harmonic spectrum contains all the triplen harmonics: these harmonics would cause the consequent circulation of triplen harmonics currents within the system through the machine winding and the battery.

1.3.3.1 Average Battery Current Calculation

As discussed before, the battery current is composed of a constant term and a variable term, which depends on the homopolar voltage. In order to obtain the average battery current, a power balance of the system must be carried out. The total machine power is provided by the battery and it can be calculated with the following expression:

$$p = \mathbf{v}_s^{\mathrm{T}} \mathbf{i}_s = V_{\mathrm{B}} i_{\mathrm{B}} \tag{1.53}$$

where $V_{\mathrm{B}} i_{\mathrm{B}}$ is the power delivered by the battery. By applying the Park transformation matrix, yields to:

$$V_{\mathrm{B}} i_{\mathrm{B}} = [\mathbf{P}^{-1} \mathbf{v}_{sdq0}]^{\mathrm{T}} [\mathbf{P}^{-1} \mathbf{i}_{sdq0}] = \mathbf{v}_{sdq0}^{\mathrm{T}} \mathbf{T}_P \mathbf{i}_{sdq0} \tag{1.54}$$

where $\mathbf{T}_P = [\mathbf{P}^{-1}]^T \mathbf{P}^{-1} = \mathrm{diag}(\frac{3}{2}, \frac{3}{2}, 3)$ therefore, by remembering that $\mathbf{v}_{sdq0} = \mathbf{v}_{pdq0} - \mathbf{v}_{\mathrm{B}dq0}$ and by using the (1.35) one obtains:

$$V_{\mathrm{B}} i_{\mathrm{B}} = R_s \mathbf{i}_{sdq0}^T \mathbf{T}_P \mathbf{i}_{sdq0} + \frac{d\boldsymbol{\lambda}_{sdq0}^T}{dt} \mathbf{T}_P \mathbf{i}_{sdq0} + \boldsymbol{\lambda}_{sdq0}^T \mathbf{T}^T \mathbf{T}_P \mathbf{i}_{sdq0} \tag{1.55}$$

by substituting the (1.28), yields to:

$$\begin{aligned} V_{\mathrm{B}} i_{\mathrm{B}} = {} & R_s \mathbf{i}_{sdq0}^T \mathbf{T}_P \mathbf{i}_{sdq0} + \frac{d\mathbf{i}_{sdq0}^T}{dt} \mathbf{L}_{dq0}^T \mathbf{T}_P \mathbf{i}_{sdq0} + \frac{d\boldsymbol{\lambda}_{Mdq0}^T}{dt} \mathbf{T}_P \mathbf{i}_{sdq0} \\ & + \mathbf{i}_{sdq0}^T \mathbf{L}_{dq0}^T \mathbf{T}^T \mathbf{T}_P \mathbf{i}_{sdq0} + \boldsymbol{\lambda}_{Mdq0}^T \mathbf{T}^T \mathbf{T}_P \mathbf{i}_{sdq0} \end{aligned} \tag{1.56}$$

remembering the (1.37) then $\frac{d\mathbf{i}_{sdq0}^T}{dt} = [0\ 0\ \frac{-di_\mathrm{B}}{dt}]$, therefore, the (1.56) becomes:

$$\begin{aligned} & V_\mathrm{B} i_\mathrm{B} \\ & = \frac{3}{2} R_s (I_s^2 + \frac{2}{9} i_\mathrm{B}^2) \\ & + \frac{1}{6} L_0 \frac{d(i_\mathrm{B}^2)}{dt} + \frac{3}{2} I_s \left[\frac{d\lambda_{\mathrm{M}q}}{dt} \cos(\gamma) - \frac{d\lambda_{\mathrm{M}d}}{dt} \sin(\gamma) \right] - \frac{d\lambda_{\mathrm{M}0}}{dt} i_\mathrm{B} \\ & + \frac{3}{2} I_s \omega_e \left[\lambda_{\mathrm{M}d} \cos(\gamma) + \lambda_{\mathrm{M}d} \sin(\gamma) + \frac{1}{2} (L_q - L_d) I_s \sin(2\gamma) \right] \end{aligned} \tag{1.57}$$

the total power is composed of three different terms:

$$\begin{aligned} P_\mathrm{J} &= \frac{3}{2} R_s (I_s^2 + \frac{2}{9} i_\mathrm{B}^2) \\ \frac{dW_\mathrm{M}}{dt} &= \frac{1}{6} L_0 \frac{d(i_\mathrm{B}^2)}{dt} + \frac{3}{2} I_s \left[\frac{d\lambda_{\mathrm{M}q}}{dt} \cos(\gamma) - \frac{d\lambda_{\mathrm{M}d}}{dt} \sin(\gamma) \right] \\ P_\mathrm{EM} &= \frac{3}{2} I_s \omega_e \left[\lambda_{\mathrm{M}d} \cos(\gamma) + \lambda_{\mathrm{M}d} \sin(\gamma) + \frac{1}{2} (L_q - L_d) I_s \sin(2\gamma) \right] \\ & \quad - \frac{d\lambda_{\mathrm{M}0}}{dt} i_\mathrm{B} \end{aligned} \tag{1.58}$$

the term P_J represents the joule losses into the machine, which depend not only on the amplitude of the current fundamental component, but also on the battery current. This means that the joule losses in a machine employed for a MFCS architecture will be higher with respect to the same machine employed in a traditional architecture and for this reason the winding conductors must be oversized to keep the same current density. The term $\frac{dW_\mathrm{M}}{dt}$ represents the variation of the magnetic energy. The term P_EM represents the electromagnetic power which features a constant term, depending on the γ angle and the current amplitude I_s, and negative term given by the variation of the magnets linked flux homopolar component and on the battery current, calculated as $P_{\mathrm{EM}0} = \frac{-d\lambda_{\mathrm{M}0}}{dt} i_\mathrm{B}$, which should be avoided since it causes a braking torque into the machine. The term $\frac{d\lambda_{\mathrm{M}0}}{dt} = e_{s0}$ represents the homopolar back-EMF, due to the homopolar component of the magnets' linked fluxes. This homopolar term is caused by the triplen harmonic components in the airgap spatial distribution of the magneto-motive force produced by the magnets on the rotor. Hence, from the (1.33) the homopolar back-EMF is equal to:

$$e_{s0} = \frac{d\lambda_{\mathrm{M}0}}{dt} = \sum_{\rho=3,6,\ldots}^{\infty} \rho \omega_e \Lambda_{\mathrm{M}\rho} \cos(\rho\theta_e + \pi/2) \tag{1.59}$$

where $\rho\omega_e\Lambda_{\mathrm{M}\rho} = E_{s\rho}$ is the amplitude of the ρ-th harmonic of the homopolar back-EMF. However, since the ρ-th harmonic linked fluxes amplitude depend on the value of the ρ-th harmonic winding factor, the homopolar linked flux and the corresponding back-EMF can be canceled by imposing equal to zero

the triplen harmonic winding factors. This result can be achieved by choosing a proper slots/poles combination, as discussed in Section 1.3.4.
The total power is composed of a variable term and constant term: the former depends on the triplen harmonics and switching frequency components in the battery current and on the harmonic distortion of the magnets linked flux, the latter is the "useful part", since it contains the electromagnetic power, and drains a constant current I_{B} from the battery:

$$V_{\mathrm{B}} I_{\mathrm{B}} = \frac{3}{2} R_s (I_s^2 + \frac{2}{9} i_{\mathrm{B}}^2) + P_{\mathrm{EM}} \tag{1.60}$$

where:

$$P_{\mathrm{EM}} = \frac{3}{2} I_s \omega_e \left[\lambda_{\mathrm{M}d} \cos(\gamma) + \lambda_{\mathrm{M}q} \sin(\gamma) + \frac{1}{2} (L_q - L_d) I_s \sin(2\gamma) \right] \tag{1.61}$$

are the battery RMS current and the electromagnetic power respectively. The calculation of the average battery current I_{B} is not straightforward since the eq. (1.60) is a recursive function where the power drained from the battery depends on the battery current itself.

1.3.3.2 Battery Current Ripple with a Sinusoidal PWM

The battery current ripple can be calculated by expanding the equation (1.35):

$$\begin{bmatrix} v_{pd} \\ v_{pq} \\ v_{p0} \end{bmatrix} - \begin{bmatrix} 0 \\ 0 \\ v_{\mathrm{B}} \end{bmatrix} = R_s \begin{bmatrix} i_{sd} \\ i_{sq} \\ i_{s0} \end{bmatrix} + \begin{bmatrix} L_d & 0 & 0 \\ 0 & L_q & 0 \\ 0 & 0 & L_0 \end{bmatrix} \frac{d}{dt} \begin{bmatrix} i_{sd} \\ i_{sq} \\ i_{s0} \end{bmatrix} + \begin{bmatrix} -\omega_e \lambda_{sq} \\ \omega_e \lambda_{sd} \\ \omega_e \lambda_{s0} \end{bmatrix} \tag{1.62}$$

by imposing the homopolar component of the magnets' linked flux equal to zero, the homopolar equation can be written as:

$$v_{p0} - v_{\mathrm{B}} = R_s i_{s0} + L_0 \frac{d i_{s0}}{dt} \tag{1.63}$$

According to [21], the series expansion of the inverter legs voltages, considering a regular sampled sine-triangle PWM modulation (SPWM), can be written in the complex form as:

$$\begin{bmatrix} v_{pa} \\ v_{pb} \\ v_{pc} \end{bmatrix} = \sum_{h=0}^{\infty} \sum_{n=-\infty}^{\infty} \mathbf{v}_{phn} \begin{bmatrix} e^{j(\Omega_{hn} t + n\frac{\pi}{2})} \\ e^{j(\Omega_{hn} t + n(\frac{\pi}{2} - \frac{2\pi}{3})} \\ e^{j(\Omega_{hn} t + n(\frac{\pi}{2} + \frac{2\pi}{3})} \end{bmatrix} \tag{1.64}$$

where $\Omega_{hn} = (h\omega_s \pm n\omega_e)$ is the pulsation, $\omega_s = 2\pi f_{\mathrm{sw}}, \omega_e = 2\pi f_e$, f_e is the fundamental harmonic frequency, f_{sw} is the switching frequency. The

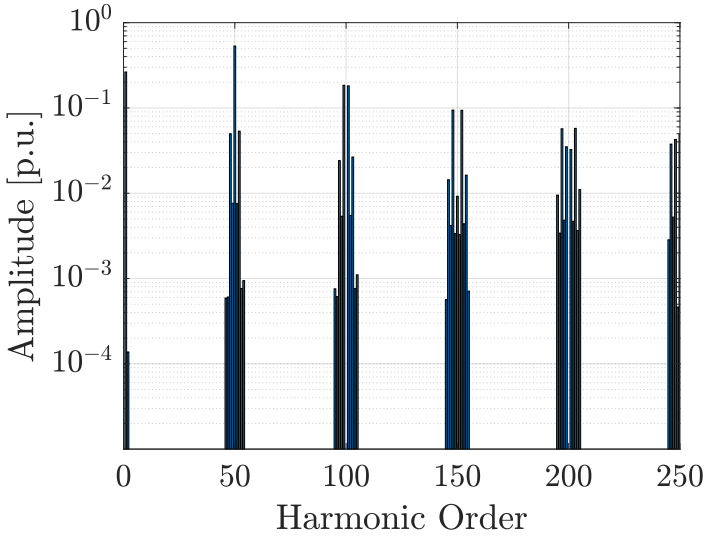

FIGURE 1.23: Example of a spectrum (in p.u.) of one inverter leg voltage obtained with $\widetilde{M}_{\mathrm{A}} = 0.53, f_{\mathrm{sw}} = 25\,\mathrm{kHz}, f_e = 500\,\mathrm{Hz}$ considering a regular sampled sine-triangle modulation. The fundamental harmonic is represented by the harmonic order 1.

quantity $\mathbf{v}_{phn}$ is the h,n-th voltage space-vector expressed as:

$$\mathbf{v}_{phn} = \begin{cases} 0, & \Omega_{hn} = 0 \\ \frac{2f_{\mathrm{sw}}}{j\Omega_{hn}} J_n\left(\frac{\widetilde{M}_{\mathrm{A}}\Omega_{hn}}{4f_{\mathrm{sw}}}\right) j^{h+n}\left[e^{-j3\pi\frac{n\omega_e}{2\omega_s}} - (-1)^{h+n} e^{-j\pi\frac{n\omega_e}{2\omega_s}}\right], & \Omega_{hn} \neq 0 \end{cases} \tag{1.65}$$

where $\widetilde{M}_{\mathrm{A}}$ is the normalized amplitude modulation index with respect to $v_{\mathrm{DC}}/2$, J_n is the bessel function of order n calculated at $\widetilde{M}_{\mathrm{A}}\Omega_{hn}/(4f_{\mathrm{sw}})$. As the (1.64) and the (1.65) show, the pole voltages spectrum is characterized by h groups of harmonics: each group defines a multiple of the switching frequency and it is characterized by sideband harmonics of order $h\omega_s \pm n\omega_e$. More important, from the expression (1.64) it is clearly shown that all the harmonics of order $h\omega_s \pm 3K\omega_e$, for $K = 0, 1, ..., \infty$ (triplen harmonics and multiples of the switching frequency) are homopolar components which produce homopolar currents, circulating within the machine winding through the neutral path given by the battery. Figure 1.23 shows an example of a spectrum of one inverter's leg voltage spectrum considering the first 5 harmonic groups ($h = 0, 1, 2, 3, 4$). The transformed $dq0$ leg voltages can be calculated starting by the definition of the following space vector:

$$\begin{aligned} V_{phn} &= 2\sqrt{(\Re\{v_{phn}\})^2 + (\Im\{v_{phn}\})^2} \\ \phi_{hn} &= \arctan\left(\frac{\Im\{v_{phn}\}}{\Re\{v_{phn}\}}\right) \\ \mathbf{v}_{phn} &= V_{phn} e^{j\phi_{hn}} \end{aligned} \tag{1.66}$$

By defining $\theta_e = \omega_e t$, the inverter's pole voltages in the $dq0$ reference frame are calculated from the *abc* reference frame by applying the Park transformation to the (1.64),(1.65), leading to:

$$\begin{bmatrix} v_{pd} \\ v_{pq} \\ v_{p0} \end{bmatrix} = \mathbf{P} \begin{bmatrix} v_{pa} \\ v_{pb} \\ v_{pc} \end{bmatrix} = \begin{bmatrix} \sum_{h=0}^{\infty} \left(\sum_{n=1,4,\dots}^{\infty} v_{phnd+} + \sum_{n=2,5,\dots}^{\infty} v_{phnd-} \right) \\ \sum_{h=0}^{\infty} \left(\sum_{n=1,4,\dots}^{\infty} v_{phnq+} - \sum_{n=2,5,\dots}^{\infty} v_{phnq-} \right) \\ \sum_{h=0}^{\infty} \sum_{n=0,3,6,\dots}^{\infty} v_{phn0} \end{bmatrix} \tag{1.67}$$

where:

$$\begin{aligned} v_{pnd+} &= V_{phn} \cos(h\omega_s t \pm (n-1)\theta_e + \phi'_{hn}) \\ v_{pnd-} &= V_{phn} \cos(h\omega_s t \pm (n+1)\theta_e + \phi'_{hn}) \\ v_{pnq+} &= V_{phn} \sin(h\omega_s t \pm (n-1)\theta_e + \phi'_{hn}) \\ v_{pnq-} &= V_{phn} \sin(h\omega_s t \pm (n+1)\theta_e + \phi'_{hn}) \\ v_{phn0} &= V_{phn} \cos(h\omega_s t \pm n\theta_e + \phi'_{hn}) \end{aligned} \tag{1.68}$$

where $\phi'_{hn} = \phi_{hn} + n\pi/2$. The homopolar component of the inverter's pole voltages is then equal to:

$$v_{p0} = \sum_{h=1}^{\infty} \sum_{n=0,3,6,\dots}^{\infty} V_{phn} \cos(h\omega_s t \pm n\theta_e + \phi'_{hn}) \tag{1.69}$$

The battery current ripple $\tilde{i}_{\mathrm{B}}$ can be calculated by introducing the (1.69) into the (1.63) and by remembering that $i_{s0} = -i_{\mathrm{B}}/3$:

$$\sum_{h=0}^{\infty} \sum_{n=0,3,6,\dots}^{\infty} V_{phn} \cos(h\omega_s t \pm n\theta_e + \phi'_{hn}) - v_{\mathrm{B}} = -\frac{R_s}{3}\tilde{i}_{\mathrm{B}} - \frac{L_0}{3}\frac{d\tilde{i}_{\mathrm{B}}}{dt} \tag{1.70}$$

The solution of eq. (1.70) is presented in Appendix A and it has the following steady-state value:

$$\tilde{i}_{\mathrm{B}} = -\sum_{h=0}^{\infty} \sum_{n=0,3,6,\dots}^{\infty} 3\tilde{I}_{\mathrm{B}hn} \cos(h\omega_s t \pm n\theta_e + \phi'_{hn} - \varphi_{0hn}) \tag{1.71}$$

where $\tilde{I}_{\mathrm{B}hn} = {}^{V_{hpn}}/_{Z_{hn}}$ is the amplitude of the n-th harmonic of the battery current, $Z_{0hn} = \sqrt{R_s^2 + (h\omega_s \pm n\omega_e)^2 L_0^2}$ is the h,n-th homopolar inductance, φ_{0hn} is the phase of the battery current with respect to the inverter's homopolar leg voltage. As the (1.71) shows, the battery current is characterized by triplen harmonics components for each harmonic group h and also by all the harmonics multiple of the switching frequency $m\omega_s$. For this reason, according to the (1.37), the homopolar current flowing through the machine and the

corresponding phase currents are characterized by the same harmonic components. This result is very important since it shows that the arise of triplen and homopolar harmonics currents in the machine depend on the fact that the neutral point voltage is fixed by the battery. Moreover, the homopolar currents increase the rms value of the machine phase current and cause a consequent increment of the machine's winding losses. Since the battery current is composed of a ripple term which can negatively affect the battery, [22], it could be beneficial to introduce a decoupling capacitor to mitigate the battery stress and thus reducing the high frequency component, at the cost of increased encumbrance and weight.

1.3.3.3 Calculation of DC Bus Voltage Ripple

The presence of triplen harmonics in the phase voltages and currents causes the arise of triplen harmonics in the DC bus current, which is given by:

$$i_{\mathrm{DC}} = -\mathbf{m}^T \mathbf{i}_s = -[\mathbf{P}^{-1}\mathbf{m}_{dq0}]^{\mathrm{T}}[\mathbf{P}^{-1}\mathbf{i}_{sdq0}] = -\mathbf{m}_{dq0}^{\mathrm{T}}\mathbf{i}_{sdq0} \tag{1.72}$$

where $\mathbf{m} = [m_a \ m_b \ m_c]^T$ are the duty-cycles of the inverter legs and $\mathbf{m}_{dq0} = [m_d \ m_q \ m_0]^T$ are the duty-cycles in the $dq0$ reference frame. By applying the Park transformation to the (1.51) the $dq0$ duty-cycles are equal to:

$$\mathbf{m}_{dq0} = \begin{bmatrix} m_d \\ m_q \\ m_0 \end{bmatrix} = M_{\mathrm{A}} \begin{bmatrix} -M_{\mathrm{A}} \sin(\phi) \\ M_{\mathrm{A}} \cos(\phi) \\ m_0 \end{bmatrix} \tag{1.73}$$

where ϕ is the phase displacement of the fundamental component of the phase voltages (i.e. for $m = 0, n = 1$). Therefore, by introducing the (1.37) and the (1.73) into the (1.72) one obtains:

$$i_{\mathrm{DC}} = -M_{\mathrm{A}} I_s \cos(\gamma - \phi) + \frac{1}{3} m_0 i_{\mathrm{B}} \tag{1.74}$$

remembering the (1.46), the DC bus current can be expressed as:

$$i_{\mathrm{DC}} = -M_{\mathrm{A}} I_s \cos(\gamma - \phi) + \frac{1}{3} m_0 I_{\mathrm{B}} + \frac{1}{3} m_0 \tilde{i}_{\mathrm{B}} \tag{1.75}$$

where I_{B} is the average battery current and $\tilde{i}_{\mathrm{B}}$ is the battery current ripple. Since $i_{\mathrm{DC}} = C\frac{dv_{\mathrm{DC}}}{dt}$ then the DC bus voltage ripple is related to the DC bus current with the following expression:

$$\frac{d^2\tilde{v}_{\mathrm{DC}}}{dt^2} = \frac{1}{C}\frac{di_{\mathrm{DC}}}{dt} \tag{1.76}$$

by inserting the (1.75) into the above the DC bus ripple relationship with respect to the battery current ripple can be obtained:

$$\frac{d^2\tilde{v}_{\mathrm{DC}}}{dt^2} = \frac{m_0}{3C}\frac{d\tilde{i}_{\mathrm{B}}}{dt} \tag{1.77}$$

by introducing the (1.71), the DC bus voltage ripple becomes:

$$\frac{d^2\tilde{v}_{\mathrm{DC}}}{dt^2} = \sum_{h=0}^{\infty}\sum_{n=0,3,6,\ldots}^{\infty} \frac{(h\omega_s \pm n\omega_e)m_0\tilde{I}_{Bhn}}{C}\sin(h\omega_s t \pm n\theta_e + \phi'_{hn} - \varphi_{0hn}) \tag{1.78}$$

where $\omega_e = \frac{d\theta_e}{dt}$, by integrating the (1.78) gives the final expression of the DC bus voltage:

$$\tilde{v}_{\mathrm{DC}} = \sum_{h=0}^{\infty}\sum_{n=0,3,6,\ldots}^{\infty} \frac{m_0\tilde{I}_{Bn}}{(h\omega_s \pm n\omega_e)C}\cos(h\omega_s t \pm n\theta_e + \phi'_{hn} - \varphi_{0hn}) \tag{1.79}$$

as the (1.79) shows, the presence of triplen harmonics in the i_{DC} current cause the arise of a triplen harmonics in the DC bus voltage, whose amplitude depend on the DC bus capacitance. This low frequency ripple causes in turns the arise of triplen harmonics components in the duty-cycles $\mathbf{m}$ of the inverter legs: the final result is that the amplitude of the pole voltages V_{pn} is not constant, but since it depends on v_{DC}, it features triplen harmonics components. This causes an increment in the leg voltages homopolar component and therefore an increment of the homopolar current. The same happens when considering the harmonics components associated with the switching frequency of order $m\omega_s$ for $m = 1, 2, \ldots$. A possible solution to reduce the DC bus voltage ripple and the consequent homopolar current amplitude is to increase the value of the DC bus capacitance: in an ideal scenario, with a constant v_{DC}, the phase voltage spectrum converges to the one calculated analytically and shown in Figure 1.23. The spectrum of the phase voltage obtained with a numerical simulation on a MFCS with a R-L load is depicted in Figure 1.24. As the figure shows, there is a sensible difference in the harmonic content of the phase voltage when the DC bus voltage is not constant and this reflects on the harmonic content of the battery current: the harmonic spectrum of the battery current is worse due to the higher harmonic content of the homopolar voltage caused by the DC bus voltage ripple.

1.3.3.4 Battery Current Ripple with a SVM

The SVM strategy is based on the reconstruction of a reference phase voltage space vector $\mathbf{v}_{s,ref} = V_{p,ref}e^{j\omega_e t}$ which rotates at the electrical speed $\omega_e(t)$. The reference can be calculated as:

$$\begin{bmatrix} v_{sa,ref} \\ v_{sb,ref} \\ v_{sc,ref} \end{bmatrix} = \begin{bmatrix} \Re\{\mathbf{v}_{s,ref}\ e^{j\theta_e}\} \\ \Re\{\mathbf{v}_{s,ref}\ e^{(j\theta_e - \frac{2\pi}{3})}\} \\ \Re\{\mathbf{v}_{s,ref}\ e^{(j\theta_e - \frac{2\pi}{3})}\} \end{bmatrix} \tag{1.80}$$

where $\mathbf{v}_{s,ref} = V_s\ e^{j\phi'}$, V_s is the amplitude, $\phi' = \phi + \pi/2$ and ϕ is the phase. For a traditional architecture, the space vector modulation is made with a digital implementation by calculating the times of the different voltage states into one switching period. By considering specific configurations of the inverter switches, the complex plane can be divided into 6 sectors to obtain a

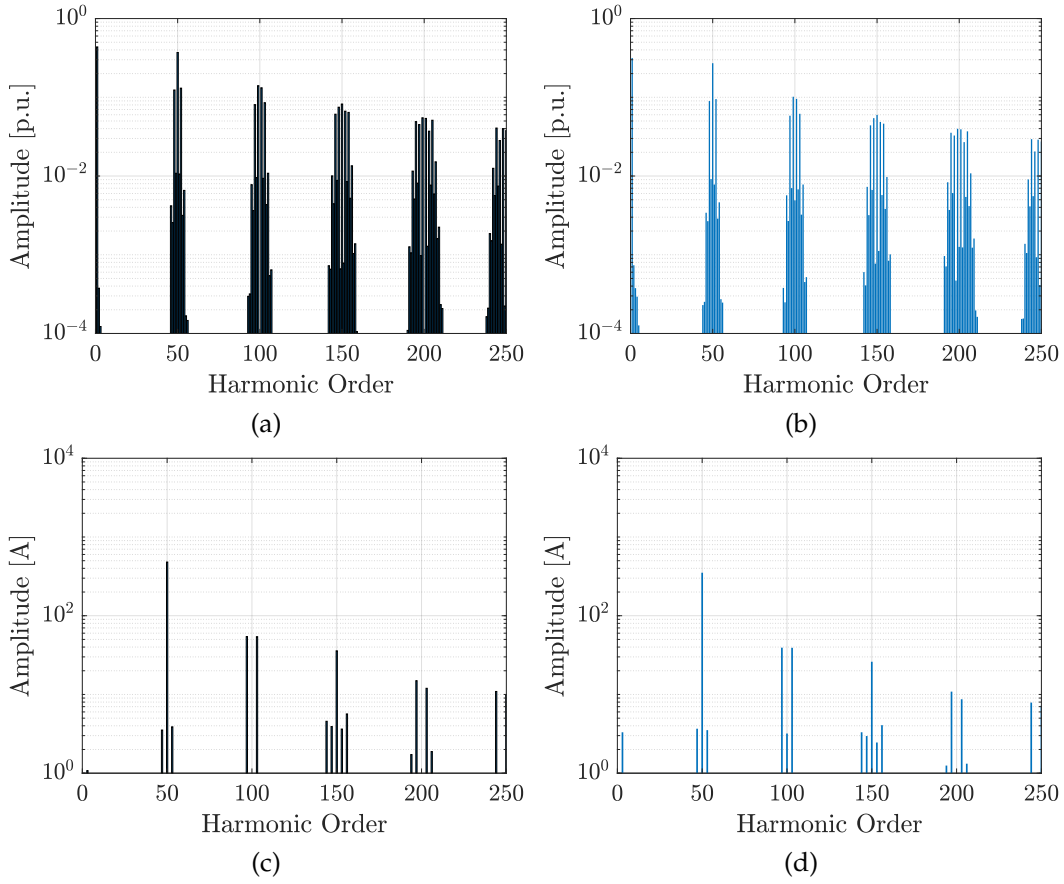

FIGURE 1.24: Example of the phase voltage spectrum (in p.u.) and battery current spectrum calculated on a R-L load with a MFCS architecture with $\widetilde{M}_{\mathrm{A}} = 0.87, f_{\mathrm{sw}} = 25\,\mathrm{kHz}, f_e = 500\,\mathrm{Hz}, C = 5\,\mathrm{m\,F}, R_s = 15\,\mathrm{m\,\Omega}, L_0 = 7\,\mu\mathrm{H}$ considering a regular sampled sine-triangle modulation (SPWM). In: (a) analytical phase voltage spectrum; (b) numerical phase voltage spectrum; (c) analytical battery current spectrum; (d) numerical battery current spectrum.

hexagon with 6 vertices, each of which is defined by a so-called "active vector", as shown in Figure 1.26-(a). If s_{X} represents the switching state of the inverter's X-th leg, when $s_{\mathrm{X}} = 1$ the upper switch is closed and the lower one is open, vice versa when $s_{\mathrm{X}} = 0$. The K-th SVM space vector $\mathbf{V}_{\mathrm{K}}$ is obtained with a specific inverter configuration (s_1, s_2, s_3): for example, the active vector $\mathbf{V}_1$ is obtained with the configuration $(1, 0, 0)$, the active vector $\mathbf{V}_2$ is obtained with the configuration $(1, 1, 0)$ and so on. The maximum amplitude of the active vectors is equal to $\frac{2}{3}v_{\mathrm{DC}}$, and therefore K-th active vector can be written as $\mathbf{V}_k = \frac{2}{3}v_{\mathrm{DC}}\ e^{j(\mathrm{K}-1)\frac{\pi}{3}}$, where $\pi/3$ is the phase displacement between two consecutive vectors. In addition to the active vectors there are 2 additional "null vectors" (whose voltage is zero), corresponding to two different configurations of the inverter: the V_0 vector is obtained by closing all the lower switches of the inverter, configuration $(0, 0, 0)$; the V_7 vector is obtained by closing all the upper switches of the inverter, configuration $(1, 1, 1)$. The location of the reference voltage vector $\mathbf{v}_{s,\mathrm{ref}}$ is equal to

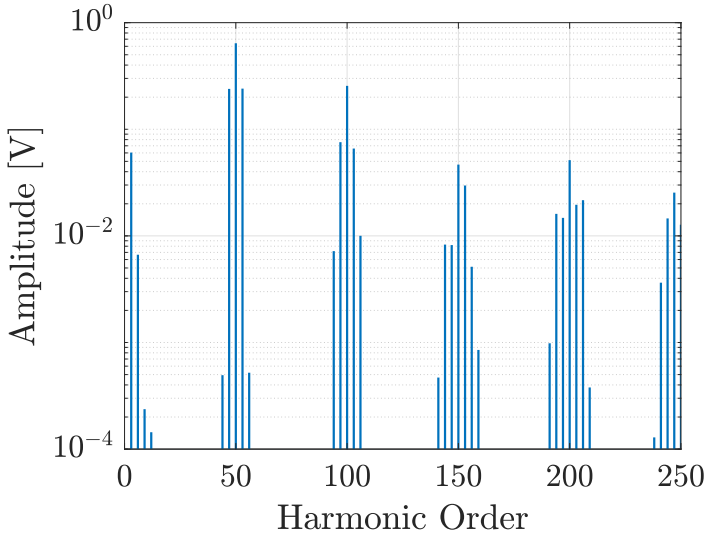

FIGURE 1.25: Harmonic spectrum of the DC bus voltage calculated with a numerical simulation on a R-L load with a MFCS architecture with $\widetilde{M}_{\mathrm{A}} = 0.87, f_{\mathrm{sw}} = 25\,\mathrm{kHz}, f_e = 500\,\mathrm{Hz}, C = 5\,\mathrm{m\,F}, R_s = 15\,\mathrm{m\,\Omega}, L_0 = 7\,\mu\mathrm{H}$ considering a regular sampled sine-triangle modulation (SPWM).

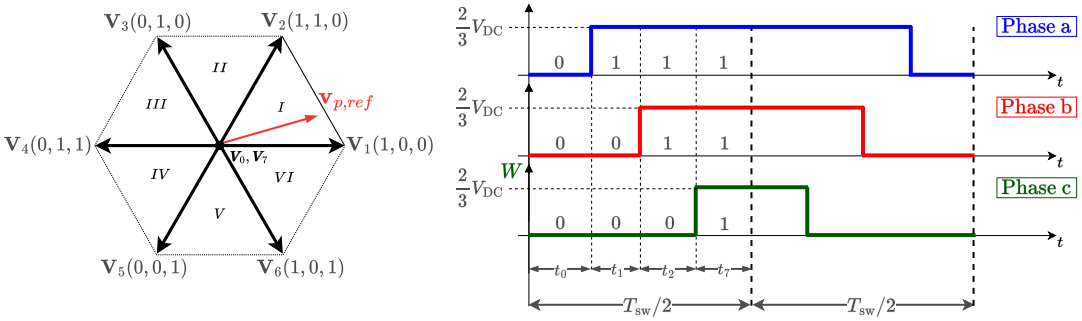

FIGURE 1.26: (a) Space-Vector-Modulation (SVM) hexagon on the complex plane (the numbers I,...VI identify the sector number) and (b) example of a switching pattern when the reference voltage space vector $\mathbf{v}_{p,ref}$ is located in the sector I.

$\theta_e = \int \omega_e(t)dt$. Depending on θ_e, the active vectors which are considered change accordingly. For example, if $0 < \theta_e < \pi/3$, the reference vector falls in the first sector where the active vectors are $\mathbf{V}_1$ and $\mathbf{V}_2$. In Figure 1.26-(a) the SVM hexagon in the complex plane is shown along with an example of the pattern of one switching period, Figure 1.26-(b), considering a reference voltage vector $\mathbf{v}_{p,ref}$ located into the first sector.

If the amplitude modulation index is calculated as $M_{\mathrm{A}} = V_{p,\mathrm{ref}}/v_{\mathrm{DC}}$ then the maximum value for M_{A} is equal to $1/\sqrt{3}$. Depending on the value of the modulation index M_{A}, within one switching period T_{sw} the active vectors are applied for a total time equal to $2(t_1 + t_2)$. On the other hand, the quantity $2(t_0 + t_7)$ is the total time of application of the null vectors V_0, V_7. The higher is the modulation index and the lower is the null vectors time, as the

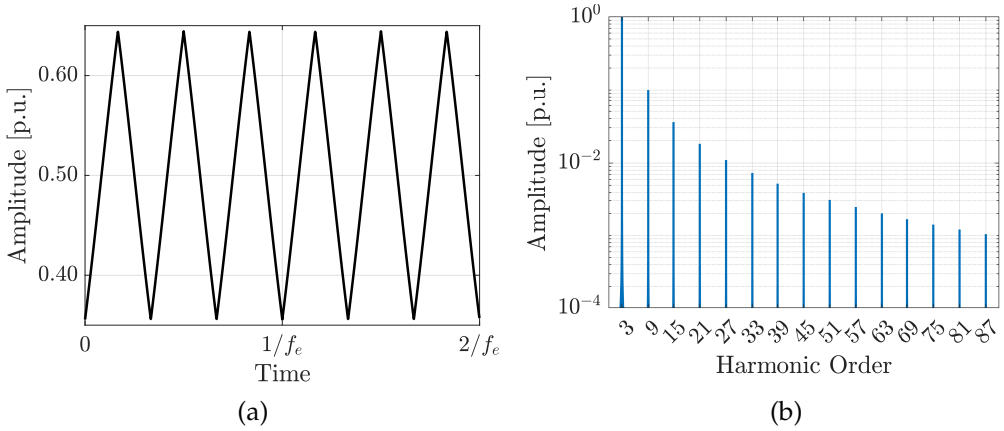

FIGURE 1.27: Homopolar component of the Space Vector Modulation: (a) time signal and (a) harmonic spectrum, calculated with $\widetilde{M}_{\mathrm{A}} = 2/\sqrt{3}$, $f_e = 100\,\mathrm{Hz}$.

Figure 1.26 shows. The homopolar component m_0 defines the distribution of the space-vector V_7 duration time t_7 with respect to the total null vectors duration time $t_0 + t_7$ and since the average value of m_0 is equal to $1/2$, this means that the application times of V_0 and V_7 are equally distributed into one switching period. The homopolar component of the inverter's duty-cycles can be calculated as:

$$m_0 = \frac{1}{2}\left[1 - \max(\mathbf{m}') - \min(\mathbf{m}')\right] \tag{1.81}$$

where $\mathbf{m}'$ is given by the (1.52). By analyzing the (1.81) it results that the homopolar component of a SVM is a triangular wave which contains group of harmonics centered in $(3 + 6K)f_e$, which correspond to the triplen harmonics of the fundamental component, as shown in Figure (1.27)(b). On the other hand, Figure (1.27)(a) shows that the average value for m_0 is $1/2$. therefore, the homopolar component for the SVM can be written as the sum of infinite triplen harmonics components:

$$m_0(t) = \frac{1}{2} + \frac{1}{2}\widetilde{M}_{\mathrm{A}} \sum_{n=3,9,15,\ldots}^{\infty} a_n \cos(n\omega_e t + \xi_n) \tag{1.82}$$

where a_n, ξ_n are the amplitude and the phase respectively of the n-th triplen harmonic of m_0. If the SVM would be used in a Multi-Functional Converter System, the triplen harmonics components of m_0 would cause the arise of corresponding triplen harmonics in the battery current, which would add to the triplen harmonics caused by the fixed potential of the machine neutral point, eq. (1.71), worsening the harmonic distortion of the phase currents and the machine winding losses. Figure 1.28 clearly shows the difference in the harmonic content of the battery current when comparing a sinusoidal PWM with a SVM: a much bigger harmonic distortion is observed when a SVM is employed. For this reason, the SVM is not a suitable modulation strategy for the control of a MFCS and it should not be used.

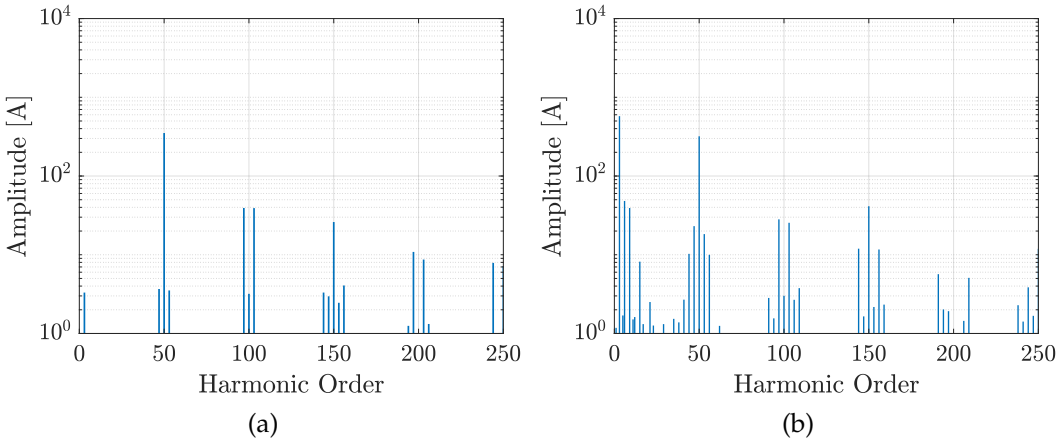

FIGURE 1.28: Battery current spectrum obtained in PLECS®, with: (a) sinusoidal PWM with $m_0 = 1/2$; (a) space vector modulation with variable m_0.

1.3.4 Considerations about the Winding Factor

The main issue given by a Multi-Functional Converter System is the circulation of a homopolar current within the machine due to the neutral path provided by the connection of the battery between the machine star point and the inverter ground. The homopolar current flows through the battery and it is composed of two terms: an average component and a ripple component. The homopolar current causes additional joule losses in the machine winding and it cannot be avoided: the average term depends on the power delivered by the machine; the ripple component is caused by the triplen harmonics and the switching frequency harmonics in the phase voltage as a consequence of the modulation and the fixed potential of the machine star point.
The circulation of triplen harmonics currents in the machine produces the arise of third harmonics in the magnetomotive force (MMF) at the airgap which increases the electromagnetic torque peak-to-peak ripple, the iron losses and the magnet losses. In addition, because of these triplen harmonics fields, the torque ripple frequency is only 3 times higher with respect to the fundamental frequency. On the contrary in a three-phase machine with an isolated neutral point, the triplen harmonics current cannot circulate and therefore the highest order harmonics of the stator magnetic field are the 5th and the 7th, which in turn produce a torque ripple with a frequency 6 times higher than the fundamental one. A reduced frequency for the machine torque ripple can be problematic and can cause a higher stress in the mechanical transmission connected to the machine shaft. Moreover, if triplen harmonics back-EMF are induced in the stator winding, they interact with the triplen harmonics current and cause the arise of a braking torque which reduces the

machine performance. Indeed, as descripted in the eq. (1.58) the electromagnetic power features two different terms:

$$P_{\mathrm{EM}} = \frac{3}{2} I_s \omega_e \left[\lambda_{\mathrm{M}d} \cos(\gamma) + \lambda_{\mathrm{M}d} \sin(\gamma) + \frac{1}{2}(L_q - L_d) I_s \sin(2\gamma) \right] - \frac{d\lambda_{\mathrm{M0}}}{dt} i_{\mathrm{B}} \tag{1.83}$$

the first term is the useful part and it is given by the fundamental component of the phase current. The second term, i.e. $-\frac{d\lambda_{\mathrm{M0}}}{dt} i_{\mathrm{B}}$ is given by the interaction of the homopolar back-EMF, given by $e_{s0} = \frac{d\lambda_{\mathrm{M0}}}{dt}$, and the battery current i_{B}. As the expression above shows, if a homopolar component exist in the back-EMF then there is a term in the electromagnetic power P_{EM} which reduces the useful component and produces a braking torque.
Following these considerations, it is hence fundamental to choose a proper winding arrangement in order to cancel the triplen harmonics linked fluxes in the stator winding and the consequent triplen harmonics back-EMFs. Moreover, the winding arrangement should be chosen in a way that in each slot there would be always two different phases whose conductors have opposite direction in the current flow: in this way the effect of the homopolar current in the stator MMF is canceled. For all the aforementioned reasons, the slot/pole combination in the machine should be carefully chosen so that an appropriate winding configuration can be obtained, in order to cancel the effect of the homopolar currents in the MMF, [9], and to have the third harmonic back-EMFs equal to zero. Since the back-EMF depends on the linked flux produced by the permanent magnets, there are two ways to obtain this result: (a) reduce the pole pitch by 1/3 in order to eliminate the third harmonic in the rotor excitation field; (b) act on the winding arrangement in order to cancel triplen harmonics winding factors. Indeed, as the (1.84) shows:

$$E_{s\rho} = \omega_e \Lambda_{\mathrm{M}\rho} = N K_{w,\rho} K_{mag,\rho} \Phi_{\mathrm{M},\rho} \tag{1.84}$$

where $\Lambda_{\mathrm{M}\rho} = N K_{w,\rho} K_{mag,\rho} \Phi_{\mathrm{M},\rho}$, the ρ-th back-EMF amplitude $E_{s\rho}$ depends on the value of ρ-th winding factor: the idea is to choose the slots/poles combination so that the third harmonic winding factor $K_{w,3}$ is equal to zero. Both the solutions cause a reduction of the torque density with respect to traditional machines, where these techniques are not adopted since the homopolar currents cannot circulate. However, the idea of reducing the magnets angle is theoretically possible, but in reality is not always feasible due to uncertainties in the manufacturing process, moreover this solution does not give any control over the winding arrangement and it is therefore not assured that in each slot the total homopolar current is canceled, since it only depends on the combination of the number of slots/poles..

The ρ-th harmonic winding factor can be written as the product of the distribution factor $K_{d\rho}$ and the pitch factor $K_{p\rho}$:

$$\begin{aligned} K_{w,\rho} &= K_{d,\rho} K_{p,\rho} \\ K_{d,\rho} &= \frac{\sin\left(\rho\frac{\pi}{6}\right)}{q\sin\left(\frac{1}{q}\rho\frac{\pi}{6}\right)} \\ K_{p,\rho} &= \cos\left(\rho\frac{\beta_r}{2}\right) \end{aligned} \tag{1.85}$$

where q is the number of slots per pole and per-phase and β_r is the chording angle:

$$\beta_r = \pi\left(1 - \frac{2p}{N_s}\right) \tag{1.86}$$

N_s is the number of slots and p is the pole-pairs number. From the (1.85), it should be noted that the distribution factor $K_{d,\rho}$ is equal to zero only when $\rho = 6$ or a multiple of 6, thus it can never be equal to zero for the triplen harmonics components of order $3, 9, 15, 21, ...$ That said, in order to have a zero $K_{w,3}$ the third-harmonic pitch factor $K_{p,3}$ must be equal to zero:

$$K_{p,3} = \cos\left(3\frac{\beta_r}{2}\right) = 0 \longrightarrow \frac{3}{2}\beta_r = \frac{\pi}{2} \longrightarrow \beta_r = \frac{\pi}{3} \tag{1.87}$$

since $\beta_r = \pi/3$ then the winding (electrical) pitch is equal to $2\pi/3$. The relationship between the poles and slots number can then be found:

$$\beta_r = \pi\left(1 - \frac{2p}{N_s}\right) = \frac{\pi}{3} \longrightarrow \left(1 - \frac{2p}{N_s}\right) = \frac{1}{3} \longrightarrow \frac{N_s}{2p} = \frac{3}{2} \tag{1.88}$$

With such a choice, it can be proved that the fundamental harmonic winding factor is always equal to $K_{w1} = 0.866$ and thus a lower motor torque density is obtained with respect to the motors with higher winding factors, [23]. Another consequence of this choice is that the number of periods of the cogging torque is equal to $N_{cogg} = \text{lcm}(N_s, 2p) = 6p$ which can be very low when a small number of pole-pairs p is employed. Finally, it can be demonstrated that if the (1.88) is satisfied and a DL tooth-wound winding is considered, in each slot there are always two conductors of two different phases with opposite orientation. This means that the total homopolar current in the slot is always zero and thus the contribution of the homopolar current to the stator magnetic field is always zero.

1.3.5 Comparison with Respect to a Traditional Architecture

In order to evaluate the performance of the Multi-Functional Converter System shown in Figure 1.22, a comparison with a traditional electric drive featuring a DC-DC bi-directional boost converter set between the battery and the DC bus, as the one shown in Figure 1.29, was carried out.

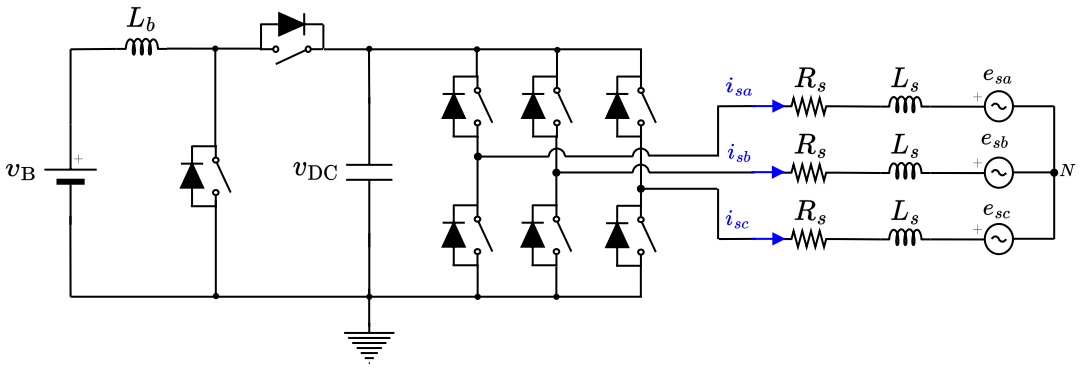

FIGURE 1.29: Electrical scheme of a traditional architecture with an external bi-directional DC-DC boost converter.

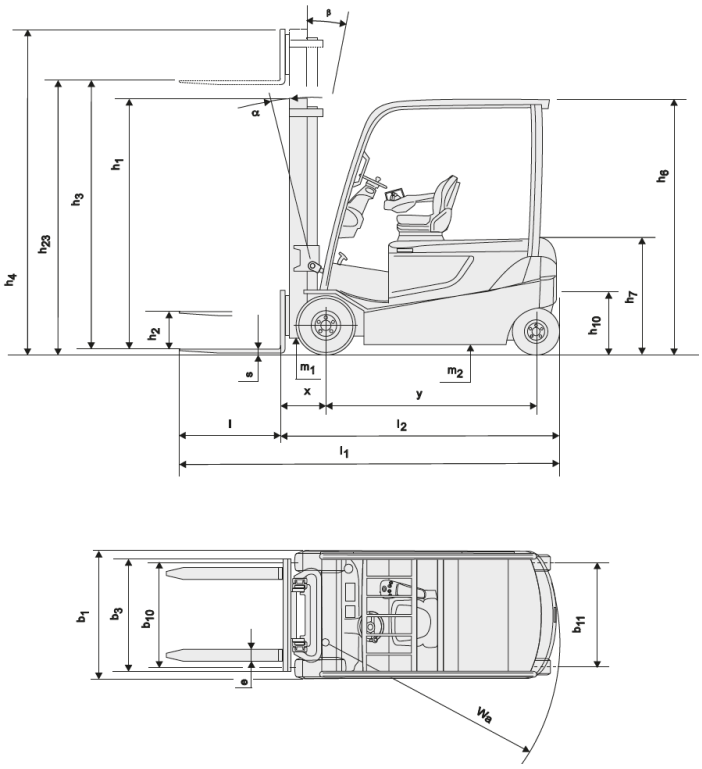

FIGURE 1.30: Schematic view of the Toyota 8FBMT35 3.5 ton class forklift.

One of the advantages of the MFCS is the integration of a boost converter, exploiting the machine and the inverter, allowing to reduce the encumbrance and the weight of the system and making it as a potential candidate for the electrification of low voltage vehicles. In this comparison, the MFCS and the traditional drive were meant to be implemented in the powertrain of a 3.5 ton class forklift with a 48 V battery, based on the Toyota 8FBMT35, Figure 1.30. For both the systems two different electric machines were designed, but the same rotor was used, therefore only the stator geometry was modified in the case of the MFCS to satisfy the constraints given by the requirements of the winding arrangement and the higher phase current rms value. From the vehicle specifications in Table 1.13, the load curves were calculated and

TABLE 1.13: Toyota 8FBMT35 forklift vehicle specifications.

Load capacity	3500 kg
Chassis weight	3730 kg
Battery weight	1863 kg
Total weight (with load)	9093 kg
Maximum vehicle speed (with load)	19 km h^{-1}
Transmission ratio	26
Wheels rolling radius	205 mm
Gradeability (with load)	15 %
Maximum gradeability (with load)	24 %

the electric machines specifications were obtained by considering the vehicle dynamics performance requirements (such as acceleration time, maximum travel speed), Table 1.14. The operating temperature was imposed to 140 °C

TABLE 1.14: Electric machines specifications.

Rated DC bus voltage	96 V
Rated speed	3500 min^{-1}
Rated torque	35 N m
Slot copper fill factor	36 %
Winding temperature	140 °C
Magnets temperature	140 °C
Stator lamination material	Cogent NO20
Magnet type	N45UH
Rotor yoke material	Stainless Steel 416

given the harsh environments where a forklift traditionally operate and the positioning of the machine which is usually located in a narrow space. The battery voltage is 48 V while, as a design specification, the DC bus rated voltage was imposed to 96 V for both the systems, thus by limiting the boost ratio to a factor of two. The rationale behind this choice is given by the fact that a traditional drive is meant to work with a 7-interval symmetric Space-Vector-Modulation (SVM) which features an average value of 0.5. However, as shown in Section 1.3.3.4, the SVM is not suitable for a MFCS since it introduces triplen harmonics in the phase voltages which worsen the homopolar current: for this reason, a sinusoidal PWM strategy was chosen for the MFCS.

In Table 1.15 the main results of the design are summarized, while in Figure 1.31 the 2D view of the two machines is shown. The machine of the traditional architecture was designed by considering a 10p/12s configuration with a tooth-wound double-layer winding. On the other hand, the MFCS' machine features a 10p/15s combination, with a tooth-wound double-layer winding, which was chosen to fulfill the constraint of having a null third-harmonic winding factor: this choices, as expected, caused a reduction in the machine torque density. In Figure 1.32 the comparison of the winding factors is depicted: it can be observed that the MFCS features null triplen

TABLE 1.15: Comparison of the electric machines design results.

	Traditional	**MFCS**
Poles/Slots	10p/12s	10p/15s
Fundamental winding factor	0.933	0.866
Number of cogging torque periods	60	30
Outer diameter	188.6 mm	197.6 mm
Airgap diameter	119.2 mm	
Stator yoke height	9.2 mm	
Slot area	410 mm^2	419 mm^2
Tooth width	21 mm	16.8 mm
Rated power density	1.3 $kW\,kg^{-1}$	1.1 $kW\,kg^{-1}$
Winding type	FSCW - DL	
Internal paths	1	5
Turns per phase	8	
Conductors per slot	4	16
Conductor section	36.9 mm^2	9.4 mm^2
Wire type	AWG 16	AWG 20
Parallel strands	28	18
Gross fill factor	35.8 %	35.6 %
Rated phase current	191 A_{rms}	244 A_{rms}
Rated current density	5.2 A_{rms}/mm^2	
Phase resistance	2.6 m Ω	1.5 m Ω
L_d, L_q, L_0	19.3,26.1 µH	18.4,20.8,0.69 µH
Λ_M	0.0176 V s	0.0185 V s

(a) (b)

FIGURE 1.31: View of a periodic 2-D cross section of the machines of the: (a) traditional architecture and (b) MFCS.

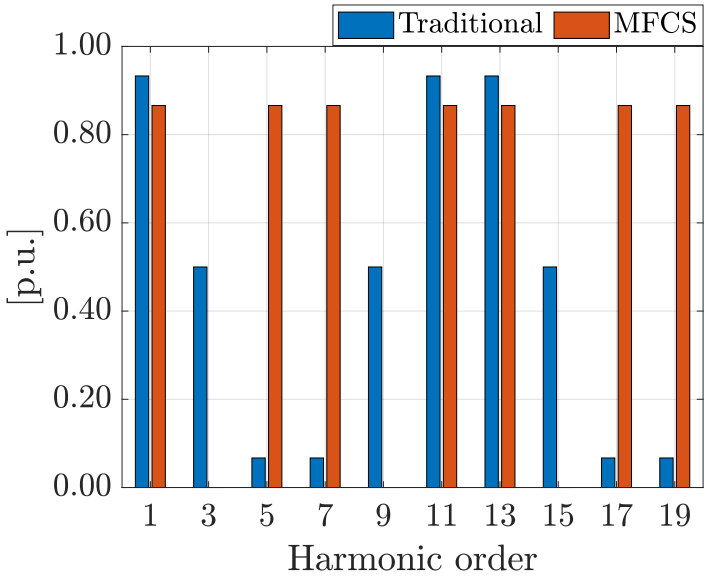

FIGURE 1.32: Comparison of the winding factors.

harmonics factors, but at the expense of higher 5-th and 7-th factors, which increase the torque ripple. In order to design the winding, the phase current of the machine in the MFCS was calculated by considering only the average component of the battery current thus neglecting the ripple component. The estimation of the average component was made based on the expected rated absorbed power and the rated battery voltage. The generic machine phase current can be written as:

$$i_s = I_s \cos(\omega_e t) - \frac{i_B}{3} \tag{1.89}$$

where I_s is the amplitude of the fundamental phase current, responsible for the torque production and i_B is the battery current. Therefore, the phase rms current can be approximately calculated as:

$$I_{srms} = \sqrt{\frac{1}{2} I_s^2 + \frac{1}{9} i_{Brms}^2} \tag{1.90}$$

the battery rms current is equal to:

$$i_{Brms} = \sqrt{I_B^2 + \frac{3}{2} \sum_{h=0}^{\infty} \sum_{n=0,3,6,\ldots}^{\infty} \tilde{I}_{Bhn}^2} \tag{1.91}$$

where I_B is the average battery current and $\tilde{I}_{Bhn}$ is the amplitude of the h,n-th harmonic of the battery current ripple. On the other hand, in the machine employed for the traditional architecture he phase current is equal to i_s and therefore the rms current is $I_s/\sqrt{2}$, since there is no homopolar current flowing through the stator winding. An important consideration is the following: since the phase current of the MFCS' machine is higher than the traditional architecture's one, if the same cooling system is used and thus the same rated

current density is chosen, the cross section of one turn of the MFCS' machine must be bigger. The result is that if the same slot fill factor is considered, the MFCS' machine slot area must be bigger than the traditional architecture's one. For this reason, the design results showed that the stator outer diameter must be approximately 4% larger in the MFCS' machine. Hence, the fundamental difference between the two machines is given by the higher volume and weight of the MFCS' machine, which features a 15% lower gravimetric power density, as shown in Table 1.15.

The comparison between the MFCS and the traditional architecture was meant also to analyze the impact in terms of system efficiency of the DC-DC boost converter, employed in the traditional architecture, located between the battery and the DC bus to boost the battery voltage. The boost converter was designed with a three-phase interleaved architecture, in order to reduce the size of the inductors: in Table 1.16 the boost converter design specifications and results are summarized. The final result is that the total weight

TABLE 1.16: Summary of the specifications and design results of the external DC-DC boost converter used in the traditional architecture.

Number of phases	3
Rated current density	$7\,A_{rms}/mm^2$
Maximum current ripple on one inductor	$10\,A_{pkpk}$
Switching frequency	25 kHz
Minimum input/output voltage	35 V / 44 V
Maximum phase inductor current	338 A
Phase resistance	2.2 mΩ
Phase inductance	28 µH

of the traditional architecture is higher because of the presence of the boost converter, Table 1.17.

1.3.5.1 Simulation Results

The comparison between the traditional architecture and the Multi-Functional Converter System was carried out with numerical simulations by using the software PLECS® to analyze the drive behavior and Finite Element Analysis (FEA) to analyze the machines behavior. The model of the machines in PLECS® was built by starting from the $dq0$ inductances caclulated with the FEA simulations and by calculating the self and the mutual inductances in the three-phase frame, Figure 1.33. For each inverter multiple power mosfet in parallel were chosen for one switch and, for a fair comparison, the same total number of devices was taken into account for both the architectures: this means that the MFCS' inverter features more devices in parallel with respect to the traditional architecture's one. The inverter and the DC-DC boost converter losses were obtained by using the numerical model in PLECS® provided by the manufacturer. Both the architectures were tested in two dif-

TABLE 1.17: Comparison between the traditional architectures and the MFCS in terms of weights of the active parts.

	Traditional	**MFCS**
Weights		
Machine	14.5 kg	16.4 kg
Boost converter	3.9 kg	
Total	18.4 kg	16.4 kg
Switch Count		
Inverter (per switch)	5	8
Boost (per switch)	3	
Inverter (total)	30	48
Boost (total)	18	
Total	48	48

TABLE 1.18: PLECS input data for both the architectures.

	Traditional		**MFCS**	
Modulation	SVM		Sinusoidal PWM	
Switching frequency	25 kHz			
Battery voltage	48 V			
Setpoints				
	Rated	**Overload**	**Rated**	**Overload**
Machine speed	$3500\,\mathrm{min}^{-1}$			
$i_{sq,ref}$	$191\,\mathrm{A_{rms}}$	$398\,\mathrm{A_{rms}}$	$204\,\mathrm{A_{rms}}$	$425\,\mathrm{A_{rms}}$
$i_{sd,ref}$	$0\,\mathrm{A_{rms}}$			
DC Bus Capacitor				
Manufacturer	Vishay MAL220213472E3			
Capacitance	4700 µF			
ESR	30 m Ω			
Power Electronics Device				
Type	MOSFET			
Manufacturer	Infioneon AUIRFP4568			
Current @ 100 °C	121 A			
MOSFET $R_{ds,on}$	11.3 m Ω			
Diode R_d	2.30 m Ω			
Diode V_γ	0.50 V			

ferent working points: rated torque point and overload torque point, considering the machine rated speed of $3500\,\mathrm{min}^{-1}$. Table 1.18 summarizes the main data used in the PLECS® simulations. As the table shows, the reference value for the i_{sq} is approximately 6% higher in the MFCS' machine in

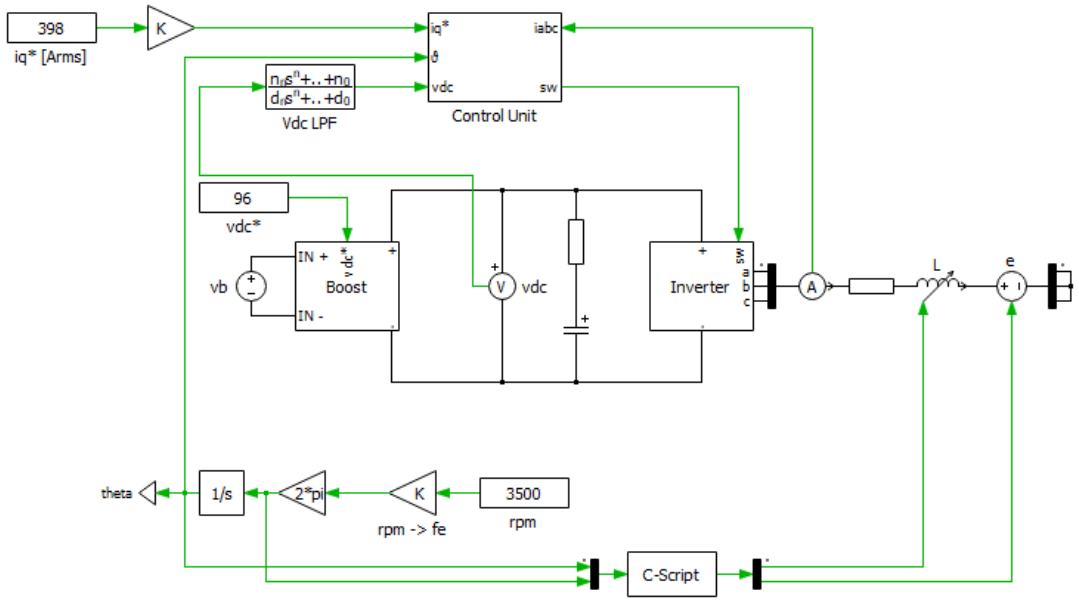

(a) Traditional architecture

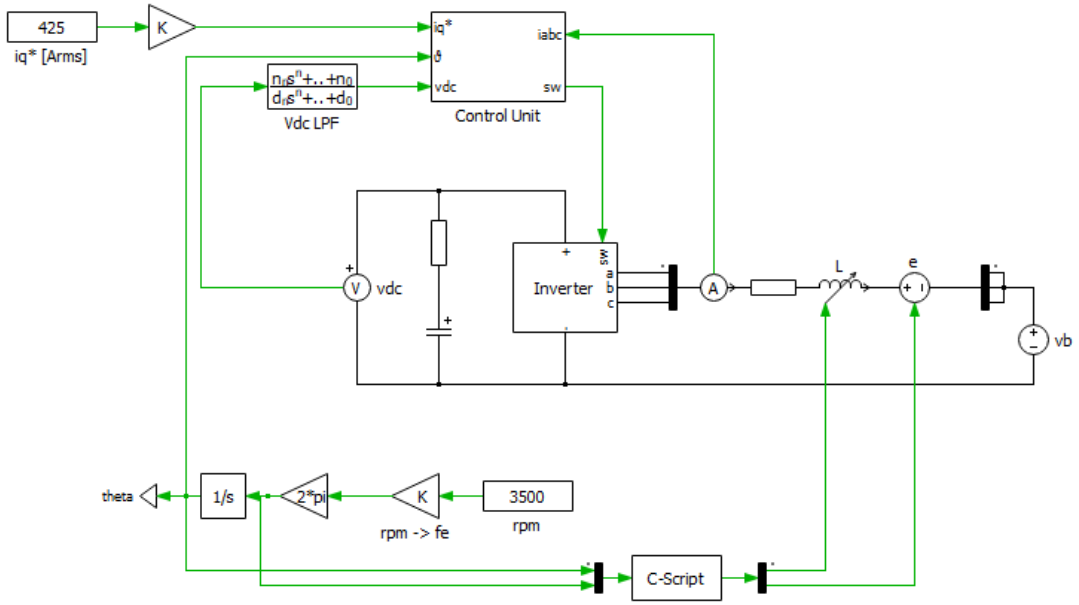

(b) Multi-Functional Converter System

FIGURE 1.33: Plecs models used for the analysis of the two architectures.

order to take into account the effect of the reduced first harmonic winding factor due to the poles/slot combination choice.

Figure 1.34 shows the results following the PLECS® numerical simulation of the traditional drive with the boost stage in the two working points analyzed. The main issue is given by the DC bus voltage ripple which is quite appreciable: this is given by the fact that the DC bus capacitor is shared between the boost converter and the inverter and therefore the total ripple is the sum of the ripple from the boost converter and the one from the inverter. Figure 1.35 shows the PLECS® results of the MFCS in the two working points

analyzed. From the figures it is clear that the battery current ripple is very high, while the DC bus voltage features a low frequency ripple, as expected. Another key point is the uneven distribution of the power electrics losses in the three-phase inverter due to the circulation of the average battery current which causes a negative offset on the phase currents causing higher losses in the lower switches with respect to the upper ones. In Figure 1.36 the phase currents i_{sa}, i_{sb}, i_{sc} obtained with the PLECS® simulations are depicted: the difference in the harmonic distortion is clearly visible where the phase currents in the MFCS architecture feature a negative offset due to the battery current, as expected, and a very high ripple at the switching frequency, which is almost equal to 1000 A and it can negatively affect the battery lifetime.

Following the PLECS® simulations, the i_{sd}, i_{sq} (and i_B for the MFCS) currents were obtained and used for the FEA simulations, in this way the effect of the PWM ripple was also considered to evaluate the impact on the machines performance and losses. The machine losses calculated in the FEA simulations include: the winding joule losses (DC and AC), the stator iron losses, the magnets losses and the rotor yoke losses. The finite element assessment completed the comparison between the traditional architecture and the Multi-Functional Converter System: in Table 1.19 the results of the comparison are hence summarized. The drive efficiency was calculated considering the total electrical absorbed power, which is calculated considering the

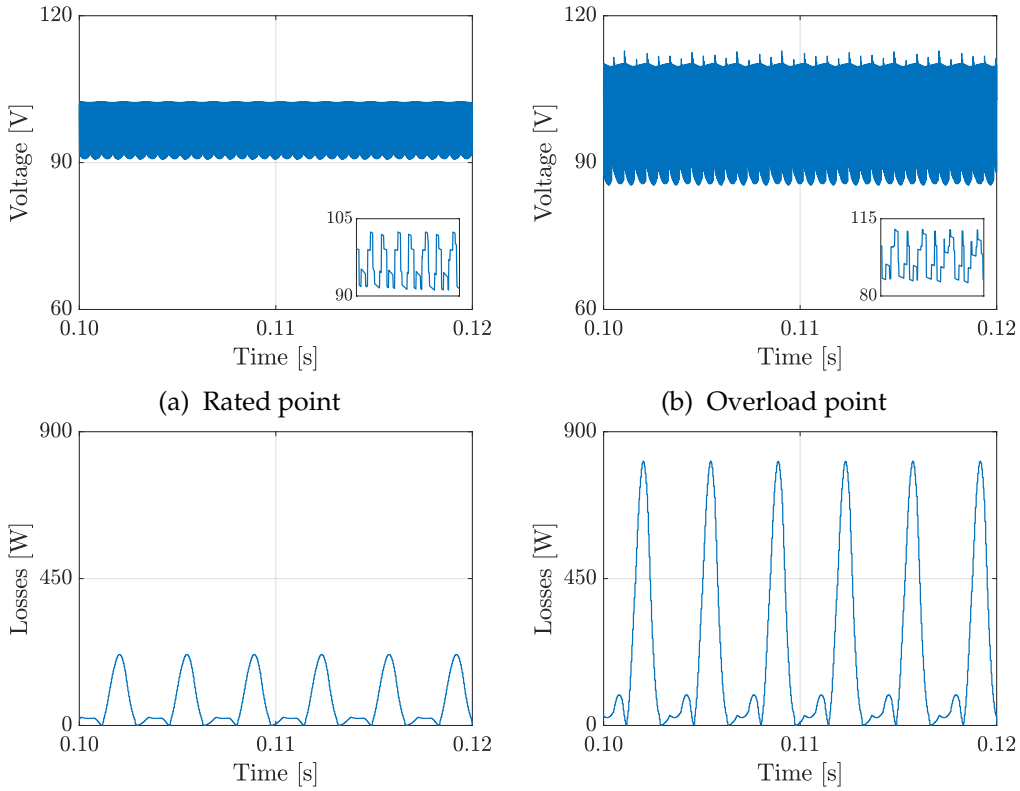

FIGURE 1.34: PLECS® results for the traditional architecture: (a-b) DC bus voltage; (c-d) inverter losses (upper switch).

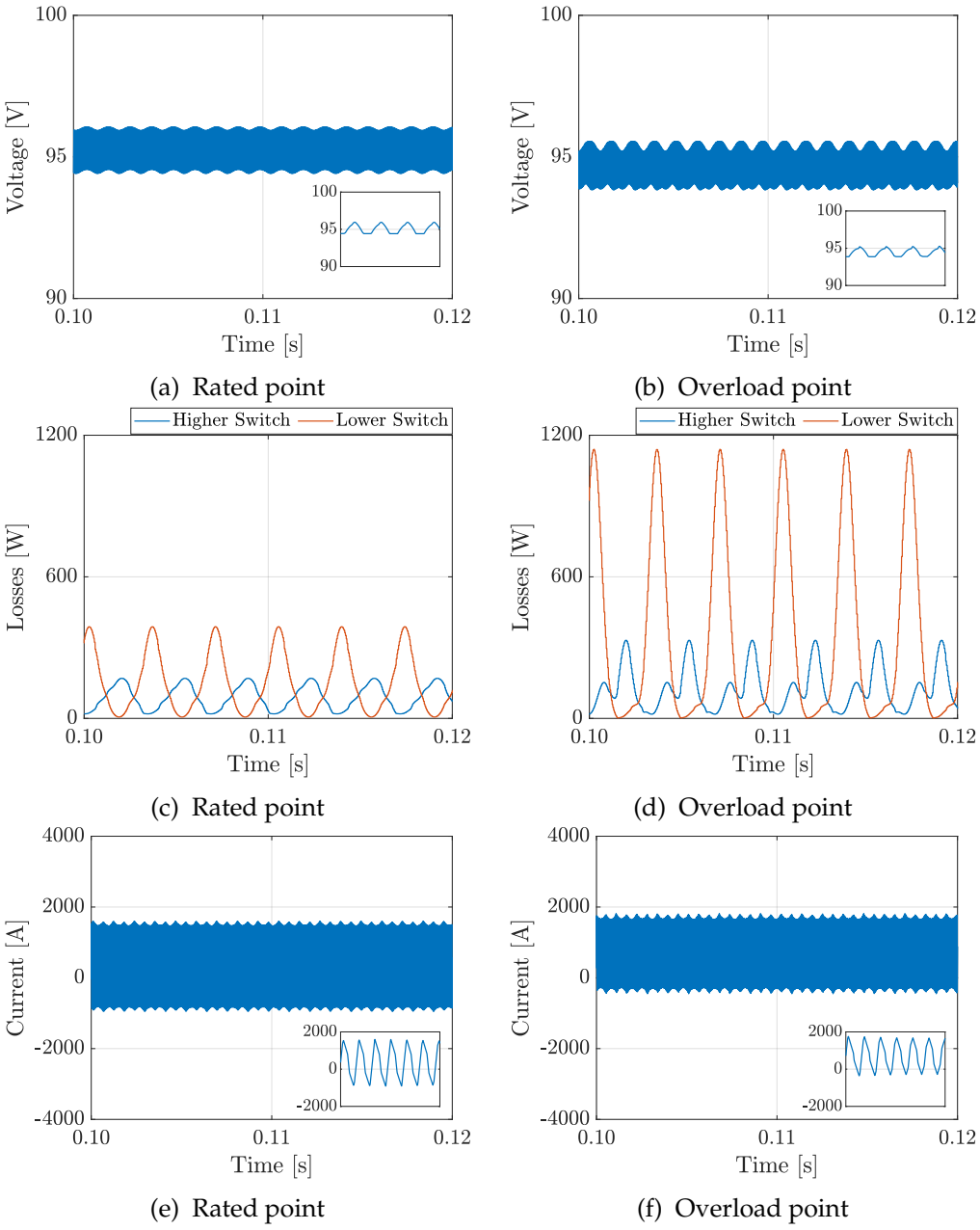

(a) Rated point (b) Overload point

(c) Rated point (d) Overload point

(e) Rated point (f) Overload point

FIGURE 1.35: PLECS® results for the Multi-Functional Converter System: (a-b) DC bus voltage; (c-d) inverter losses (upper and lower switch); (e-f) battery current.

mechanical output power and the drive's total losses, including: the electric machine losses, the DC-DC converter losses (only in the traditional architecture) and the inverter (considering only the power electronics losses). The DC-DC boost converter's losses include the inductors' losses (winding losses and iron losses) and the power-electronics (PE) losses in the solid-state devices. Since in the MFCS there is a homopolar current flowing through the stator winding, which is only limited by the machine homopolar inductance which is in turn very low, the machine phase current is approximately 30 %

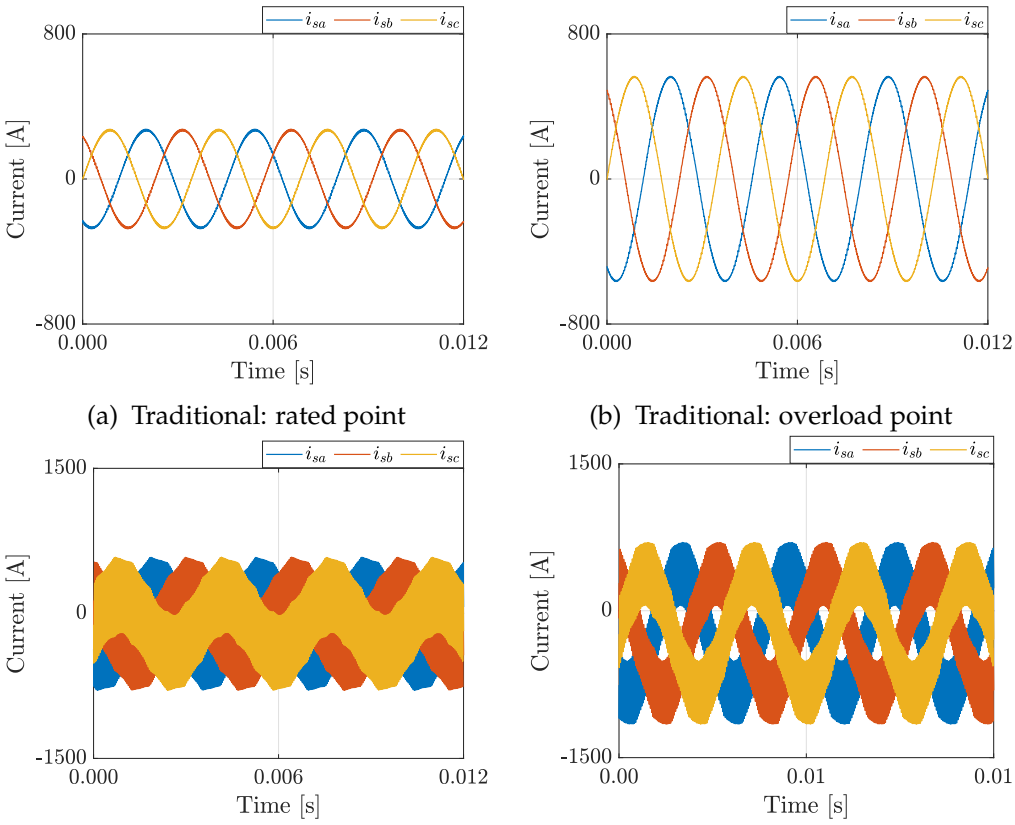

(a) Traditional: rated point

(b) Traditional: overload point

(c) MFCS: rated point

(d) MFCS: overload point

FIGURE 1.36: Phase currents from the PLECS® numerical simulations.

higher and it causes additional winding losses hence, as expected, the traditional architecture's machine is more efficient than the MFCS' one. The conclusion is that the MFCS' machine and drive efficiencies at the rated point are approximately 7 % and 13 % lower than the traditional architecture, which is not acceptable for a traction application, since it would require a significant oversizing of the battery. On the other hand, the drive efficiency in the overload point is quite similar, thanks to the absence of the boost converter losses in the MFCS. It is important to point out that the homopolar current in the MFCS' machine does not cause a reduction of the machine performance: this is thanks to the proper choice of the poles/slots combination which eliminates the contribution of the homopolar current to the stator magnetic field and therefore does not produce triplen harmonics magneto-motive forces at the airgap. However, a design tradeoff exists since the torque ripple in the MFCS' machine is much higher than the traditional architecture's machine, due to the intrinsically higher 5th and 7th harmonics winding factor, and which can cause a higher stress in the mechanical transmission.

To summarize, the following considerations can be made regarding the comparison between the MFCS and a traditional architecture with a DC-DC boost converter:

TABLE 1.19: Comparison results from PLECS numerical and FEA simulations.

	Traditional		**MFCS**	
	Rated	**Overload**	**Rated**	**Overload**
Electric frequency		291.7 Hz		
DC bus voltage	96.1 V	96.1 V	95.1 V	94.5 V
Average battery current	297 A	664 A	313 A	717 A
Phase current	191 A_{rms}	398 A_{rms}	339 A_{rms}	522 A_{rms}
Emag. torque average	34.5 N m	68.5 N m	34.0 N m	68.4 N m
Emag. torque ripple	12.8 %	7.2 %	57.2 %	42.5 %
Machine losses	899 W	3271 W	3774 W	4473 W
Inverter PE losses	403 W	1305 W	725 W	1422 W
Boost inductors losses	400 W	669 W		
Boost PE losses	214 W	722 W		
Drive total losses	1915 W	5997 W	4499 W	5895 W
Output power	12.6 W	25.0 W	12.3 kW	25.0 kW
Machine efficiency	93.3 %	88.4 %	76.6 %	84.8 %
Inverter efficiency	97.2 %	95.8 %	95.7 %	95.4 %
Drive efficiency	86.8 %	80.7 %	73.3 %	80.9 %

- both the architectures need a high DC bus capacitance. In the traditional architecture it is needed because the DC bus capacitor must withstand the high frequency ripple from the boost converter and the inverter. In the MFCS because there is a low frequency ripple due to the homopolar current which then increases the low frequency distortion of the phase currents;
- the MFCS features a low fundamental winding factor which reduces the torque density. In addition, it features higher winding factors for the 5-th and the 7-th harmonic;
- due to the circulation of the battery current in the stator winding, the phase currents in the MFCS have a negative offset which cause an uneven distribution of the power electronics losses in the three-phase inverter: this fact can reduce the lifetime of the devices and leads to a non equal cumulative damage in the converter.
- due to the circulation of the battery current in the stator winding, the phase currents in the MFCS' machine have a higher rms value which increases the winding losses in the machine;
- the MFCS features a high battery current ripple, due to both low frequency and switching frequency harmonics, which cause a harmonic distortion in the phase currents, which can reduce the lifetime of the battery and increases the harmonic distortion of the machine phase currents;

- the MFCS is 11 % lighter due to the absence of the boost converter;
- the MFCS drive is characterized by a 13 % lower efficiency in the rated point and a similar efficiency in the overload point. In general, it is expected that the lower is the power delivered by the machine and the higher is the difference in terms of efficiency between the two architectures.

1.4 Discussion

This chapter presented two case studies regarding two industrial vehicles: a hydraulic excavator and a forklift.

In the first case study, the work was aimed at the design and analysis of a multi-three-phase machine intended for the hybridization of a 5-ton bucket-excavator. The main purpose of the hybrid power system was to downsize the internal combustion engine, by using the electric drive to supply the peak power demand during the machine operation. In order to define the machine specifications and analyze its behavior, a reference trench digging work cycle was used and consequently a quadruple three-phase machine was designed to satisfy: the constraint for the integration in the P1 position and also to supply the peak torque and peak power demand during the test cycle. Given the harsh environment where the machine was supposed to operate, the primary target of the design assessment was the analysis of the machine losses to estimate the temperatures following the working conditions given by the test cycle. By adopting a forced air blown cooling with axial fins all over the machine housing, the temperatures were then calculated in the two cases: considering the PWM ripple a maximum winding hotspot temperature near 180 °C and a magnet temperature of 143 °C were observed. For this reason, in order to reduce the temperatures, the machine cooling was modified and a slot water jacket was adopted. Thanks to this modification the hotspot temperature in the winding was reduced to 125 °C while the magnets temperature was reduced to 98 °C. Finally, finite element simulations considering different fault case scenarios were run in order to assess the fault operation capability and the unbalanced airgap radial force acting on the rotor. The simulations highlighted a particular fault configuration characterized by a peak radial force equal to 287 N: this condition happens when two adjacent sets are healthy and the other two are in fault. However, this represents a second-order fault state and even if an high radial force is observed, it could be sustained by the bearings by taking into consideration the fault scenario during the design phase.

In the second case study, a comparison between a traditional architecture and a Multi-Functional Converter System (MFCS) was carried out. The analysis of the PWM spectrum showed that, by fixing the machine star point potential, the homopolar components of the pole voltages do not cancel out and this causes the circulation of very high homopolar currents in the machine with a significant ripple at the switching frequency. Therefore the battery current is composed of two fundamental terms: an average term, which is responsible for the power flow from the battery to the inverter, and a ripple component, which is limited only by the machine homopolar inductance, and it is caused by the modulation. If the ratio between the number of slots and the number of poles is 3/2, the effect of the homopolar voltages does not affect the machine magneto-motive force at the airgap and thus the machine performance is preserved. The drawback of this choice is the reduction of the first harmonic winding factor and the consequent increment of the phase current fundamental harmonic to obtain the same torque. In addition to that,

this specific poles/slots combination produces a higher harmonic content in the winding factor and the consequent increment of the torque peak-to-peak ripple.

In order to assess the advantages and the drawbacks of the Multi-Functional Converter System, a comparison with respect to a traditional architecture with a DC-DC boost converter, placed between the battery and the DC bus, was carried out. Two different electric machines were designed to satisfy the constraints given by the application: due to the higher phase current, the MFCS' machine resulted to be 14% heavier, since a higher slot area was necessary. Nevertheless, the total active parts weight of the traditional architecture's drive resulted to be higher because of the presence of the DC-DC boost converter. The two systems were modeled and analyzed in two working points (rated power and overload power) by using a 1-D model in PLECS® to obtain the actual waveforms of the dq and battery currents. The currents were then used for the finite element analysis of the machines to assess the performance and calculate the losses in the different parts. On the other hand, the power electronics losses in the inverters and the DC-DC boost converter were obtained by exploiting the PLECS® thermal models provided by the manufacturers . The results of the comparison showed that the traditional drive is more efficient by approximately 13% than the MFCS in the rated point, mainly because of the higher winding losses in the MFCS' machine due to the additional homopolar current. Nevertheless, considering the overload point, the two architectures showed a similar drive efficiency. From the analysis of this architecture, it was found out that the most aspect of the MFCS is the harmonic distortion in battery current which can negatively affect the battery lifetime: it could then be useful to introduce a decoupling capacitor in parallel to mitigate the stress at the cost of a higher encumbrance and weight. A future work could include the analysis of the MFCS MTPA curve in order to find if the requested torque, in the analyzed working points, can be achieved with a lower current, thus increasing the efficiency of the system.

Chapter 2

Electric Rim-Driven Propellers for Inland Waterways Vessels

Electric mobility on water is in the early stage of development but has a great potential, especially when considering inland waterway vessels, which are the best candidate to benefit from a battery electric propulsion system. Indeed, they typically operate in environments with restrictions on noise and emissions, they have short ranges and are relatively close to charging infrastructures. In this framework, rim-driven propellers actuated by large diameter hollow-shaft electrical machines are a promising technology since they present a number of advantages when compared to standard propellers, such as increased efficiency and a compact structure that is particularly suitable for small and lightweight boats. On the other hand, also multi-phase drives are the subject of great interest for the transportation electrification. Multi-three-phase machines are used with modular three-phase converters to obtain a redundant structure and one of their great advantage is the fault-tolerance capability, moreover, by exploiting a symmetrical multi-three-phase machine, a reconfigurable drive can be obtained. The benefit is the ability to change the winding configuration to better match the operating point, specifically the machine speed, to the actual operating conditions and thus reducing the number of active converters when the machine operates at low speed, lowering the total converters power losses. However, system complexity increases, since reconfiguration cells are needed to interconnect the winding sets. The present chapter details two different studies, one focusing on the design and numerical simulation of an electric machine for a rim-driven propeller pod applied to a speedboat to be used on lakes and rivers and the other focusing on a reconfigurable multi-three-phase-drive, which exhibits two main benefits at low speed operation: increased efficiency and reduced phase current ripple for a given switching frequency. The electric machine was designed and simulated by considering some distinctive features like a high power density, a thin radial section and a hairpin winding construction, while the reconfigurable drive was assessed by means of analytical as well as numerical simulations, and the benefits obtainable at low speed operation were also demonstrated experimentally on a reduced scale prototype, capable of a "on the fly" reconfiguration without stopping the machine.

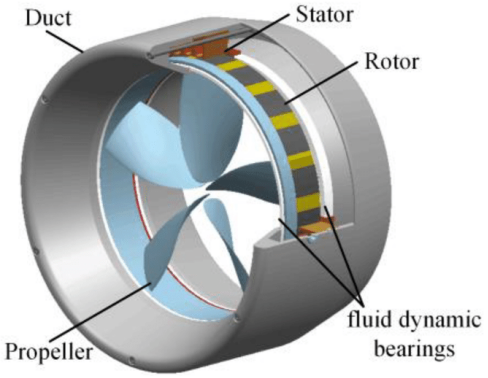

FIGURE 2.1: 3-D view of a rim-Driven propulsor, from [30].

2.1 Introduction

Electric mobility on water is in the early stage of development but has a great potential of growth when applied to inland waterway vessels and specifically to motorboats, speedboats and sailboats for recreational use on lakes and waterways. In fact, those areas are becoming more and more regulated, with restrictions on noise and pollutant emissions. Seafaring vessels are characterized by long range operation, requiring the additional burden of auxiliary generators/range extenders, adding complexity to the power-plant installation. On the contrary, inland waterway vessels operate on much shorter ranges, and are always relatively close to charging infrastructures. In case of sailboats to be used on lakes, electric propulsion is clearly a winning choice: the propulsion engines are used for a very short time, on the order of minutes, usually only for maneuvering in or out of the marina. An internal combustion engine would not even reach the operating temperature, resulting in high pollutant emissions. For this reason, inland waterway vessels are the best candidate to benefit from a modular, self contained battery electric propulsion system that can be easily incorporated in an existing boat design, completely substituting an internal combustion engine power-plant without sacrificing performance.

In the framework of naval propulsion electrification, distributed propulsion by means of self-contained "pods", as shown in Figure 2.1, is attractive since it provides the naval architect more freedom of placement of the units along the hull, not being constrained by line shaft or outboard gearboxes as in the case of centralized designs, [24]. Rim-driven propellers present a number of advantages when compared to standard propellers, such as increased efficiency and a compact structure that is particularly suitable for distributed propulsion, [25], [26]. Also, distributed electrical propulsion is easily scalable in size, from small remote operated vehicles and yachting boats, up to larger vessels, [27]–[29]. In addition, hub-less construction provides less risk of entanglement in case of foreign objects ingestion by the propeller.

Multi-phase drives take a special place in the transportation electrification thanks to their redundant structure and the possibility to operate in fault conditions. In accordance with that, multi-three-phase machines have become

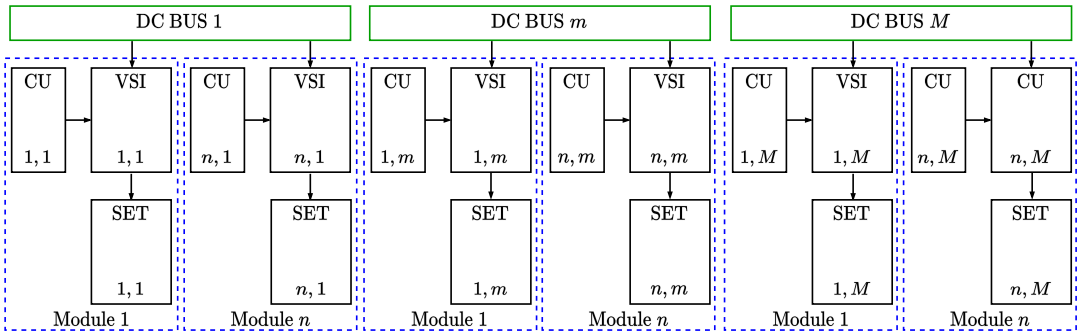

FIGURE 2.2: Segmented multi-phase machine with N modules and M DC bus connections. Each module is composed of a control unit (CU), a three-phase inverter (VSI) and a three-phase set.

more and more popular in the last few years, thanks to the fact that readily available three-phase power converters can be used to supply each three-phase set of the machine, with no necessity to build custom multi-phase converters, reducing also the manufacturing costs. In addition, the number of solid-state devices in parallel for each converter can be lower, since the current rating of each converter is reduced. Another positive aspect of multi-three-phase drives is their inherent modular construction, Figure 2.2, where one module can be seen as the union of a three-phase winding set, a three-phase converter and a control unit, with the advantage of the reduction in complexity of both manufacturing and maintenance of the system. Moreover, if sectorized machines are used, the three-phase sets are located into one sector of the machine stator and the mutual coupling between them is strongly reduced, [16]. This kind of arrangement, along with a single-layer winding allows to create a multi-three-phase machine with totally independent three-phase sets and thus further increase the fault-tolerance. The drawback is that a radial force can arise in case of fault of one (or more) three-phase sets, [31], [32].

Reconfigurable drives can be derived from the basic multi-three-phase structure described before: by connecting in series or in parallel the stator's three-phase sets, the machine torque constant is respectively increased or reduced. When operating at reduced speed, reconfiguring the multi-three-phase machine in series results in the reduction of the number of active converters feeding the machine, with the ultimate goal of increasing system efficiency by reducing the converter losses, that for a given line current are proportional to the number of active converters. The reconfigurable architecture has already been proposed in [33]–[35] with different structures: a possible control method to change the winding configuration is discussed in [35] and is based on the modulation index. Among the benefits of the reconfigurable architecture, one is the ability to operate with a reduced base speed but with full torque and balanced electric machine operation, even in case of multiple converter failures. However, since the machine winding reconfiguration is achieved using bi-directional switches, additional conduction losses must be taken into account. The benefit in terms of efficiency is related only on the

number of active converters, therefore it is independent on the power rating of the particular application. A secondary beneficial aspect is the reduction of the phase current ripple when the machine's windings are series connected.

This chapter is organized as follows: in Section 2.2 the case study of an electric machine design for a rim-driven propeller is presented and in Section 2.2.1 some fundamental design considerations about the design of the hairpin-wound machine are carried out. In Section 2.2.2 the FEA simulations results of the machine and the consequent thermal analysis are carried out to calculate the machine performance and temperatures following the specified operating conditions. On the other hand, in Section 2.3 the reconfigurable architecture is introduced and in Section 2.3.1 the analysis of the system is carried out, highlighting the converters and reconfiguration cells (RCs) topologies. Section 2.3.2 discusses the challenges associated with the RC networks and describes the RC implementation using solid-state switches and electromechanical ones, and the impact of a RC fault on the drive operability is analyzed. In Section 2.3.3 the reconfigurable architecture performance is assessed by means of analytical calculation of the power electronics components losses, while in Section 2.3.4 the analytic results are compared against the numerical simulations carried out in PLECS® environment. Section 2.3.5 reports the experimental results obtained with a double three-phase low voltage laboratory prototype, demonstrating the mode of operation of the reconfigurable drive and its advantages in terms of current ripple and efficieny.

Finally, the conclusion and comments of the chapter are presented in Section 2.4.

2.2 A Proof of Concept of a High Power Density Machine for a Rim-Driven Propulsor

This section details the design and the numerical simulation of an electric machine meant for a rim-driven propeller pod, applied to a speedboat, to be used on lakes and rivers. The electric machine main distinctive features are:

- high power density;
- thin radial section;
- hairpin winding.

The adoption of a hairpin winding allows to create electric machines with very high torque densities which are particularly suitable for traction applications, [36]–[39]. The major benefit provided by the adoption of a hairpin winding is the possibility to increase the winding slot fill factor up to very high values (usually around or higher than 70 %), which allows to: reduce the slot area needed to place the conductors and increase the slot thermal conductivity thanks to the increased copper cross-section with respect to the air content. These are two key factors which allow to reduce the machine stator size and guarantee a better heat conduction from within the machine to the external ambient. The drawback is that a hairpin winding is made by rectangular conductors with a high cross-section: this causes an increment in the AC winding losses, due to skin and proximity effects, with respect to a classic random wound winding. In addition, the AC losses are worsened by the high electric frequency usually reached with high power density motors, rotating at very high speed, [40], [41]. For this reason, the additional heat caused by the AC eddy currents losses in the conductors must be properly dissipated, [42]–[45]. One workaround can be the adoption of a high number of parallel paths in order to employ thinner conductors and thus reduce the AC losses. In [46] a segmented hairpin technology to reduce the eddy current losses associated with the AC operation is shown. Another workaround can be the employment of the aluminum winding which, thanks to the higher resistivity of the aluminum, it can provide an advantage in the reduction of the AC losses with respect to a copper winding, especially when the machine is fed with high frequency currents (i.e. above 1 kHz). Moreover, an aluminum winding is lighter hence allowing to increase the machine gravimetric torque density. Another drawback of a hairpin winding is given by the more complex manufacturing process, which requires expensive tooling investments. However, once the production line is built, the manufacturing of hairpin-wound machines can be cost effective when large series production is considered. The bibliography regarding the hairpin winding is extensive, in [47], [48] two AC losses model for hairpin windings are presented, while in [49] some guidelines to reduce the AC losses are provided. A comparison between an aluminum hairpin winding and a copper hairpin winding is presented in [50], [51] while in [52] a comparison between a random wound winding and a hairpin winding is shown.

TABLE 2.1: Electric motor specifications and constraints.

DC bus voltage	800 V
Rated power	440 kW
Maximum speed	$4000\,\mathrm{min}^{-1}$
Peak power density	$\geq 10\,\mathrm{kW\,kg}^{-1}$
Peak torque density	$\geq 20\,\mathrm{N\,m\,kg}^{-1}$
Rotor internal diameter	≥ 240 mm

The preliminary design of the electric motor started from the specifications listed in Table 2.1 and it is related to a propulsion plant for a generic 7 m, 2500 kg speedboat. The aim of the design was to reach a rated power of 600 HP, in order to have a comparable power rating with the usual internal combustion engines found on the market. In addition, target values for the gravimetric peak power density and for the peak torque density were defined. The aim of the design was also to have a machine which is able to reach a transient peak power in order to provide a temporary acceleration capability to the boat, for example to improve the maneuvering phase. The rotor internal diameter was chosen in accordance with the power rating of the application and defined after some studies regarding the fluid dynamics of the propeller, which was conducted by other groups. However, the design considerations of the inner rotor propeller blades are outside the scope of the present work and for this reason they will not be detailed. The specifications were completed by imposing a maximum distance of 40 mm between the rotor internal diameter and the stator outer diameter. The fundamental requirement for a rim-driven propeller is to have a large inner rotor space, in order to leave enough space for the propeller's blades, [30]. In addition, the distance between the inner rotor diameter and the stator outer diameter should be as little as possible, in order to reduce the hydrodynamic drag. For this reason, an electric motor employed as a rim-driven propulsor should feature an annular-type construction.

The requirement of an annular construction imposes the following constraints on the motor design:

- the radial width of the stator back-iron and the rotor back-iron should be reduced as much as possible;
- the rotor back-iron must be solid and mechanically robust, in order to be able to mount the propeller.

The first requirement can be obtained if a high number of poles is employed. Indeed, the stator and rotor back-iron width is directly proportional to the number of poles, therefore the higher is the pole number the narrower are the back-iron widths. For this reason, if the same outer and inner diameters are considered, the narrower are the back-iron widths and the higher can be the magnets width and the slot height, which in turn produce a higher magnetic and electrical loading which lead to a higher torque density. Indeed, since the slot area can be increased, considering the same slot fill-factor, the

copper cross-section is increased and, for the same current density, the phase current is then increased. Moreover, since the distance between the copper (and the magnets) and the external housing is reduced, the heat produced by the winding (and the magnets) losses can be more easily dissipated, allowing to increase the current density and consequently the torque density. The second requirement to obtain an annular construction can be achieved only if a surface permanent magnet (SPM) synchronous machine is adopted: in this way, a solid stainless steel rotor back-iron can be used, leaving the necessary space inside to place the propeller blades, avoiding the usage a laminated rotor structure, as for example needed in a internal permanent magnet (IPM) or in an asynchronous machine.

2.2.0.1 Choice of the Poles/Slots Combination

As mentioned before, the design of the electrical machine defines an annular geometry as a specification hence leading to the choice of a high pole number to narrow the stator and rotor back-irons. However, in order to keep the number of slots within a reasonable value, the adoption of high number of poles usually requires a fractional slot concentrated winding (FSCW), which however does not represent the best choice for high power machines. Moreover, FSCW produce non-negligible sub-harmonics in the stator magnetomotive force (MMF), causing high rotor losses in both the magnets and the rotor banding surrounding the magnets (which are directly exposed to the airgap magnetic field), nonetheless a higher torque ripple and reduced performance. For this reason, given the machine power rating in this specific case and also the high magnetomotive force (given by the high current density) the choice of having a FSCW scheme is then not advisable and an integer-slot winding scheme was chosen for this machine. However, when dealing with a high pole number, the manufacturing process of an integer-slot winding is harder due to several factors and especially due to the high number of superimposed coils and the higher difficulty to place the conductors in the slots. The choice of the poles number should be made in order to have a limited number of slots to ease the stator and the winding manufacturing and also by adopting a single layer winding, with one slot per pole/phase, to facilitate the winding coils placement. Nevertheless, a single-layer winding brings with it some positive and negative aspects: the positive aspect is the unitary first harmonic winding factor which allows to increment the machine torque density; the drawback is the higher harmonic content in the magneto-motive force which primarily increases the rotor losses and the torque ripple. Following the aforementioned rules, the poles/slots combinations summarized in Table 2.2 were selected. The electric frequency was calculated considering the maximum speed of $4000\,\mathrm{min}^{-1}$, while the stator back-iron width was taken equal to 1 p.u. for the 12p36s (12 poles and 36 slots) configuration and then re-calculated for all the others. The choice of the right poles/slots combination is not straightforward: for a given stator outer diameter, an higher pole count allows the reduction of the stator back-iron width and thus increases the available slot area and the heat exchange towards the outside. On the other hand, the electric frequency increases as

TABLE 2.2: Selected poles/slots combinations.

Poles	Slots	Electrical Frequency	Stator Back-Iron Width
12	36	400 Hz	1.00 p.u.
14	42	467 Hz	0.86 p.u.
16	48	533 Hz	0.75 p.u.
18	54	600 Hz	0.67 p.u.
20	60	667 Hz	0.60 p.u.
22	66	733 Hz	0.55 p.u.
24	**72**	**800** Hz	**0.50 p.u.**
26	78	867 Hz	0.46 p.u.
28	84	933 Hz	0.43 p.u.
30	90	1000 Hz	0.40 p.u.

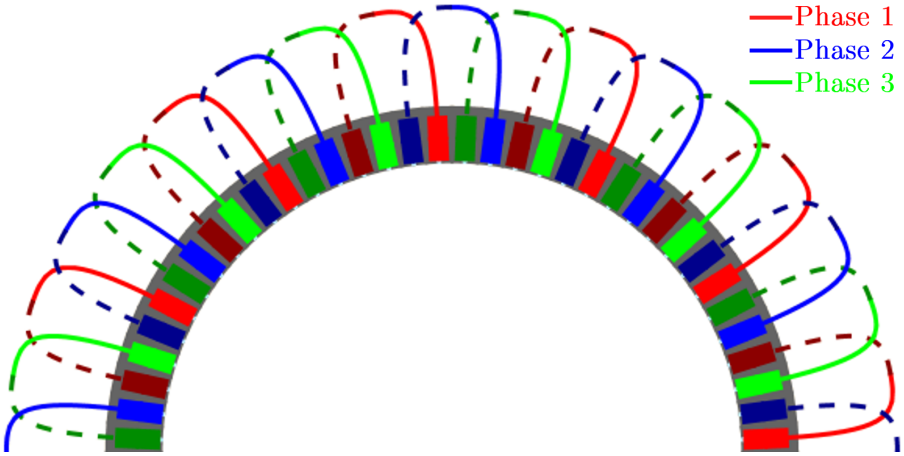

FIGURE 2.3: 2-D half radial view of the 24p72s machine with the corresponding winding scheme, obtained from Altair®FluxMotor®.

well, leading to higher AC copper losses (due to the proximity and skin effects), which in turn cause additional heat and thus reduce the machine performance, given the thermal constraints of the adopted cooling system, and also a reduced efficiency, which is not advisable in a battery-powered application. Therefore, after some design iterations, which will not be explained in detail, the 24p72s combination was chosen, since it is considered a good compromise between the different analyzed poles/slots combinations, satisfying the constraints of having a reasonable number of slots and an acceptable fundamental electrical frequency. In Figure 2.3 the radial view of the integer-slot single-layer winding scheme adopted on the 24p72s combination is shown: the winding pitch is equal to 3 slots, i.e. 15°.

2.2.1 Motor Design Considerations

In order to reach the specified peak torque density and the peak power density, the design process was iterated many times however, to facilitate the

TABLE 2.3: Preliminary design choices.

Airgap width (with banding)	2.0 mm
Rotor banding width	0.5 mm
Winding temperature	200 °C
Magnets temperature	40 °C
Rotor banding temperature	40 °C
Stator lamination	Cogent NO20
Rotor back-iron	Ugitech UGI®4113
Magnets	N45UH
Rotor banding	AISI 304

reading, in this subsection only the main design considerations and the final results of the design will be shown. In order to speed up this first phase, the preliminary simulations were carried out by using Altair®FluxMotor®, which allows the rapid simulation of many geometries in a small amount of time. To reduce the number of iterations, some constraints were imposed:

- the airgap was chosen large enough to ensure ad adequate water flow within the airgap itself, to ease the machine cooling. Even if a larger airgap reduces the machine peformance, this requirement is in accordance also to the fact that, since the specified inner rotor diameter is large, a higher mechanical tolerance must be considered during the manufacturing process and therefore a higher airgap is necessary to avoid the rotor/stator rubbing;
- a hairpin winding was chosen to increase the torque density and improve the stator motor cooling. This resulted in a machine featuring a parallel slot type geometry;
- the maximum height of one phase conductor was imposed to stay below the skin depth value at the maximum electric frequency;
- a minimum limit on the synchronous inductance at full load was imposed in order to avoid an excessive PWM current ripple at the maximum DC bus voltage.

The other preliminary design choices, along with the chosen materials, are listed in Table 2.3. One of the advantages of an electric motor employed for a rim-driven propeller is the possibility to have a great amount of cold water flowing through the motor's hollow shaft in addition, since the propeller is submerged, the motor is also surrounded by a high-speed cold water flow, which depends on the boat speed. These operating conditions allow to obtain a very good heat dissipation with the external ambient which is particularly important when the machine delivers a high power. The higher is the boat speed, the higher is the power produced by the motor and the higher are the losses. At the same time, the higher is the boat speed and the higher is the water flow inside and outside the machine which improves the losses dissipation and the power deliver. An important role is played by the water

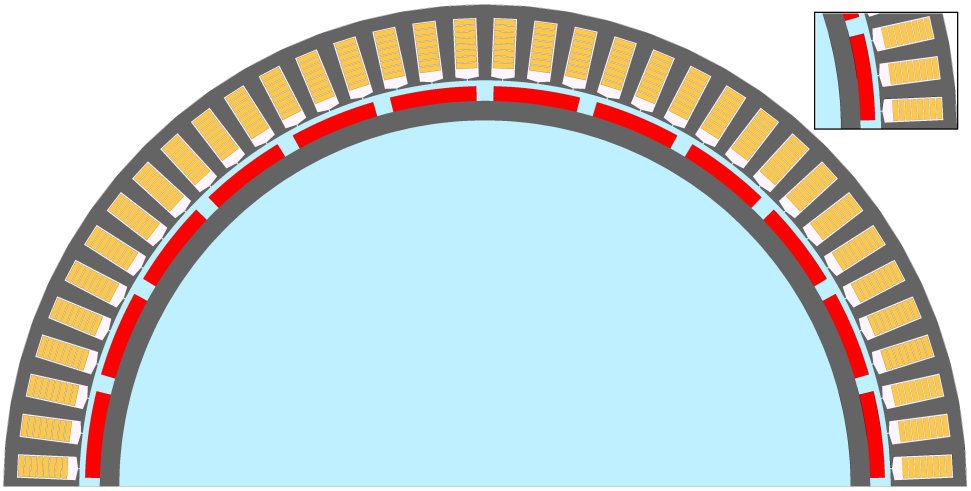

FIGURE 2.4: Half 2-D view of the final machine geometry with hairpin winding. The airgap and the rotor internal shaft are flooded into the water.

flow inside the airgap since it hits directly the most sensitive parts of the machine, mainly the winding and the magnets, which are also responsible for the highest share of the machine's total losses. Therefore, as already highlighted before, it is important to have a sufficient large airgap to make sure that a continuous water flow through the airgap itself is guaranteed, which is particularly important when the machine rotates at high speed and delivers the maximum power. Another advantage for the thermal management of the machine is provided by the adoption of a hairpin winding, which improves the winding-to-ambient heat exchange, thanks to the higher thermal conductivity allowed by the higher copper section in the slot.

The machine design process was carried out by means of an iterative procedure, taking into account the aforementioned constraints and targets, by considering carrying out 2-D finite element electromagnetic analysis (with Altair®FluxMotor®) and also thermal simulations (with Ansys Motor-CAD). In Figure 2.4 the 2-D view of the final geometry is shown, while in Figure 2.5 the dq fluxes map along with the torque map with the MTPA curve is presented. The aim of the design was to keep the winding temperature below 180 °C, corresponding to a class H insulation, when the rated power is delivered, and to not exceed 190 °C during the overload phase, in order to not reduce significantly the life of the insulation material. Indeed, from the Arrhenius law, every 10 °C the life of the insulation is halved and for this reason it is important to keep the temperature near to the specifications provided by the manufacturer. The resulting geometric parameters of the final designed machine are summarized in Table 2.4, along with their graphical description in Figure 2.6: the stator is characterized by a parallel slot geometry in order to fit the hairpin winding inside the slot area and achieve a high fill factor. On the other hand, Table 2.5 summarizes the main electrical and winding data of the final motor geometry. The nominal L_d, L_q inductances were calculated from the dq linked fluxes obtained at the nominal i_d, i_q currents by means of 2-D FEA magnetostatic simulations. It can be seen that dq unsaturated in-

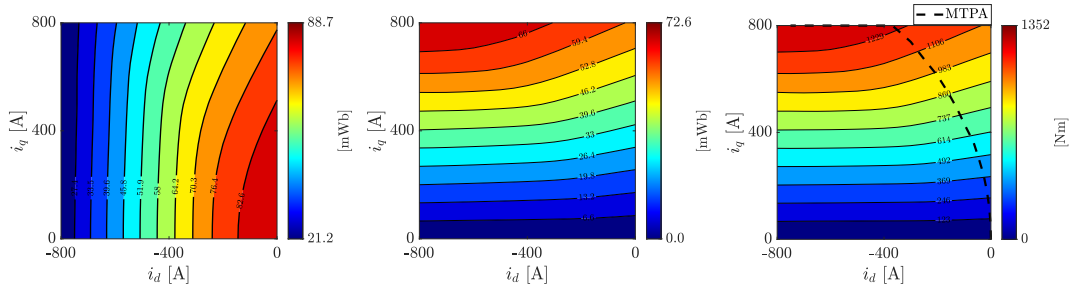

FIGURE 2.5: (a-b) dq fluxes maps and (c) torque map (with the MTPA trajectory) of the final designed machine.

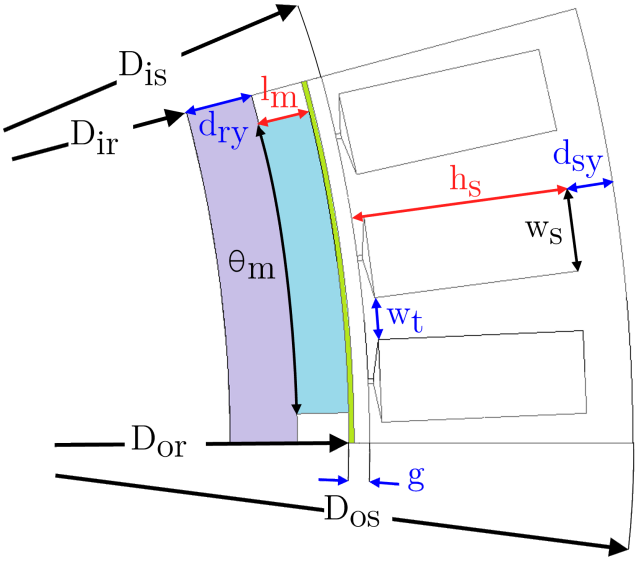

FIGURE 2.6: Description of the motor geometric parameters.

ductances are the same, i.e. $L_d = L_q$, as expected from a SPM machine while their value is much higher than the dq inductances at the nominal current: this result is given by the saturation occurring in the stator magnetic circuit when the nominal current is applied. This aspect is very important since it is clear that the machine saturation produces a magnetic anisotropy between the d axis and the q axis which is clearly visible from the ratio between L_q and L_d. This anisotropy can be exploited to increase the electromagnetic torque by means of an additional reluctance torque term, which is obtained by imposing a non-zero i_d current. Another aspect which should be highlighted is the low AC/DC resistance ratio which was possible to achieve thanks to the adoption of 8 conductors per slot, due to the fact that 4 internal paths for each phase were chosen, allowing to reduce the conductors height and therefore distribute more evenly the current inside the conductors. Moreover, the hairpin winding was supposed to be transposed during the manufacturing process, following the rules of the conductors positioning for this kind of winding, in order to induce the same back electromotive force (back-EMF) in each phase and this is particularly important when multiple parallel paths

TABLE 2.4: Geometric parameters of the final designed machine.

Stack length	L_{stk}	200.0 mm
Airgap width	g	2.0 mm
Stator outer diameter	D_{os}	325.0 mm
Stator bore	D_{is}	274.0 mm
Rotor inner diameter	D_{ir}	247.0 mm
Rotor yoke width	d_{ry}	6.5 mm
Magnets width	l_m	5.0 mm
Magnets arc	θ_m	12.5°
Slot height	h_s	8.0 mm
Opening slot width		0.5 mm
Slot width	w_s	5.0 mm
Stator yoke width	d_{sy}	4.5 mm
Stator teeth width (min.)	w_t	4.9 mm
Active parts mass		53.5 kg
Active parts volume		16.6 L

TABLE 2.5: Electrical and winding data of the final designed machine.

Conductor section	12.6 mm^2
Slot fill factor (gross)	62.4%
Rated current density	10.9 A_{rms}/mm^2
Parallel paths	4
Conductors per phase	48
Conductors per slot	8
Conductor width/height	7.0 mm / 1.8 mm
DC phase resistance @20 °C	0.0056 Ω
Maximum electrical frequency	800 Hz
AC/DC resistance ratio @800 Hz	2.6
Stacking factor	0.928
L_d, L_q (unsaturated)	132 µH , 132 µH
L_d, L_q (nominal current)	31 µH , 61 µH

are employed.

2.2.2 Simulation Results

In this section the results of the electromagnetic and the thermal analysis carried out on the machine final geometry will be shown. Two different working points were analyzed: the rated working point, corresponding to an output power of 600 HP, approximately equal to 440 kW, and the overload working point, corresponding to an output power of 730 HP, approximately equal to 540 kW. Given the application of a naval propulsion system and in order to

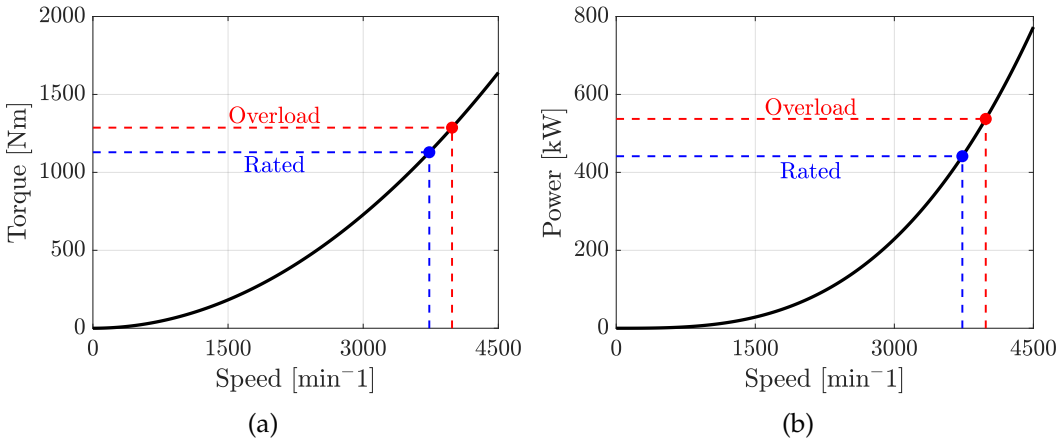

FIGURE 2.7: (a) load torque and (b) power of a pumping-type load.

TABLE 2.6: Load torque and power of the analyzed working points.

	Rated	**Overload**
Speed	3750 min^{-1}	4000 min^{-1}
Torque	1127 N m	1284 N m
Power	441 kW	537 kW

analyze the effect of this operating conditions, a pumping-load type was simulated, by considering the quadratic speed-torque curve depicted in Figure 2.7. In Table 2.6, the two analyzed point are summarized.

2.2.2.1 2-D FEA Electromagnetic Analysis

The finite element analysis (FEA) was carried out by means of transient magnetic simulations, by using the commercial software Altair®Flux®, in the two aforementioned operating points. The transient FEA takes into account the time dependence of all the variables and allows also to calculate the different losses terms: iron losses, AC and DC winding losses, magnet losses, rotor banding losses. Table 2.7 shows the input values used for the FEA simula-

TABLE 2.7: 2-D FEA input data.

	Rated	**Overload**	**Overload w/ PWM**
Speed	3750 min^{-1}	4000 min^{-1}	i_{sd},i_{sq} currents
Phase current	550 A_{rms}	650 A_{rms}	from
Control angle	20°	27°	PLECS®
i_{sd}	−266 A	−417 A	with
i_{sq}	731 A	819 A	$f_{sw} = 25$ kHz
Magnet temperature		40 °C	
Winding temperature		200 °C	

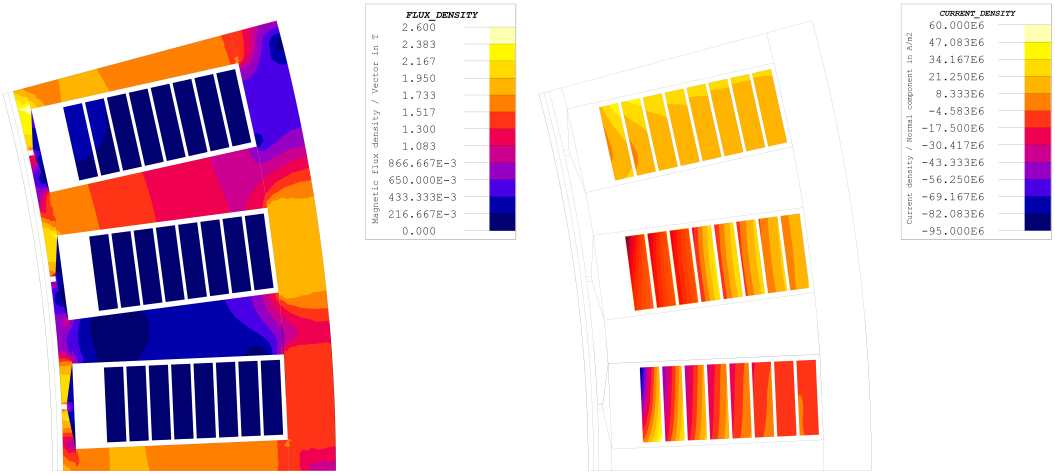

(a) (b)

FIGURE 2.8: Colored maps obtained from the Altair®Flux® simulation in the overload point: (a) stator magnetic circuit flux density (in T) and (b) current density in the winding conductors (in A_{rms}/m^2).

tions: an i_d current is necessary to maintain the line voltage below the admissible value, but also to exploit the magnetic anisotropy of the machine, as already shown in Table 2.5, where it can be seen that the ratio between L_q and L_d at the nominal current is almost 2. For the overload point an additional analysis was carried out in order to take into account the PWM ripple on the phase currents to evaluate the impact on the machine efficiency and performance. In order to do so, a PLECS® simulation was carried out, by using a dq model of the machine obtained from the magnetostatic FEA simulations, afterwards the dq currents were used as input for the FEA analysis.

In Figure 2.8 the flux density map in the stator circuit and the current density map in the winding conductors are shown: the stator yoke induction is higher than 1.7 T, while the current density distribution inside the conductors is not even due to the skin and proximity effects, which are worsened by the conductors geometry. Figure 2.9 shows the line voltage waveforms for both the rated and the overload working point. The curves show that the line voltage signal features a great harmonic content, which is caused by the stator MMF harmonics due to the single-layer winding. The higher harmonic distortion increases the peak value of the line voltage and thus the required DC bus voltage to drive the motor. Another figure of merit to analyze the electric motor is defined by the output torque waveform with respect to the rotor position. As the Figure 2.10 shows, the peak-to-peak torque ripple is appreciable, approximately equal to 15%. Even if this torque ripple produces no harm to the operation of the rim-driven propeller, which does not feature a line shaft, it may causes slip of the rolling bearings elements. The adoption of hybrid bearings, with ceramic rolling elements, can solve this issue, since the reduced mass of the ceramic rolling elements reduces the centrifugal load on the outer ring and also the slip chance of the rolling elements subjected to torque ripple. Figure 2.11 shows the waveforms versus the rotor electri-

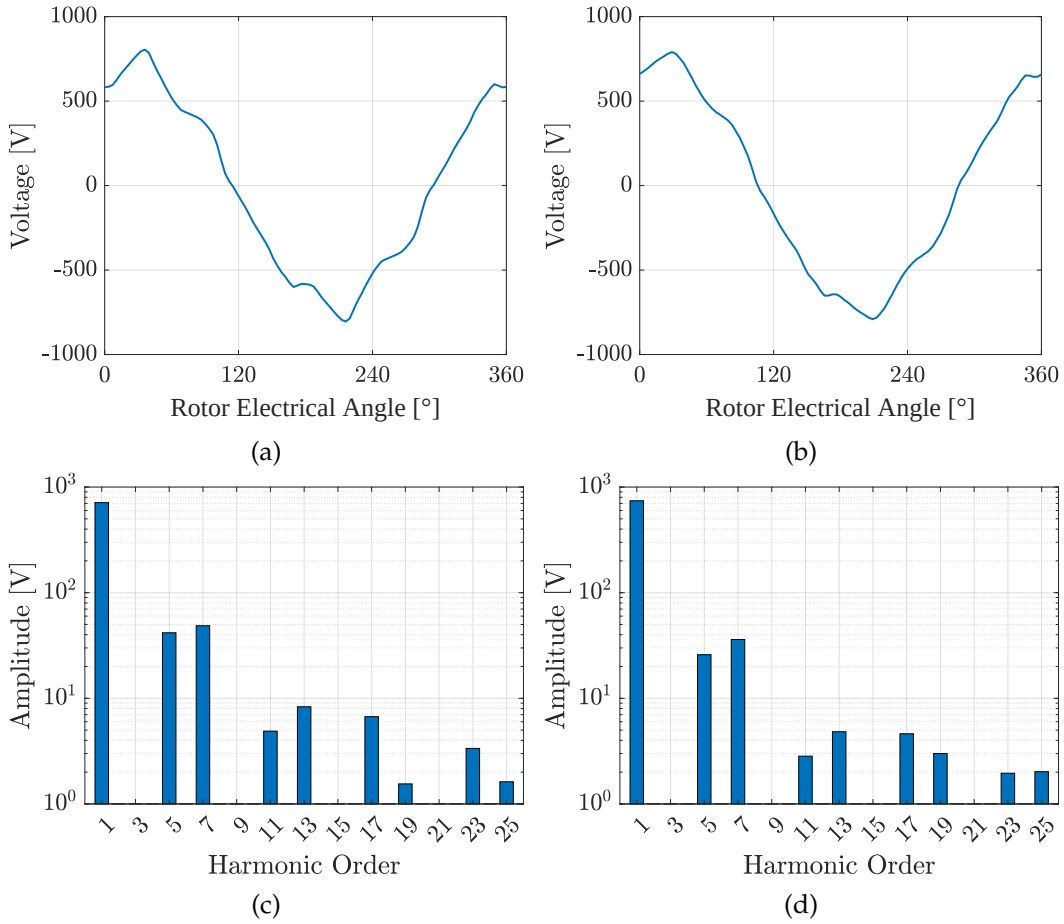

FIGURE 2.9: Line voltage curve and spectrum obtained from the 2-D FEA simulation for (a-c) the rated working point and (b-d) the overload working point.

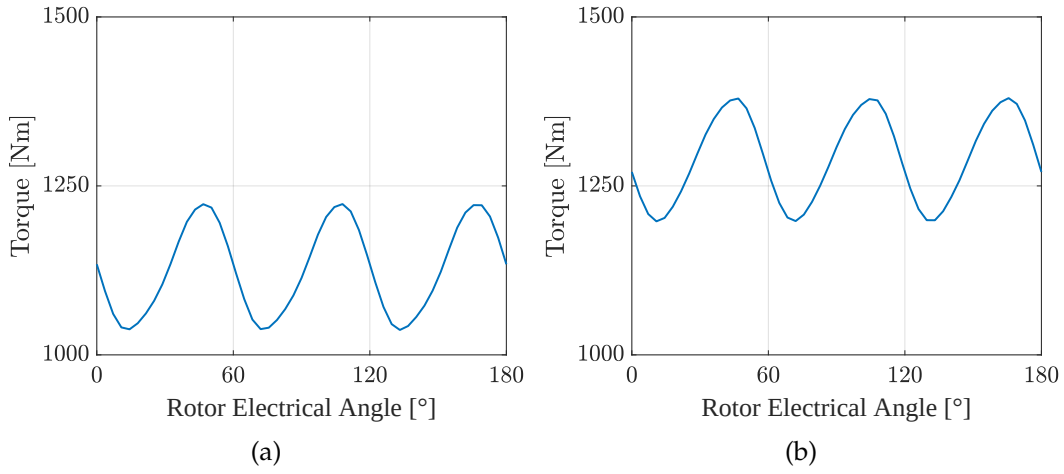

FIGURE 2.10: Mechanical torque evolution over the rotor electrical angle obtained from the 2-D FEA simulation for (a) the rated working point and (b) the overload working point. Only one half of the electrical period was considered.

cal angle of the losses in the different parts of the machine obtained from

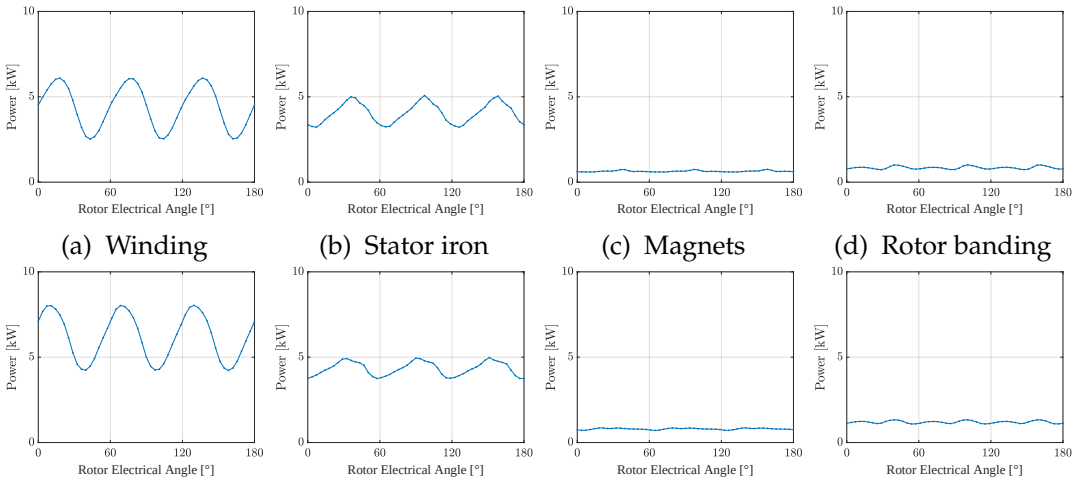

(a) Winding (b) Stator iron (c) Magnets (d) Rotor banding

(e) Winding (f) Stator iron (g) Magnets (h) Rotor banding

FIGURE 2.11: Losses evolution over the rotor electrical angle for the rated and overload points obtained with the FEA simulations (one half of the electrical period): (a-d) rated point; (e-h) overload point.

TABLE 2.8: Summary of the losses obtained by the 2-D FEA.

	Rated	**Overload**	**Overload w/ PWM**
Winding DC	8750 W	12 150 W	12 150 W
Winding AC	4400 W	6200 W	6650 W
Stator iron	4080 W	4400 W	4600 W
Magnets	650 W	800 W	1025 W
Rotor banding	850 W	1200 W	1475 W
Rotor back-iron	125 W	100 W	150 W

the FEA simulations. The periodicity of the losses is equal to 6, therefore, since only half electrical period is shown, three periods of the losses can be counted. As it can be observed, the main percentage of the losses are located into the stator, especially in the winding which, given by the sum of DC and AC winding losses, reach more than 18 kW at the peak power. Nevertheless, despite the high electric frequency, the AC losses can be considered acceptable, since the ratio between the AC and the DC resistance is equal to 2.6. This result is obtained thanks to the adoption of multiple parallel paths, leading to a higher number of conductors in the slot, which reduces the cross-section of the conductors, and thus the losses given by the skin effect. Figure 2.12 shows the waveforms of the line voltage, the dq currents and the mechanical torque considering the PWM ripple on the phase currents. The summary of the losses in both working points are detailed in Table 2.8, for the overload point the losses with the PWM ripple are also shown. It should be noted that the winding losses were prudently calculated at the temperature of 200 °C. In Table 2.9 the results of the finite element analysis are summarized: the main result is that an efficiency of almost 96% is reached when the rated power is delivered, and in the overload point the efficiency is still very high.

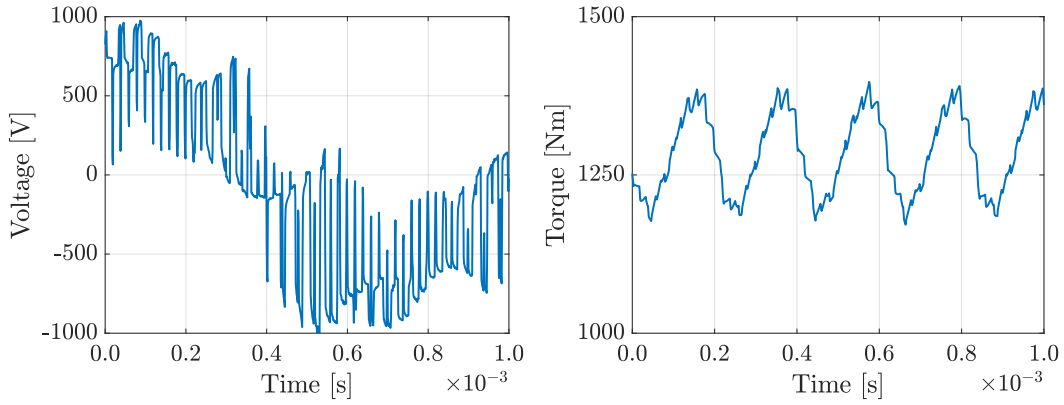

FIGURE 2.12: Output waveforms obtained after the PLECS and 2-D FEA simulations: (a) line voltage and (b) mechanical torque in the overload working point, one full electric period is shown.

TABLE 2.9: Summary of the 2-D FEA results.

	Rated	**Overload**	**Overload w/ PWM**
Average mechanical torque	1127 N m	1289 N m	1285 N m
Torque ripple	187 N m	183 N m	226 N m
Torque ripple %	16.6%	14.2%	17.6%
Mechanical power	443 kW	540 kW	538 kW
Total losses	18.9 kW	24.9 kW	26.1 kW
Efficiency	95.9%	95.6%	95.4%

Another important result to highlight is that a peak torque of almost 1300 N m was obtained, leading to a gravimetric torque density of approximately 24 N m kg^{-1}. On the other hand, since the calculated peak power was equal to 540 kW, a gravimetric power density of 10 kW kg^{-1} was reached. Both the torque and the power density were calculated considering only the machine active parts, Table 2.10. It is worth to notice that the peak line voltage in the overload point is lower compared to the value at the rated point: this is mainly due to the combination of a lower inductance (caused by the higher saturation level) and a higher control angle, which increases the flux weakening term (i.e. $\lambda_d = L_d i_{sd}$) and thus reduces the linked flux along the d axis.

TABLE 2.10: Torque and power densities calculated from the 2-D FEA results of the peak power working point.

Peak gravimetric power density	10.1 kW kg^{-1}
Peak gravimetric torque density	24.1 N m kg^{-1}
Peak volumetric power density	32.6 kW L^{-1}
Peak volumetric torque density	77.7 N m L^{-1}

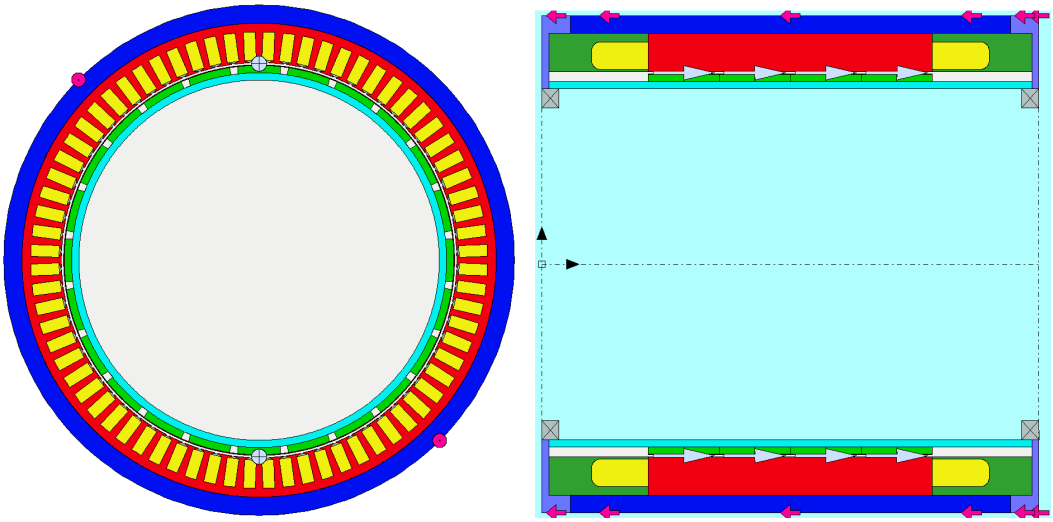

(a) (b)

FIGURE 2.13: Machine 2-D view in Motor-CAD: (a) radial view, (b) axial view.

2.2.2.2 Thermal Analysis

TABLE 2.11: Motor-CAD settings used for the thermal analysis.

Housing outer cooling	Blown over
Motor orientation	Horizontal
Cooling systems	Wet rotor, Submersible, Flooded
Fluid type	Water
Ambient temperature	20 °C
Outer flow velocity	10 m s^{-1}
Wet rotor flow path	Front inlet
Effective fluid velocity in airgap	26.3 m s^{-1}

The thermal analysis was carried out with Ansys Motor-CAD, which allows to calculate the temperatures in the machine by using an equivalent thermal network of the machine, as already shown in Chapter 1. The settings used for the simulation are summarized in Table 2.11: the machine cooling was considered as a combination of three different systems (the water is forced to flow outside and inside the machine) and the thermal analysis was carried out considering a water temperature of 20 °C. Figure 2.13 shows the front and axial view of the machine used in the Motor-CAD simulation. As an hypothesis, the water flow speed outside the machine is the same as the boat speed, therefore it was imposed equal to 10 m s^{-1}, while inside the airgap the flow speed is mainly defined by the shaft rotating speed, which was assumed equal to 3750 min^{-1}. According to the load curve of Figure 2.6 the higher is the machine speed and the higher is the power delivered, for this reason the highest heat dissipation is needed when the machine rotates at the highest speed. The water flow speed at the external housing diameter and

TABLE 2.12: Steady-state temperatures.

	Rated	**Overload**	**Overload w/ PWM**
Winding hotspot	159 °C	207 °C	210 °C
Winding average	120 °C	150 °C	154 °C
Winding coolspot	94 °C	115 °C	118 °C
Magnets	35 °C	36 °C	37 °C
Rotor back-iron	35 °C	36 °C	37 °C
Rotor banding	32 °C	33 °C	33 °C
Stator back-iron	63 °C	71 °C	72 °C
Stator tooth	75 °C	87 °C	89 °C

in the internal rotor diameter was imposed to $10\,\mathrm{m\,s^{-1}}$, while for the airgap a fluid volume rated of $500\,\mathrm{L\,min^{-1}}$ was assumed. In Table 2.12 the steady-state temperatures of the machine when delivers the rated and the overload power are summarized: the losses detailed in Table 2.8 were used as a input for the simulation. As expected, the winding is the hottest component

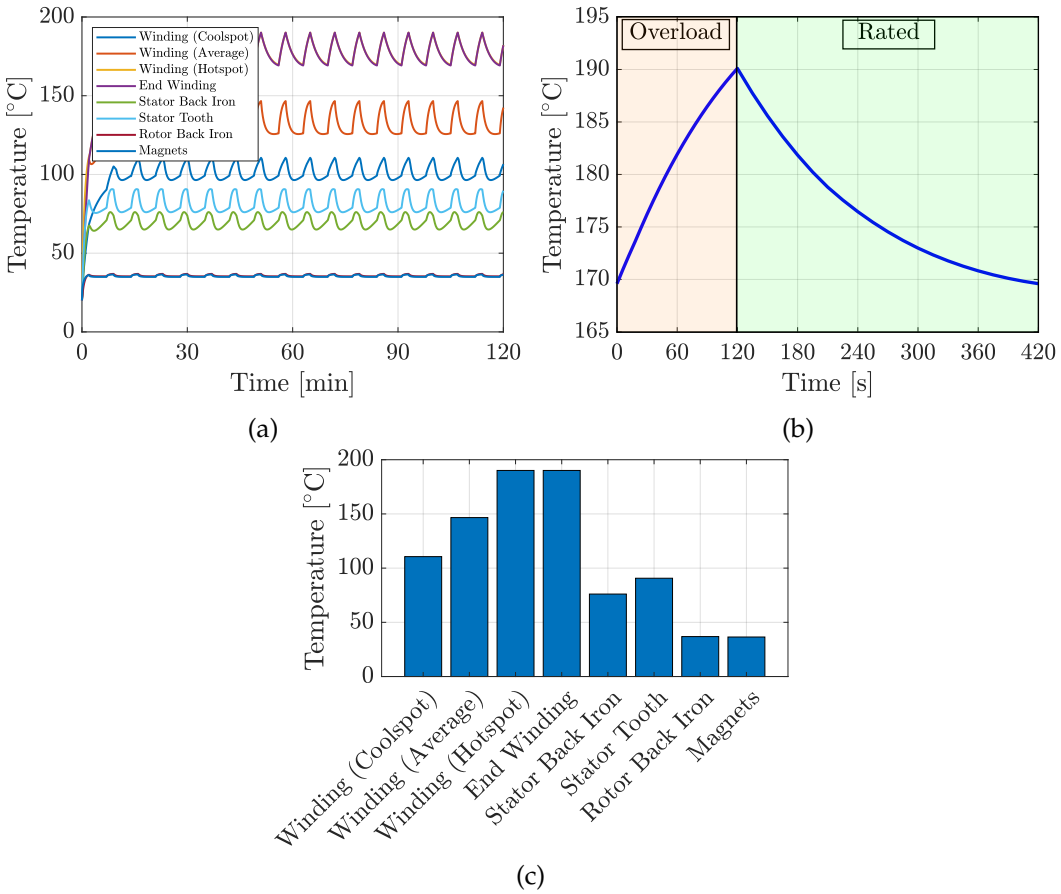

FIGURE 2.14: Machine temperatures after 20 repetitions of the sample duty-cycle: (a) temperature evolution, (b) winding hotspot evolution detail, (c) maximum temperatures reached in the different machine parts.

and reaches a 210 °C steady state temperature value when the peak power is delivered and considering also the PWM ripple on the phase currents. This temperature is higher than the admissible value for class H insulation however, since it is expected that the peak power should be demanded only for short transients, the actual winding temperatures should be lower.

To verify this assumption, a simple duty-cycle was defined in order to analyze the impact of the peak power transient on the machine temperature. The duty-cycle was supposed to have two different phases: a first overload phase of 120 s (for example simulating the acceleration of the boat to the maximum speed) and a second cruise phase of 300 s, in which the rated power is delivered. In Figure 2.14 the machine temperatures after 20 cycles are shown. As the Figure 2.14(b) shows, the winding peak temperature reaches 190 °C: if this condition would be maintained for a long time it would cause a reduction of the insulation life which, according to the Arrhenius law, would be almost halved. However, the analyzed duty-cycle is not representative of a real life user experience and it is expected that the actual boat driving cycle would be more conservative with respect to this one. On the other hand, when the machine delivers the rated power of 600HP, the winding hotspot is well below the maximum admissible temperature of 180 °C, therefore it can be considered as an acceptable result. It should be noted that the magnets are always very cool in both working points, below the chosen temperature during the design phase, thanks to the elimination of the sub-harmonics in the magnetomotive force at the airgap, which was achieved by adopting a distributed winding arrangement, and the flooded rotor operation with the forced water flow through the airgap.

2.3 A Reconfigurable Multi-Three-Phase Drive for Naval Propulsion Systems

A reconfigurable drive is derived from a multi-three-phase system with the aim is to exploit the modularity and the segmentation to increment the drive efficiency when the electric machine is operated at partial load. The analysis of the benefits of the reconfigurable architecture, including the system efficiency, was discussed in [53]. The case study consisted of a quadruple three-phase machine intended for a rim driven propeller used for yachting application. In the present work the analysis of advantages and disadvantages of a multi-three-phase reconfigurable drive used for electric propulsion applications are summarized, also including experimental results on a reduced scale laboratory prototype. Multi-three-phase machines can be classified into two main groups: asymmetric and symmetric, [3], [28]. In asymmetric machines the N three-phase winding sets are electrically shifted of a quantity equal to $\gamma = \frac{\pi}{3N}$ on the contrary, in symmetric machines the N three-phase winding sets are in phase. The latter topology is completely equivalent to the case of a three-phase machine winding with multiple parallel paths. In this case, in order to obtain a redundant structure, each path is supplied by one three-phase converter, which provides a fraction of the total power. In this way, each three-phase set has its own independent star-point connection, which is separated from the others. However, if the phases are balanced (i.e. feature the same turn number and therefore have the same electrical parameters) as it usually happens in a well built machine, the potential of all the neutral points is the same and the sets can be considered as if they were in parallel allowing the possibility to fed each set independently.

The main goal of the reconfigurable architecture is to reduce the number of active converters when the operating speed and requested power is below the rated value. Figure 2.15-(e) shows the effect of winding reconfiguration on the output torque-speed characteristic in case of a quadruple three-phase machine. As it can be seen, the machine torque does not change with the number of connected sets since the torque depends only on the slot current, which is a function of the electrical and magnetic loading, i.e. on the slot current and on the magnet grade. The only variable which depends on the number of connected sets is the maximum power the machine can deliver since it is the drive base speed that changes with the drive configuration. The drive base speed ω_{mb} is defined as the maximum speed the machine can reach without the necessity of the flux-weakening term, i.e. it is the point where the requested line voltage peak is equal to the DC bus voltage and the machine delivers the maximum torque per current (MTC). Since the line voltage depends on the induced back-EMF in the stator winding, which in turns depends on the linked flux, it is a function of the number of turns of the winding: for the same flux per pole, the higher is the number of turns and the higher is the requested line voltage and the lower is the drive base speed. Therefore, by changing the connection of the three-phase sets, the number of turns of the equivalent three-phase machine (i.e. seen by one inverter) changes. In the specific case of Figure 2.15, with 4 three-phase set it is

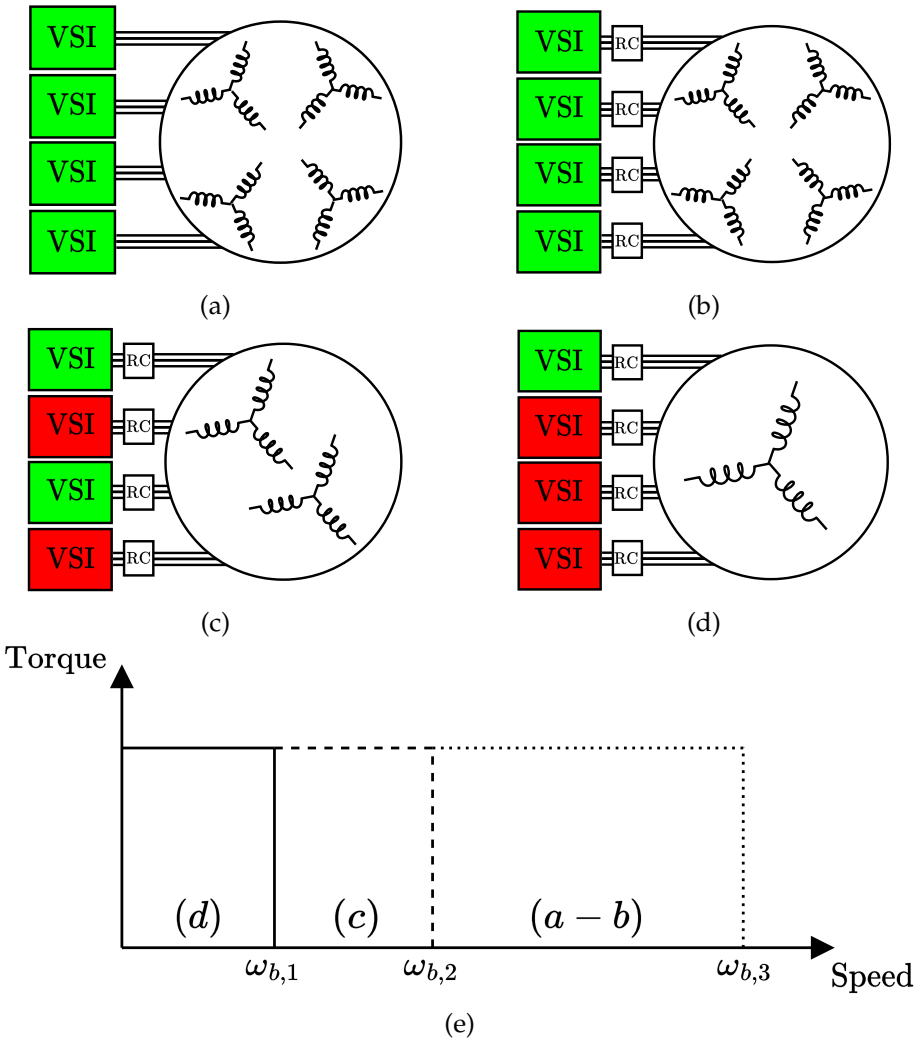

FIGURE 2.15: Example of a quadruple-three-phase drive in: (a) the standard multi-three-phase drive (without reconfiguration cells); (b-d) reconfigurable drive (with reconfiguration cells). In case of a reconfigurable drive: (b) each three-phase set supplied by a converter (Parallel configured drive); (c) two series connected three-phase sets supplied by two converters (Series/Parallel configured drive); (d) all the three-phase sets in series supplied by a single converter (Series configured drive).

possible to obtain 3 different configurations, each of which features its own base speed:

1. $\omega_{mb,1}$, all the winding sets are series connected, only one inverter is active (case d). The number of turns seen by the inverter (n_1) is 4 times the turns of one set ($n_1 = 4n$);

2. $\omega_{mb,2}$, two groups of winding sets are series-connected and each group has two winding sets in parallel. Two inverters are active (case c): the number of turns seen by one inverter (n_2) is 2 times the turns of one set ($n_2 = 2n$);

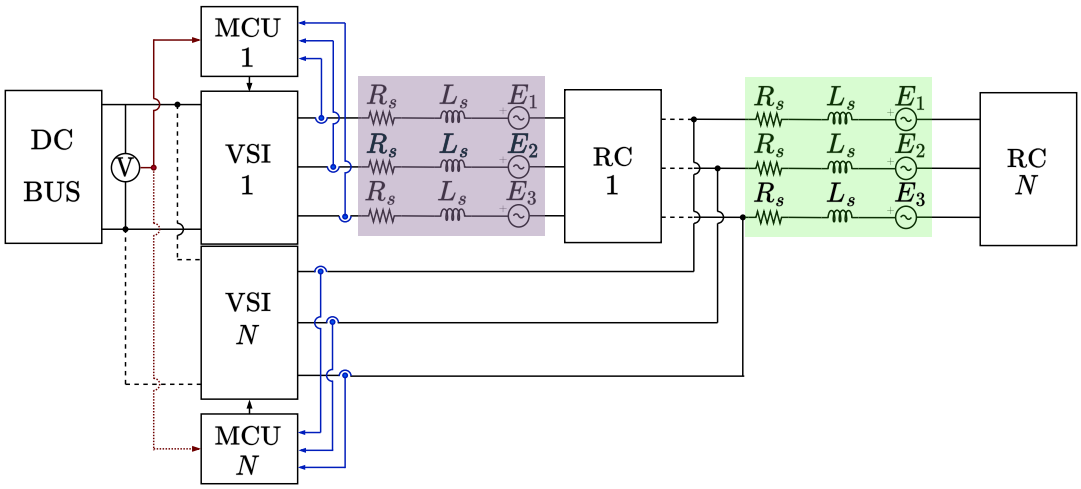

FIGURE 2.16: Reconfigurable architecture with N modules connected to the same dc bus.

3. $\omega_{mb,3}$, all the winding sets are parallel connected, all the inverters are active (case b). This case is equivalent to the one of a traditional multi-three-phase drive with each three-phase set supplied by its own inverter: the number of turns seen by one inverter (n_3) is equal to the turns of one set ($n_3 = n$).

where n is the number of turns of one set. Therefore it is possible to conclude that in the reconfigurable architecture, since the equivalent number of turns change, the base speed changes when the machine passes from one configuration to another: $\omega_{mb,3} = 2\omega_{mb,2} = 4\omega_{mb,1}$.

In the following discussion, when the machine has all the three-phase sets connected in series, and thus the machine is fed by a single inverter, the reconfigurable drive will be referred as a SC (Series Configured) drive. On the other hand, when each three-phase winding set is fed by its own inverter (a condition identical to the original standard drive), the reconfigurable drive will be referred as PC (Parallel Configured) drive.

2.3.1 Reconfigurable Architecture Analysis

In order to better understand the reconfigurable architecture, a symmetrical multi-three-phase machine with N three-phase modules is considered, Figure 2.16. In a parallel configured drive (PC drive), if all the modules are identical, under the hypothesis that the phase current is sinusoidal, each inverter supplies the machine with the same rms phase current, $I^1_{s,\mathrm{rms}}$. The electromagnetic torque delivered by the machine with only one active three-phase inverter (i.e. with all the other inverters off) can be expressed as:

$$T^1_{\mathrm{EM}} = k^1_{\mathrm{T}} I^1_{s,\mathrm{rms}} \tag{2.1}$$

where k^1_{T} is the torque constant of one three-phase set. If the number of active inverters N_{act} is equal to N, the total electromagnetic torque delivered by the

machine in the PC drive is:

$$T_{\mathrm{EM}}^{PC} = N k_{\mathrm{T}}^{PC} I_{s,\mathrm{rms}}^{1} \tag{2.2}$$

where k_{T}^{PC} is the machine torque constant of the machine in the PC drive, expressed in [$\mathrm{Nm/A_{rms}}$], which is equal to the torque constant of one three-phase winding, since the N three-phase windings act as they were in parallel.

When the drive is series configured (SC drive), the N machine windings are connected in series hence the machine torque constant is N times higher than the PC drive. In this case, only one inverter supplies the machine, $N_{act} = 1$, thus:

$$T_{\mathrm{EM}}^{SC} = k_{\mathrm{T}}^{SC} I_{s,\mathrm{rms}}^{1} = N k_{\mathrm{T}}^{PC} I_{s,\mathrm{rms}}^{1} \tag{2.3}$$

where $k_{\mathrm{T}}^{SC} = N k_{\mathrm{T}}^{PC}$ is the machine torque constant in the SC drive, expressed in [$\mathrm{Nm/A_{rms}}$]. Comparing eqs. (2.2) and (2.3), it is clear that the torque delivered by the machine does not change when the drive is reconfigured from series to parallel, or vice versa. When keeping the same DC bus voltage and the same slot current density in both the PC drive and the SC drive, the maximum power decreases when the drive is series configured, because its base speed is reduced by a factor equal to the number of modules, N.

The phase back-EMF of the machine can be written as:

$$E_s = K_e n p \omega_{\mathrm{m}} = K_e n \omega_e \tag{2.4}$$

where $K_e = K_m K_w \Phi_{\mathrm{M}}$ is a constant depending on the winding factor K_w, the magnet distribution factor (if a Permanent Magnet Synchronous Machine, PMSM, is considered) and the flux per pole Φ_{M}; n is the number of turns per phase of the machine; p is the pole-pairs number. The machine mechanical speed is ω_{m} and it is expressed in [$\mathrm{rad\,s^{-1}}$], while $\omega_e = p\omega_{\mathrm{m}}$ is the machine electrical speed in [$\mathrm{rad\,s^{-1}}$]. When the drive is parallel configured, the N three-phase sets are in parallel, thus the number of turns of the machine is equal to $n = n^1$, where n^1 is the number of turns of one three-phase set. On the other hand, when the drive is series configured, the N three-phase sets are in series, thus the number of turns of the machine is equal to $n = Nn^1$. The result is that the $E_s^{SC} = N E_s^{PC}$ therefore, as expected, the back-EMF in the SC drive is N times higher than the back-EMF in the PC drive: this is due to the higher linked flux caused by the increased turn number.

In steady-state conditions, considering a sinusoidal phase current, the equation of one machine phase (of one set) can be written in phasorial terms as:

$$\mathbf{V}_s^1 = R_s^1 \mathbf{I}_s^1 + j\omega_e L_s^1 \mathbf{I}_s^1 + \mathbf{E}_s^1 \tag{2.5}$$

where $\mathbf{V}_s^1 = v_{sd}^1 + j v_{sq}^1$ and $\mathbf{I}_s^1 = i_{sd}^1 + j i_{sq}^1$ are the phasor of the phase voltage and current of one three-phase set respectively, R_s^1 and L_s^1 are the machine resistance and inductance of one set respectively, $\mathbf{E}_s^1$ is the phasor of the back-EMF of one set. In a well designed machine, the winding resistance is usually negligible with respect to the voltage drop across the machine reactance $\omega_e L_s^1$,

therefore it can be neglected:

$$\mathbf{V}_s^1 = j\omega_e L_s^1 \mathbf{I}_s^1 + \mathbf{E}_s^1 \tag{2.6}$$

by introducing the modulation index expression $\mathbf{m} = m_d + jm_q$, the phase voltage can be written as $\mathbf{V}_s^1 = \mathbf{m}v_{\mathrm{DC}}$, where v_{DC} is the dc bus voltage. The drive (electrical) base speed $\omega_{e,b}$ can thus be calculated by imposing the maximum modulation index $\mathbf{m}_{\max} = m_{d,\max} + jm_{q,\max}$:

$$\mathbf{m}_{\max} v_{\mathrm{DC}} = j\omega_{e,b} L_s \mathbf{I}_s^1 + K_e n^1 \omega_{e,b} \tag{2.7}$$

where $K_e n^1 \omega_{e,b} = E_{s,b}^1$ is the back-EMF required in the base speed point, n^1 is the number of turns of one set and $\mathbf{m}_{\max} v_{\mathrm{DC}}$ is the phasor of the maximum available phase voltage, which does not depend on the drive configuration. In fact, the maximum modulation index depends only on the modulation strategy adopted to control the inverter therefore $\mathbf{m}_{\max} v_{\mathrm{DC}} = \mathbf{V}_{\max}$. It is then possible to calculate the (electrical) base speed $\omega_{e,b} = p\omega_{m,b}$:

$$\omega_{e,b}^1 = \frac{\mathbf{V}_{\max}}{jL_s^1 \mathbf{I}_s^1 + K_e n^1} \tag{2.8}$$

Remembering that for the PC drive: $n^{PC} = n^1$ and $L_s^{PC} = L_s^1$, then:

$$\omega_{e,b}^{PC} = \omega_{e,b}^1 \tag{2.9}$$

while for a SC drive: $n^{SC} = Nn^1$ and $L_s^{SC} = NL_s^1$, then:

$$\omega_{e,b}^{SC} = \frac{\mathbf{V}_{\max}}{jNL_s^1 \mathbf{I}_s^1 + K_e N n^1} \tag{2.10}$$

hence, the ratio between the SC drive base speed and the PC drive base speed is obtained:

$$\frac{\omega_{e,b}^{SC}}{\omega_{e,b}^{PC}} = \frac{jL_s^1 \mathbf{I}_s^1 + K_e n^1}{N(jL_s^1 \mathbf{I}_s^1 + K_e n^1)} \longrightarrow \omega_{e,b}^{SC} = \frac{\omega_{e,b}^{PC}}{N} \tag{2.11}$$

as a consequence it results that the SC drive base speed is N times lower than the PC drive base speed. This means that, since the electromagnetic torque does not change with the drive configuration, the power rating of the SC drive is N times lower than the PC drive power rating.
The drive reconfiguration from parallel to series has also effect on the modulation index. For a given electrical speed ω_e, provided that it is below the SC drive base speed, if $\mathbf{m}^{SC}$ is the SC drive modulation index, the phase voltage is equal to:

$$\mathbf{m}^{SC} v_{\mathrm{DC}} = \omega_e N(jL_s^1 \mathbf{I}_s^1 + K_e n^1) \tag{2.12}$$

For the PC drive, considering a modulation index $\mathbf{m}^{PC}$, the phase voltage is equal to:

$$\mathbf{m}^{PC} v_{\mathrm{DC}} = \omega_e (jL_s^1 \mathbf{I}_s^1 + K_e n^1) \tag{2.13}$$

the end result is that:

$$\mathbf{m}^{SC} = N\mathbf{m}^{PC} \tag{2.14}$$

the SC drive modulation index is N times higher than the PC drive modulation index.

Another benefit provided by the reconfigurable architecture is a reduction of the phase current ripple when the drive operates with the series configuration. By considering a 7-interval Space Vector Modulation (SVM), according to [54], the maximum current ripple expression depends on the entity of the modulation index:

$$I_{s,pp} = \begin{cases} \dfrac{v_{\mathrm{DC}}}{2f_{\mathrm{sw}}} \dfrac{M_{\mathrm{A}}}{L_s} \left(1 - \dfrac{3}{2} M_{\mathrm{A}}\right), & M_{\mathrm{A}} \leq 0.282 \\ \dfrac{v_{\mathrm{DC}}}{2f_{\mathrm{sw}}} \dfrac{M_{\mathrm{A}}}{L_s} \dfrac{1}{\sqrt{3}}, & M_{\mathrm{A}} > 0.282 \end{cases} \tag{2.15}$$

where $M_{\mathrm{A}} = \sqrt{m_d^2 + m_q^2}$ is the amplitude modulation index, which for a SVM features a maximum value of 0.577. However, for a given working point $\omega_e \leq \omega_{e,b}^{SC}$, the PC drive works with a lower modulation index with respect to the SC drive. For example, if $N = 2$ and $0.564 < M_{\mathrm{A}}^{SC} \leq 0.577$ the PC drive modulation index is halved, $0.282 < M_{\mathrm{A}}^{PC} \leq 0.288$. In this case the current ripple is the same for both the configurations. Considering $N = 2$, the current ripple ratio between SC drive and PC drive can be expressed for the other values of M_{A} as:

$$\frac{I_{s,pp}^{SC}}{I_{s,pp}^{PC}} = \begin{cases} \dfrac{1 - \frac{3}{2} M_{\mathrm{A}}^{SC}}{1 - \frac{3}{2} \frac{M_{\mathrm{A}}^{SC}}{N}}, & 0 < M_{\mathrm{A}}^{SC} \leq 0.282 \\ \dfrac{1}{\sqrt{3}\left(1 - \frac{3}{2} \frac{M_{\mathrm{A}}^{SC}}{N}\right)}, & 0.282 < M_{\mathrm{A}}^{SC} < 0.564 \end{cases} \tag{2.16}$$

it is important to notice that, when $N > 2$, the SC drive current ripple is always lower than the PC drive, even when $M_{\mathrm{A}}^{SC} > 0.564$. Figure 2.17 shows the evolution of the current ripple ratio between the SC drive and the PC drive for different values of N: there is a point of diminishing return in increasing the number of three-phase modules to reduce the current ripple, as it can be seen for $N > 8$ the difference is negligible.

Finally, Table 2.13 summarizes the results of the comparison between the PC drive and the SC drive main parameters.

2.3.2 Reconfiguration Cells Analysis

In order to connect and disconnect the three-phase sets and achieve the desired configuration is it necessary to employ bi-directional switches, which

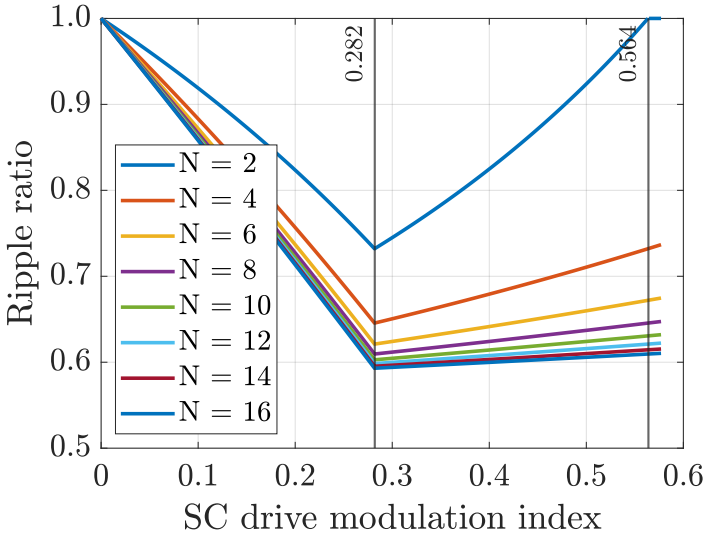

FIGURE 2.17: Evolution of the SC drive/PC drive current ripple ratio (p.u.) evolution over the SC drive modulation index, for different values of N.

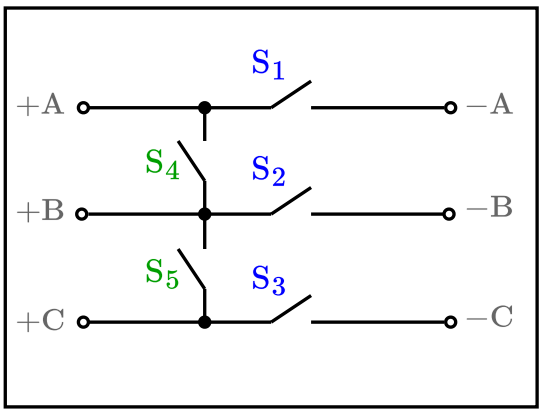

FIGURE 2.18: Reconfiguration Cell with five bi-directional switches. When the drive is parallel connected S_1, S_2 and S_3 are closed. When the drive is series connected S_4 and S_5 are closed.

allow the sinusoidal current to flow. For this reason, the reconfigurable architecture needs a so-called reconfiguration cell (RC), as shown in Figure 2.16. Each RC is composed by five bi-directional switches that must be sized according to the maximum phase current (peak value), Figure 2.18. When a three-phase set must be short-circuited, the transversal switches are closed and the longitudinal switches are open. Vice versa, when two three-phase sets must be series-connected, the transversal switches are open and the longitudinal switches are closed. The bi-directional switches can be fully solid-state, electromechanical or hybrid and they are used to short-circuit a three-phase set or connect two sets in series. Since the RC require bi-directional reverse-blocking switches, which can be implemented using full solid-state devices, electromechanical devices or a hybrid combination of the two, they

TABLE 2.13: Nameplate data comparison between parallel and series configurations.

	PC drive	**SC drive**
Turns per phase	n^1	Nn^1
Torque constant	k_{T}^1	Nk_{T}^1
Back-EMF amplitude	E_s^1	NE_s^1
Active converters	N	1
Base speed	$\omega_{e,b}^{PC}$	$\omega_{e,b}^{PC}/N$
Amplitude modulation index	M_{A}	M_{A}/N
Electromagnetic torque	T_{EM}	T_{EM}
Electromagnetic power	P_{EM}	P_{EM}/N
Stator resistance	R_s^1	NR_s^1
Synchronous inductance	L_s^1	NL_s^1

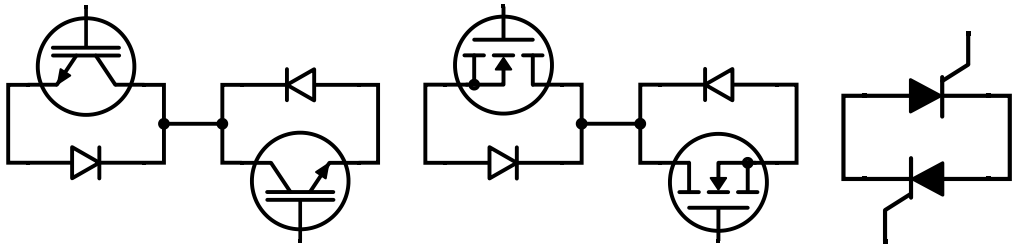

(a) (b) (c)

FIGURE 2.19: Solid-state bi-directional switch topologies: (a) IGBT; (b) MOSFET; (c) SCR.

adversely affects the system efficiency. For this reason, a preliminary assessment of the losses produced by one reconfiguration cell with different switches technologies was carried out. Figure 2.19 shows three possible architectures to obtain a full solid-state bi-directional reverse-blocking switch: IGBT, MOSFET and SCR. An analytical calculation was made in order to analyze the conduction losses of each switch and then compare the performance between them, in order to assess the impact on system efficiency, also considering an additional switch composed of an electromechanical relay coupled with a solid-state device (hybrid-relay): the results are summarized in Table 2.15. The devices used for the comparison are summarized in Table 2.14. The SCR losses were determined by datasheet by using the phase current average value over one half fundamental period. The bi-directional switch

TABLE 2.14: Devices used for the reconfiguration cell analysis.

SCR	ST Microelectronics TN5050H
IGBT	Infineon IKQ50N120CT2
MOSFET	Infineon SPW55N80C3
Relay	Panasonic HEV2aNP12v

TABLE 2.15: Conduction losses of a single bi-directional switch .

Switch type	SCR	IGBT	MOSFET	Hybrid Relay
Conduction losses	20 W	39 W	62 W	20 W

The Losses were calculated with a rms phase current of 20 A_{rms} for different power semiconductors employed in the RC.

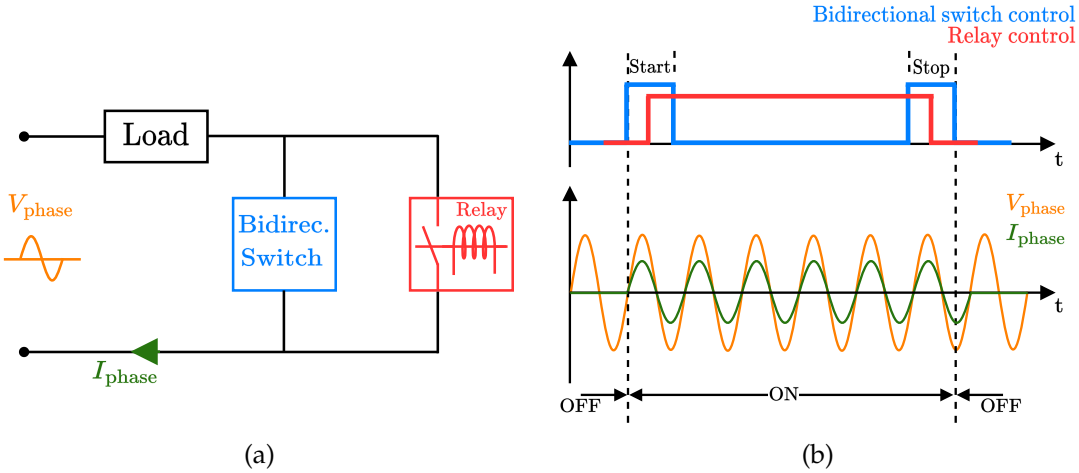

FIGURE 2.20: Hybrid relay topology combining a traditional electromechanical relay with a bi-directional switch (a) and switch control law (b).

obtained with MOSFETs or IGBTs belongs to the series topology (composed of a transistor and a diode connected in series), hence the total voltage drop across the switch is higher with respect to the SCR one and hence resulting in higher conduction losses. The SCR architecture is a parallel topology, given the intrinsic reverse blocking capability of SCR, hence it is characterized by a lower voltage drop and therefore the total conduction losses are lower. Even so, since the SCR devices are usually employed in grid frequency applications, their natural turn-off commutation performs poorly in switching applications, where the dV/dt ratio is extremely large. It is therefore possible that the SCR may fail to turn on/off during the drive operation: it is not advisable the usage of this kind of devices alone. A possible solution to overcome these limitations, given by the high power losses of the IGBT and MOSFET and the poor performance of the SCR, can be achieved with a hybrid configuration, shown in Figure 2.20-(a). Given the nature of this device, it is especially suited for large power sizes, e.g. when the power rating of the machine is in the order of hundreds of kW. The RC represented in Figure 2.18 can be obtained e.g. with a single throw electromechanical relay, assisted by bi-directional solid-state switches, to avoid arcing and premature wear of the contacts. According to the diagram in Figure 2.20-(b), the sequence of operation of a hybrid relay can be summarized into three main steps:

- Start: the solid-state switch is turned ON, establishing connection. Then, right after connection is established, the electromechanical relay is also

turned ON. Now the current flows through the mechanical switch that has a lower resistivity. The solid-state switch is then turned OFF.

- Conduction: current flows only through the relay, with the benefits of low power losses during this phase.
- Stop: the solid-state switch is turned ON again. The relay is then turned OFF while the voltage across the contacts is kept low and avoid possible arcing among relay contacts. Finally, the solid-state switch is turned OFF.

2.3.2.1 Reconfiguration Cell Failure Analysis

As already mentioned, the reconfigurable architecture features a certain number of reconfiguration cells (RCs), each of which is composed of 5 bi-directional switches. This section discusses the drive operation capability in case of fault to one of the switches composing the RC, when one or two different bi-directional switches are short-circuited or open-circuited, while the others are healthy. For the sake of simplicity, the analysis is performed in case of a double three-phase drive, but the method of analysis can be extended to any number of three-phase winding sets. Considering a double three-phase drive, only two configurations are possible: series configuration (the two sets are connected in series and only one inverter is active) and parallel configuration (each set is fed by its own inverter). In this scenario, if one of the sets is always short-circuited then only one reconfiguration cell is needed to obtain the two drive configurations: the series configuration is obtained by closing the RC's longitudinal switches (e.g. Figure 2.18 S_1, S_2, S_3) and by opening the transversal ones (e.g. Figure 2.18 S_4, S_5); the parallel configuration is obtained by closing the RC's transversal switches (S_4, S_5) and by opening the longitudinal ones (S_1, S_2, S_3).

The aim of this analysis is to find out in which cases the drive cannot operate anymore or how the output power capabilities of the drive change, when the operation is still possible. It is important to point out that in case of a forced series configuration scenario, the drive maximum output power is reduced since the maximum speed the machine can operate is halved with respect to its rated value. As Tables 2.16 and 2.17 show, in case of a single fault in one longitudinal (e.g. Figure 2.18 S_1) or one transversal switch (e.g. Figure 2.18 S_4), the drive can still operate, but the remaining possible configuration is determined by the type of failure on the switch (i.e. if permanently open or closed). Considering a second fault scenario, where another of the remaining healthy switches develops a short- or open- circuit fault, by analyzing the fault combinations, it is interesting to notice that the reconfigurable drive has still a 50% possibility to maintain operation. A final consideration regarding the RC architectures presented in the previous section is the following: if a hybrid relay switch is chosen, the most common failure is the electromechanical relay contacts sticking together, which causes the switch to be permanently closed.

TABLE 2.16: Drive operation analysis with one longitudinal switch fault (S_1) and in case of a second fault in another longitudinal switch (S_2) or in a transversal switch (S_4).

Case	S_1	S_2	S_3	S_4	S_5	Configuration
1	*CL*	*H*	*H*	*H*	*H*	Series configuration
2	*OP*	*H*	*H*	*H*	*H*	Parallel configuration
3	*CL*	*CL*	*H*	*H*	*H*	Series configuration
4	*CL*	*OP*	*H*	*H*	*H*	Not possible
5	*OP*	*CL*	*H*	*H*	*H*	Not possible
6	*OP*	*OP*	*H*	*H*	*H*	Parallel configuration
7	*CL*	*H*	*H*	*CL*	*H*	Not possible
8	*CL*	*H*	*H*	*OP*	*H*	Series configuration
9	*OP*	*H*	*H*	*CL*	*H*	Parallel configuration
10	*OP*	*H*	*H*	*OP*	*H*	Not possible

Each switch can be: Permanently Closed (CL), Permanently Open (OP) or Healthy (H).

TABLE 2.17: Drive operation analysis with one transversal switch fault (S_4) and in case of a second fault in the other transversal switch (S_5) or in a longitudinal switch (S_1).

Case	S_1	S_2	S_3	S_4	S_5	Configuration
1	*H*	*H*	*H*	*CL*	*H*	Parallel configuration
2	*H*	*H*	*H*	*OP*	*H*	Series configuration
3	*H*	*H*	*H*	*CL*	*CL*	Parallel configuration
4	*H*	*H*	*H*	*CL*	*OP*	Not possible
5	*H*	*H*	*H*	*OP*	*CL*	Not possible
6	*H*	*H*	*H*	*OP*	*OP*	Series configuration
7	*CL*	*H*	*H*	*CL*	*H*	Not possible
8	*OP*	*H*	*H*	*CL*	*H*	Parallel configuration
9	*CL*	*H*	*H*	*OP*	*H*	Series configuration
10	*OP*	*H*	*H*	*OP*	*H*	Not possible

Each switch can be: Permanently Closed (CL), Permanently Open (OP) or Healthy (H).

2.3.3 Reconfigurable Drive Performance Evaluation

As already mentioned before, a preliminary analytical calculation was carried out on a reconfigurable quadruple three-phase drive intended for a rim driven propeller used in yachting application, in order to assess the performance of the reconfigurable architecture and evaluate its benefits, especially in terms of efficiency and current ripple. Simple analytic equations can be implemented to quickly obtain a first approximation result which can be used as a guideline for preliminary design choices. Indeed, according to [55], [56],

the datasheet parameters can be used to estimate the conduction and switching losses of a solid-state device. However, in chapter 3, a more in-depth analysis of the conduction losses and switching losses of a power electronics device will be shown.

Considering a sinusoidal PWM (SPWM) modulation strategy, for a three-phase inverter connected to a three-phase set of the machine, featuring a power factor equal to $\cos\varphi$, the conduction losses of an inverter's switch can be calculated by considering separately the transistor and the diode. The diode (D) conduction losses are calculated using the diode no-load voltage (also called gamma voltage) $V_{D,0}$ and the diode on-resistance $R_{on,D}$:

$$P_{\mathrm{c}D} = V_{D0} I_s \left(\frac{1}{2\pi} - \frac{\widetilde{M}_{\mathrm{A}} \cos\varphi}{8} \right) + R_{\mathrm{on}D} I_s^2 \left(\frac{1}{8} - \frac{\widetilde{M}_{\mathrm{A}} \cos\varphi}{3\pi} \right) \tag{2.17}$$

where I_s is the inverter phase current peak and $\widetilde{M}_{\mathrm{A}} \in [0, 1]$ is the normalized amplitude modulation index, which is calculated as $\widetilde{M}_{\mathrm{A}} = \frac{2V_s}{v_{\mathrm{DC}}}$, where V_s is the phase voltage peak and v_{DC} is the DC bus voltage. In the case of a transistor (Q), the conduction losses depend on the kind of device used: MOSFET or IGBT. If a MOSFET transistor is considered, the conduction losses are calculated by using only the on-resistance $R_{on,Q}$:

$$P_{\mathrm{c}Q} = R_{\mathrm{on}Q} I_s^2 \left(\frac{1}{8} + \frac{\widetilde{M}_{\mathrm{A}} \cos\varphi}{3\pi} \right) \tag{2.18}$$

while in the case of a IGBT transistor the losses are calculated by considering the no-load voltage V_{Q0} and the on-resistance $R_{\mathrm{on}Q}$:

$$P_{\mathrm{c}Q} = V_{Q0} I_s \left(\frac{1}{2\pi} + \frac{\widetilde{M}_{\mathrm{A}} \cos\varphi}{8} \right) + R_{\mathrm{on}Q} I_s^2 \left(\frac{1}{8} + \frac{\widetilde{M}_{\mathrm{A}} \cos\varphi}{3\pi} \right) \tag{2.19}$$

On the other hand, the switching losses for the transistor and the diode can be calculated as:

$$\begin{aligned} P_{\mathrm{sw}Q} &= E_{\mathrm{on}Q} f_{\mathrm{sw}} + E_{\mathrm{off}Q} f_{\mathrm{sw}}, \qquad \text{transistor} \\ P_{\mathrm{sw}D} &\cong \frac{1}{4} q_{rr} v_{\mathrm{DC}} f_{\mathrm{sw}}, \qquad \text{diode} \end{aligned} \tag{2.20}$$

where $E_{\mathrm{on}Q}$ and $E_{\mathrm{off}Q}$ are the transistor turn-on and turn-off energies respectively, q_{rr} is the diode reverse-recovery charge, v_{DC} is the DC bus voltage and f_{sw} is the inverter switching frequency. The energies $E_{\mathrm{on}Q}$ and $E_{\mathrm{off}Q}$ are usually a function of the transistor current, the gate resistance, the transistor junction temperature and ultimately the voltage across the transistor.

Considering the conduction and the switching losses, the overall losses of one three-phase inverter, which is composed of 6 switches with H parallel

devices, each of which has a transistor and a diode, can thus be calculated as:

$$P_{\text{inv}}^{1} = \sum_{h=1}^{6H} \left(P_{\text{c}Q}^{h} + P_{\text{c}D}^{h} + P_{\text{sw}Q}^{h} + P_{\text{sw}D}^{h} \right) \tag{2.21}$$

where $P_{\text{c}Q}^{h}$, $P_{\text{sw}Q}^{h}$ are the conduction and switching losses of the h-th transistor and $P_{\text{c}D}^{h}$, $P_{\text{sw}D}^{h}$ are the conduction and switching losses of the h-th anti-parallel diode. The total number of devices is equal to $6H$, where H is the number of parallel devices for each switch: in case of multiple parallel devices, the value of the peak current used in the equations (2.17)-(2.19) must be split accordingly as I_s/H. Provided that the drive has N converters connected to the machine, the total losses associated with the three-phase inverters $P_{\text{inv,tot}}$ are proportional to the number of active inverters N_{act}:

$$P_{\text{inv,tot}} = N_{act} P_{\text{inv}}^{1} \tag{2.22}$$

The number of active inverters depends on the drive configuration: in case of the PC drive, $N_{act} = N$; in case of the SC drive $N_{act} = 1$.

The losses of one inverter are the sum of the switching losses and the conduction losses of the individual power semiconductor devices. The individual switching losses are equal in both the SC and the PC drive since they depend on variables that do not change with the drive configuration: the inverter phase current, the switching frequency and the DC bus voltage. On the other hand, the individual conduction losses are the sum of the losses on the transistor and the diode: the lower is the normalized amplitude modulation index $\widetilde{M}_{\text{A}}$, the higher is the circulation time of the current through the anti-parallel diode, (2.17), hence the variation of $\widetilde{M}_{\text{A}}$ causes a different distribution of the conduction losses between the transistor and the diode. However, in case of a MOSFET, which is a reverse conducting device, it can happen that the reverse current flows entirely through the transistor: this is the case when the diode gamma voltage V_{D0} is higher than the voltage drop across the MOSFET, which is equal to $v_{\text{on}Q} = R_{\text{on}Q} I_s$. Under this hypothesis, the MOSFET conduction losses do not depend on the value of the amplitude modulation index $\widetilde{M}_{\text{A}}$ since the current flows always through the transistor and never through the diode. On the other hand, if an IGBT is considered, the sum of the conduction losses on the transistor and the diode change with $\widetilde{M}_{\text{A}}$. The reason is that since the IGBT is not a reverse conducting device, the entire reverse current flows through the diode and, since the diode on-voltage is usually lower than the IGBT on-voltage, the diode conduction losses are lower if compared to the IGBT ones. As the analytical and simulation results show, the amount of losses saving with the series-configurated drive is appreciable, since there is only one active inverter instead of N: the main benefit is the reduction of the switching losses, which are zeroed for the inactive inverters. This is especially true when high current rating devices are considered, as for example IGCTs, where the losses reduction is even more highlighted due to the devices high on-voltage rating. Indeed, IGCTs are characterized by turn on/off energies of several orders of magnitude higher

TABLE 2.18: IGBT with diode data.

Manufacturer	Infineon
Part number	IKQ50N120CT2
Rated voltage	1200 V
Rated current @100 °C	50 A
Transistor no-load voltage @175 °C, V_{Q0}	0.9 V
Transistor on-resistance @175 °C, $R_{\text{on}Q}$	30.6 mΩ
Diode gamma voltage @175 °C, V_{D0}	1.14 V
Diode on-resistance @175 °C, $R_{\text{on}D}$	20.2 mΩ

with respect to common devices with lower current rating (IGBTs and MOSFETs) and for this reason even if an IGCT is switched at a much lower frequency (sub- kHz), [57], the switching losses are larger than the commonly used devices. It is important to highlight that, despite the overall inverters losses reduction with respect to a standard multi-three-phase drive, a reconfigurable architecture needs the implementation of reconfiguration cells which inevitably affect the system efficiency caused by the associated conduction losses, as already discussed before.

2.3.3.1 Analysis Results

In this analysis, an Infineon IGBT discrete device was chosen for the three-phase inverters. In order to calculate the conduction losses with the analytical expression presented in eqs. (2.17-2.20) it is necessary to find the values of the no-load voltage and equivalent resistance of both the IGBT $(V_{Q0}, R_{\text{on}Q})$ and the diode $(V_{D0}, R_{\text{on}D})$. These parameters can be obtained from the manufacturer datasheet of the chosen device and they are summarized in Table 2.18. On the other hand, the reconfiguration cell losses were calculated by using two different types of bi-directional switch. The first type is a full solid-state architecture and employs the same IGBT devices of the inverters, Table 2.18. The reason of choosing an IGBT full bi-directional switch was to optimize the system costs and dimensions, given the smaller footprint of a solid-state device with respect to a hybrid-relay device. The second type is a hybrid-relay device, Table 2.19. In this case, the losses are the sum of two terms: the conduction losses, due to contact resistance, and the coil hold power, which is independent from the current. For both the solid-state and the hybrid-relay RCs, only the conduction losses were considered: the switching losses were neglected since the reconfiguration event frequency is very low because the machine is supposed to work with a specific winding configuration for long time periods. Table 2.20 summarizes the drive data of different configurations on a common operating point: the chosen speed for the comparison is equal to the machine base speed when the winding sets are series connected (SC drive). Table 2.21 summarizes the results of the performance evaluation. The machine efficiency, the reconfiguration cells and the converter losses were calculated analytically. The modulation index was normalized with respect to the maximum value, which is equal to 0.577 since a

TABLE 2.19: Hybrid relay nameplate data.

Manufacturer	Panasonic
Part number	HEV2aNP12v
Contact material	AgNi type
Max switching voltage	1000 V
Max switching current	20 A
Contact resistance (typical)	50 mΩ
Nominal coil power	2 W
Coil hold power (after 100ms)	0.25 W

TABLE 2.20: Standard and reconfigurable drive nameplate data.

	STD drive	**PC drive**	**SC drive**
Active converters	4	4	1
RCs active switches	0	8	11
Phase resistance	0.338 Ω		1.352 Ω
Phase inductance	0.0018 H		0.0072 H
Mech. speed	$900\,\text{min}^{-1}$		
Mechanical torque	107 N m		
Mechanical power	10 kW		
Power factor	0.78		
Phase current RMS	$20\,\text{A}_{\text{rms}}$		
Switching frequency	16 kHz		
DC bus voltage	600 V		

Space Vector Modulation (SVM) strategy was implemented. The table shows that the system total efficiency is higher when a hybrid-relay RC is adopted, thanks to the lower conduction losses of this type of switch when compared to the IGBT one. Secondly, the system efficiency in the series configuration drive is higher when compared to the standard drive: the increase in complexity of this architecture is counterbalanced by a noticeable improvement of the system efficiency.

Taking the standard (STD) drive as the reference and considering the Hybrid-Relay RC architecture, the reconfigurable drive with the series configuration is able to reduce the converters losses by 75%. Even when taking into account the additional RCs losses, the reduction of the total power electronics losses is greater than 59%. Of course, the drawback is given by the additional RC losses which exist also when operating in parallel configuration at the full speed / full power operating point. For this reasons, a reconfigurable architecture is more convenient than a plain multi-three-phase drive if the machine must operate frequently at low speed / low power, featuring the added benefit to work at higher speed points without requiring flux-weakening control.

TABLE 2.21: Standard and reconfigurable drives analytical results.

	STD drive	**PC drive**	**SC drive**
Normalized modulation index	0.25		1.00
Converters losses	1407 W		352 W
RC losses (IGBT)	0 W	310 W	426 W
RC losses (Hyb-Rel)	0 W	162 W	223 W
Machine efficiency		84.9%	
Drive efficiency (IGBT)	75.9%	74.2%	79.7%
Drive efficiency (Hyb-Rel)	75.9%	75.0%	81.0%
Losses difference vs STD (IGBT)		+ 22.0%	- 44.7%
Losses difference vs STD (Hyb-Rel)		+ 11.5%	- 59.1%

2.3.4 Numerical Simulations

The numerical simulation of the reconfigurable drive presented in Section 2.3.3, were performed in PLECS® by implementing a master/slave centralized control with 4 slave units: each slave unit was dedicated to a three-phase module. The detail of the implemented model is shown in Figure 2.21. The machine and drive specifications along with the speed-torque working point used in the simulation were the same used for the analytical analysis and summarized in Table 2.20. In order to distribute the stress among the three-phase converters when the drive is in the series configuration, a rotation policy between the three-phase converters can be implemented. This is obtained by using not three, but four RCs, which add the flexibility to choose what three-phase converter must be used in the full series configuration.

A reconfiguration control logic was implemented by using a machine base speed estimation algorithm. According to this logic, the master unit controls the RC switches by comparing the machine actual speed ω_m with the estimated base speed of the actual K-th configuration $\omega_{mb,K}$. As shown in Figure 2.15, for this drive three different configurations are possible, each of which features its own base speed:

1. series configuration, when $0 < \omega_m < \omega_{mb,1}$;
2. parallel-series configuration, when $\omega_{mb,1} \leq \omega_m < \omega_{mb,2}$;
3. parallel configuration, when $\omega_{mb,2} \leq \omega_m < \omega_{mb,3}$.

Tables 2.22 and 2.23 show the comparison between the analytical calculations obtained in Section 2.3.3 and the results of the numerical simulations in PLECS®. The analytical losses calculated with the analytical approach are in good agreement with the numerical ones, while the maximum current ripple shows some major differences, especially in the SC drive.

For the sake of clarity, a numerical simulation of the reduced-scale double three-phase prototype, used for the experimental validation, was also carried out. Since this prototype is characterized by two three-phase sets, only two

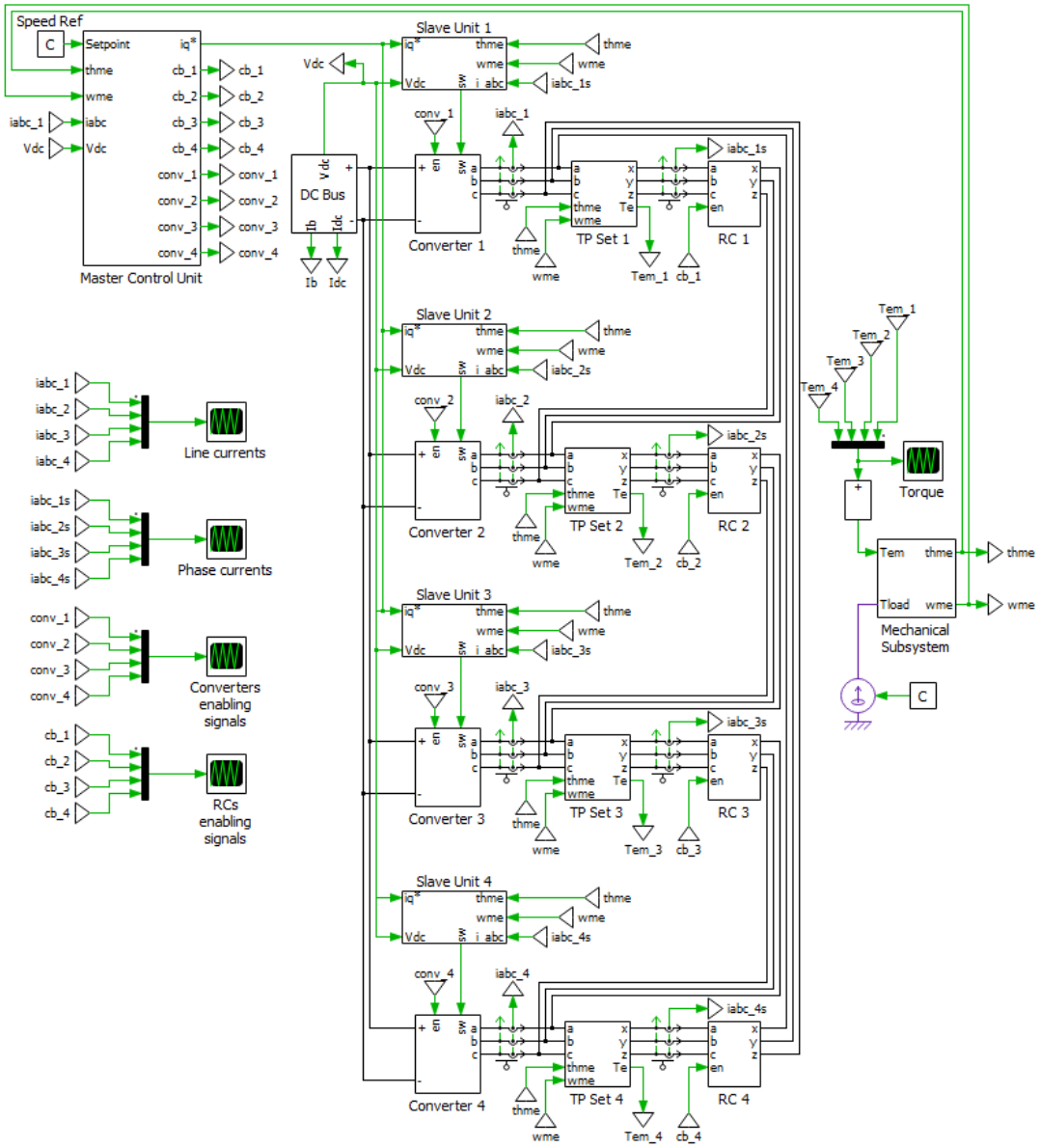

FIGURE 2.21: PLECS model of the reconfigurable architecture with 4 three-phase sets and 4 connection cells. The circular architecture allows to dynamically change the single star-point in the SC drive.

configurations are possible: series configuration and parallel configuration. The aim of this simulation was primarily to assess the differences in terms of phase current ripple when the drive operates in series configuration or in parallel configuration. Figure 2.22 shows the phase current waveform in both the drive configurations. From the Figure 2.22(a) it is clear that in the series configuration the current ripple is appreciably lower with respect to the parallel configuration one, Figure 2.22(b). This result provides another degree of freedom for the reconfigurable architecture: if the same maximum phase current ripple value is considered in both the PC drive and in the SC drive, a lower switching frequency could be used in the SC drive. This would cause a further reduction of the three-phase converter switching losses and a

TABLE 2.22: Current ripple comparison.

Configuration	Analytical	Numerical
STD drive	1.178 A	0.897 A
PC drive	1.178 A	0.897 A
SC drive	0.868 A	0.398 A

TABLE 2.23: Total inverters losses comparison.

Configuration	Analytical	Numerical
STD drive	1407 W	1046 W
PC drive	1407 W	1046 W
SC drive	352 W	252 W

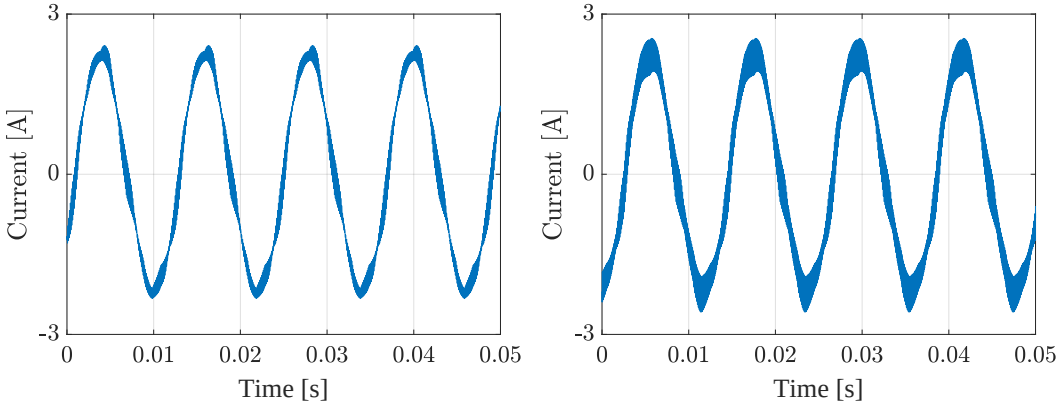

FIGURE 2.22: One set phase current in the series (a) and parallel (b) configurations, obtained from simulation with 10 kHz switching frequency and 1 µs dead-time.

further increase of the system efficiency at low speed / low power operation.

2.3.5 Experimental Results

A reduced scale demonstration prototype was fabricated in order to demonstrate the mode of operation of the reconfigurable drive and assess the impact on the system efficiency and on the current ripple.

The laboratory prototype shown in Figure 2.23 comprises: a custom six-phase sector-wound reconfigurable machine; one reconfiguration cell with solid-state switches, controlled by a dedicated secondary MCU usign a SPI to communicate wit the main MCU; two three-phase GaN inverters (called inverter A and inverter B), based on TI LMG5200MOFT half bridge modules. For the main MCU a dual-core Microcontroller (TI TMS320F28379D) was used and a master-slave control strategy was implement. Indeed, one core was used as the master to close the speed loop and the inverter A while

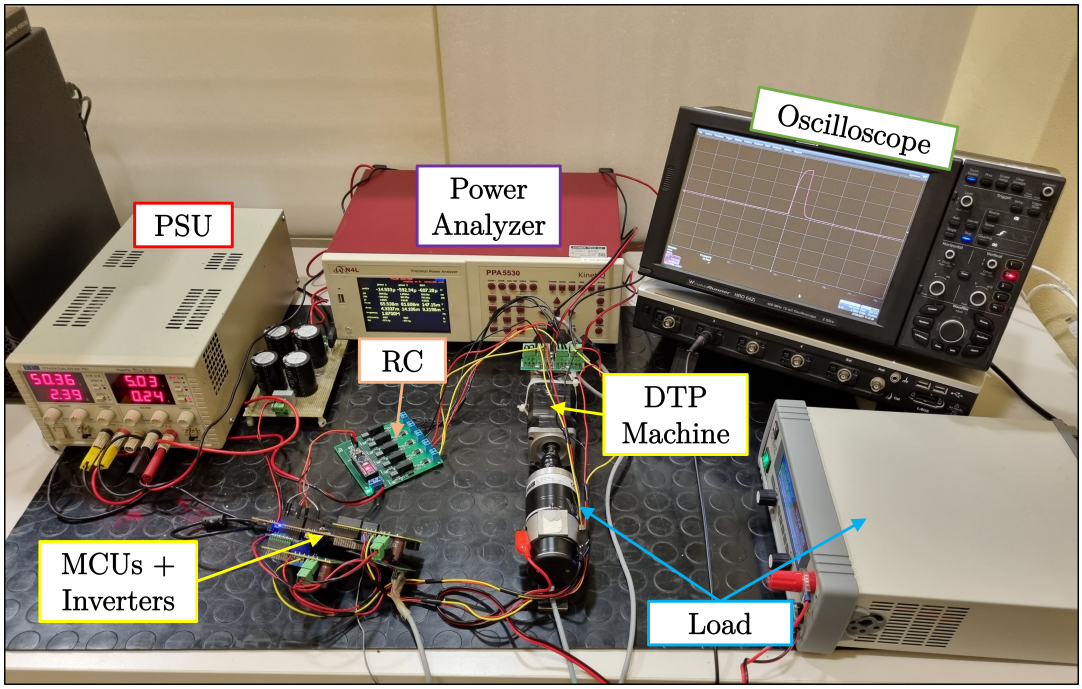

FIGURE 2.23: Low voltage experimental setup comprising custom six-phase sector-wound reconfigurable machine; reconfiguration cell PCB; double three-phase GaN inverters and master MCU. The setup comproses also an electronically programmable load and the power analyzer

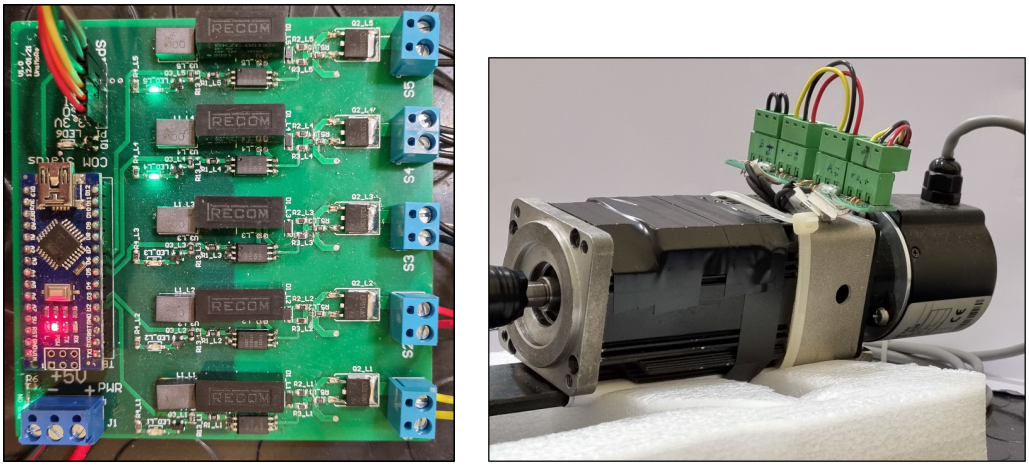

(a) (b)

FIGURE 2.24: Detail of (a) the reconfiguration cell PCB, comprising five isolated bi-directional switches and slave control unit connected to master MCU via SPI; (b) the sector-wound double three-phase machine under test with a 3000 PPR encoder.

the other core was used to control the inverter B by using the current reference from the core 1. The machine under test (MUT) is a 4p/12s Surface Per-

TABLE 2.24: Nameplate data of the reconfigurable drive prototype.

Poles/Slots	4p/12s
Turns per phase (per set)	53
DC bus voltage	48 V
Rated phase current (per set)	1.2 A_{rms}
SC drive max. mech. speed	3000 min^{-1}
PC drive max. mech. speed	6000 min^{-1}
Torque constant (per set)	0.065 N m A^{-1}
Phase resistance (per set)	0.889 Ω
Synchronous inductance (per set)	611 µH

manent Magnet (SPM) Synchronous Machine (SM) machine with two three-phase sets (A and B), which was sectorized in order to minimize the mutual coupling between the winding sets, Figure 2.24(b): this means that each three-phase set was located into one sector of the stator. Each three-phase set was connected to a three-phase inverter independently. Speed and position feedback are provided by a 3000 PPR incremental encoder. Table 2.24 summarizes the drive and electric machine parameters. The MUT is coupled to a brushed DC machine, connected to an EA-EL 3080-60 B electronic load. For the sake of modularity, the PCB of the reconfiguration cell shown in Figure 2.24(a) was developed as a standalone unit, comprising five isolated bi-directional switches and a slave control unit (ATmega328 - Arduino Nano) and is controlled by the master MCU via SPI interface. Since the demonstration prototype operates at low voltage (48 V) the RC implements full solid-state switches based on Si MOSFET STD100N10F7, because of their very low on-resistance $R_{Q,on}$, which is even lower than the contact resistance of an electromechanical relay. The master control unit defines the configuration of the system (i.e. the state of the switches in the RC) depending on MUT speed, as reported in Section 2.3.4.

Table 2.25 summarizes the results obtained. The MUT speed for the tests was chosen to be in an overlapping region of the two configurations (i.e. choosing a speed which can be achieved in both), in order to fairly compare the two configurations in the same working point and thus assess the differences. For the sake of comparison, in both the experimental tests, inverter A's line current and modulation index are reported. The interconnection of the two three-phase sets is determined by the status of the switches in the reconfiguration cell. In case of parallel configuration, the RC's longitudinal switches are open and each three-phase set is supplied by its own three-phase inverter (inverter A and B), each of which is controlled by one MCU core. In case of series configuration, the RC's longitudinal switches are closed: with this configuration, the three-phase sets are connected in series and only one inverter (inverter A) supplies the machine. For the sake of simplicity, the second three-phase neutral connection is hardware short-circuited at the terminals hence it is always the inverter A which supplies the entire machine when the drive is series configurated.

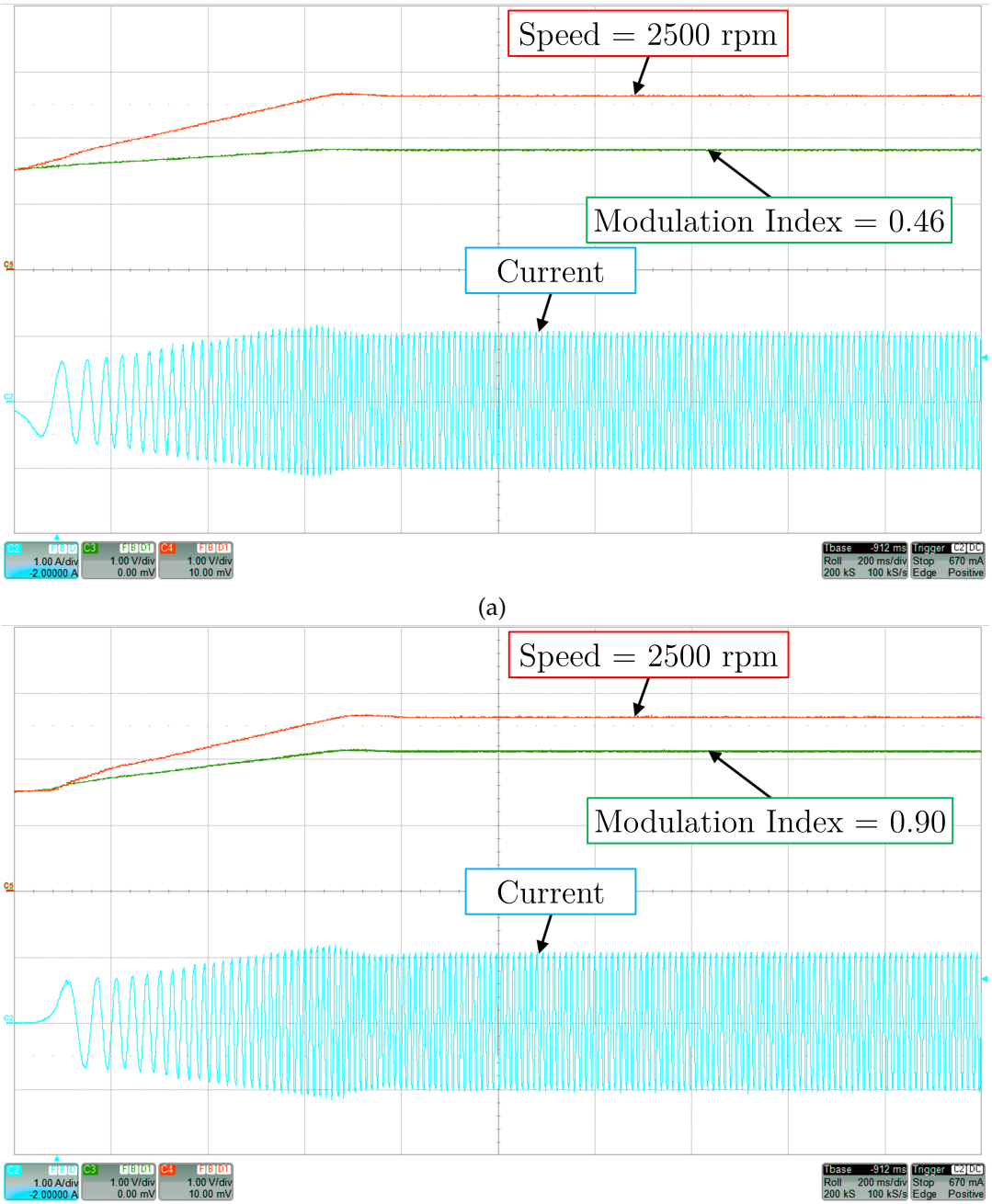

FIGURE 2.25: Speed, modulation index and line current waveforms in: (a) parallel configuration (two active inverters); (b): series configuration (one active inverter). Time scale: 200 ms/div. Current scale: 1 A/div. The modulation index and the line current are referred to the inverter A.

Figure 2.25 shows the evolution of the inverter A's modulation index and line current in the series and parallel configurations along with the machine mechanical speed. In both of the configurations, the fundamental rms current supplied by a single inverter is the same hence, since the mechanical torque is the same, the machine torque constant in the parallel configurated

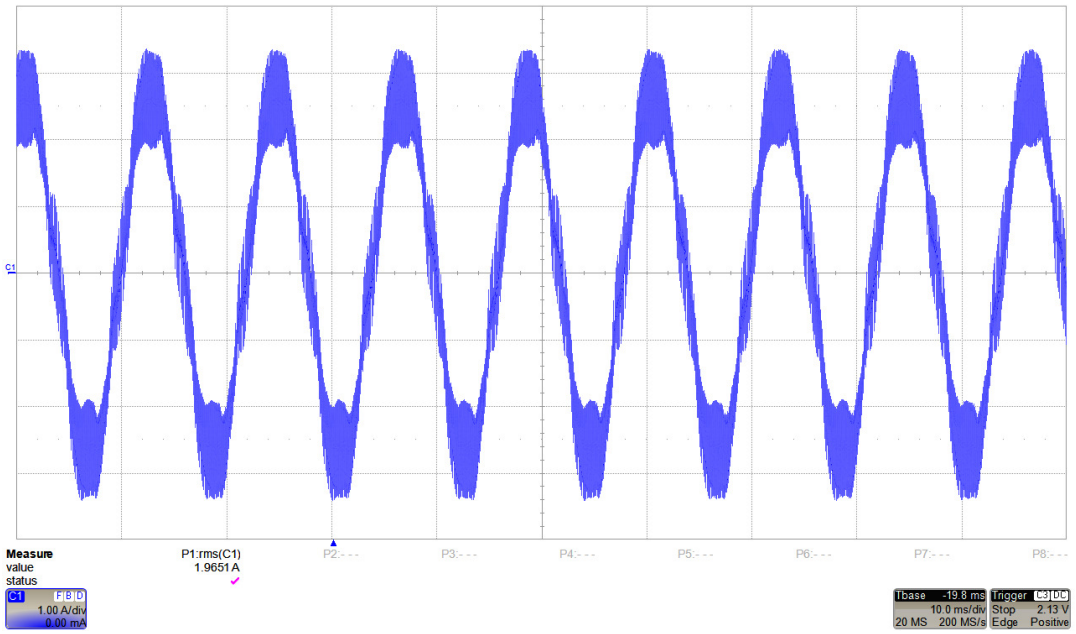

(a)

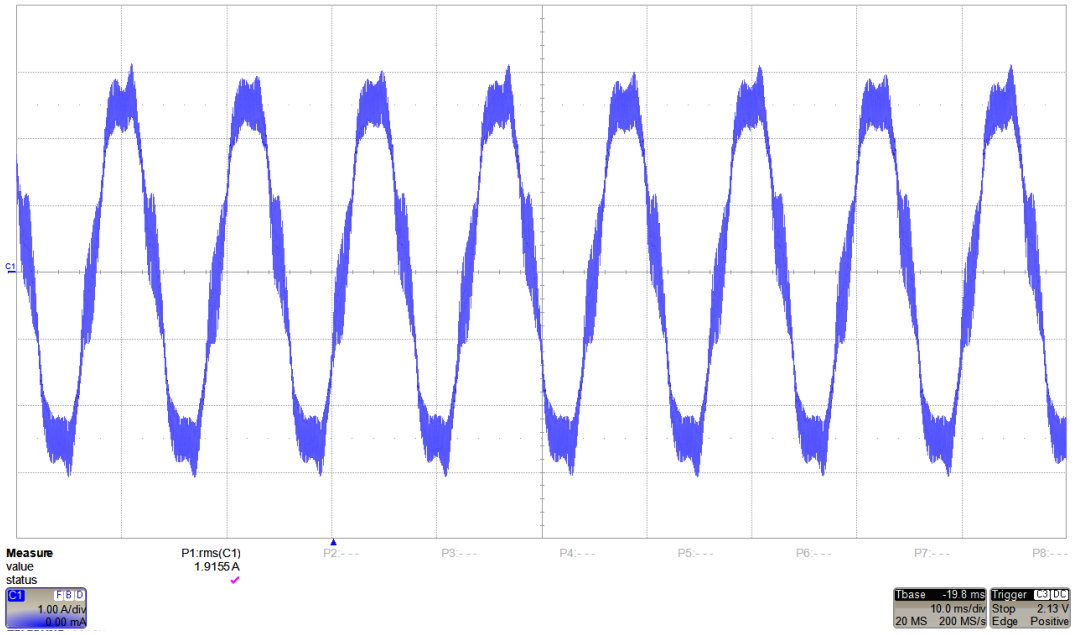

(b)

FIGURE 2.26: Detail of inverter A's line current in: (a) parallel configuration (two active inverters); (b) series configuration (one active inverter). Switching frequency: 10 kHz. Time scale: 10 ms/div. Current scale: 1 A/div.

drive is lower, as expected. This is also clear by comparing the modulation indexes: in the series configuration the modulation index is higher because of the higher induced back-EMF in the machine, which in turn depends on the machine torque constant.

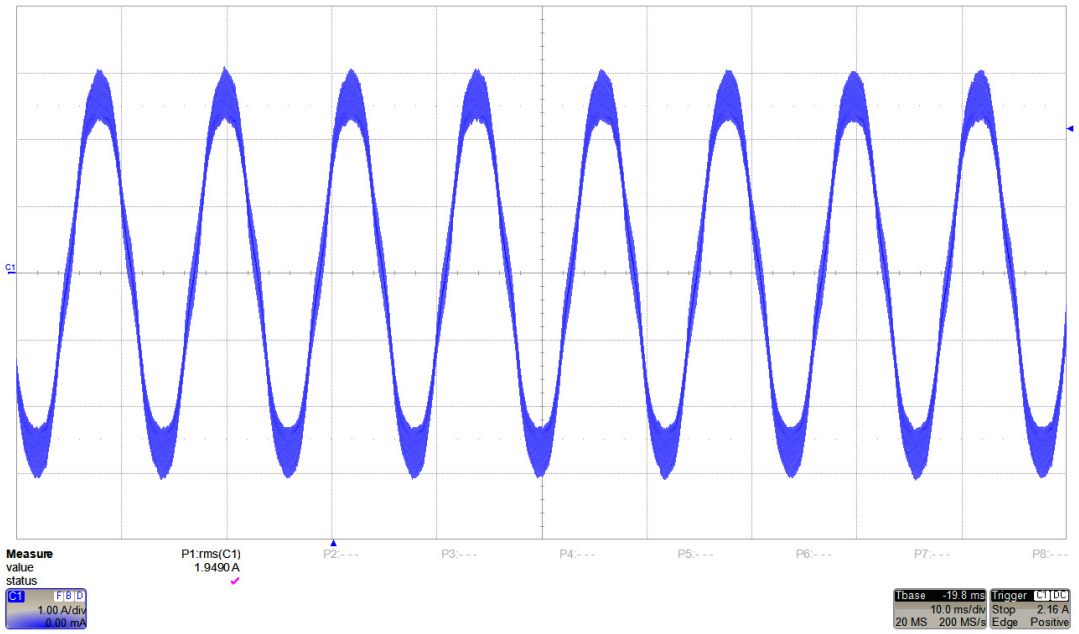

(a)

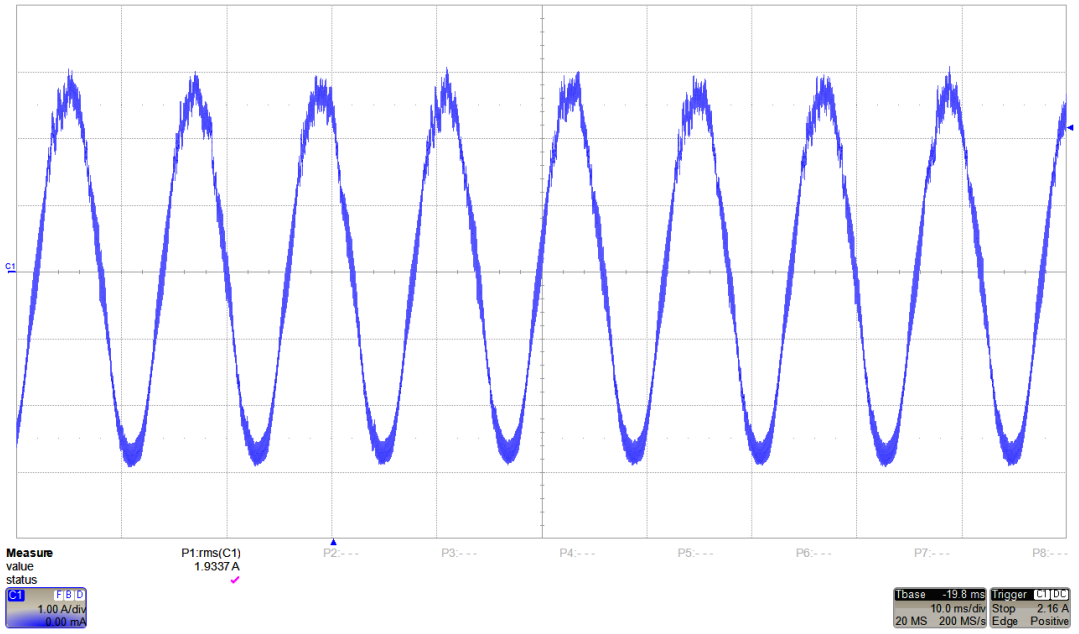

(b)

FIGURE 2.27: Detail of inverter A's line current in: (a) parallel configuration (two active inverters); (b) series configuration (one active inverter). Switching frequency: 25 kHz. Time scale: 10 ms/div. Current scale: 1 A/div.

Additional tests were conducted, by using two different switching frequencies: the lowest one, f_{sw} = 10 kHz, was chosen in order to better highlight the effect of the current ripple. Figure 2.26 shows a detail of the inverter A's line current in case of parallel and series configuration with the lowest switching frequency, while Figure 2.27 shows the same scenario but with f_{sw} = 25 kHz. By comparing the line current waveforms in both the experimental

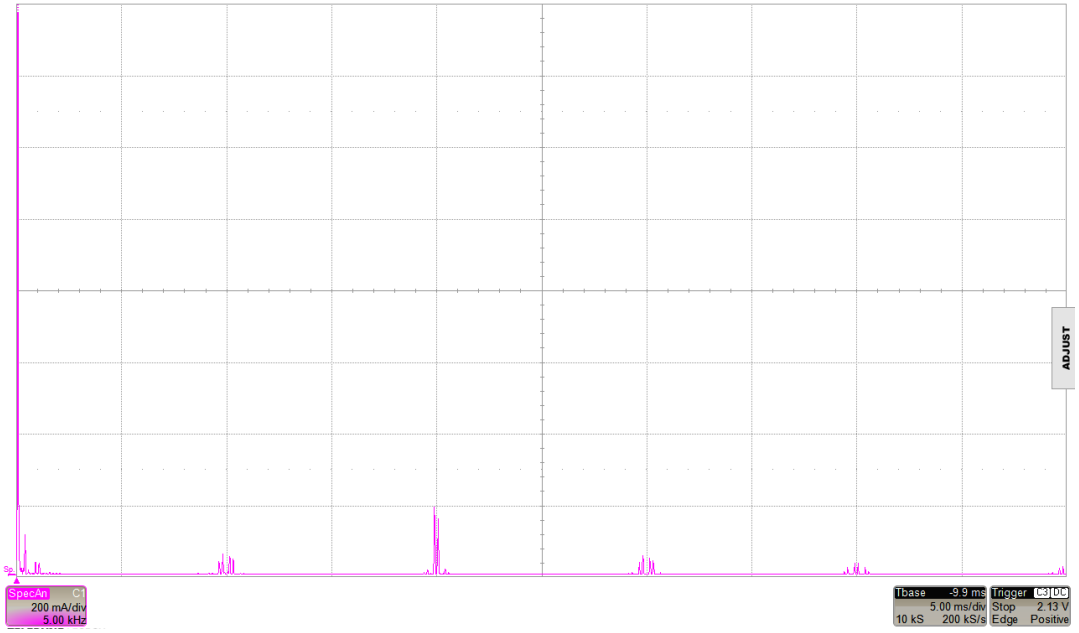

(a)

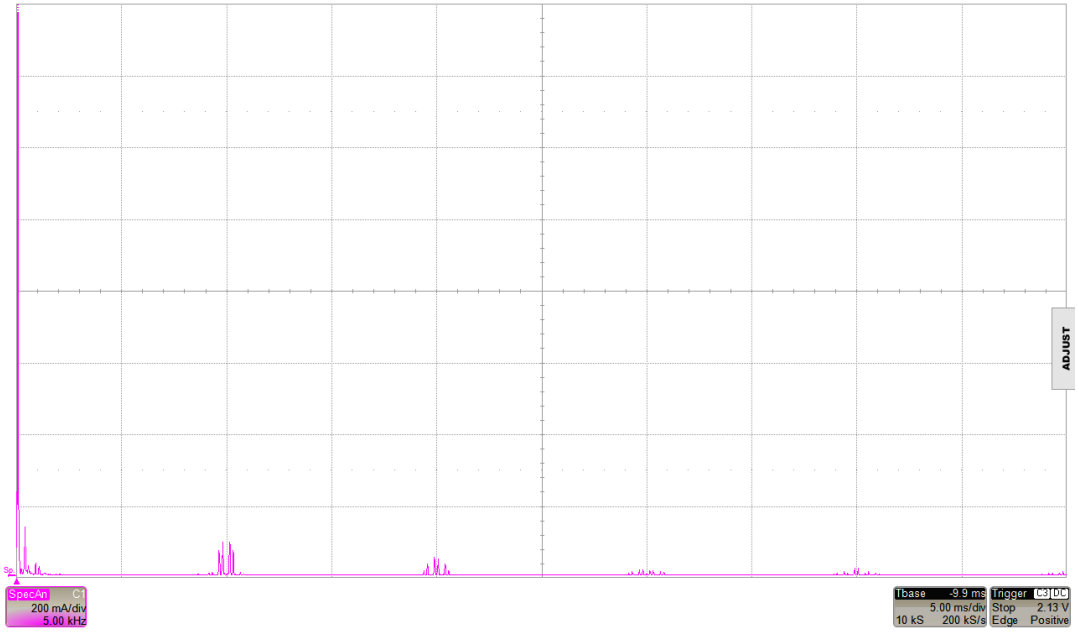

(b)

FIGURE 2.28: Inverter A's line current FFT in: (a) parallel configuration (two active inverters); (b) series configuration (one active inverter). Switching frequency: 10 kHz. Frequency scale: 5 kHz/div. Current scale: 0.2 A/div.

conditions, hence operating at the same switching frequency, the current's harmonic content in the series configuration is lower. This is also confirmed by the current's FFT, Figure 2.28. This result, since the current ripple is inversely proportional to the switching frequency and the machine inductance, leads to an additional degree of freedom when operating with a reconfigurable drive. In fact, since the SC drive exhibits a higher inductance than the

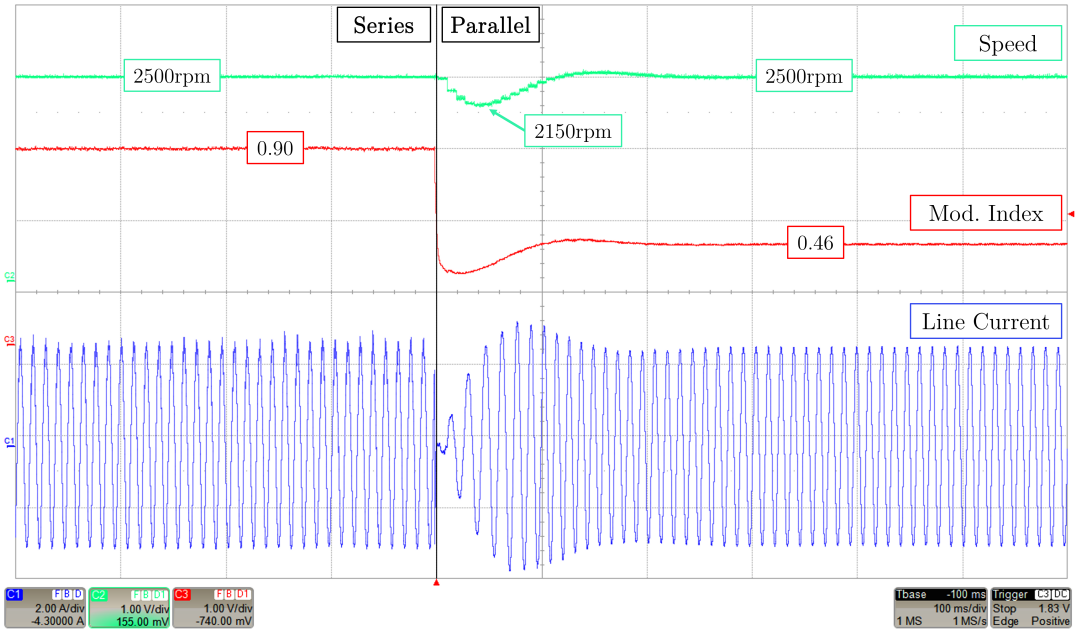

FIGURE 2.29: "On the fly" series to parallel reconfiguration under load: speed, modulation index and line current waveforms are reported. Switching frequency: 25 kHz; current scale: 2 A/div. The reconfiguration time is equal to 1.5 µs. The modulation index and the line current are referred to the inverter A.

PC drive, there is the possibility to choose between two operating scenarios when the drive is series configured:

- keeping the same switching frequency as the PC drive, thus operating with a reduced current ripple;
- reducing the switching frequency to achieve the same current ripple as the PC drive, thus further reducing the switching losses.

Figure 2.29 shows the relevant waveforms during an "on the fly" reconfiguration transition, passing from the series to the parallel configuration during operation under load. The RC commutation requires about 1.5 µs to change the winding configuration. After the reconfiguration happens, the drive takes another 200 ms to recover and return the steady-state operating condition.

Finally, by using a N4L PPA5530 power analyzer, the inverter A losses were measured in both the configurations, as shown in the diagram of Figure 2.30. Since only one power analyzer was available, to calculate the total efficiency in the parallel configuration, the inverter A losses were multiplied by a factor of 2. Indeed, since a master/slave control is used and the two inverters are identical, it is reasonable to assume that each inverter supplies the MUT with the same current therefore it is expected the losses to be the same for both the inverters. Tables 2.26 and 2.27 show the result of the power measurement with 10 kHz and 25 kHz switching frequency respectively. The total inverters efficiency in the parallel configuration is lower when compared to the efficiency in the series configuration, due to the fact that two inverters

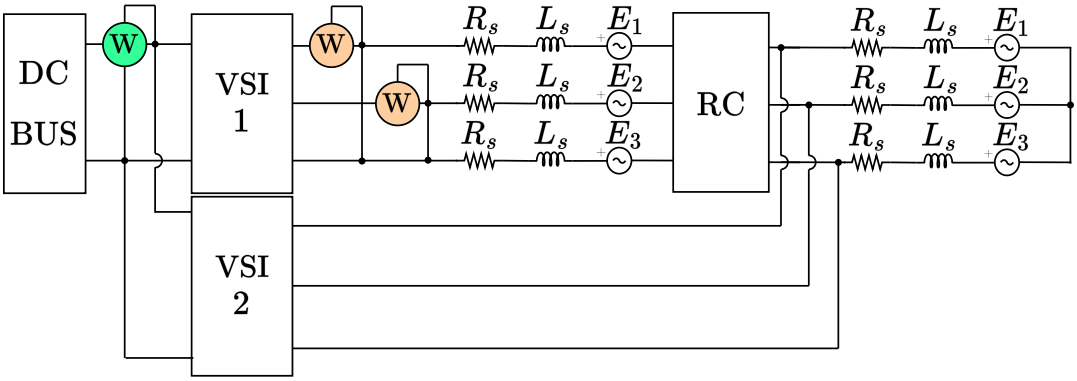

FIGURE 2.30: Electric scheme used for the power measurement in the experimental validation. The three-phase power was measured only on the inverter A by using an Aron circuit. The measured DC side power was the total absorbed power (logic board losses).

TABLE 2.25: Summary of the experimental conditions.

Switching frequencies	10 kHz & 25 kHz
Dead time (@10 kHz)	1.0 µs
Dead time (@25 kHz)	0.4 µs
MUT mech. speed	2500 min^{-1}
MUT mech. torque	0.208 N m
Inverter A i_{sq} current	1.6 A
Inverter A SC drive modulation index	0.90
Inverter A PC drive modulation index	0.46

TABLE 2.26: Losses and efficiency at 2500 min^{-1}, f_{sw} = 10 kHz, i_q = 1.6 A.

	STD drive	**PC drive**	**SC drive**
Total DC input power	100.51 W		95.95 W
Logic board absorbed power		0.77 W	
One inverter output power	46.32 W		92.31 W
One inverter losses	3.55 W		2.87 W
Total inverters losses	7.10 W		2.87 W
Total inverters efficiency	92.2%		96.2%

are used instead of one, confirming the analysis shown in Section 2.3.3: the advantage of the reconfigurable architecture is the efficiency improvement when the drive operates at low speed / low power and thus the drive is able to work in the series configuration, allowing to use only one inverter to fed the machine. The efficiency gain highlighted in the experimental tests carried out with this low power prototype machine is more significative when the power rating of the electric drive is in the order of hundreds of kW. In fact, in this case the reduction of the losses is more prominent and produces

TABLE 2.27: Losses and efficiency at 2500 min^{-1}, f_{sw} = 25 kHz, i_q = 1.6 A.

	STD drive	**PC drive**	**SC drive**
Total DC input power	99.16 W		95.07 W
Logic board absorbed power		0.77 W	
One inverter output power	45.26 W		91.96 W
One inverter losses	3.93 W		2.34 W
Total inverters losses	7.86 W		2.34 W
Total inverters efficiency	91.3%		96.7%

an increment of the efficiency: even a low efficiency gain is translated into a high saving in the system total requested energy, leading to a reduction of the fuel consumption.

2.4 Discussion

In this chapter, two studies were carried out about the electrification and hybridization of inner waterway vessels: the first one was focused on the design of an electric machine for a rim-driven propulsor; the second one on the analysis of a multi-three-phase drive featuring a reconfigurable architecture.

In the first part of the chapter the design of a high power density electric motor for a rim-driven propulsor was presented: the electric machine featured a thin radial section and a hairpin winding construction. The target application was a rim-driven propeller pod for a speedboat application, meant to be used in inland waterway vessels like lakes and rivers. The conductors of the hairpin winding were designed in order to reduce the AC losses due to the skin and proximity effects: the final result was the adoption of multiple parallel paths in to increase the number of conductors inside the slots and thus reducing their length.

The electric machine was designed and simulated via 2D finite element analysis (FEA) using transient magnetic simulations. The aim of these simulations was, first of all, to analyze the machine performance in order to evaluate if the requirements in terms of rated and peak power values were met and, secondly, to calculate the losses, especially in the winding, to estimate the machine efficiency and temperatures in different working points. By exploiting the FEA losses calculation, a thermal analysis was carried out to evaluate the temperatures in the different parts of the machine, by considering not only the steady-state operation, but also a sample duty-cycle, conceived to analyze the machine behavior in a more realistic operating conditions. Thanks to the particular application, the electric machine cooling was guaranteed by a submerged operation and a wet rotor construction, allowing the water to flow inside the machine airgap and rotor, hence highly increasing the heat dissipation capability. This particular, yet simple cooling method was the main condition which allowed to design a machine with a very high torque and power density, comparing favourably against a traditional internal combustion engine.

In the second part of the chapter a reconfigurable multi-three-phase drive architecture for naval propulsion was presented. This architecture is capable of performing the machine winding reconfiguration, connecting them in series, in parallel or a mixing of the two, thanks to additional circuits named reconfiguration cells (RCs). The impact of the reconfiguration cells (RCs) was evaluated both in terms of additional losses as well as fault sensitivity of the reconfigurable drive. To overcome the issue given by the additional conduction losses associated to full solid-state RCs (i.e. by employing SCR, IGBT and MOSFET) a hybrid relay topology was considered, in order to mitigate their impact on the system efficiency, especially when dealing with large power sizes.

The advantages of the reconfigurable multi-three-phase drive over a standard multi-three-phase drive, i.e. without the possibility of changing the winding configuration, were assessed by means of a preliminary analytical

analysis and then by numerical simulations on a sample quadruple three-phase drive. It was found that when the electric machine operates at reduced speed and power, the reconfigurable drive allow to increase the system efficiency and reduce the phase current ripple (for the same switching frequency), by series connecting the machine winding (series-configured drive). The advantages in terms of efficiency and current ripple of the reconfigurable drive at low speed operation were also demonstrated experimentally on a reduced scale prototype, capable of "on the fly" reconfiguration of the machine's winding when operating under load, without stopping. Taking the standard multi-three-phase drive architecture as the reference and considering the Hybrid-Relay RCs reconfigurable architecture, the SC drive was able to reduce the converters losses by 75%. Nevertheless, even when taking into account the additional RCs losses, the total power converter losses reduction was approximately equal to 59%. This advantage mainly came from the elimination of both conduction and switching losses associated with the other deactivated converters. An additional benefit was the reduced current ripple when the drives operates in series configuration. This benefit can be exploited to further increase the system efficiency: assuming to keep the current ripple constant, it is possible to reduce the switching frequency when the reconfigurable drive operates in series configuration to further reduce the switching losses in the active converter. All the considerations carried out in this chapter are valid for any kind of three-phase drive since the efficiency difference between the series and the parallel configurations is given by the number of active converters. For this reason, a reconfigurable drive can be beneficial when the rated power of the electric machine is in the order of hundreds of kW, providing a substantial increment in the drive efficiency when the machine rotates at low speed.

Chapter 3

An Ultra-Fast Thermal Model for Converters Long-term Damage Evaluation

Thermal analysis of power converters is currently a hot topic due to the increasingly high reliability requirements of power electronics systems. The power devices degradation highly depends on the presence of thermal cycles corresponding to the power profile. Thermal models help making accurate estimations of the power devices remaining useful lifetime in order to define optimal maintenance strategies however these models have a very high computational burden that limits their use in real-time applications. The proposed thermal model approach for 2-levels voltage source inverters allow to take into account the effect of the temperature ripple at the fundamental frequency of the current. The main advantage of this model is that it reduces the computational cost without losing accuracy, making it possible to carry out real-time damage estimations, allowing to adapt the converter operation to follow the optimal maintenance directives. The proposed approach is compared with the thermal model provided by PLECS demonstrating its accuracy. A sample case study is then presented, in which the developed analytical solution is used to build a fast charger model to analyze the effect on the power devices of a three-phase active rectifier of different charging strategies.

3.1 Introduction

Among the most critical components of power converters, the power semiconductors are among the most fragile ones [58]. Recent advances in materials and packaging have been making the power devices more and more reliable. However, they are still one of the most important fault causes in power converters operation. Nowadays, modern power electronic systems require accurate lifetime prediction of power converters in order to optimally define the maintenance scheduling in order to get operation cost savings, [59]–[61]. Power semiconductors manufacturers and power converter suppliers are investing vast research effort in developing tools to estimate the damage in power semiconductors based on their thermal behavior during the converter operation, [62]–[66].

In academia, many approaches have been presented, taking into account converter measurements and power converter components data-sheets in order to estimate the power semiconductors damage. The most conventional approach is represented in Figure 3.1 where the block diagram to estimate the damage in power semiconductors is summarized, [67]. The power semiconductors damage estimation is carried out taking into account the thermal cycles that the devices undergoes, considering a typical mission power profile. In the end, these thermal cycles lead to a degradation of the device materials that leads to the failure of the devices. However, the damage depends on the average operation temperature and the thermal cycle amplitude, so an accurate thermal model of the power devices is required in order to make accurate damage estimations.

In [68] a thermal model of a three-phase IGBT module is presented and analyzed by taking into account different layers, modeled by the thermal network with their specific impedance; in [69] a comparison between a IGBT module and a SiC module is carried out. In [70], [71] a detailed calculation of SiC MOSFETs conduction losses is presented for a traditional Sinusoidal PWM (SPWM), while in [70] the conduction loss model is brought by considering a Space Vector Modulation (SVM) strategy. On the other hand, the analytical conduction losses calculation of a MOSFET power device is presented in [72], where two different modulation strategies are considered: a traditional SPWM modulation, and the consequent Third Harmonic Injection (THI) and takes also into account the effect of the dead-times. In the

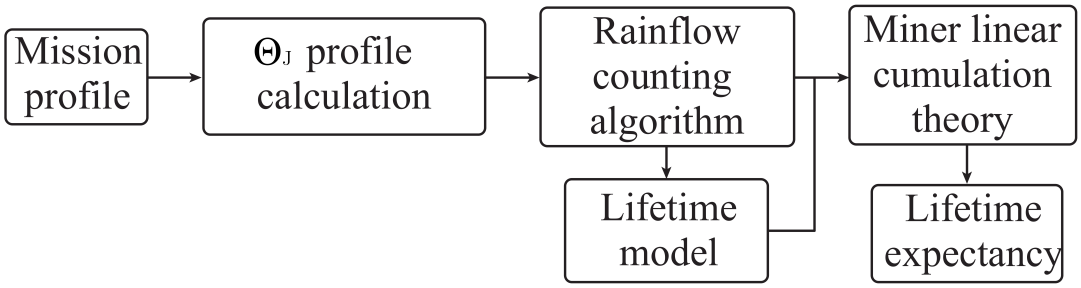

FIGURE 3.1: Conventional procedure for lifetime estimation of power devices.

same paper the switching losses are calculated by exploiting the switching energies lookup tables of the device. In [73], [74] a detailed analytical model for IGBT devices taking into account the instantaneous losses waveform and the consequent temperature fluctuation is presented. This model relies on the discretization of the conduction losses curve of an IGBT when the inverter is driven with a SPWM strategy, leading to very accurate results for the calculation of the temperature ripple by exploiting an equivalent foster network.

One important issue to be addressed is that the current power semiconductor thermal models have a high computational burden. This represents a clear challenge to be overcome since the resulting models can only be executed offline. In addition, and even representing a more important limitation of the thermal models applicability, long term damage estimations can be hardly achieved since the required simulation time is greater than the simulated operation time span of the converter. If a long term damage estimation considering years of normal operation is required, the amount of data to be managed is huge and the required computational cost is so high that the estimations need a significantly long time to get a result. The thermal model approach introduced in this work is addressing this issue reducing the computational cost making possible to carry out long term damage estimations with affordable execution time. In fact, by using the traditional numerical approach, the estimation of the power semiconductors damage corresponding to a month of operation of the power converter can take half a year to be obtained. In the proposed approach, the same result is obtained in less than a week. This fact enables to use the proposed thermal model to carry out very long term damage estimations. This fact opens the scenario of calculating the remaining useful lifetime of the device and hence allowing to modify the power converters operation, following the predictive maintenance directives.

This chapter is organized as follows: in Section 3.2 the analytical loss model for a two-level voltage source inverter (VSI) is presented. In 3.2.1 the average conduction losses for a MOSFET and a diode are calculated by considering a SPWM modulation strategy and a THISPWM; in 3.2.2 the average losses are calculated for the IGBT and diode, finally in 3.2.3 the average switching losses calculation is presented. In 3.2.4 the thermal model of a power electronics device aimed at calculating the junction temperature is presented. Finally, in 3.2.5 the numerical simulations are carried out by comparing the analytical model with PLECS numerical simulations for both the MOSFET and the IGBT, while in 3.2.6 the experimental results for the IGBT power loss model are used to validate the proposed model. In 3.3 the analytical loss model for a buck/boost converter is shown. By exploiting the proposed models, in 3.4 a vehicle fast charger model is presented while in 3.4.1 the three-phase grid and the active-rectifier models used in the simulation are descripted. In 3.4.2 a brief discussion about the cumulative damage model for the power electronics devices is carried out. Finally, in 3.4.3 several charging strategies of different cars manufacturers are analyzed with the aim of comparing their effect on the damage in electronics devices.

3.2 Analytical Loss Model for Two-Level Voltage Source Inverter

In this section, the average loss calculation method in a switch with an anti-parallel diode for a three-phase 2 Level Voltage Source Inverter (2L-VSI) is carried out. In Figure 3.2(a), one leg of the three-phase inverter is shown, where each switch is composed of a transistor (Q) and a diode (D): the upper switch is named H and the lower switch is named L. The total loss of one device (transistor or diode) is given by the sum of the conduction losses P_c and the switching losses P_{sw}.

The calculation of the conduction losses depends on the modulation strategy adopted in the power converter. In the following section, the conduction losses will be calculated considering two different modulation strategies: a Sinusoidal PWM (SPWM) and Sinusoidal PWM with Third Harmonic Injection (THISPWM), which allows to increase the maximum amplitude of the modulation index by 15%.

Neglecting the ripple at the switching frequency, (which it is demonstrated that is not affecting to the lifetime of the power device [73], [74]) the output current of one leg of a three-phase inverter can be approximated to a sinusoidal current with a fundamental frequency f_1. This sinusoidal variation causes a variation in the instantaneous conduction losses which leads to a junction temperature ripple in the power device. This temperature ripple should be included in the thermal analysis of the device in order to obtain a better estimation of the device junction temperature and the consequent calculation of the cumulative damage. It is important to highlight that the presented model is valid only for continuous PWM strategies, therefore it is not applicable in case of discontinuous PWM strategies (DPWM), as for example the 60° DPWM clamping strategy, or if the modulator works in overmodulation zone. However, future works are aimed at the extension of this approach to a more general PWM modulation strategy with a generic harmonic content.

3.2.1 Average Conduction Power Loss considering a MOSFET and Diode

The average conduction losses of a power semiconductor device (defined as P_c) are obtained from the instantaneous conduction losses (namely p_c), which are expressed as:

$$p_c(i_{\text{on}}, \Theta_{\text{J}}) = m(\alpha) v_{\text{on}}(i_{\text{on}}, \Theta_{\text{J}}) i_{\text{on}} \tag{3.1}$$

where $m(\alpha)$ is the duty-cycle applied to the device, and $v_{\text{on}}(i_{\text{on}}, \Theta_{\text{J}})$ and i_{on} are the device on-voltage and on-current during the conduction phase, respectively. Finally, Θ_{J} is the device junction temperature.

In case of a MOSFET transistor (Q), the on-voltage can be simply expressed as:

$$v_{Q\text{on}}(i_{Q\text{on}}, \Theta_{\text{J}Q}) = R_{Q\text{on}}(i_{Q\text{on}}, \Theta_{\text{J}Q}) i_{Q\text{on}} \tag{3.2}$$

where $R_{Q\text{on}}(i_{Q\text{on}}, \Theta_{\text{J}Q})$ is referred to the MOSFET on-resistance, which it also depends on the MOSFET junction temperature $\Theta_{\text{J}Q}$ and the on-current $i_{Q\text{on}}$. On the other hand, in case of a diode the on-voltage can be expressed as:

$$v_{D\text{on}}(i_{D\text{on}}, \Theta_{\text{J}D}) = R_{D\text{on}}(i_{D\text{on}}, \Theta_{\text{J}D}) i_{D\text{on}} + V_{D0}(\Theta_{\text{J}D}) \tag{3.3}$$

where $R_{D\text{on}}(i_{D\text{on}}, \Theta_{\text{J}D})$ is the diode on-resistance when it is directly polarized, which also depends on the diode junction temperature $\Theta_{\text{J}D}$ and the on-current $i_{D\text{on}}$. Finally, $V_{D0}(\Theta_{\text{J}D})$ is the diode no-load voltage, which depends on the diode junction temperature.

In the following analysis, the dependency of the $R_{Q\text{on}}$ with respect to the MOSFET on-current, and the dependency of $R_{D\text{on}}$ with respect to the diode on-current will be neglected. Only the dependency with respect to the junction temperature Θ_{J} will be considered. This assumption simplifies the calculation of the currents during the reverse phase, but at the cost of a lower accuracy with respect to a numerical simulation (as for example a thermal analysis made with PLECS®), which takes into account the proper $v_{\text{on}} - i_{\text{on}}$ curve of each device. On the other hand, considering for example a PLECS simulation, the thermal and the electrical domains are independent from each other and the calculation of the devices' currents during the reverse phase is made by considering constant parameters ($R_{Q\text{on}}, R_{D\text{on}}, V_{D0}$), which do not depend neither on the junction temperature nor the current. For this reason, the actual currents in the converter could be different from the calculated ones, leading to accuracy errors in the calculation of the conduction losses. The average value in a fundamental period of the conduction losses can be calculated as:

$$P_{\text{c}} = \frac{1}{2\pi} \int_0^{2\pi} p_c(\alpha) d\alpha \tag{3.4}$$

where $\alpha = 2\pi f_1 t$ and f_1 is the fundamental frequency of the on-current.

Under the assumption that the switching frequency is sufficiently high and the converter operates in the linear modulation region, the output current can be considered as an ideal sinusoidal waveform:

$$i_o(\alpha) = I_p \sin(\alpha) \tag{3.5}$$

where I_p is the peak value of the current. As shown in Figure 3.2, two different conduction phases should be considered: a forward conduction phase and a reverse conduction phase. If the conduction losses are calculated in the upper switch (Q_H, D_H), the forward conduction phase happens when:

$$\text{if } i_o(\alpha) > 0, \qquad \text{for } 0 \leq \alpha \leq \pi \tag{3.6}$$

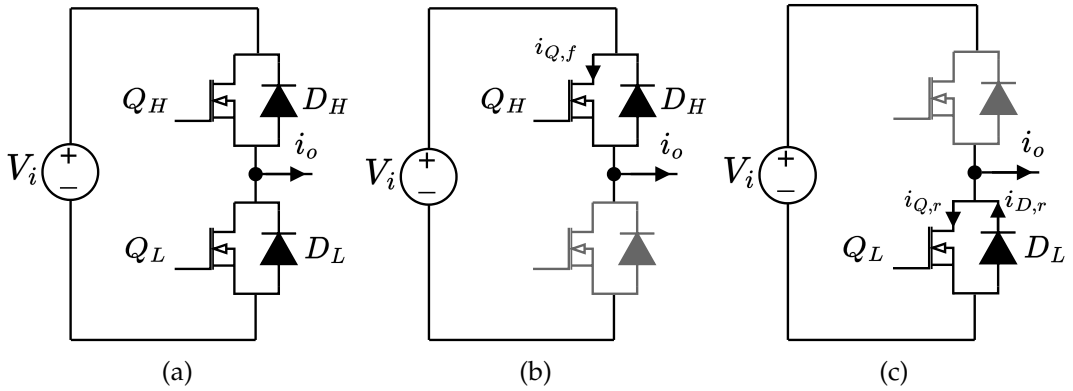

FIGURE 3.2: (a) Half-bridge corresponding to a phase of a buck converter; (b) forward conduction state for a half-bridge converter; (c) reverse conduction state for a half-bridge.

while the reverse conduction phase happens when:

$$\text{if } i_o(\alpha) < 0, \qquad \text{for } \pi \leq \alpha \leq 2\pi \tag{3.7}$$

During the forward conduction phase, Figure 3.2(b), only the MOSFET conducts whereas during the reverse conduction phase, Figure 3.2(c), the MOSFET and the diode conduct in parallel, but only if the diode is directly polarized, otherwise only the MOSFET conducts. The condition to be satisfied in order to have the diode directly polarized is given by $v_{Q\text{on}} \geq V_{D0}$. By defining the angle conduction angle β, the condition for the diode to be directly polarized is hence defined as, [70]:

$$R_{Q\text{on}} I_p \sin\beta \geq V_{D0} \tag{3.8}$$

therefore the diode conducts only if:

$$\sin\beta \geq \frac{V_{D0}}{R_{Q\text{on}} I_p} \tag{3.9}$$

The forward conduction phase can be defined when the output current angle is in the range $-\beta \leq \alpha \leq \pi + \beta$, [72].

In the following analysis the dependency of the on-resistances with respect to the junctions temperatures will be implicit. The MOSFET average conduction losses over one fundamental period considering the forward conduction phase, $P_{\text{c}Q,f}$, can be calculated as:

$$P_{\text{c}Q,f} = \frac{1}{2\pi} \int_{-\beta}^{\pi+\beta} p_{\text{c}Q,f}(\alpha) d\alpha \tag{3.10}$$

where $p_{\text{c}Q,f}(\alpha)$ are the MOSFET instantaneous forward conduction losses:

$$p_{\text{c}Q,f}(\alpha) = m_H(\alpha) v_{Q\text{on}}(\alpha) i_{Q,f}(\alpha) = m_H(\alpha) R_{Q\text{on}} i^2_{Q,f}(\alpha) \tag{3.11}$$

$m_H(\alpha)$ is the duty-cycle of the upper switch and depends on modulation

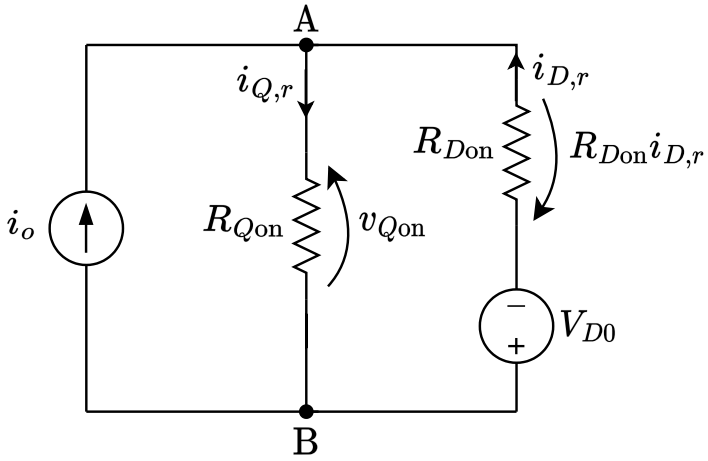

FIGURE 3.3: MOSFET and diode equivalent circuit used to calculate the currents during the reverse phase

strategy adopted in the power converter, while $i_{Q,f}$ is the current flowing through the MOSFET during the forward phase. By introducing the (3.11) into the (3.12):

$$P_{\text{c}Q,f} = \frac{1}{2\pi} \int_{-\beta}^{\pi+\beta} m_H(\alpha) R_{Q\text{on}} i_o^2(\alpha) d\alpha \tag{3.12}$$

where $i_{Q,f} = i_o(\alpha)$.

On the other hand, the reverse conduction phase happens when $\pi + \beta < \alpha < 2\pi - \beta$ and the output current is split-off between the MOSFET and the diode. By using the circuit shown in Figure 3.3, the MOSFET and the diode currents can be obtained:

$$i_{Q,r}(\alpha) = \frac{-V_{D0} + R_{D\text{on}} i_o(\alpha)}{R_{D\text{on}} + R_{Q\text{on}}} \tag{3.13}$$

$$i_{D,r}(\alpha) = \frac{-V_{D0} - R_{Q\text{on}} i_o(\alpha)}{R_{D\text{on}} + R_{Q\text{on}}} \tag{3.14}$$

Using the expressions above, the MOSFET and the diode conduction losses during the reverse phase are obtained as:

$$P_{\text{c}Q,r} = \frac{1}{2\pi} \int_{\pi+\beta}^{2\pi-\beta} p_{\text{c}Q,r}(\alpha) d\alpha \tag{3.15}$$

$$P_{\text{c}D,r} = \frac{1}{2\pi} \int_{\pi+\beta}^{2\pi-\beta} p_{\text{c}D,r}(\alpha) d\alpha \tag{3.16}$$

where:

$$\begin{aligned} p_{cQ,r}(\alpha) &= m_H(\alpha) v_{Q\text{on}}(\alpha) i_{Q,r}(\alpha) \\ &= m_H(\alpha) R_{Q\text{on}} i_{Q,r}^2(\alpha) \end{aligned} \tag{3.17}$$

$$\begin{aligned} P_{cD,r}(\alpha) &= m_H(\alpha) v_{D\text{on}}(\alpha) i_{D,r}(\alpha) \\ &= m_H(\alpha) \left[R_{D\text{on}} i_{D,r}^2(\alpha) + V_{D0} i_{D,r}(\alpha) \right] \end{aligned} \tag{3.18}$$

are the instantaneous MOSFET and diode conduction losses respectively, during the reverse phase. By introducing the (3.17-3.18) into the (3.15-3.16) yields to:

$$P_{cQ,r} = \frac{1}{2\pi} \int_{\pi+\beta}^{2\pi-\beta} m_H(\alpha) R_{Q\text{on}} i_{Q,r}^2(\alpha) d\alpha \tag{3.19}$$

$$P_{cD,r} = \frac{1}{2\pi} \int_{\pi+\beta}^{2\pi-\beta} m_H(\alpha) \left[R_{D\text{on}} i_{D,r}^2(\alpha) + V_{D0} i_{D,r}(\alpha) \right] d\alpha \tag{3.20}$$

By introducing the (3.5) into the (3.12) as well as (3.19) and (3.20), the forward and reverse losses for the MOSFET and the diode are determined:

$$P_{cQ,f} = 2K_1 \int_{-\beta}^{\pi+\beta} m_H(\alpha) \sin^2(\alpha) d\alpha \tag{3.21}$$

$$\begin{aligned} P_{cQ,r} = {} & 2K_2 \int_{\pi+\beta}^{2\pi-\beta} m_H(\alpha) \sin^2(\alpha) d\alpha \\ & - 2K_3 \int_{\pi+\beta}^{2\pi-\beta} m_H(\alpha) \sin(\alpha) d\alpha \\ & + 2K_4 \int_{\pi+\beta}^{2\pi-\beta} m_H(\alpha) d\alpha \end{aligned} \tag{3.22}$$

$$\begin{aligned} P_{cD,r} = {} & 2K_5 \int_{\pi+\beta}^{2\pi-\beta} m_H(\alpha) \sin^2(\alpha) d\alpha \\ & - 2K_6 \int_{\pi+\beta}^{2\pi-\beta} m_H(\alpha) \sin(\alpha) d\alpha \\ & - 2K_4 \int_{\pi+\beta}^{2\pi-\beta} m_H(\alpha) d\alpha \end{aligned} \tag{3.23}$$

where auxiliary variables are:

$$\begin{aligned} K_1 &= a I_p^2 & K_2 &= ab R_{D\text{on}}^2 I_p^2 \\ K_3 &= 2ab R_{D\text{on}} V_{D0} I_p & K_4 &= ab V_{D0}^2 \\ K_5 &= ab R_{D\text{on}} R_{Q\text{on}} I_p^2 & K_6 &= ab V_{D0} (R_{D\text{on}} - R_{Q\text{on}}) I_p \\ a &= \frac{R_{Q\text{on}}}{4\pi} & b &= \frac{1}{(R_{Q\text{on}} + R_{D\text{on}})^2} \end{aligned} \tag{3.24}$$

Expressions developed in (3.21), (3.22) and (3.23) are completely general and

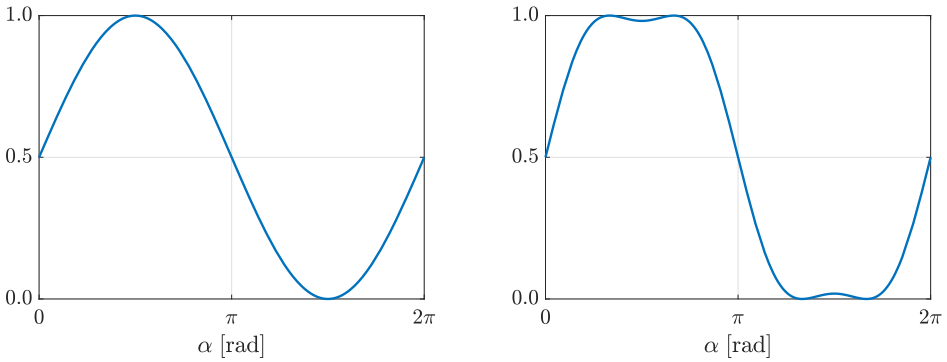

(a) (b)

FIGURE 3.4: Examples of duty-cycles: (a) SPWM; (b) THIS-PWM.

they should be particularized according on the modulation technique used in the power converter. In the following, this particularization is solved for conventional SPWM and also considering a THISPWM. In Appendix B the detailed calculation of the losses in the two cases is presented, in the following only the final result for each case will be shown.

3.2.1.1 Average Conduction Power Loss with a Sinusoidal PWM

Considering a SPWM method, the duty-cycle applied to the upper switch follows:

$$m_H^{\text{SPWM}}(\alpha) = \frac{1}{2}\left[1 + \widetilde{M}_{\text{A}} \sin(\alpha + \varphi)\right] \tag{3.25}$$

where $\widetilde{M}_{\text{A}} \in [0, 1]$ is the (normalized) amplitude of the modulation index and φ is the power factor of the load connected to the half-bridge. By introducing the (3.25) into the (3.21), (3.22) and (3.23), the conduction losses in the MOSFET and the diode are obtained as:

$$P_{\text{cQ},f}^{\text{SPWM}} = K_1\left(C_1 + \frac{\pi}{2}\right) \tag{3.26}$$

$$P_{\text{cQ},r}^{\text{SPWM}} = K_2\left(-C_1 + \frac{\pi}{2}\right) - K_3 C_2 + K_4 C_3 \tag{3.27}$$

$$P_{\text{cD},r}^{\text{SPWM}} = K_5\left(-C_1 + \frac{\pi}{2}\right) + K_6 C_2 - K_4 C_3 \tag{3.28}$$

where auxiliary variables are defined as:

$$\begin{aligned} C_1 &= \beta - A_1 + \frac{3}{2}\widetilde{M}_{\text{A}} A_2 - \frac{1}{6}\widetilde{M}_{\text{A}} A_3 \\ C_2 &= A_4 + \frac{1}{2}\widetilde{M}_{\text{A}} A_5 + \frac{\pi}{2}\widetilde{M}_{\text{A}} \cos(\varphi) \\ C_3 &= -2\beta - 2\widetilde{M}_{\text{A}} A_2 + \pi \end{aligned} \tag{3.29}$$

and:

$$\begin{aligned} A_1 &= \frac{1}{2}\sin(2\beta) \\ A_2 &= \cos(\beta)\cos(\varphi) \\ A_3 &= \cos(3\beta)\cos(\varphi) \\ A_4 &= -2\cos(\beta) - \beta\widetilde{M}_{\mathrm{A}}\cos(\varphi) \\ A_5 &= \sin(2\beta)\cos(\varphi) \end{aligned} \tag{3.30}$$

3.2.1.2 Average Conduction Power Loss with a Sinusoidal PWM and Third Harmonic Injection

If a THISPWM is used, the upper switch duty-cycle is characterized by a Third Harmonic Component (THC) which is added to the sine PWM duty-cycle (3.25):

$$m_H^{\mathrm{THISPWM}}(\alpha) = m_H^{\mathrm{SPWM}}(\alpha) + m_H^{\mathrm{THC}}(\alpha) \tag{3.31}$$

where:

$$m_H^{\mathrm{THC}}(\alpha) = \frac{1}{12}\widetilde{M}_{\mathrm{A}}\sin(3\alpha + 3\varphi) \tag{3.32}$$

In this case, the maximum value for the (normalized) modulation index is $\widetilde{M}_{\mathrm{A}} = 1.15$. The additional conduction loss given by the third harmonic component can be calculated by introducing (3.32) into general conduction loss expressions:

$$P_{\mathrm{cQ},f}^{\mathrm{THC}} = K_1 D_1\Big(- D_2\Big) \tag{3.33}$$

$$P_{\mathrm{cQ},r}^{\mathrm{THC}} = K_2 D_1 D_2 - K_3 D_1 D_3 + K_4 D_1 D_4 \tag{3.34}$$

$$P_{\mathrm{cD},r}^{\mathrm{THC}} = K_5 D_1 D_2 + K_6 D_1 D_3 - K_4 D_1 D_4 \tag{3.35}$$

where auxiliary variables are defined as:

$$\begin{aligned} D_1 &= \frac{1}{6}\widetilde{M}_{\mathrm{A}}\cos(3\varphi) \\ D_2 &= \frac{1}{2}\cos(\beta) - \frac{1}{3}\cos(3\beta) + \frac{1}{10}\cos(5\beta) \\ D_3 &= -2\cos(\beta)\sin^3(\beta) \\ D_4 &= -\frac{2}{3}\widetilde{M}_{\mathrm{A}}\cos(3\beta) \end{aligned} \tag{3.36}$$

Since:

$$P_{\mathrm{cQ},f}^{\mathrm{THISPWM}} = P_{\mathrm{cQ},f}^{\mathrm{SPWM}} + P_{\mathrm{cQ},f}^{\mathrm{THC}} \tag{3.37}$$

$$P_{\mathrm{cQ},r}^{\mathrm{THISPWM}} = P_{\mathrm{cQ},r}^{\mathrm{SPWM}} + P_{\mathrm{cQ},r}^{\mathrm{THC}} \tag{3.38}$$

$$P_{\mathrm{cD},r}^{\mathrm{THISPWM}} = P_{\mathrm{cD},r}^{\mathrm{SPWM}} + P_{\mathrm{cD},r}^{\mathrm{THC}} \tag{3.39}$$

the average conduction power loss for a MOSFET and diode with a THIS-PWM become:

$$P_{\mathrm{c}Q,f}^{\mathrm{THISPWM}} = K_1\left(C_1 - D_1D_2 + \frac{\pi}{2}\right) \tag{3.40}$$

$$P_{\mathrm{c}Q,r}^{\mathrm{THISPWM}} = K_2\left(-C_1 + D_1D_2 + \frac{\pi}{2}\right) - K_3\left(C_2 + D_1D_3\right) + K_4\left(C_3 + D_1D_4\right) \tag{3.41}$$

$$P_{\mathrm{c}D,r}^{\mathrm{THISPWM}} = K_5\left(-C_1 + D_1D_2 + \frac{\pi}{2}\right) + K_6\left(C_2 + D_1D_3\right) - K_4\left(C_3 + D_1D_4\right) \tag{3.42}$$

3.2.2 Average Conduction Power Loss with an IGBT and Diode

If a switch composed of an IGBT transistor and a diode is considered, the calculation of the conduction losses is different since the IGBT does not conduct during the reverse phase. Therefore, if i_o is the output current, during the forward phase (i.e. $i_o > 0$) only the IGBT conducts and the IGBT current is equal to i_o; during the reverse phase only the diode conducts and the diode current is equal to i_o. The instantaneous conduction losses of a power device can be obtained as:

$$p_c(i_{\mathrm{on}}, \Theta_{\mathrm{J}}) = m(\alpha)v_{\mathrm{on}}(i_{\mathrm{on}}, \Theta_{\mathrm{J}})i_{\mathrm{on}} \tag{3.43}$$

where $m(\alpha)$ is the duty-cycle applied to the device, and $v_{\mathrm{on}}(i_{\mathrm{on}}, \Theta_{\mathrm{J}})$ and i_{on} are the device on-voltage and on-current during the conduction phase, respectively. Finally, Θ_{J} is the device junction temperature.

In case of an IGBT transistor (Q), the (collector-emitter) on-voltage can be expressed as:

$$v_{Q\mathrm{on}}(i_{Q\mathrm{on}}, \Theta_{\mathrm{J}Q}) = R_{Q\mathrm{on}}(i_{Q\mathrm{on}}, \Theta_{\mathrm{J}Q})i_{Q\mathrm{on}} + V_{Q0}(\Theta_{\mathrm{J}Q}) \tag{3.44}$$

where $R_{Q\mathrm{on}}(i_{Q\mathrm{on}}, \Theta_{\mathrm{J}Q})$ is referred to the IGBT on-resistance, which it also depends on the IGBT junction temperature $\Theta_{\mathrm{J}Q}$ and the on-current $i_{Q\mathrm{on}}$; $V_{Q0}(\Theta_{\mathrm{J}Q}$ is the IGBT no-load voltage, which depends on the IGBT junction temperature. In case of a diode, the on-voltage can be expressed as:

$$v_{D\mathrm{on}}(i_{D\mathrm{on}}, \Theta_{\mathrm{J}D}) = R_{D\mathrm{on}}(i_{D\mathrm{on}}, \Theta_{\mathrm{J}D})i_{D\mathrm{on}} + V_{D0}(\Theta_{\mathrm{J}D}) \tag{3.45}$$

where $R_{D\mathrm{on}}(i_{D\mathrm{on}}, \Theta_{\mathrm{J}D})$ is the diode on-resistance when it is directly polarized, which also depends on the diode junction temperature $\Theta_{\mathrm{J}D}$ and the on-current. Finally, $V_{D0}(\Theta_{\mathrm{J}D})$ is the diode no-load voltage, which depends on the diode junction temperature.

By considering the half-bridge architecture of Figure 3.2, the instantaneous conduction losses of the upper switch (composed of a IGBT and a

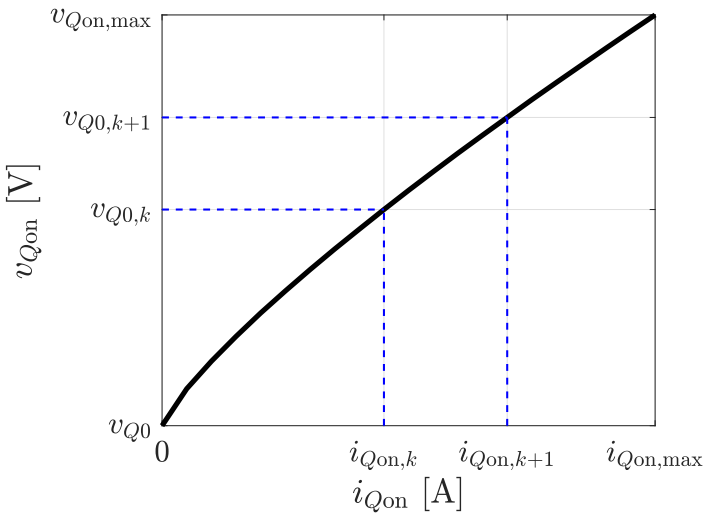

FIGURE 3.5: IGBT forward characteristic $v_{Q\text{on}} - i_{Q\text{on}}$ for a given junction temperature.

diode) can expressed as:

$$p_{\text{c}Q,f}(\alpha) = m_H(\alpha) v_{Q\text{on}}(\alpha) i_o(\alpha) \tag{3.46}$$

$$p_{\text{c}D,r}(\alpha) = m_H(\alpha) v_{D\text{on}}(\alpha) \Big(- i_o(\alpha) \Big) \tag{3.47}$$

where $i_{Q\text{on}} = i_o(\alpha)$ and $i_{D\text{on}} = -i_o(\alpha)$. Indeed, the diode on-current is positive when flows from the anode to the cathode therefore the diode on-current is equal to the opposite of the output current, which is directed from the cathode to the anode hence. The average value in a fundamental period of the conduction losses can hence be calculated as:

$$P_{\text{c}Q,f} = \frac{1}{2\pi} \int_0^{\pi} p_{\text{c}Q,f}(\alpha) d\alpha \tag{3.48}$$

$$P_{\text{c}D,r} = \frac{1}{2\pi} \int_{\pi}^{2\pi} p_{\text{c}D,r}(\alpha) d\alpha \tag{3.49}$$

when $\alpha \in [0, \pi]$ the forward conduction phase happens, while when $\alpha \in [\pi, 2\pi]$ the reverse conduction phase happens.

In order to improve the results of the losses calculation and take into account the non-linear variation of the IGBT on-voltage with respect to the on-current, a modified model for the IGBT and the diode was developed. In order to do so, the device $v_{on} - i_{on}$ forward characteristic is divided into K segments, and for each k-th segment the on-voltage can be written as:

$$v_{Q\text{on}} = \text{R}_{Q\text{on}}|_k \Big(i_{Q\text{on}} - \text{I}_{Q\text{on}}|_k \Big) + \text{V}_{Q0}|_k, \quad i_{Q\text{on}} \in \Big(\text{I}_{Q\text{on}}|_k, \text{I}_{Q\text{on}}|_{k+1} \Big) \tag{3.50}$$

$$v_{D\text{on}} = \text{R}_{D\text{on}}|_k \Big(i_{D\text{on}} - \text{I}_{D\text{on}}|_k \Big) + \text{V}_{D0}|_k, \quad i_{D\text{on}} \in \Big(\text{I}_{D\text{on}}|_k, \text{I}_{D\text{on}}|_{k+1} \Big) \tag{3.51}$$

where:

$$\mathrm{R}_{Q\mathrm{on}}|_k = \frac{\mathrm{V}_{Q0}|_{k+1} - \mathrm{V}_{Q0}|_k}{\mathrm{I}_{Q\mathrm{on}}|_{k+1} - \mathrm{I}_{Q\mathrm{on}}|_k} \tag{3.52}$$

$$\mathrm{R}_{D\mathrm{on}}|_k = \frac{\mathrm{V}_{D0}|_{k+1} - \mathrm{V}_{D0}|_k}{\mathrm{I}_{D\mathrm{on}}|_{k+1} - \mathrm{I}_{D\mathrm{on}}|_k} \tag{3.53}$$

Since the characteristic of Figure 3.5 can be obtained for different values of the junction temperature, the values of R_{on} and V_0 can be calculated at different temperatures in order to take also into account the dependency of the conduction losses with respect to the device junction temperature. By introducing the (3.50),(3.51) into the (3.46),(3.47), the instantaneous conduction losses can be written as:

$$\begin{aligned} p_{\mathrm{c}Q,f(\alpha)} &= m_H(\alpha)\left[\mathrm{r}_{Q\mathrm{on,bp}}\left(i_{Q\mathrm{on}} - \mathrm{i}_{Q\mathrm{on,bp}}\right) + \mathrm{v}_{Q0,\mathrm{bp}}\right] i_{Q\mathrm{on}} \\ &= \mathrm{r}_{Q\mathrm{on,bp}} m_H(\alpha) i_{Q\mathrm{on}}^2 + \left(\mathrm{v}_{Q0,\mathrm{bp}} - \mathrm{r}_{Q\mathrm{on,bp}}\mathrm{i}_{Q\mathrm{on,bp}}\right) m_H(\alpha) i_{Q\mathrm{on}} \end{aligned} \tag{3.54}$$

$$\begin{aligned} p_{\mathrm{c}D,r}(\alpha) &= m_H(\alpha)\left[\mathrm{r}_{D\mathrm{on,bp}}\left(i_{D\mathrm{on}} - \mathrm{i}_{D\mathrm{on,bp}}\right) + \mathrm{v}_{D0,\mathrm{bp}}\right] i_{D\mathrm{on}} \\ &= \mathrm{r}_{D\mathrm{on,bp}} m_H(\alpha) i_{D\mathrm{on}}^2 + \left(\mathrm{v}_{D0,\mathrm{bp}} - \mathrm{r}_{D\mathrm{on,bp}}\mathrm{i}_{D\mathrm{on,bp}}\right) m_H(\alpha) i_{D\mathrm{on}} \end{aligned} \tag{3.55}$$

The terms $\mathrm{r}_{Q\mathrm{on,bp}}, \mathrm{r}_{D\mathrm{on,bp}}$ are the on-resistances functions of the on-current and the junction temperature, while $\mathrm{v}_{Q0,\mathrm{bp}}, \mathrm{v}_{D0,\mathrm{bp}}$ are the no-load voltages functions of the on-current and the temperature. The model presented allows to take into account the variation of the forward characteristic with respect to the on-current and then provide more accurate results for the conduction losses of the device. Since $i_{Q\mathrm{on}} = i_o(\alpha)$ and $i_{D\mathrm{on}} = -i_o(\alpha)$, the (3.54),(3.55) become:

$$\begin{aligned} &p_{\mathrm{c}Q,f(\alpha)} \\ &= \mathrm{r}_{Q\mathrm{on,bp}} m_H(\alpha) i_o^2(\alpha) + \left(\mathrm{v}_{Q0,\mathrm{bp}} - \mathrm{r}_{Q\mathrm{on,bp}}\mathrm{i}_{Q\mathrm{on,bp}}\right) m_H(\alpha) i_o(\alpha) \end{aligned} \tag{3.56}$$

$$\begin{aligned} &p_{\mathrm{c}D,r}(\alpha) \\ &= \mathrm{r}_{D\mathrm{on,bp}} m_H(\alpha) i_o^2(\alpha) - \left(\mathrm{v}_{D0,\mathrm{bp}} - \mathrm{r}_{D\mathrm{on,bp}}\mathrm{i}_{D\mathrm{on,bp}}\right) m_H(\alpha) i_o(\alpha) \end{aligned} \tag{3.57}$$

By introducing the (3.56),(3.57) into the (3.48), (3.49) leads to:

$$P_{\mathrm{c}Q,f} = \mathrm{r}_{Q\mathrm{on,bp}} I_{Q\mathrm{rms}}^2 + \left(\mathrm{v}_{Q0,\mathrm{bp}} - \mathrm{r}_{Q\mathrm{on,bp}}\mathrm{i}_{Q\mathrm{on,bp}}\right) I_{Q\mathrm{avg}} \tag{3.58}$$

$$P_{\mathrm{c}D,r} = \mathrm{r}_{D\mathrm{on,bp}} I_{D\mathrm{rms}}^2 - \left(\mathrm{v}_{D0,\mathrm{bp}} - \mathrm{r}_{D\mathrm{on,bp}}\mathrm{i}_{D\mathrm{on,bp}}\right) I_{D\mathrm{avg}} \tag{3.59}$$

where:

$$I_{Q\text{avg}} = \frac{1}{2\pi}\int_0^{\pi} m_H(\alpha) i_o(\alpha) d\alpha \qquad I^2_{Q\text{rms}} = \frac{1}{2\pi}\int_0^{\pi} m_H(\alpha) i_o^2(\alpha) d\alpha$$
$$I_{D\text{avg}} = \frac{1}{2\pi}\int_{\pi}^{2\pi} m_H(\alpha) i_o(\alpha) d\alpha \qquad I^2_{D\text{rms}} = \frac{1}{2\pi}\int_{\pi}^{2\pi} m_H(\alpha) i_o^2(\alpha) d\alpha$$

By remembering that the output current can be expressed as $i_o(\alpha) = I_p \sin(\alpha)$, yields to:

$$I_{Q\text{avg}} = \frac{I_p}{2\pi}\int_0^{\pi} m_H(\alpha)\sin(\alpha) d\alpha \tag{3.60}$$
$$I^2_{Q\text{rms}} = \frac{I_p^2}{2\pi}\int_0^{\pi} m_H(\alpha)\sin^2(\alpha) d\alpha \tag{3.61}$$
$$I_{D\text{avg}} = \frac{I_p}{2\pi}\int_{\pi}^{2\pi} m_H(\alpha)\sin(\alpha) d\alpha \tag{3.62}$$
$$I^2_{D\text{rms}} = \frac{I_p^2}{2\pi}\int_{\pi}^{2\pi} m_H(\alpha)\sin^2(\alpha) d\alpha \tag{3.63}$$

in order to obtain the best results, the on-resistances and the no-load voltages were calculated by considering the peak phase current I_p:

$$\mathrm{r}_{Q\text{on,bp}} = f(I_p, \Theta_{\mathrm{J}Q}) \qquad \mathrm{v}_{Q0,\text{bp}} = f(I_p, \Theta_{\mathrm{J}Q})$$
$$\mathrm{r}_{D\text{on,bp}} = f(I_p, \Theta_{\mathrm{J}D}) \qquad \mathrm{v}_{D0,\text{bp}} = f(I_p, \Theta_{\mathrm{J}D})$$

In the following subsections, the conduction power loss in two different cases will be shown: considering a SPWM and also a THISPWM, Figure 3.4. In Appendix B the detailed calculation of the losses in the two cases is presented and in the following pages only the final result for each case will be shown.

3.2.2.1 Average Conduction Power Loss with a Sinusoidal PWM

Considering a SPWM method, the duty-cycle applied to the upper switch follows:

$$m_H^{\text{SPWM}}(\alpha) = \frac{1}{2}\left[1 + \widetilde{M}_{\mathrm{A}}\sin(\alpha + \varphi)\right] \tag{3.64}$$

where $\widetilde{M}_{\mathrm{A}} \in [0, 1]$ is the (normalized) amplitude of the modulation index and φ is the power factor of the load connected to the half-bridge. By introducing the (3.64) into the (3.60-3.63), and considering the (B.40-B.43), the average

conduction power loss for a SPWM become:

$$P_{\mathrm{c}Q,f}^{\mathrm{SPWM}} = \mathrm{r}_{Q\mathrm{on,bp}} I_p^2 \left[\frac{1}{8} + \frac{\widetilde{M}_{\mathrm{A}} \cos(\varphi)}{3\pi}\right] + \left(\mathrm{v}_{Q0,\mathrm{bp}} - \mathrm{r}_{Q\mathrm{on,bp}} \mathrm{i}_{Q\mathrm{on,bp}}\right) I_p \left[\frac{1}{2\pi} + \frac{\widetilde{M}_{\mathrm{A}} \cos(\varphi)}{8}\right] \tag{3.65}$$

$$P_{\mathrm{c}D,f}^{\mathrm{SPWM}} = \mathrm{r}_{D\mathrm{on}} I_p^2 \left[\frac{1}{8} - \frac{\widetilde{M}_{\mathrm{A}} \cos(\varphi)}{3\pi}\right] + \left(\mathrm{v}_{D0,\mathrm{bp}} - \mathrm{r}_{D\mathrm{on,bp}} \mathrm{i}_{D\mathrm{on,bp}}\right) I_p \left[\frac{1}{2\pi} - \frac{\widetilde{M}_{\mathrm{A}} \cos(\varphi)}{8}\right] \tag{3.66}$$

3.2.2.2 Average Conduction Power Loss with a Sinusoidal PWM and Third Harmonic Injection

If a THISPWM is used, the upper switch duty-cycle is characterized by a THC which is added to the sine PWM duty-cycle (3.64):

$$m_H^{\mathrm{THISPWM}}(\alpha) = m_H^{\mathrm{SPWM}}(\alpha) + m_H^{\mathrm{THC}}(\alpha) \tag{3.67}$$

where:

$$m_H^{\mathrm{THC}}(\alpha) = \frac{1}{12} \widetilde{M}_{\mathrm{A}} \sin(3\alpha + 3\varphi) \tag{3.68}$$

In this case, the maximum value for the (normalized) modulation index is $\widetilde{M}_{\mathrm{A}} = 1.15$. The additional conduction loss given by the third harmonic component can be calculated by introducing (3.68) into the (3.60-3.63), and considering the (B.46-B.49), yields to:

$$P_{\mathrm{c}Q,f}^{\mathrm{THC}} = -r_{Q\mathrm{on}} I_p^2 \frac{\widetilde{M}_{\mathrm{A}} \cos(3\varphi)}{90\pi} \tag{3.69}$$

$$P_{\mathrm{c}D,f}^{\mathrm{THC}} = r_{D\mathrm{on}} I_p^2 \frac{\widetilde{M}_{\mathrm{A}} \cos(3\varphi)}{90\pi} \tag{3.70}$$

therefore, since:

$$P_{\mathrm{c}Q,f}^{\mathrm{THISPWM}} = P_{\mathrm{c}Q,f}^{\mathrm{SPWM}} + P_{\mathrm{c}Q,f}^{\mathrm{THC}} \tag{3.71}$$

$$P_{\mathrm{c}D,f}^{\mathrm{THISPWM}} = P_{\mathrm{c}D,f}^{\mathrm{SPWM}} + P_{\mathrm{c}D,f}^{\mathrm{THC}} \tag{3.72}$$

the average conduction power loss for a IGBT and diode with a THISPWM become:

$$P_{\mathrm{c}Q,f}^{\mathrm{THISPWM}} = \mathrm{r}_{Q\mathrm{on}} I_p^2 \left[\frac{1}{8} + \frac{\widetilde{M}_{\mathrm{A}}\cos(\varphi)}{3\pi} - \frac{\widetilde{M}_{\mathrm{A}}\cos(3\varphi)}{90\pi}\right] + \left(\mathrm{v}_{Q0,\mathrm{bp}} - \mathrm{r}_{Q\mathrm{on},\mathrm{bp}}\mathrm{i}_{Q\mathrm{on},\mathrm{bp}}\right) I_p \left[\frac{1}{2\pi} + \frac{\widetilde{M}_{\mathrm{A}}\cos(\varphi)}{8}\right] \tag{3.73}$$

$$P_{\mathrm{c}D,f}^{\mathrm{THISPWM}} = \mathrm{r}_{D\mathrm{on}} I_p^2 \left[\frac{1}{8} - \frac{\widetilde{M}_{\mathrm{A}}\cos(\varphi)}{3\pi} + \frac{\widetilde{M}_{\mathrm{A}}\cos(3\varphi)}{90\pi}\right] + \left(\mathrm{v}_{D0,\mathrm{bp}} - \mathrm{r}_{D\mathrm{on},\mathrm{bp}}\mathrm{i}_{D\mathrm{on},\mathrm{bp}}\right) I_p \left[\frac{1}{2\pi} - \frac{\widetilde{M}_{\mathrm{A}}\cos(\varphi)}{8}\right] \tag{3.74}$$

3.2.3 Average Switching Losses

The calculation of the switching losses is carried out considering the devices switching energies E_{sw} that are usually provided in the manufacturer datasheet. These energy loss depend on the output current i_o, the gate resistance R_g, the input voltage V_i as well as the junction temperature Θ_{J}. For this reason, the switching energies can be obtained by using a multi-dimensional look-up-table defining $E_{\mathrm{sw}} = f(i_o, \Theta_{\mathrm{J}}, R_g, V_i)$.

The transistor switching loss are caused by the turn-on and the turn-off of the device, while for the diode they are only given by the reverse recovery effect. However, if the diode is a Schottky type, the reverse recovery losses can be neglected. For a given junction temperature Θ_{J}, gate resistance R_g and input voltage V_i, the switching energies depend on the output current i_o and the switching losses can be expressed as a function of the switching energy as $p_{\mathrm{sw}}(\alpha) = f_{\mathrm{sw}} E_{\mathrm{sw}}(i_o(\alpha))$.

During the forward conduction phase (i.e. when $i_o > 0$), the upper transistor works in hard-switching since the $v_{Q\mathrm{on}}$ voltage is equal to the input voltage V_i. On the other hand, the lower transistor (Q_L) works in almost zero voltage switching (ZVS) since the $v_{Q\mathrm{on}}$ voltage is equal to the diode no-load voltage V_{D0}. Conversely, during the reverse conduction phase (i.e. when $i_o < 0$), the upper transistor works in ZVS, while the lower transistor works in hard-switching. In both cases, the reverse recovery losses are given by the opposite diode with respect to the transistor working in hard-switching. For example, considering the half-bridge architecture of Figure 3.2(a), switching losses are present in the upper transistor (Q_H) when $0 \leq \alpha \leq \pi$, while they are present in the upper diode (D_H) when $\pi \leq \alpha \leq 2\pi$. Analogous phenomenon happens for the lower switch.

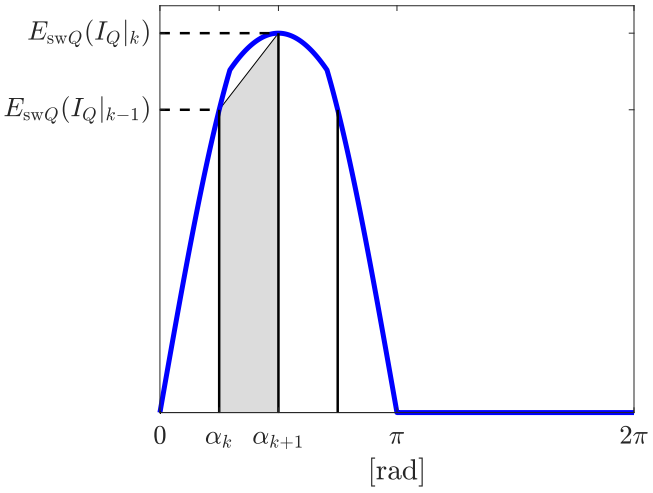

FIGURE 3.6: Example of a switching losses curve for a transistor with discretization.

Taking into account these concepts, the average switching loss of the transistor and the diode over one period can be calculated as:

$$\begin{aligned} P_{swQ} &= \frac{f_{sw}}{2\pi}\int_0^{\pi} e_{swQ}(\alpha)d\alpha \\ P_{swD} &= \frac{f_{sw}}{2\pi}\int_{\pi}^{2\pi} e_{swD}(\alpha)d\alpha \end{aligned} \tag{3.75}$$

where $e_{swQ}(\alpha)$ is the transistor instantaneous switching energy curve, and $e_{swD}(\alpha)$ is the diode instantaneous switching energy curve. The integrals expressions in (3.75) can be approximated by means of a discretization of the switching energy curve $e_{sw}(\alpha)$ into N intervals, as shown in Figure 3.6. By defining $\Delta\alpha = \frac{\pi}{N} = \alpha_{k+1} - \alpha_k$, and by applying the trapezoidal integration method, the integrals in (3.75) can be calculated as:

$$\begin{aligned} \int_0^{\pi} e_{swQ}(\alpha)d\alpha &= \frac{\Delta\alpha}{2}\sum_{k=1}^{N}\left[E_{swQ}(I_Q|_k) + E_{swQ}(I_Q|_{k-1})\right] \\ \int_{\pi}^{2\pi} e_{swD}(\alpha)d\alpha &= \frac{\Delta\alpha}{2}\sum_{k=1}^{N}\left[E_{swD}(I_D|_k) + E_{swQ}(I_D|_{k-1})\right] \end{aligned} \tag{3.76}$$

where $I_Q|_k = I_p \sin(k\Delta\alpha)$ is the transistor current in the k-th interval (first semi-period), and $I_D|_k = I_p|\sin(k\Delta\alpha + \pi)|$ is the diode current in the k-th interval (second semi-period). The terms $E_{swQ} = f(I_Q|_k)$ and $E_{swD} = f(I_D|_k)$ are the transistor and the diode switching energies evaluated in the k-th

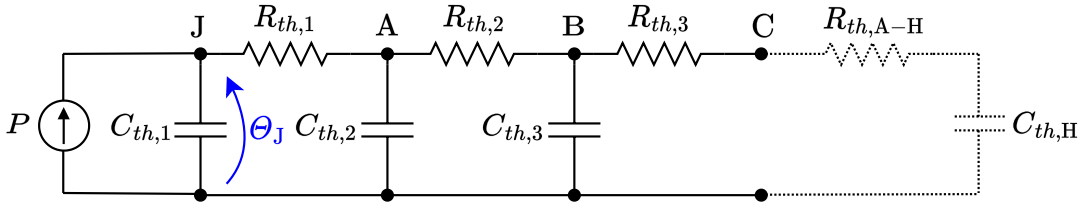

FIGURE 3.7: Generic Cauer thermal network of a power electronics device, with a possible external heatsink impedance. The node J is referred to the junction, the node C is referred to the device case.

point. Finally, the average switching losses can be obtained as:

$$P_{\mathrm{sw}Q} = \frac{f_{\mathrm{sw}}}{2N} \sum_{k=1}^{N} E_{\mathrm{sw}Q}(I_Q|_k) \tag{3.77}$$

$$P_{\mathrm{sw}D} = \frac{f_{\mathrm{sw}}}{2N} \sum_{k=1}^{N} E_{\mathrm{sw}D}(I_D|_k) \tag{3.78}$$

Therefore, for a given gate resistance R_g, junction temperature Θ_J and input voltage V_i, the transistor average switching losses can be calculated as:

$$P_{\mathrm{sw}Q}(i_o, R_g, \Theta_{\mathrm{J}Q}, V_i) = \frac{f_{\mathrm{sw}}}{2N} \sum_{k=1}^{N} \left[E_{\mathrm{on}Q} + E_{\mathrm{off}Q} \right] \tag{3.79}$$

where $E_{\mathrm{on}Q}$ and $E_{\mathrm{off}Q}$ are the transistor on-energy and off-energy respectively. On the other hand, the diode average switching losses can be calculated as:

$$P_{\mathrm{sw}D}(i_o, R_g, \Theta_{\mathrm{J}D}, V_i) = \frac{f_{\mathrm{sw}}}{2N} \sum_{k=1}^{N} E_{\mathrm{rr}D} \tag{3.80}$$

where $E_{\mathrm{rr}D}$ is the diode reverse recovery energy. It is important to point out that the reverse recovery of the opposite diode causes the increment of the transistor turn-on energy, which is usually already taken into account in the manufacturer datasheet.

3.2.4 Thermal Model

The thermal network of a power electronics device can be represented by a Cauer thermal network, with a certain number of branches, each one composed of a capacitor and a resistor. The thermal network can be expanded to an indefinite number of impedances, but the thermal behavior of the device is usually well represented with a three impedances model as shown in Figure 3.7. In order to obtain the temperature variation, the losses P in the thermal model are represented as a heat generator connected to the device junction node J. The node C represents the case connection where the heatsink impedance should be added.

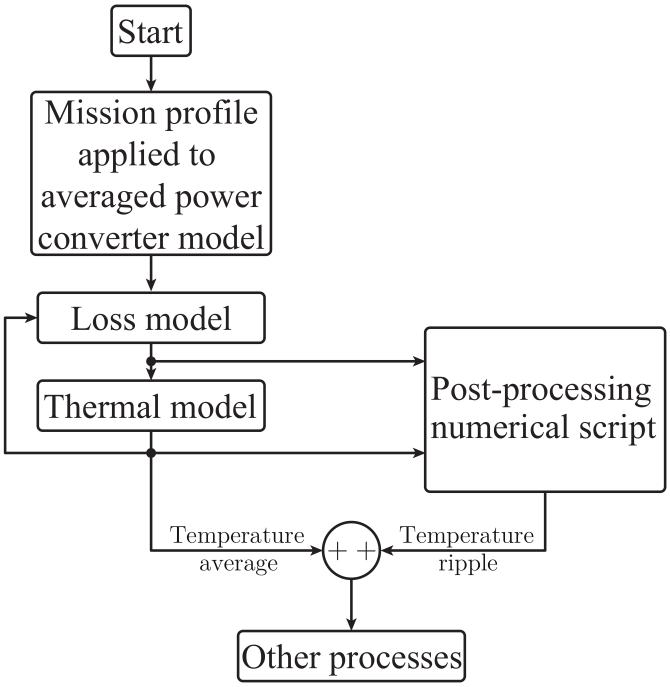

FIGURE 3.8: Flowchart of the method to calculate the power device temperature based on the average conduction losses and the periodic profile at the fundamental frequency

The Cauer thermal network of a device can be directly provided by the manufacturer, or it can be obtained from the single pulse thermal response of the device, which is usually provided in the manufacturer datasheet. Indeed, by fitting the thermal response curve of the device, the impedances of the Foster thermal network are calculated, which is afterwards converted into a Cauer network. Each element of the Cauer network has a physical meaning and each node represents a real connection point of the device on the other hand, the Foster thermal network does not have any physical meaning and it is only used for calculation purposes. The Cauer network allows to add external components to the case of the device and then perform a more complex thermal analysis by simply adding a further branch to the network. The Foster network, on the contrary, must be re-calculated because each element depends on the whole network configuration, [75].

In order to obtain the temperature variation, the losses produced in the device are given as a input into a heat generator which is connected to the junction node J. The case node C is where the impedance of a external heatsink can be added. It is worth to notice that, since the device thermal capacitance are much smaller than the heatsink thermal capacitance, the transient response of the device temperature can be very well approximated by considering only the internal impedance of the device, thus neglecting the connection to the heatsink and the influence of the nearby devices.

The procedure for of the temperature estimation is composed of three fundamental steps, Figure 3.8:

1. calculation of the average temperature;

2. calculation of the temperature ripple;

3. sum of the two previous results to obtain the final instantaneous temperature signal.

The temperature estimation is composed of two independent parts: the first one relies on a numerical simulation in Matlab Simulink, the converter is modeled by using the average losses equations presented in Section 3.2.1. This numerical simulation provides the average temperature profile given a mission profile, which however is not periodic because it depends on the load variations causing a non-regular average temperature profile. The final application of the power converter defines the mission profile: for instance, if the converter is employed in a charging station, the temperature depends on the user behavior, which cannot be foreseen. The second part of the temperature estimation algorithm is composed of a post-processing script which, by receiving the operating conditions and the power devices data, after the Simulink model run, calculates the periodic temperature ripple at the fundamental current frequency, to superimpose on the average temperature profile.

In order to calculate the temperature profile of one switch of a three-phase converter, the following quantities are needed: the output current fundamental frequency f_1 (considering a sinusoidal profile and neglecting the switching frequency ripple component), the load power factor φ, the phase current peak I_p and the (normalized) amplitude modulation index $\widetilde{M}_{\mathrm{A}}$. The switching frequency f_s, the device gate resistance R_g and the DC bus voltage v_{DC} are also necessary.

3.2.4.1 Average Temperature Calculation

After defining the modulation strategy (SPWM or THISPWM), the analytical losses for the MOSFET and diode are calculated by using the equations (3.26-3.28) or (3.40-3.42), depending on the modulation strategy. While for the IGBT and diode are calculated by using the equations (3.65-3.66) or (3.73-3.74), depending on the modulation strategy. Then, by using (3.79) and (3.80), the average switching losses are also calculated. The sum of the average conduction and switching losses of each device are used as the input value for the heat generator employed into the Cauer network of each device. From the Cauer network, the junction temperature is obtained, which is then used as a feedback for the calculation of the aforementioned coefficients for the next simulation step.

The electrical quantities which are necessary for the losses calculation, i.e. phase current, DC bus voltage and modulation index, are calculated with an integrated high-speed electrical model of the converter.

3.2.4.2 Temperature Ripple at the Phase Current Frequency

The junction temperature ripple is very important since it has a very high impact on the device damage evaluation: the higher is the fundamental frequency of the current, the higher is the repetition ratio of the temperature

ripple and the higher is the device cumulative damage. In order to calculate the temperature ripple, the variation of the losses due to the sinusoidal output current must be considered. In order to do so, a mathematical model of the instantaneous losses was obtained by means of a Matlab script. This model, taking into account the converter working point data (current, modulation index, power factor, switching frequency, etc), allows to calculate the device losses ripple which must be added to the average value.

The procedure to calculate the temperature ripple is composed of different steps. First of all, the devices average temperature profiles are divided into a certain number of time intervals, which depend on the fundamental frequency f_1 of the phase current, and on the total time of the simulation. For instance, if the total simulation time is $t_{\max}$ and the fundamental frequency changes during the simulation, for each fundamental frequency $f_1|_k$, the number of intervals considered for that frequency are equal to $\Delta t|_k f_1|_k$, where $\Delta t|_k$ is the k-th time interval corresponding to the fundamental frequency $f_1|_k$ and $\sum_k \Delta t_k = t_{\max}$.

After that, each interval $\Delta t|_k = t_{k+1} - t_k$ is discretized with Z points, where $\delta t|_z = \dfrac{\Delta t|_k}{Z}$ is the sub-interval of each k-th time interval. Finally, depending on the modulation strategy, the duty-cycle of the switch is calculated and then, for each device and for each time interval $\Delta t|_k$ the following procedure is applied:

1. the instantaneous conduction losses and switching losses curves are calculated, and the total loss curve $p|_k(t) = p_{\mathrm{c}}|_k(t) + p_{\mathrm{sw}}|_k(t)$ is obtained;

2. the fourier transform is performed on the total losses curve $p|_k(t)$ and N harmonics are obtained (the DC value is excluded since only the ripple is evaluated);

3. for each n-th harmonic, a losses phasor $\boldsymbol{P}|_{\boldsymbol{k,n}} = \hat{P}|_{k,n} e^{j\zeta|_{k,n}}$ is calculated;

4. the n-th thermal impedance of the Cauer network $\boldsymbol{Z}|_{\boldsymbol{k,n}} = \hat{Z}|_{k,n} e^{j\psi|_{k,n}}$ is evaluated at each harmonic frequency $f_n = nf_1$ and pulsation $\omega_n = 2\pi f_n$:

$$\boldsymbol{Z}|_{\boldsymbol{k,n}} = \cfrac{1}{j\omega_n C_{th,1} + \cfrac{1}{R_{th,1} + \cfrac{1}{j\omega_n C_{th,2} + \cfrac{1}{R_{th,2} + \cfrac{1}{j\omega_n C_{th,3} + \cfrac{1}{R_{th,3}}}}}}} \tag{3.81}$$

TABLE 3.1: Specifications of the workstation used for the simulations.

CPU	AMD Ryzen 7 5800H 3.2 GHz
GPU	NVIDIA GeForce RTX 3080 Laptop GPU
Storage	SAMSUNG MZVLB1T0HBLR-000L2
Motherboard	Lenovo LNVNB161216
Memory	Kingston 32GB (2x16GB) 2666MHz DDR4 CL15
Operating system	Windows 11 Pro

5. the temperature ripple phasors are calculated by dividing the losses phasors by the thermal impedance:

$$\widetilde{\boldsymbol{\Theta}}_{\mathbf{J}}|_{\boldsymbol{k,n}} = \hat{\Theta}_{\mathrm{J}}|_{k,n} e^{j(\zeta|_{k,n} - \psi|_{k,n})} \tag{3.82}$$

$$\hat{\Theta}_{\mathrm{J}}|_{k,n} = \frac{\hat{P}|_{k,n}}{\hat{Z}|_{k,n}} \tag{3.83}$$

6. the time-variant signal is reconstructed from the N phasors and thus the temperature ripple profile is obtained:

$$\widetilde{\Theta}_{\mathrm{J}}|_k(t) = 2 \sum_{n=1}^{N} \hat{\Theta}_{\mathrm{J}}|_{k,n} \cos\left(2\pi n f_1 t + \zeta|_{k,n} - \psi|_{k,n}\right), \quad t \in (t_k, t_{k+1}) \tag{3.84}$$

3.2.4.3 Total Temperature Estimation

The final temperature profile of the power devices is achieved by superimposing the temperature ripple profile $\widetilde{\Theta}_{\mathrm{J}}|_k(t)$ to the average temperature profile:

$$\Theta_{\mathrm{J}}|_k(t) = \overline{\Theta}_{\mathrm{J}}|_k(t) + \widetilde{\Theta}_{\mathrm{J}}|_k(t), \qquad t \in (t_k, t_{k+1}) \tag{3.85}$$

where $\overline{\Theta}_{\mathrm{J}}|_k(t)$ is the average temperature profile of the device in the k-th interval.

3.2.5 Numerical Simulations

In this section, the numerical simulations carried out in order to validate the analytical loss models are shown. In this sense, the proposed analytical model structure follows the flowchart diagram shown in Figure 3.8 and executed in Matlab whereas the simulations were carried out in Simulink with the PLECS® simulation environment. Please note that the proposed modeling technique can be developed in any programming language with a good mathematical library. Both simulations were executed in the same computer so that the results can be fairly compared: the workstation specifications are summarized in Table 3.1.

TABLE 3.2: Calculation times comparison between PLECS and the proposed model (considering a SPWM modulation) for a 10 s simulated time period.

	PLECS	**Proposed Model**
MOSFET	267 s	5.8 s
IGBT	271 s	5.2 s

The aim of the simulation evaluation was to compare the temperature profile obtained with the proposed method against the temperature profile obtained with the conventional approach based on a numerical simulation in PLECS, considering the same working points and ambient conditions. The advantage of the analytical model is the very fast execution time which allows to simulate a very large time period in a reduced time, also taking into account the temperature ripple at the fundamental current frequency. On the contrary, the PLECS simulation approach requires much more time to be executed also with the necessity of a great amount of memory. As a clear example of this fact, a 10 seconds thermal simulation using the thermal model provided by PLECS takes around five minutes to be completed while it takes only two seconds (including the compiling time, which is constant and does not depend on the total simulated time) using the proposed model to provide the temperature profile, including the ripple at the fundamental frequency, Table 3.2. This fact enables the possibility to apply the proposed thermal model to make power converter damage estimations in real-time imposing an specific power profile. The obtained results can be used by a predictive maintenance method to define the optimal converter operation, what is currently limited with the existing thermal models approaches. In the end, it is important to point out that the PLECS simulation cannot be fully representative of the device real behavior since the device thermal model is obtained from the manufacturer datasheet, which does not take into account the different operating conditions. The thermal analysis in PLECS is carried out by first calculating the conduction and switching losses and then by obtaining the junction temperature by using the device thermal network. The losses are calculated by combining two different and separated domains: the electrical domain and the thermal domain. The electrical quantities calculated in the electrical domain are passed to the thermal domain which then calculates the devices losses and temperatures.

In the following analysis, both the results regarding the MOSFET and the IGBT will be shown, considering different modulation techniques. Table 3.3 summarizes the common input data used for all the simulations. For an easier setup, in all the simulations a balanced three-phase R-L load connected to a conventional three-phase two-level voltage source inverter (2L-VSI) was considered. Moreover, the power module case (thermal) node was connected directly to a (fixed) ambient temperature source, in order to maintain the same boundary conditions. Finally, a sinusoidal phase current was imposed.

TABLE 3.3: Thermal comparison input data.

DC bus voltage v_{DC}	900 V
Switching frequency f_{sw}	10 kHz
Current fundamental frequency f_1	50 Hz
Ambient temperature Θ_{amb}	40 °C
Output impedance (module) $\hat{Z}_o$	1 Ω

TABLE 3.4: PLECS input data for the MOSFET and diode.

Power device	ROHM BSM400D12P2G003
Gate resistance R_g	0.2 Ω
Transistor on-resistance R_{Qon}	5.8 m Ω
Diode on-resistance R_{Don}	2.1 m Ω
Diode no-load voltage V_{D0}	0.895 V

3.2.5.1 MOSFET and Diode

In order to validate the analytical power loss model of a switch composed of a MOSFET and diode, a 400 A,1200 V ROHM SiC-MOSFET power module was chosen. The election of this power device was actually very convenient

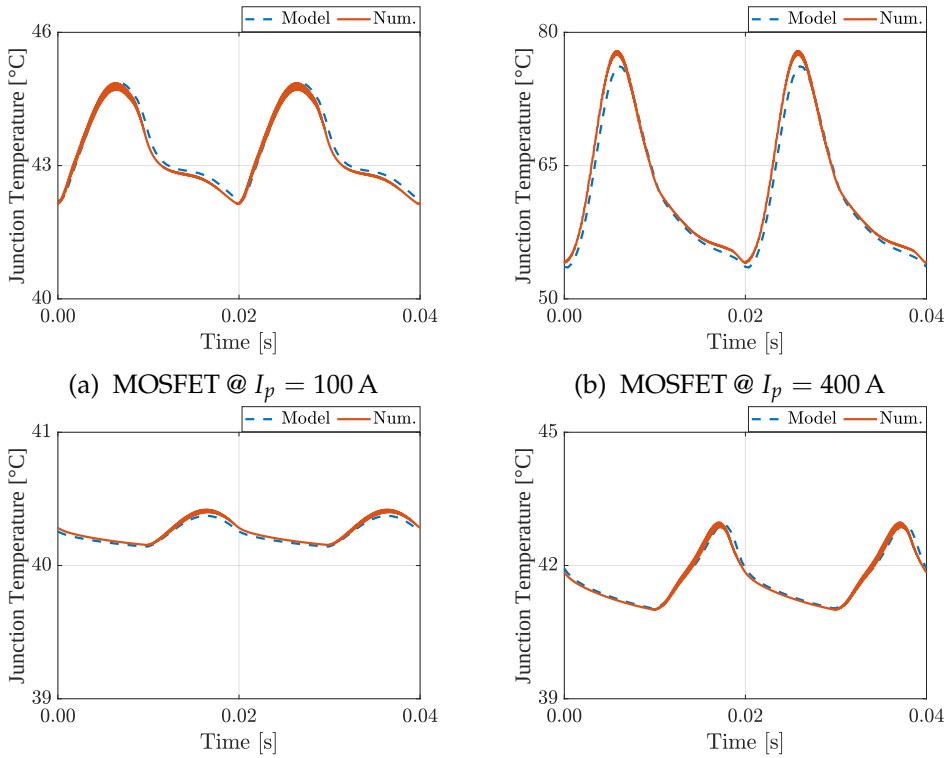

(a) MOSFET @ $I_p = 100$ A (b) MOSFET @ $I_p = 400$ A

(c) Diode @ $I_p = 100$ A (d) Diode @ $I_p = 400$ A

FIGURE 3.9: Comparison of MOSFET and diode junction temperature evolution over time with SPWM @ $\cos(\varphi) = 0.9$.

because the PLECS electrical and thermal model are already available in the

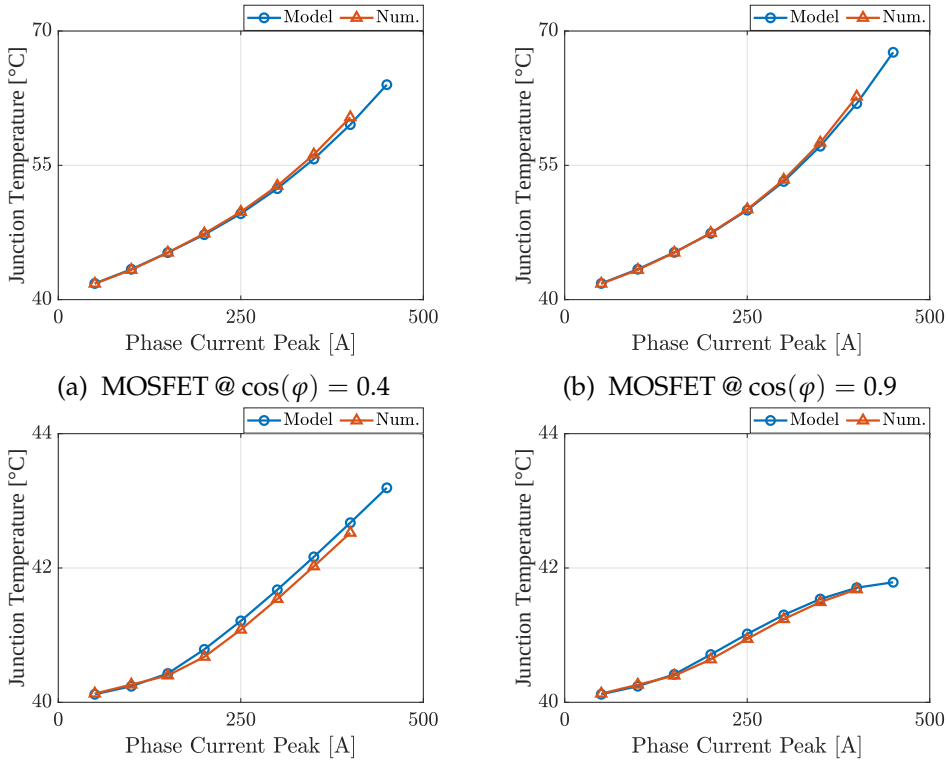

(a) MOSFET @ $\cos(\varphi) = 0.4$ (b) MOSFET @ $\cos(\varphi) = 0.9$

(c) Diode @ $\cos(\varphi) = 0.4$ (d) Diode @ $\cos(\varphi) = 0.9$

FIGURE 3.10: Comparison of MOSFET and diode junction temperature average with SPWM.

manufacturer website, avoiding therefore the risk of a bad characterization of the device. In addition, for a fair comparison, the same lookup tables used of the device PLECS model were employed to build the analytical model. In Table 3.4 the MOSFET and diode on-resistances and no-load voltages used for the PLECS simulation (in the electrical domain) are summarized. Indeed, it is important in the case of a MOSFET and a diode to provide the on-resistances and the no-load voltages to allow PLECS to calculate the current distribution, in the electrical domain, between the MOSFET and the diode during the reverse conduction phase. In fact, the PLECS electrical model of a power devices can be characterized only with constant terms for the electrical parameters, which hence do not depend on the junction temperature or the on-current, therefore approximation errors can arise when the device current and temperature change with respect to the nominal values. On the contrary, in the thermal domain, the device $v_{\text{on}} - i_{\text{on}}$ curve is used by PLECS for the conduction loss evaluation, by interpolating the calculated currents in the electrical domain. The switching losses are calculated in the same way, by considering a lookup table of the switching energies as a function of the on-current, the junction temperature, the gate resistance and the input voltage.

On the other hand, the proposed analytical model features a more accurate calculation of the currents during the reverse phase due to the fact that the on-resistances are calculated by considering the actual junction temperature of the device. However, it does not take into account the dependency of

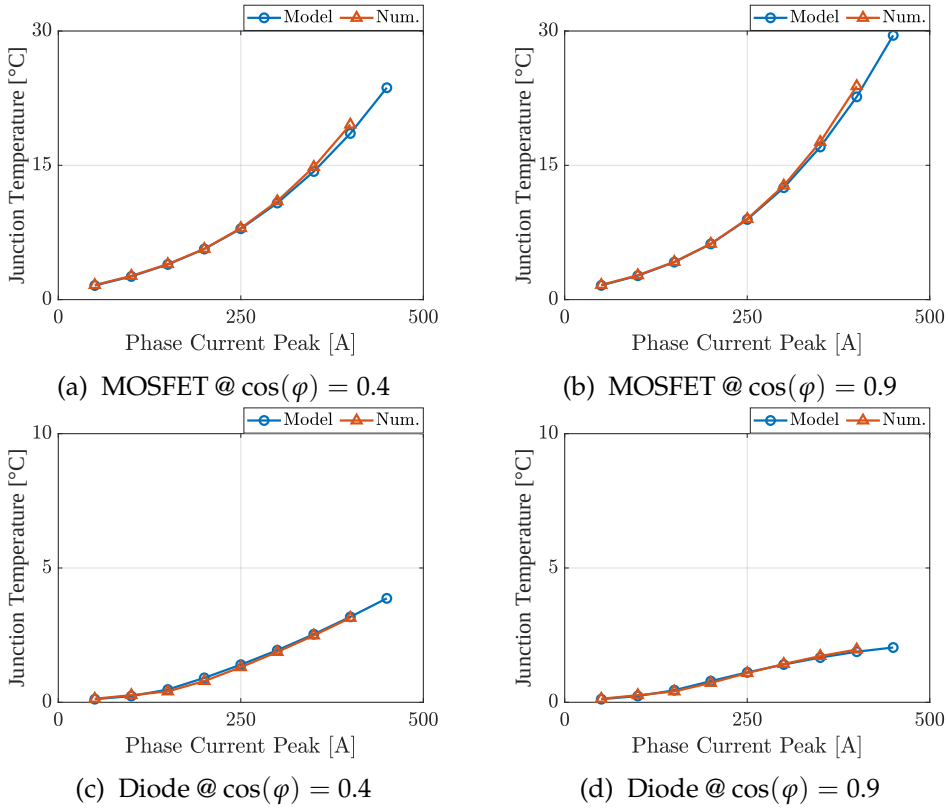

(a) MOSFET @ $\cos(\varphi) = 0.4$ (b) MOSFET @ $\cos(\varphi) = 0.9$

(c) Diode @ $\cos(\varphi) = 0.4$ (d) Diode @ $\cos(\varphi) = 0.9$

FIGURE 3.11: Comparison of MOSFET and diode junction temperature peak-to-peak ripple with SPWM.

the on-resistances with respect to the on-current.

3.2.5.1.1 SPWM

The results of the thermal comparison considering the SPWM modulation strategy are hereafter summarized.

In Figure 3.9 the time waveform of the MOSFET Θ_{JQ} and the diode junction temperatures Θ_{JD} profiles obtained analytically are compared with the temperature profiles obtained with the PLECS numerical simulation, considering a power factor equal to 0.9. It is possible to see a very good agreement between the analytical and the numerical profile, with a slight difference in the MOSFET peak temperature, which could be caused by the difference in the reverse currents calculation. Additionally, the comparison was extended for several phase current peak values and two different power factor values. In Figure 3.10 the average junction temperature comparison is shown while in Figure 3.11 the temperature (peak-to-peak) ripple is shown. Both the figures show a very good agreement between the analytical and the numerical model.

3.2.5.1.2 THISPWM

The results of the thermal comparison considering the THISPWM modulation strategy are hereafter summarized.

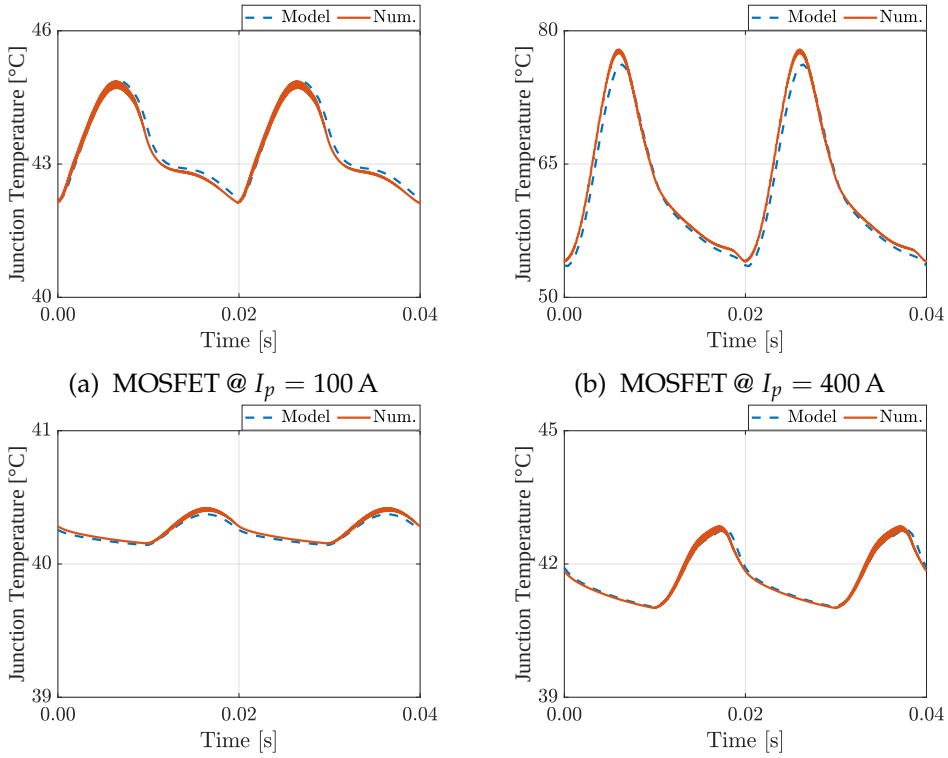

(a) MOSFET @ $I_p = 100\,\text{A}$ (b) MOSFET @ $I_p = 400\,\text{A}$

(c) Diode @ $I_p = 100\,\text{A}$ (d) Diode @ $I_p = 400\,\text{A}$

FIGURE 3.12: Comparison of MOSFET and diode junction temperature evolution over time with THISPWM @ $\cos(\varphi) = 0.9$.

TABLE 3.5: PLECS input data for the IGBT and diode.

Power device	Infineon FZ400R12KE4
Gate resistance R_g	$1.8\,\Omega$
Transistor on-resistance $R_{Q\text{on}}$	$2.0\,\text{m}\,\Omega$
Transistor no-load voltage V_{Q0}	0.766 V
Diode on-resistance $R_{D\text{on}}$	$1.5\,\text{m}\,\Omega$
Diode no-load voltage V_{D0}	0.796 V

In Figure 3.12 the time waveform of the MOSFET Θ_{JQ} and the diode junction temperatures Θ_{JD} profiles obtained analytically are compared with the temperature profiles obtained with the PLECS numerical simulation. The temperature profile in this case result to be very similar to the one obtained with the SPWM, with a major difference in the diode profile. Also in this case it is possible to see a very good agreement between the analytical and the numerical profile. Figures 3.13 and 3.14 show the average and the (peak-to-peak) ripple junction temperature for different phase current peak values and two different power factors. The same considerations made for the SPWM are valid in this case since the results are very similar.

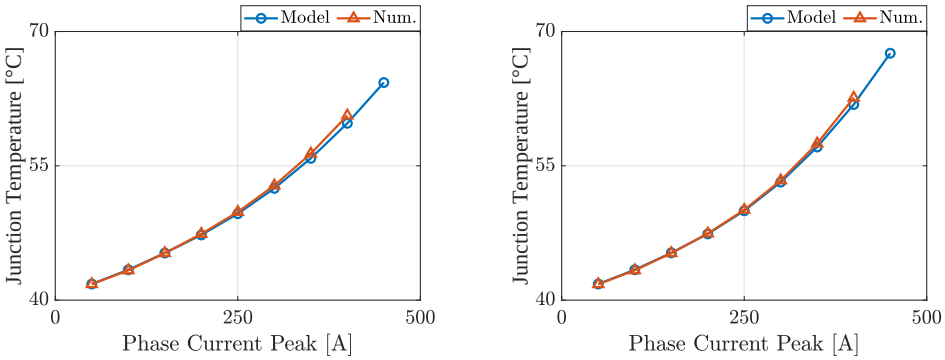

(a) MOSFET @ $\cos(\varphi) = 0.4$

(b) MOSFET @ $\cos(\varphi) = 0.9$

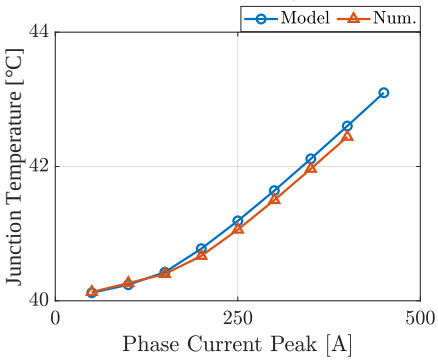

(c) Diode @ $\cos(\varphi) = 0.4$

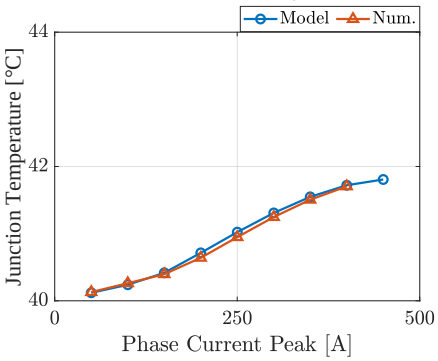

(d) Diode @ $\cos(\varphi) = 0.9$

FIGURE 3.13: Comparison of MOSFET and diode junction temperature average with THISPWM.

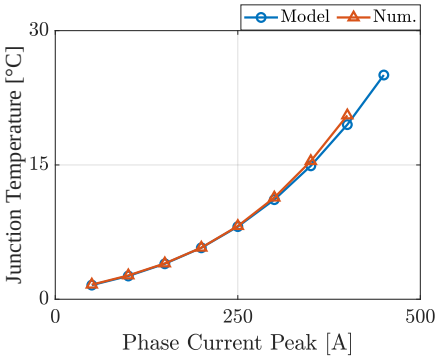

(a) MOSFET @ $\cos(\varphi) = 0.4$

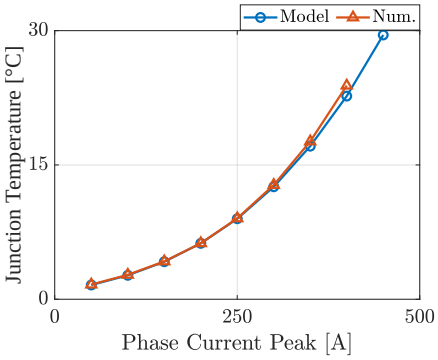

(b) MOSFET @ $\cos(\varphi) = 0.9$

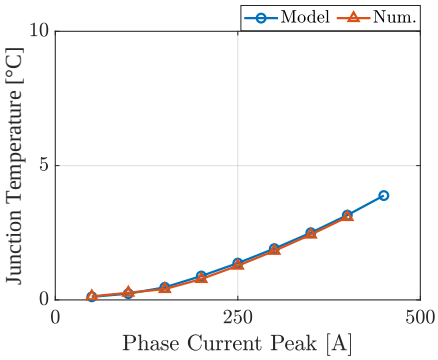

(c) Diode @ $\cos(\varphi) = 0.4$

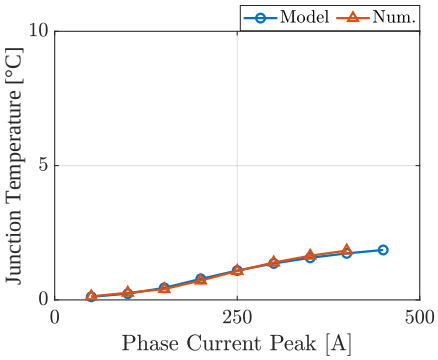

(d) Diode @ $\cos(\varphi) = 0.9$

FIGURE 3.14: Comparison of MOSFET and diode junction temperature peak-to-peak ripple with THISPWM.

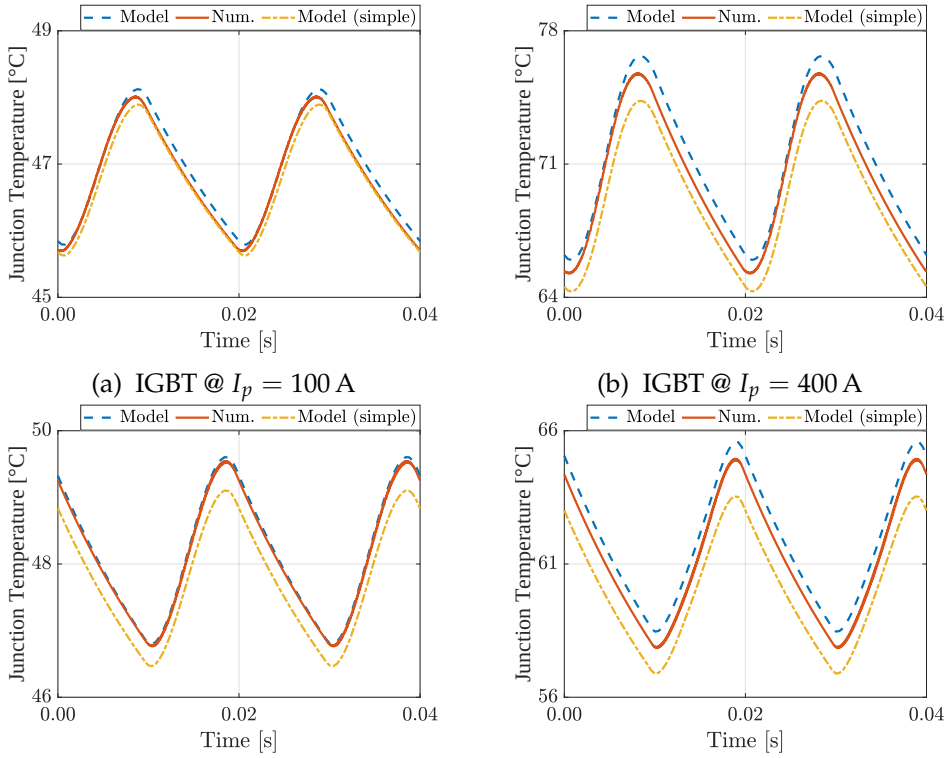

(a) IGBT @ $I_p = 100$ A (b) IGBT @ $I_p = 400$ A

(c) Diode @ $I_p = 100$ A (d) Diode @ $I_p = 400$ A

FIGURE 3.15: Comparison of IGBT and diode junction temperature evolution over time with SPWM @ $\cos(\varphi) = 0.9$.

3.2.5.2 IGBT and Diode

In order to validate the analytical power loss model of a switch composed of a IGBT and diode, a 400 A,1200 V Infineon IGBT power module was chosen. The election of this power device was actually very convenient because the PLECS thermal model is already available in the manufacturer website, avoiding therefore the risk of a bad characterization of the device. In addition, for a fair comparison, the same lookup tables used for the PLECS simulation were employed to build the analytical model of the devices. In Table 3.5 the IGBT and diode on-resistances and no-load voltages used for the PLECS simulation (in the electrical domain) are summarized.

Differently from the MOSFET, the IGBT does not conduct during the reverse phase and therefore the PLECS electrical parameters do not change the reverse current flowing through the diode, which is equal to the phase current. Regarding the thermal domain, the PLECS calculations are carried out by considering the lookup tables of the device forward characteristic, for the conduction power loss, and the switching energies, for the switching power loss. On the other hand, the analytical model does not take into account the variation of the IGBT and diode parameters (on-resistances and no-load voltages) with respect to the phase current peak, but only the junction temperature. However, a modification of the conduction power loss was presented, where the IGBT and diode forward characteristic are divided into sub-intervals and for each of them the on-resistance and the no-load voltage

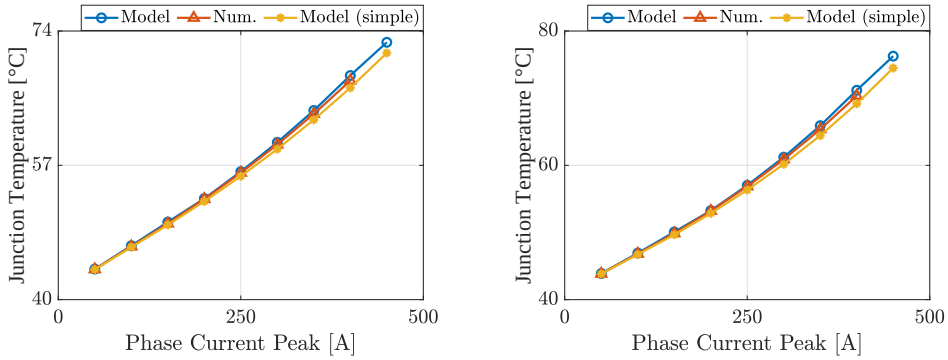

(a) IGBT @ $\cos(\varphi) = 0.4$ (b) IGBT @ $\cos(\varphi) = 0.9$

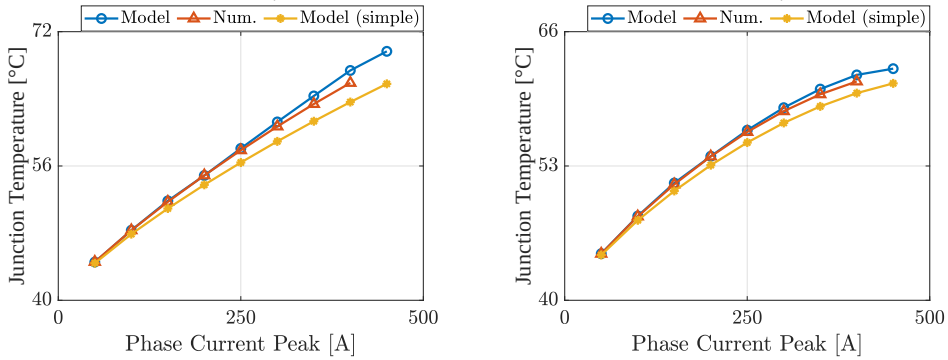

(c) Diode @ $\cos(\varphi) = 0.4$ (d) Diode @ $\cos(\varphi) = 0.9$

FIGURE 3.16: Comparison of IGBT and diode junction temperature average with SPWM.

are calculated by considering the current in that interval. In the following analysis, the numerical results will be compared to two different analytical models: the first one is the modified model, the second one is a simple model, where constant parameters are used.

3.2.5.2.1 SPWM

Figure 3.15 show the junction temperatures waveforms of the IGBT and the diode with two different phase current peak values and a power factor of 0.9, considering a SPWM strategy. The main result is the noticeable difference which lies between the simple model and the modified one, proving that the modifications are effective into increasing the accuracy of the analytical model. The figure also show a good agreement with the numerical waveform.

Figures 3.16 and 3.17 show the average and the (peak-to-peak) ripple trend with respect to the phase current peak value and with two different power factors. The difference between the modified and the simple model is very noticeable, especially when considering the diode junction temperature. On the other hand, the numerical and the modified analytical model show a very good agreement.

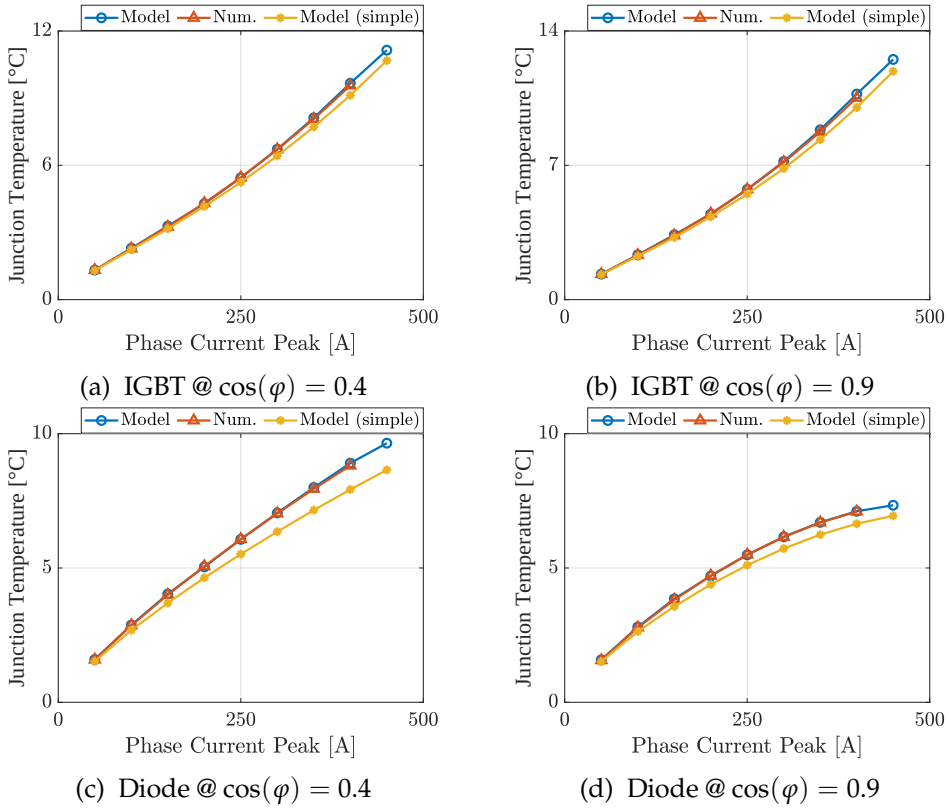

(a) IGBT @ $\cos(\varphi) = 0.4$ (b) IGBT @ $\cos(\varphi) = 0.9$

(c) Diode @ $\cos(\varphi) = 0.4$ (d) Diode @ $\cos(\varphi) = 0.9$

FIGURE 3.17: Comparison of IGBT and diode junction temperature peak-to-peak ripple with SPWM.

3.2.5.2.2 THISPWM

Figure 3.18 show the junction temperatures waveforms of the IGBT and the diode with two different phase current peak values and a power factor of 0.9, considering a THISPWM strategy. As it happened for the MOSFET and diode, there are no appreciable variations with respect to the SPWM strategy and there is a noticeable difference between the simple model and the modified one, which features a good agreement with the numerical model.

Figures 3.19 and 3.20 show the average and the (peak-to-peak) ripple trend with respect to the phase current peak value with two different power factors. As highlighted before, the difference between the modified and the simple model is important, especially when considering the diode junction temperature. On the other hand, the numerical and the modified analytical model are in very good agreement, in particular when considering the temperature ripple.

3.2.6 Experimental Validation

In order to validate the analytical model, an experimental test was carried out using a IGBT power semiconductor. The tests were conducted in collaboration with the Universidad Técnica Federico Santa María (UTFSM), Valparaíso, Chile.

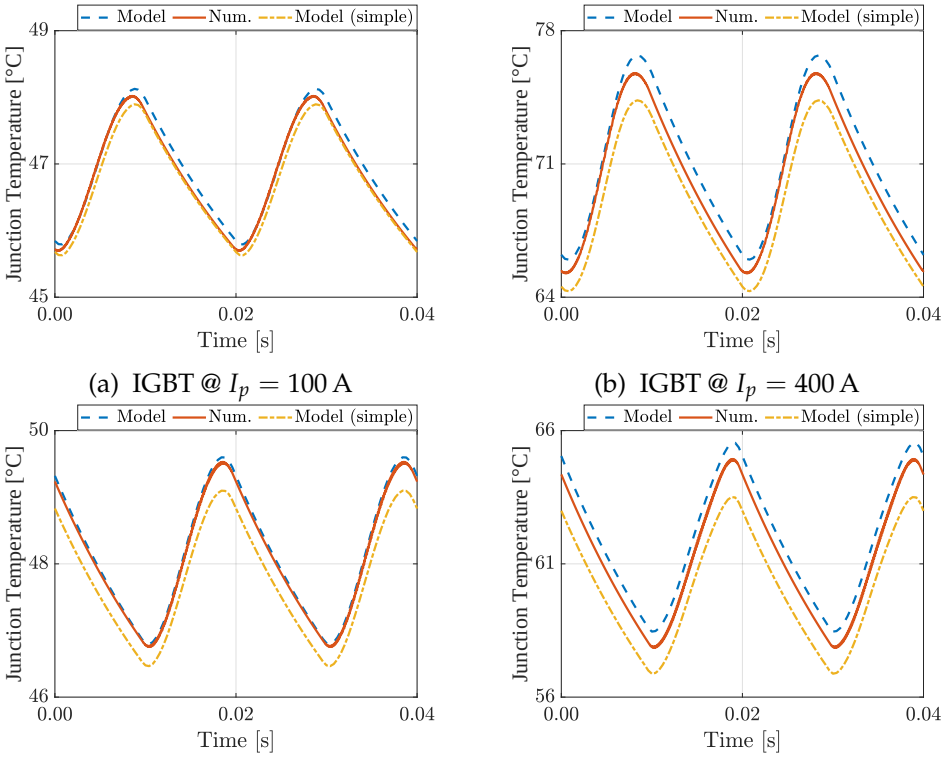

(a) IGBT @ $I_p = 100$ A (b) IGBT @ $I_p = 400$ A

(c) Diode @ $I_p = 100$ A (d) Diode @ $I_p = 400$ A

FIGURE 3.18: Comparison of IGBT and diode junction temperature evolution over time with THISPWM @ $\cos(\varphi) = 0.9$.

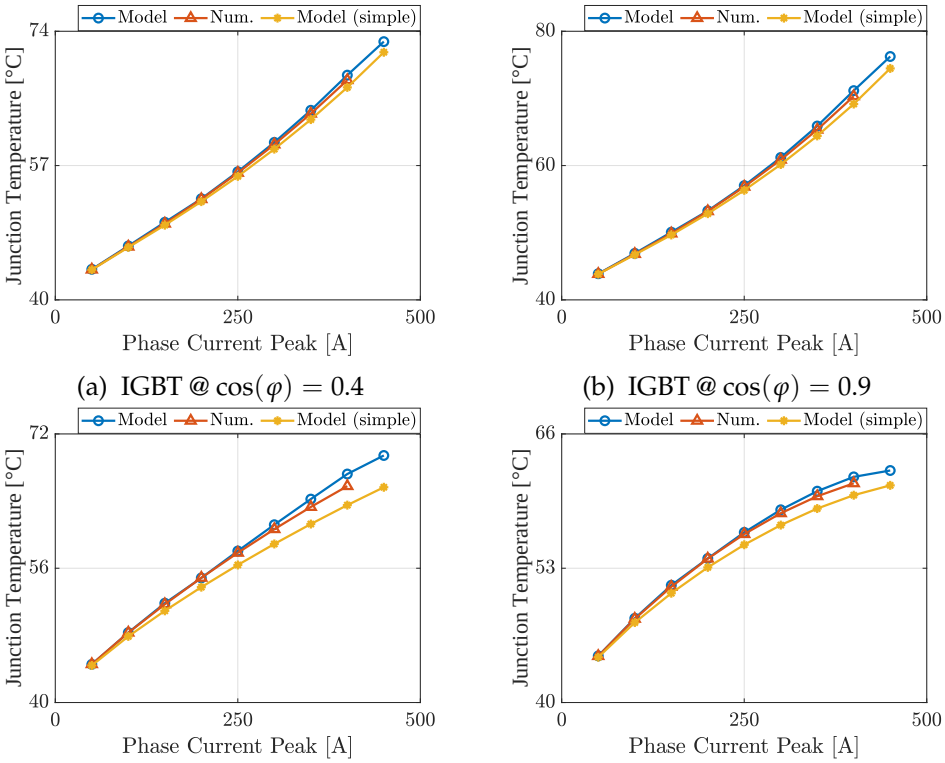

(a) IGBT @ $\cos(\varphi) = 0.4$ (b) IGBT @ $\cos(\varphi) = 0.9$

(c) Diode @ $\cos(\varphi) = 0.4$ (d) Diode @ $\cos(\varphi) = 0.9$

FIGURE 3.19: Comparison of IGBT and diode junction temperature average with THISPWM.

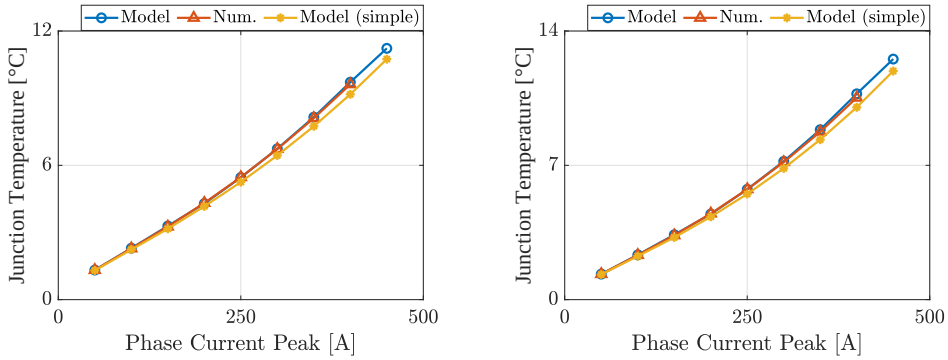

(a) IGBT @ $\cos(\varphi) = 0.4$ (b) IGBT @ $\cos(\varphi) = 0.9$

(c) Diode @ $\cos(\varphi) = 0.4$ (d) Diode @ $\cos(\varphi) = 0.9$

FIGURE 3.20: Comparison of IGBT and diode junction temperature peak-to-peak ripple with THISPWM.

The tests were conducted on a down-scaled laboratory prototype, shown in Figure 3.21. The experimental rig was composed bof a two-level IGBT-based inverter feeding a RL load. The chosen IGBT device is the SK25GH12T4 from Semikron manufacturer. In order to acquire the junction temperature of the power device, a high-performance infrared ImageIR 8300 hp camera and the WD300 microscope lens from Infratech was used. For measuring purposes, one power module was opened and the protector gel was carefully removed. The rest of the passive elements as well as operational parameters are reported in Table 3.6. The system was operated in a closed-loop form by using a dq-frame by using a DSP1103 control platform from dSpace company.

In Figure 3.22 the IGBT transistor junction temperature in two fundamental periods is shown. The measurement were taken with two different modulations: SPWM and THISPWM. The experimental temperature profile features a very good agreement with the analytical and numerical profile with both the strategies, demonstrating the validity of the proposed model.

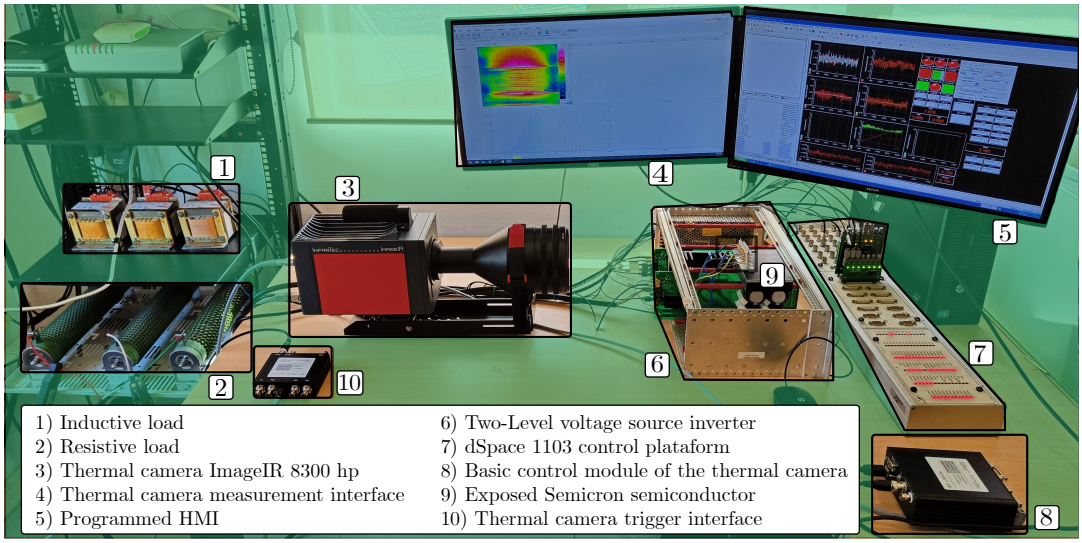

(a) Setup

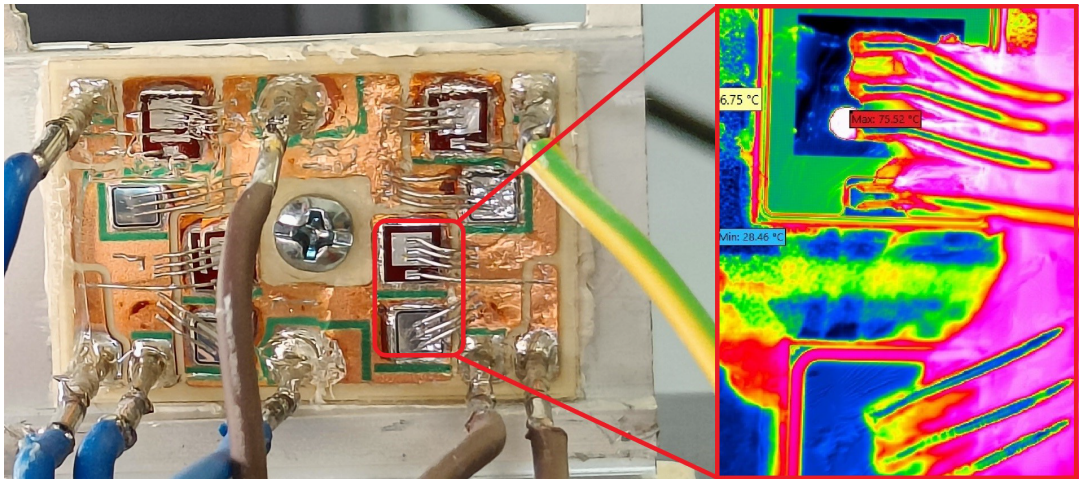

(b) IGBT Semiconductor under study

FIGURE 3.21: Experimental setup used for the thermal analysis of the IGBT semiconductor.

TABLE 3.6: Experimental validation input data.

Power device type	IGBT and diode
Power device name	Semikron SK15GH066
Thermal camera sampling frequency f_{st}	200 Hz
Gate resistance R_g	1 Ω
DC bus voltage v_{DC}	250 V
Switching frequency f_{sw}	10 kHz
Current fundamental frequency f_1	1 Hz
Ambient temperature Θ_{amb}	68.5 °C
Output resistance R_o	10 Ω
Output inductance L_o	15 mH
Output phase current peak I_p	4 A

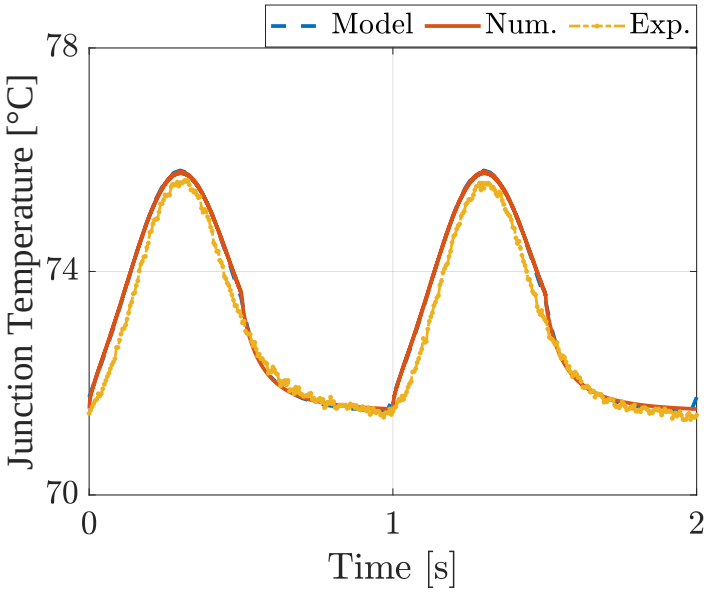

(a) Sinusoidal PWM

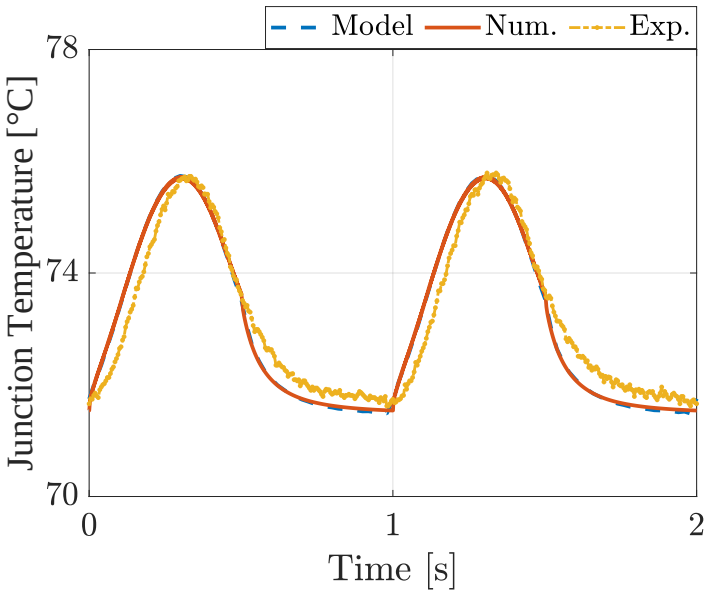

(b) Sinusoidal PWM with third harmonic injection

FIGURE 3.22: IGBT transistor junction temperature evolution in two fundamental periods: comparison between the analytical and numerical model and the experimental measurement.

3.3 Analytical Loss Model of a Buck/Boost Converter

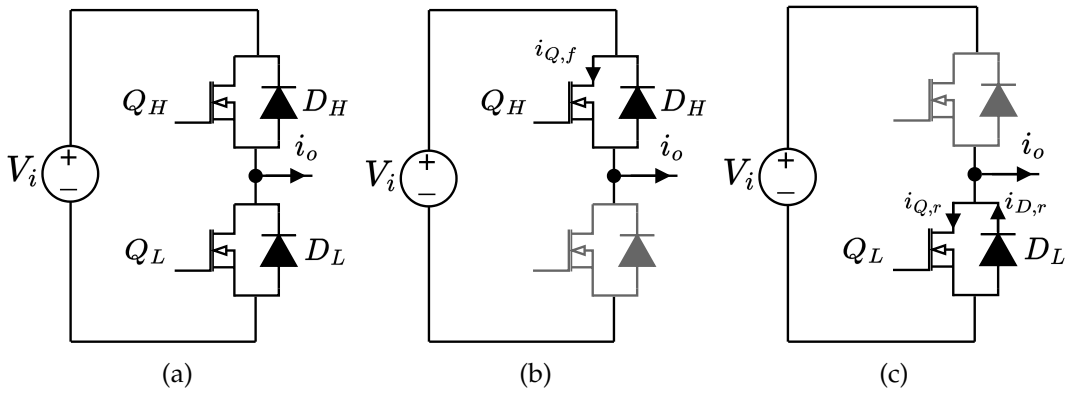

FIGURE 3.23: (a) Half-bridge corresponding to a phase of a buck converter; (b) forward conduction state for a half-bridge converter; (c) reverse conduction state for a half-bridge.

In case of a bi-directional buck/boost converter, the half-bridge circuit of Figure 3.23 is used. Each half-bridge represents a phase of the buck converter and each phase is composed of two switches: each switch features a transistor (Q) and a diode (D). The upper switch is named as H and the lower switch is named as L. Neglecting the ripple given by the switching frequency, the output current i_o is constant therefore the instantaneous conduction losses of one device are constant.

3.3.1 Conduction Losses Model with MOSFET and Diode

Considering the half bridge of Figure 3.23, each switch is composed of a MOSFET and a diode. Two different conduction phases can be observed: the ON phase, when $i_o > 0$, and the OFF phase, when $i_o < 0$. During the ON phase, the upper switch is closed and the lower switch is open. The inductor current $i_o > 0$ hence only the MOSFET conducts and the instantaneous conduction losses on the MOSFET can be expressed as:

$$p_{\mathrm{cQ},f} = v_{Q\mathrm{on}}(i_{Q,f}, \Theta_{\mathrm{JQ}}) i_{Q,f} \tag{3.86}$$

where $i_{Q,f}$ is the MOSFET on-current during the forward phase and it is equal to the output current i_o, $v_{Q\mathrm{on}}$ is the (drain-source) on-voltage, which depends on the $i_{Q,f}$ current and on the MOSFET junction temperature Θ_{JQ}. The average forward conduction losses of the upper MOSFET over one switching period can be calculated as:

$$P_{\mathrm{cQ},f} = \frac{1}{T_{\mathrm{sw}}} \int_0^{m_H T_{\mathrm{sw}} - t_{\mathrm{BT}}} p_{\mathrm{cQ},f}\, dt = (m_H - t_{\mathrm{BT}} f_{\mathrm{sw}}) v_{Q\mathrm{on}}(i_o, \Theta_{\mathrm{JQ}}) i_o \tag{3.87}$$

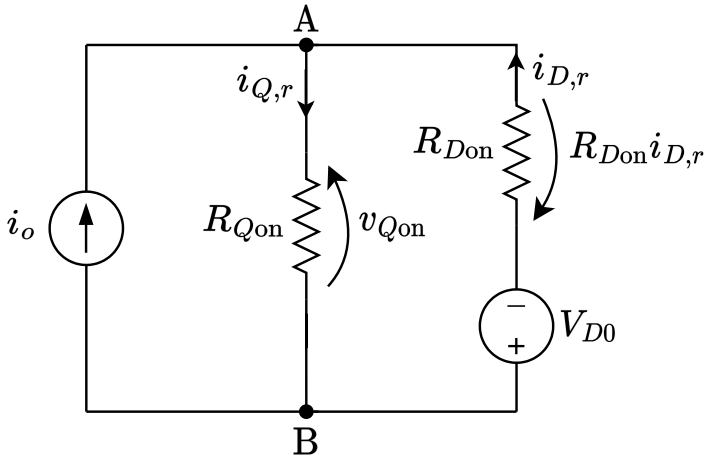

FIGURE 3.24: MOSFET and diode equivalent circuit used to calculate the currents during the reverse phase

where $i_{Q,f} = i_o$, $m_H = T_{\text{on}}/T_{\text{sw}}$ is the duty-cycle of the upper switch, t_{BT} is the dead-time, $T_{\text{sw}} = 1/f_{\text{sw}}$ is the switching period, T_{on} is the upper switch ON time, f_{sw} is the switching frequency.

During the OFF phase, the lower switch is closed and the upper switch is open. The losses of the lower switch must be calculated by considering that the MOSFET and the diode conduct in parallel, since the MOSFET is a reverse-conducting device. However, the parallel conduction happens only if $v_{Q\text{on}} > V_{D0}$, thus only if $i_o > \frac{V_{D0}}{R_{Q\text{on}}}$. The currents on the MOSFET and the diode can be calculated with the circuit of Figure 3.24, which are equal to:

$$\begin{aligned} i_{Q,r} &= -\frac{R_{D\text{on}}}{R_{Q\text{on}} + R_{D\text{on}}} \left(i_o + \frac{V_{D0}}{R_{D\text{on}}} \right) \\ i_{D,r} &= \frac{R_{Q\text{on}}}{R_{Q\text{on}} + R_{D\text{on}}} \left(i_o - \frac{V_{D0}}{R_{D\text{on}}} \right) \end{aligned} \tag{3.88}$$

since i_o is constant, then $i_{Q,r}$ and $i_{D,r}$ are constant. The instantaneous conduction losses can then be defined as:

$$\begin{aligned} p_{\text{c}Q,r} &= v_{Q\text{on}}(i_{Q,r}, \Theta_{\text{J}Q}) i_{Q,r} \\ p_{\text{c}D,r} &= v_{D\text{on}}(i_{D,r}, \Theta_{\text{J}D}) i_{D,r} \end{aligned} \tag{3.89}$$

where $v_{D\text{on}}$ is the diode on-voltage, which depends on the diode current and junction temperature. The average conduction losses are then equal to:

$$\begin{aligned} P_{\text{c}Q,r} &= \frac{1}{T_{\text{sw}}} \int_0^{(1-m_H)T_{\text{sw}} - t_{\text{BT}}} p_{\text{c}Q,r} \, dt \\ &= (1 - m_H - t_{\text{BT}} f_{\text{sw}}) v_{Q\text{on}}(i_{Q,r}, \Theta_{\text{J}Q}) i_{Q,r} \\ P_{\text{c}D,r} &= \frac{1}{T_{\text{sw}}} \int_0^{(1-m_H)T_{\text{sw}} - t_{\text{BT}}} p_{c,D} \, dt \\ &= (1 - m_H - t_{\text{BT}} f_{\text{sw}}) v_{D\text{on}}(i_D, \Theta_{\text{J}}) i_{D,r} \end{aligned} \tag{3.90}$$

where $(1 - m_H)T_{\text{sw}} - t_{\text{BT}}$ is the OFF time, i.e. how much the lower switch is closed. During the dead-time, only the diode conducts and it is subjected to additional conduction losses which can be calculated as:

$$P_{\text{c}D,0} = 2t_{\text{BT}} f_{\text{sw}} v_{D\text{on}}(i_o, \Theta_{\text{J}D}) i_o \tag{3.91}$$

For both the IGBT and the diode, the on-voltage can be expressed in the form of a 2-D lookup table, $v_{\text{on}} = f(i_{\text{on}}, \Theta_{\text{J}})$, where the variables are the on-current and the junction temperature. In this way, the losses calculation is more accurate since the variation of the on-voltages with respect to the devices on-current is taken into account.

3.3.2 Conduction Losses Model with IGBT and Diode

Considering the half bridge of Figure 3.23, each switch is composed of a IGBT and a diode. Two different conduction phases can be observed: the ON phase, when $i_o > 0$, and the OFF phase, when $i_o < 0$. The difference with respect to the MOSFET is that during the OFF phase the IGBT does not conduct and therefore all the reverse current flows through the diode. During the ON phase, the upper switch is closed and the lower switch is open. Since $i_o > 0$ only the IGBT conducts and the instantaneous conduction losses can be expressed as:

$$p_{\text{c}Q,f} = v_{Q\text{on}}(i_{Q,f}, \Theta_{\text{J}Q}) i_{Q,f} \tag{3.92}$$

where $i_{Q,f}$ is the IGBT on-current during the forward phase and it is equal to the output current i_o, $v_{Q\text{on}}$ is the (collector-emitter) on-voltage, which depends on the $i_{Q,f}$ current and on the IGBT junction temperature $\Theta_{\text{J}Q}$. The average forward conduction losses of the upper IGBT over one switching period can thus be calculated as:

$$P_{\text{c}Q,f} = \frac{1}{T_{\text{sw}}} \int_0^{m_H T_{\text{sw}} - t_{\text{BT}}} p_{\text{c}Q,f}\, dt = (m_H - t_{\text{BT}} f_{\text{sw}}) v_{Q\text{on}}(i_o, \Theta_{\text{J}Q}) i_o \tag{3.93}$$

where $m_H = T_{\text{on}}/T_{\text{sw}}$ is the duty-cycle of the upper switch, t_{BT} is the (blanking) dead-time, $T_{\text{sw}} = 1/f_{\text{sw}}$ is the switching period, T_{on} is the upper switch ON time, f_{sw} is the switching frequency.

During the OFF phase, the lower switch is closed and the upper switch is open. The losses of the lower switch are calculated by considering that only the diode conducts, since the IGBT is not a reverse-conducting device. Therefore, the instantaneous losses on the diode can be calculated by considering that all the output current flows through the diode itself:

$$p_{\text{c}D,r} = v_{D\text{on}}(i_{D,r}, \Theta_{\text{J}D}) i_{D,r} \tag{3.94}$$

the average losses are then equal to:

$$\begin{aligned} P_{\text{c}D,r} &= \frac{1}{T_{\text{sw}}} \int_0^{(1-m_H)T_{\text{sw}} - t_{\text{BT}}} p_{\text{c}D,r}\, dt \\ &= (1 - m_H - t_{\text{BT}} f_{\text{sw}}) v_{D\text{on}}(i_o, \Theta_{\text{J}}) i_o \end{aligned} \tag{3.95}$$

where $i_{D,r} = i_o$ and $(1 - m_H)T_{\text{sw}} - t_{\text{BT}}$ is the OFF time, i.e. how much the lower switch is closed. During the dead-time, only the diode conducts and it is subjected to additional conduction losses which can be calculated as:

$$P_{\text{c}D,0} = 2t_{\text{BT}} f_{\text{sw}} v_{D\text{on}}(i_o, \Theta_{\text{J}D}) i_o \tag{3.96}$$

For both the IGBT and the diode, the on-voltage can be expressed in the form of a 2-D lookup table, $v_{\text{on}} = f(i_{\text{on}}, \Theta_{\text{J}})$, where the variables are the on-current and the junction temperature. In this way, the losses calculation is more accurate since the variation of the on-voltages with respect to the devices on-current is taken into account.

3.3.3 Switching Losses Model

The switching losses for the buck/boost converter are calculated in a similar way as the method used for the 2L-VSI. If $i_o > 0$, the upper transistor works in hard switching and it is subjected to the whole output current while the lower transistor works in zero voltage switching (ZVS) hence its switching losses are zero. Vice versa, if $i_o < 0$, the lower transistor works in hard switching, and it is subjected to the whole output current, while the upper transistor works in ZVS. The diode switching losses are given by the reverse recovery phenomenon which happens at every switching period because of the dead-time.

The switching losses are obtained by multiplying the switching energies by the switching frequency f_{sw}. The switching energies can be obtained by interpolating the multi-dimensional lookup tables by considering the output current i_o along with the junction temperature Θ_{J}, the gate resistance R_g and the input voltage V_i:

$$P_{\text{sw}Q}(i_o, R_g, \Theta_{\text{J}Q}, V_i) = f_{\text{sw}} \Big[E_{\text{on}Q} + E_{\text{off}Q} \Big] \tag{3.97}$$

$$P_{\text{sw}D}(i_o, R_g, \Theta_{\text{J}D}, V_i) = f_{\text{sw}} E_{\text{rr}D} \tag{3.98}$$

where $E_{\text{on}Q} = f(i_o, R_g, \Theta_{\text{J}Q}, V_i)$ and $E_{\text{off}Q} = f(i_o, R_g, \Theta_{\text{J}Q}, V_i)$ are the transistor on-energy and off-energy respectively, while $E_{\text{rr}D} = f(i_o, R_g, \Theta_{\text{J}D}, V_i)$ is the diode reverse recovery energy.

3.4 Thermal Analysis of an Active Rectifier for a Vehicle Fast Charger

The proposed analytical model was used to build the model of a vehicle fast charging station. The aim was to estimate the thermal behavior of the charger, taking into account a full charging event of a Battery Electric Vehicle (BEV) with different charging strategies, by also considering the temperature ripple at the grid frequency.

The proposed fast charger is based on the commercial solution of ABB Terra HP150, Figure 3.25, which is characterized by three identical modules: each module features a power rating of 50 kW and is composed of a three-phase active rectifier and three-phase bi-directional buck/boost converters. All the modules are connected in parallel to the AC grid on the rectifier side, while are connected in parallel to the vehicle battery on the buck/boost converter side. The active rectifier thermal model was built by using the proposed solution in 3.2, while the buck/boost converter was modeled with the solution presented in 3.3. Taking the information about the thermal behavior of the power devices of the EV fast charger, the main target of these simulations was to calculate the cumulative damage in the power devices of the three-phase active rectifier. In fact, due to the grid frequency temperature ripple, the rectifier's devices are the most critical components of the fast charger from the maintenance point of view.

3.4.1 Model of the Three-Phase Grid and Active Rectifier

In the considered BEV fast charger, the active rectifier and the bi-directional buck/boost converters are connected to a common DC-link. The rectifier is used to manage the power flow from the grid with the aim of keeping the DC bus voltage fixed to a given value. The DC bus voltage depends on the dynamics across the capacitor, which in turns depends on the power requested by the vehicle battery charger.

In order to speed up the simulation, it is necessary to avoid the variation of the main electrical variables (currents, voltages, duty-cycles) at the fundamental phase current frequency. For this reason the three-phase grid was modeled in a stationary dq reference frame. From Figure 3.27 the grid phase

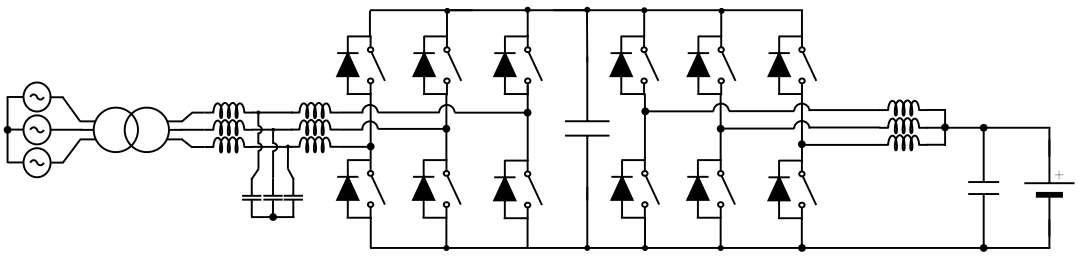

FIGURE 3.25: Electric scheme of one module of the ABB Terra HP 150 fast charger.

equations can be written as:

$$\begin{bmatrix} v_{ga} \\ v_{gb} \\ v_{gc} \end{bmatrix} = -R_g \begin{bmatrix} i_{ga} \\ i_{gb} \\ i_{gc} \end{bmatrix} - L_g \frac{d}{dt} \begin{bmatrix} i_{ga} \\ i_{gb} \\ i_{gc} \end{bmatrix} + \begin{bmatrix} e_{ga} \\ e_{gb} \\ e_{gc} \end{bmatrix} \tag{3.99}$$

which can be written in a compact form as:

$$\mathbf{v}_g = -R_g \mathbf{i}_g - L_g \frac{d\mathbf{i}_g}{dt} + \mathbf{e}_g \tag{3.100}$$

where:

$$\mathbf{v}_g = \begin{bmatrix} v_{ga} \\ v_{gb} \\ v_{gc} \end{bmatrix}, \quad \mathbf{i}_g = \begin{bmatrix} i_{ga} \\ i_{gb} \\ i_{gc} \end{bmatrix}, \quad \mathbf{e}_g = \begin{bmatrix} e_{ga} \\ e_{gb} \\ e_{gc} \end{bmatrix} \tag{3.101}$$

are the phase voltages at the grid terminals, the phase currents and the grid electromotive forces (EMFs), which can be written as:

$$\mathbf{e}_g = E_g \begin{bmatrix} \cos(\theta_g) \\ \cos(\theta_g - \frac{2\pi}{3}) \\ \cos(\theta_g + \frac{2\pi}{3}) \end{bmatrix} \tag{3.102}$$

the term E_g represents the peak value of grid electromotive force, which is calculated as $E_g = \sqrt{2}/\sqrt{3} E_{gLL\text{rms}}$, where $E_{gLL\text{rms}}$ is the grid line-to-line voltage rms value.

By introducing the $abc \rightarrow dq$ Park transform matrix (neglecting the homopolar component), and assuming that the d axis is synchronous with the e_{ga}, Figure 3.28:

$$\mathbf{P} = \frac{2}{3} \begin{bmatrix} \cos(\theta_g) & \cos(\theta_g - \frac{2\pi}{3}) & \cos(\theta_g + \frac{2\pi}{3}) \\ -\sin(\theta_g) & -\sin(\theta_g - \frac{2\pi}{3}) & -\sin(\theta_g + \frac{2\pi}{3}) \end{bmatrix} \tag{3.103}$$

TABLE 3.7: Fast charger general data.

Ambient temperature	40 °C
DC bus capacitance	5.0 m F
DC bus voltage	600 V
Rectifier modulation strategy	THISPWM
Grid line-to-line voltage $E_{gLL\text{rms}}$	400 V_{rms}
Grid inductance (secondary transformer side) L_g	1.0 mH
Grid resistance (secondary transformer side) R_g	200 m Ω
Grid frequency f_g	50 Hz

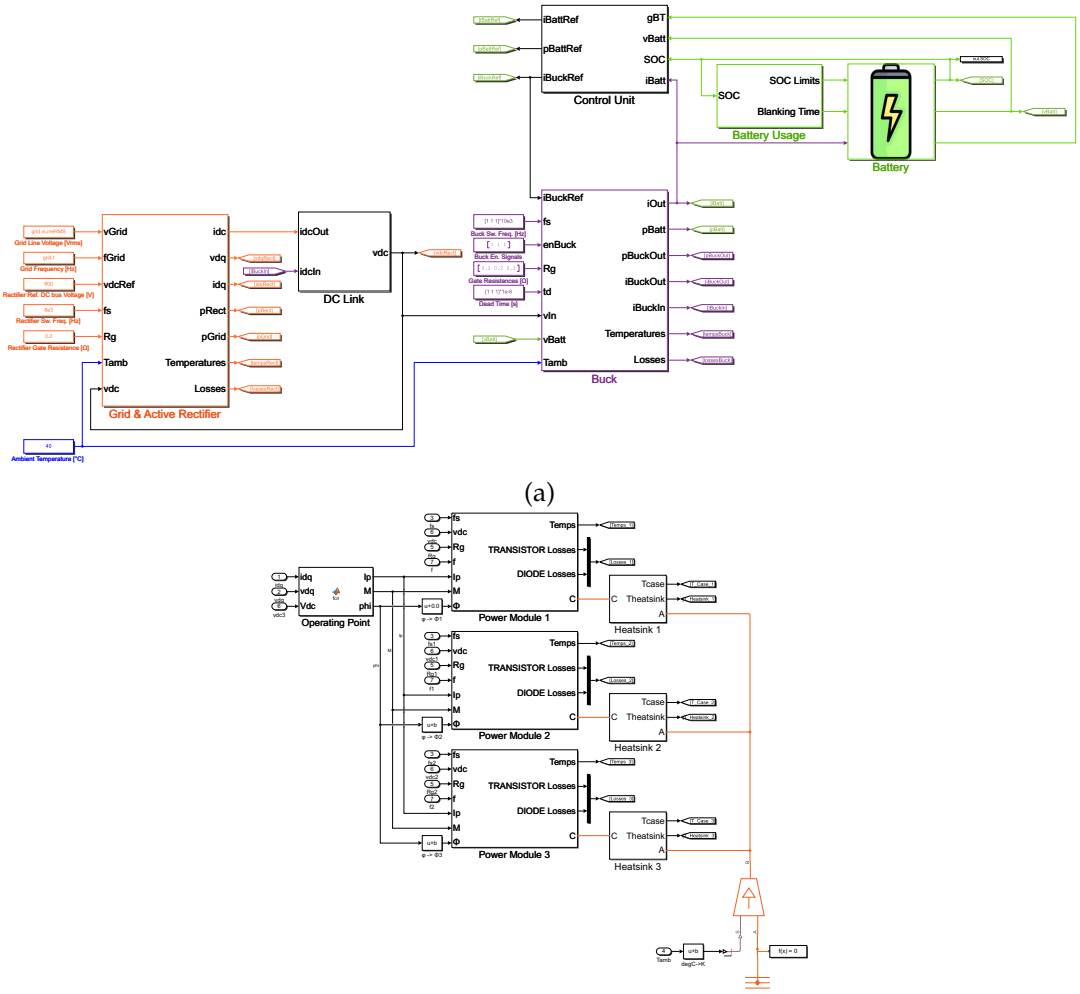

FIGURE 3.26: Overview of the Simulink scheme of the (a) fast-charger with a three-phase active rectifier connected to a grid, a bi-directional buck/boost converter and the vehicle battery and (b) detail of the active rectifier thermal model.

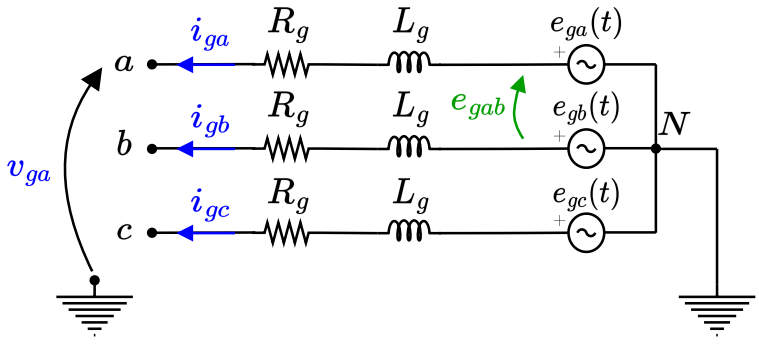

FIGURE 3.27: Electric scheme of a three-phase grid.

where $\theta_g = \int \omega_g dt$ is the d-axis position with respect to e_{ga}, the following anti-transformation can be defined:

$$\begin{aligned} \mathbf{v}_g &= \mathbf{P}^{-1}\mathbf{v}_{gdq} \\ \mathbf{i}_g &= \mathbf{P}^{-1}\mathbf{i}_{gdq} \\ \mathbf{e}_g &= \mathbf{P}^{-1}\mathbf{e}_{gdq} \end{aligned} \tag{3.104}$$

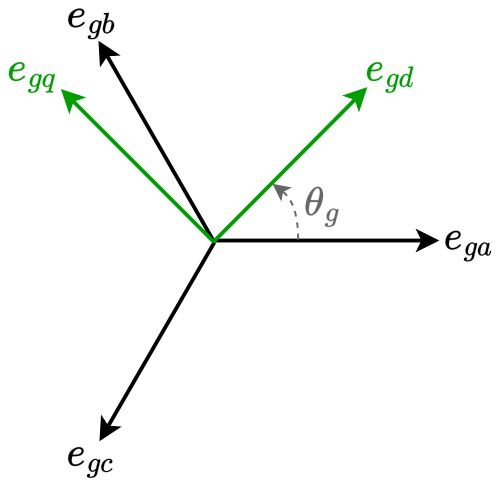

FIGURE 3.28: Visual representation of the grid $abc \rightarrow dq$ Park transform.

where:

$$\mathbf{P}^{-1} = \begin{bmatrix} \cos(\theta_g) & -\sin(\theta_g) \\ \cos(\theta_g - \frac{2\pi}{3}) & -\sin(\theta_g - \frac{2\pi}{3}) \\ \cos(\theta_g + \frac{2\pi}{3}) & -\sin(\theta_g + \frac{2\pi}{3}) \end{bmatrix} \tag{3.105}$$

and:

$$\mathbf{v}_{gdq} = \begin{bmatrix} v_{gd} \\ v_{gq} \end{bmatrix}, \quad \mathbf{i}_{gdq} = \begin{bmatrix} i_{gd} \\ i_{gq} \end{bmatrix}, \quad \mathbf{e}_{gdq} = \begin{bmatrix} e_{gd} \\ e_{gq} \end{bmatrix} \tag{3.106}$$

by remembering the (3.102), the grid electromotive forces in the dq frame become:

$$\mathbf{e}_{gdq} = \begin{bmatrix} E_g \\ 0 \end{bmatrix} \tag{3.107}$$

By introducing the (3.104) into the (3.100) yields to:

$$\mathbf{P}^{-1}\mathbf{v}_{gdq} = -R_g\mathbf{P}^{-1}\mathbf{i}_{gdq} - L_g\frac{d}{dt}[\mathbf{P}^{-1}\mathbf{i}_{gdq}] + \mathbf{P}^{-1}\mathbf{e}_{gdq} \tag{3.108}$$

by multiplying both sides of the (3.108) by the Park matrix yields to:

$$\mathbf{v}_{gdq} = -R_g\mathbf{i}_{gdq} - L_g\frac{d\mathbf{i}_{gdq}}{dt} - \mathbf{T}L_g\mathbf{i}_{gdq} + \mathbf{e}_{gdq} \tag{3.109}$$

where:

$$\mathbf{T} = \mathbf{P}\frac{d}{dt}[\mathbf{P}^{-1}] = \begin{bmatrix} 0 & -\omega_g \\ \omega_g & 0 \end{bmatrix} \tag{3.110}$$

By expanding the (3.109) and introducing the (3.107) one obtains:

$$\begin{bmatrix} v_{gd} \\ v_{gq} \end{bmatrix} = -\begin{bmatrix} R_g & -\omega_g L_g \\ \omega_g L_g & R_g \end{bmatrix}\begin{bmatrix} i_{gd} \\ i_{gq} \end{bmatrix} - L_g\frac{d}{dt}\begin{bmatrix} i_{gd} \\ i_{gq} \end{bmatrix} + \begin{bmatrix} E_g \\ 0 \end{bmatrix} \tag{3.111}$$

TABLE 3.8: Active rectifier and buck/boost data for one fast charger module.

	Rectifier	Buck/Boost
Type of power device	Half-bridge power module	
Power device manufacturer and part no.	ROHM BSM400D12P2G003	
Number of devices in parallel	1	
Gate resistance	0.2 m Ω	
Switching frequency	10 kHz	
Input voltage	600 V	
Dead-time	1 µs	
Output inductance	1.0 mH	3.0 mH
Output resistance	200 m Ω	
Heatsink thermal capacitance	921 J K^{-1}	
Case-to-heatsink thermal resistance	35 m K W^{-1}	
Heatsink-to-ambient thermal resistance	150 m K W^{-1}	

In steady-state, by considering a balanced three-phase system with sinusoidal phase currents, the v_{gdq} voltages and the i_{gdq} currents are constant in the dq reference frame. The balanced operation is assured if a balanced three-phase load is considered, the sinusoidal profile is obtained if the converter operates in the linear modulation region and the switching frequency is high enough to neglect the PWM current ripple.

In the proposed fast charger model, the rectifier is connected to a low voltage AC grid, simulating the connection to the secondary side of the transformer which is in turn connected to a medium voltage grid. Since the grid is modeled in a stationary dq reference frame, the model of the three-phase active rectifier must be converted to an equivalent dq model. This can be done by considering that each axis of the dq grid reference frame is supplied by a full-bridge converter, in order to control the dq currents injected into the grid, i_{gdq}. The voltage limits in dq frame are then modified in order to stay within the phase voltage limit in the three-phase system for the chosen modulation strategy. For example, if a Sinusoidal PWM with Third Harmonic Injection (THISPWM) strategy is chosen, the phase voltage limit is equal to $v_{DC}/\sqrt{3}$. Therefore the PI limits with the anti-windup strategy are arranged so that the maximum modulation index would be equal to $1\sqrt{3}$.

3.4.2 Cumulative Damage of a Power Device

Power devices usually represent the most critical component in the converter lifetime. Failure happening in the power devices are mainly given by two type of phenomena: bond-wire lift-off and die solder cracking. In Figure 3.29 a 2-D cross-section view of a power module is shown. The failure phenomena are mainly due by the thermal stress, which in turn causes a mechanical stress in the junction (expansion and retraction) aggravated by the fact that different materials, with different thermal expansion coefficients, can be

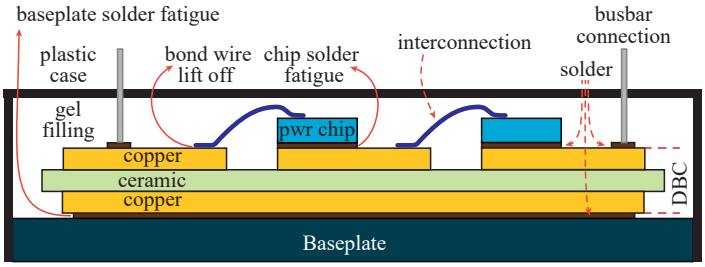

FIGURE 3.29: Cross section scheme of a conventional power module.

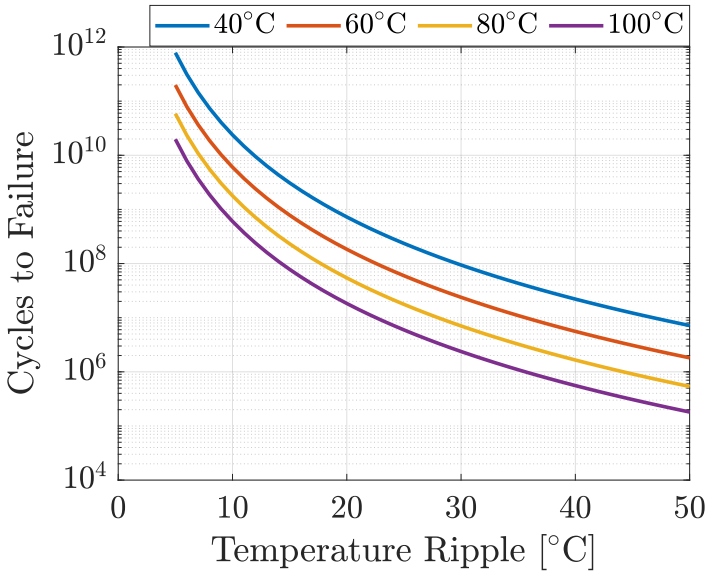

FIGURE 3.30: Number of cycles to failure evolution over temperature ripple for different temperatures with the Semikron lifetime model.

found in this part of the device. In the end, a repetitive thermal waving, due to the swing of the junction temperature, causes the power device to fail after a certain number of cycles. The estimation of the number of cycles the device can undergo before the failure happens is not easy and different models can be found in literature.

For example, according to [76], the damage estimation in power electronics devices is obtained by adopting a modified version of the Arrhenius lifetime model, in which the term reaction rate N_f defines the number of cycles before the device fails. This model defines the damage as a function of the average and the peak-to-peak junction temperature of the power device, and it can be expressed as:

$$N_f = A \cdot \left(\widetilde{\Theta}_{\mathrm{J}}\right)^{-\alpha} \cdot e^{\left(\frac{E_a}{k_B \overline{\Theta}_{\mathrm{J}}}\right)} \tag{3.112}$$

where A, α are two constant and depend on the device, E_a is the activation energy in joule, which defines the least amount of energy required to start the reaction and it is independent from the temperature, finally $k_B =$

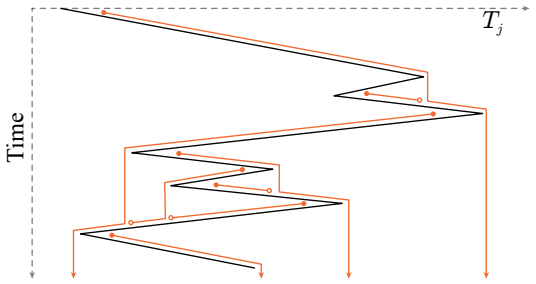

FIGURE 3.31: An example of the rainflow counting algorithm.

$1.38 \cdot 10^{-23} \mathrm{J\,K^{-1}}$ is the Boltzmann constant. The terms $\widetilde{\Theta}_\mathrm{J}, \overline{\Theta}_\mathrm{J}$ are the junction temperature ripple and the average temperature, respectively. As the (3.112) shows, the damage is tied to the average temperature with an exponential law: the higher is the average temperature and the lower is the number of cycles the device can sustain before the failure. On the other hand, also the temperature ripple plays a fundamental role and reduces the device lifetime, since the exponent of the equation is negative. Figure 3.30 shows the number of cycles to failure with respect to the temperature ripple for different temperatures at rated voltage. The figure clearly shows that the temperature has a huge impact on the lifetime of the device, which reduces by approximately 4 orders of magnitude when the ripple passes from 10 °C to 50 °C. For the same ripple, when the average temperature changes from 40 °C to 80 °C, the devices lifetime is reduced by approximately 2 orders of magnitude.

In the case of the fast charger model, the cumulative damage of the active rectifier was calculated in the following way:

1. the temperature vector, including the peak-to-peak ripple, is acquired;
2. by means of an already available rainflow algorithm, developed by the Power Electronics Group in Seville, the number of events with a certain temperature average and temperature ripple is calculated. Hence, for each k-th even the rainflow provides: the number of repetitions M_k of that event and the corresponding average temperature value and peak-to-peak ripple;
3. the model of (3.112) is applied to each event, to calculate the number of cycles to failure $N_{f,k}$ due to that event;
4. the damage of the k-th event D_k is calculated by dividing the number of repetitions M_k by $N_{f,k}$;
5. the total damage in the device D is calculated by summing the damages of each event.

In order to obtain realistic values for A and α, the lifetime model was implemented by using the data provided by Semikron for an IGBT power device. However, even if the considered fast charger features a SiC-MOSFET rectifier, since the aim of this work is to compare the different charging strategies, the absolute damage values are not considered, but normalized with respect to one specific strategy.

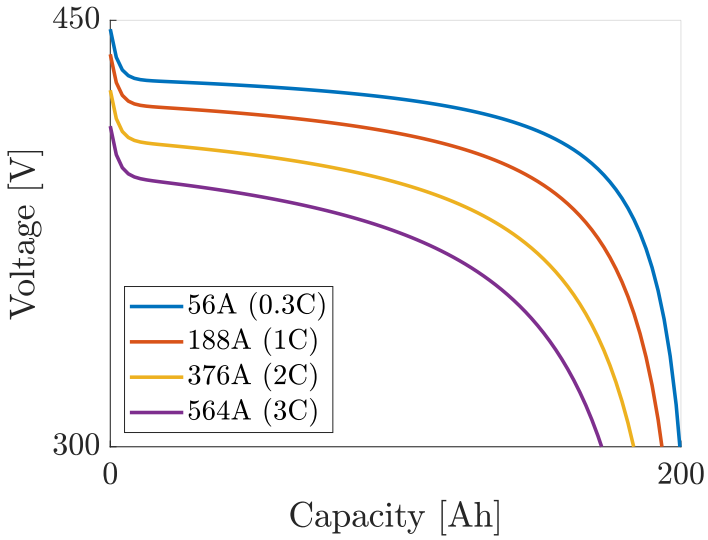

FIGURE 3.32: Battery pack voltage-capacity curve analyzed at different discharge rates. The lower level represents the cut-off voltage, the upper level the maximum voltage.

3.4.3 Analysis of Different Charging Strategies

In order to analyze the fast charger behavior and the corresponding cumulative damage in the active rectifier devices, one charging event of a sample vehicle battery was analyzed. The simulation scenario considered to analyze the converter behavior by considering different charging strategies of different car models and manufacturers, Figure 3.33. The charging power profiles were normalized with respect to the fast charger maximum output power, namely 100 kW, in order to compare them in the same conditions. Table 3.7 summarizes the general data of the fast charger model used for the simulations, while in Table 3.8 the active rectifier and the buck/boost data is presented. The battery was modeled by using the Simulink built-in block, and it was based on the Samsung SDI 94Ah cell, whose data obtained from [77], and listed in Table 3.9(a), while the battery pack data is summarized in Table 3.9(b). Figure 3.32 shows the battery pack curve with different discharge rates: it is clear that the higher is the discharge current and the lower is the total pack capacity.

Figure 3.34 shows the junction temperature evolution over the battery SoC, in the IGBT and the diode, considering one charging event with the different charging strategies presented. All the temperature profiles are characterized by the peak-to-peak ripple superimposed to the average temperature curve. For all the strategies, the maximum temperature is below 100 °C: the least stress charging strategy appears to be the Polestar 2, with a maximum temperature of 80 °C followed by rapid decline until the ambient temperature is reached, in about 60 minutes, Figure 3.34(f). The Porsche Taycan strategy, Figure 3.34(g) shows a similar behavior as well as the Peugeot e-208, Figure 3.34(e).

Figure 3.35 shows the comparison of the cumulative damage in the IGBT and the diode by taking into account the different charging strategies. The

TABLE 3.9: Battery cell and pack data used for the simulations.

(a) Cell

Part no.	Samsung SDI94
Maximum voltage	4.15 V
Rated voltage	3.68 V
Cut-off voltage	2.70 V
Rated capacity	94 A h
Maximum capacity	100 A h
Rated current	31 A (0.3C)
Internal resistance	0.000 73 Ω

(b) Pack

Cells in series	108
Parallel strings	2
Rated voltage	397 V
Cut-off voltage	292 V
Rated capacity	188 A h
Rated energy	75 kW h
Maximum power	100 kW
Maximum current	375 A (2C)

damage of both the IGBT and the diode is normalized with respect to the IGBT damage obtained with the Audi e-tron charging strategy (damage equal to 100 %). It is worth to notice that the amount of damage in the diode is lower with respect to the IGBT. The main result is that the best charging strategy in terms of cumulative damage in both the transistor and the diode appears to be the strategy of the Polestar 2, followed by the Peugeot e-208 and the Porsche Taycan, even if by a very large margin. On the other hand, the other charging curves do not differ very much, with the Volkswagen ID.4 causing the highest transistor damage while the Hyundai Kona the highest diode damage, followed by Audi. This result shows that even if the Audi strategy causes the devices to stay at a very high temperature for a long SoC range, the temperature swing consequent of the Volkswagen strategy causes a noticeable damage. On the other hand, the progressive reduction of the charging power (like in the Polestar 2, Porsche Taycan and Peugeot e-208) produces a progressive reduction of the devices temperature, thus limiting the damage.

Another important fact that should be highlighted is the temperature ripple hugely increase the damage, even if the peak-to-peak value is limited, as shown in Figure 3.35(b-d). This underlines the importance of taking into account the temperature swing at the current frequency to have a more reliable lifetime model of a power device.

By the analysis carried out, it was found that the amount of damage in the devices is strictly tied to the type of charging strategy used, since they have a significant impact on the junction temperature profile. On the other hand, each charging strategy also defines the amount of time to recharge the battery. To this end, Figure 3.36 shows that the Polestar 2 needs the highest time to charge the vehicle battery from a 10% to a 90% battery SoC, followed by the Porsche Taycan, while the Audi e-tron features the lowest charging time, followed by the Mercedes EQV. Therefore, it seems to be a relation between the charging time and the damage caused in the power device: the lower is the charging time and the higher is the rms power in one charging cycle, enabling higher losses and temperatures in the device and a consequent bigger damage.

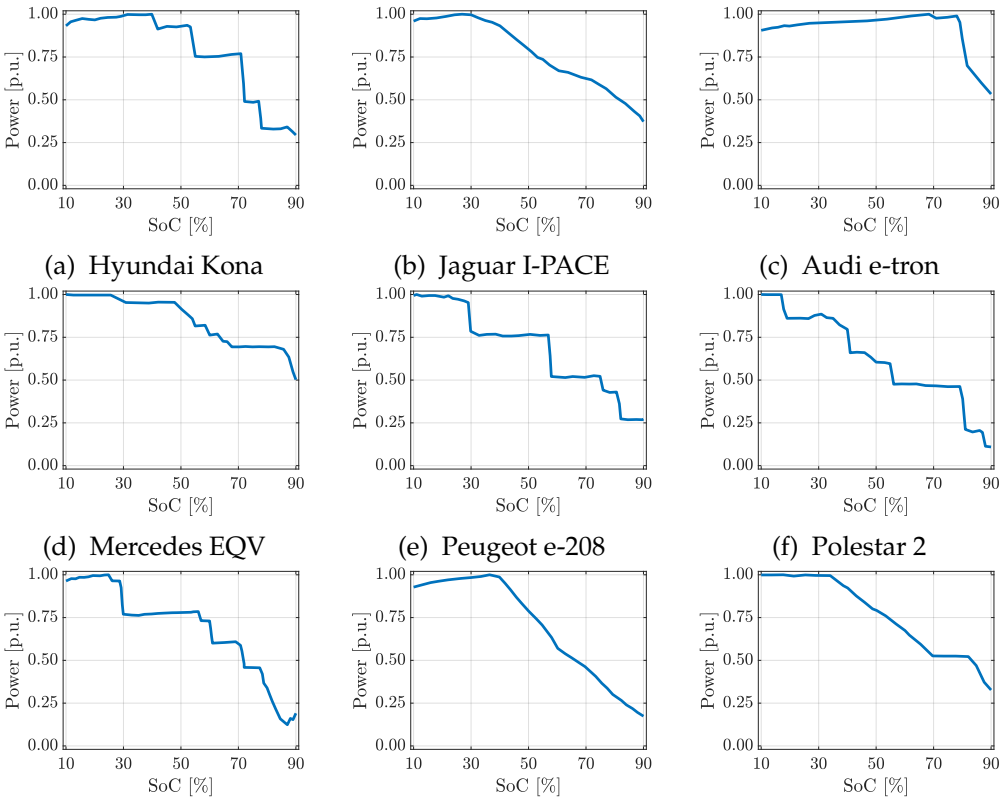

(a) Hyundai Kona (b) Jaguar I-PACE (c) Audi e-tron

(d) Mercedes EQV (e) Peugeot e-208 (f) Polestar 2

(g) Porsche Taycan (h) Tesla Model 3 LR (i) Volkswagen ID.4

FIGURE 3.33: Battery charging power (in p.u.) over SoC.

The proposed fast charger model made possible the analysis of the different charging strategies within a few minutes using the workstation of Table 3.10, on the other hand if the thermal analysis was conducted by using PLECS, the amount of time needed to run the thermal simulations would have been very large, up to some days for each charging event (by using the same workstation).

As an example of the analytical model simulation capabilities in terms of speed, in Figure 3.37 the scenario of one full month of the fast charging operation is presented. The figure is just a quick representation of the possible analysis scenarios which could be carried out by using this tool. As an example, in this simulation, for each day the number of charging events was randomly generated and, for each charging event, the initial and final SoC,

TABLE 3.10: Specifications of the workstation used for the simulations.

CPU	AMD Ryzen 7 5800H 3.2 GHz
GPU	NVIDIA GeForce RTX 3080 Laptop GPU
Storage	SAMSUNG MZVLB1T0HBLR-000L2
Motherboard	Lenovo LNVNB161216
Memory	Kingston 32GB (2x16GB) 2666MHz DDR4 CL15
Operating system	Windows 11 Pro

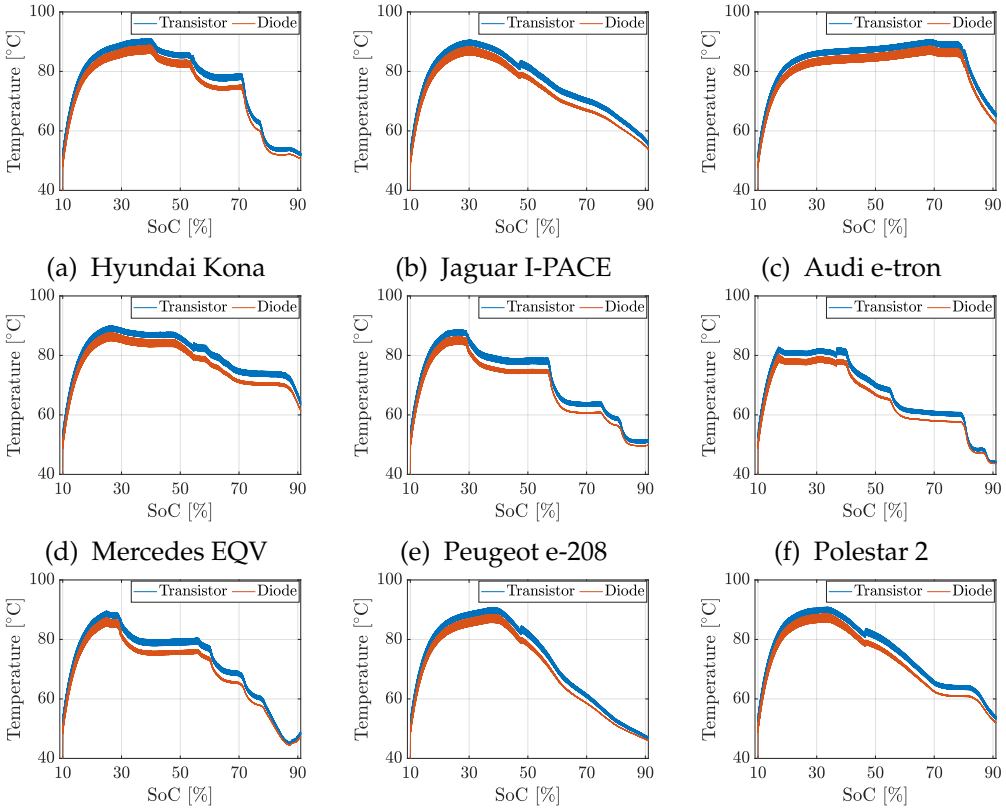

(a) Hyundai Kona (b) Jaguar I-PACE (c) Audi e-tron

(d) Mercedes EQV (e) Peugeot e-208 (f) Polestar 2

(g) Porsche Taycan (h) Tesla Model 3 LR (i) Volkswagen ID.4

FIGURE 3.34: IGBT and diode temperature over SoC.

TABLE 3.11: Execution times (average after 10 runs) of the fast charger model to obtain the temperature profile with ripple.

Simulated Period	**Simulink**	**Post-Processing**	**Total**
1 hour	13 s	16 s	28 s
2 hours	13 s	33 s	46 s
3 hours	13 s	48 s	61 s

the charging strategy, and the time period between two different charging events were randomly generated too. Finally, also the ambient temperature was randomly modified within the range 30 °C - 45 °C to simulate different conditions. From the figure it can be seen how the different charging events impact on the bi-directional buck/boost converter and on the active rectifier in a different way. Indeed, the rectifier's devices are subjected to a higher thermal stress, with a peak temperature of approximately 90 °C, while the buck's IGBT reach a maximum temperature of approximately 60 °C.

In the end, Table 3.11 summarizes the time necessary to run the fast charger model with different simulated times, including also the post-processing script to obtain the full junction temperature profile. The table shows that the post-processing script needs much more time to be executed with respect to the Simulink model, since it increases linearly with the number of hours simulated. However, since the script allows to provide an accurate profile of

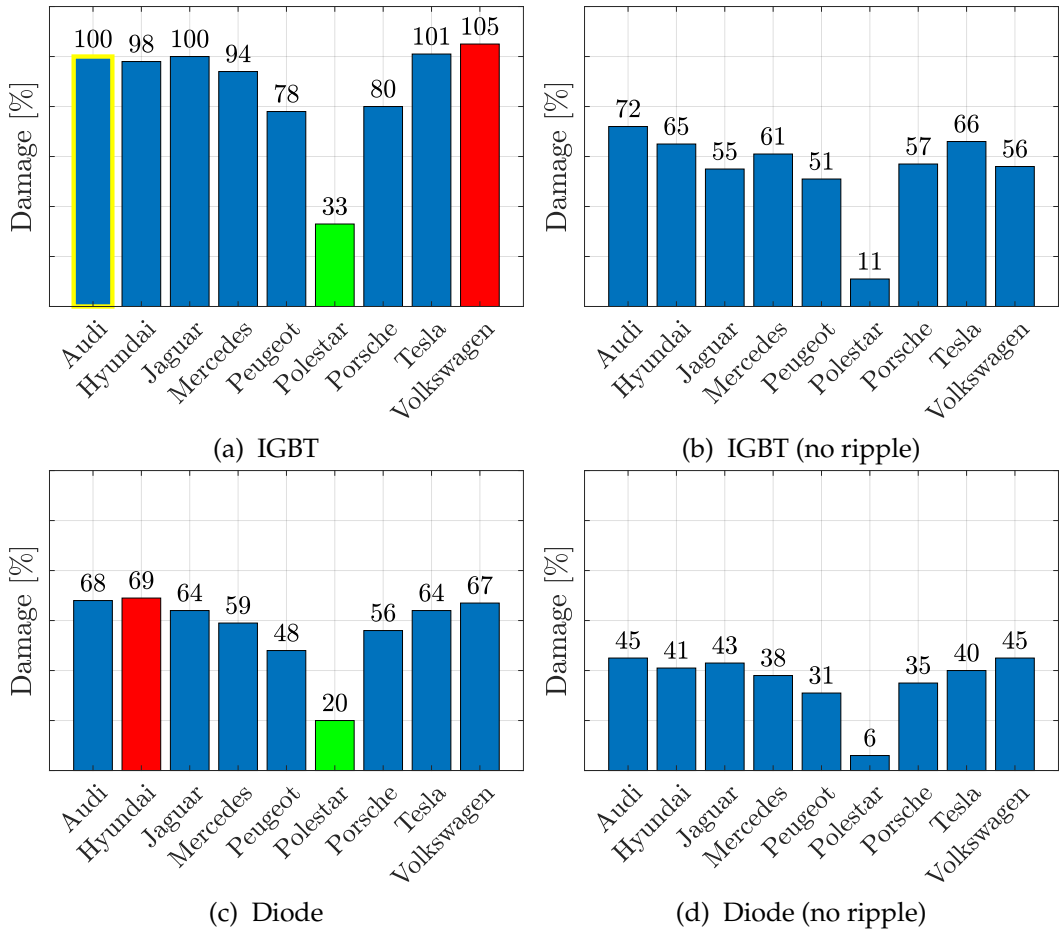

(a) IGBT (b) IGBT (no ripple)

(c) Diode (d) Diode (no ripple)

FIGURE 3.35: Calculated damage, after one charging event (SoC from 10 % to 90%), of the different charging strategies with and without the temperature ripple. The results are normalized with respect to the IGBT damage with the Audi charging strategy.

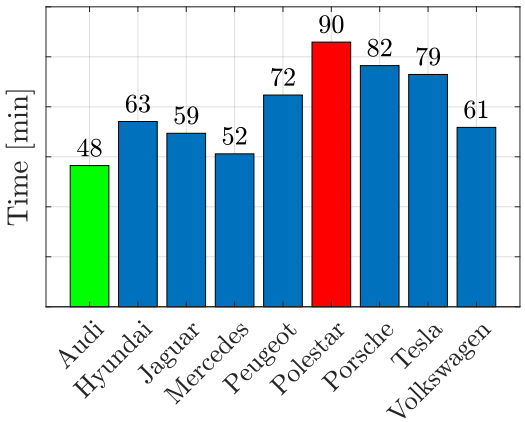

FIGURE 3.36: Comparison of the charging times of the different cars manufacturer strategies (battery SoC from 10 % to 90 %).

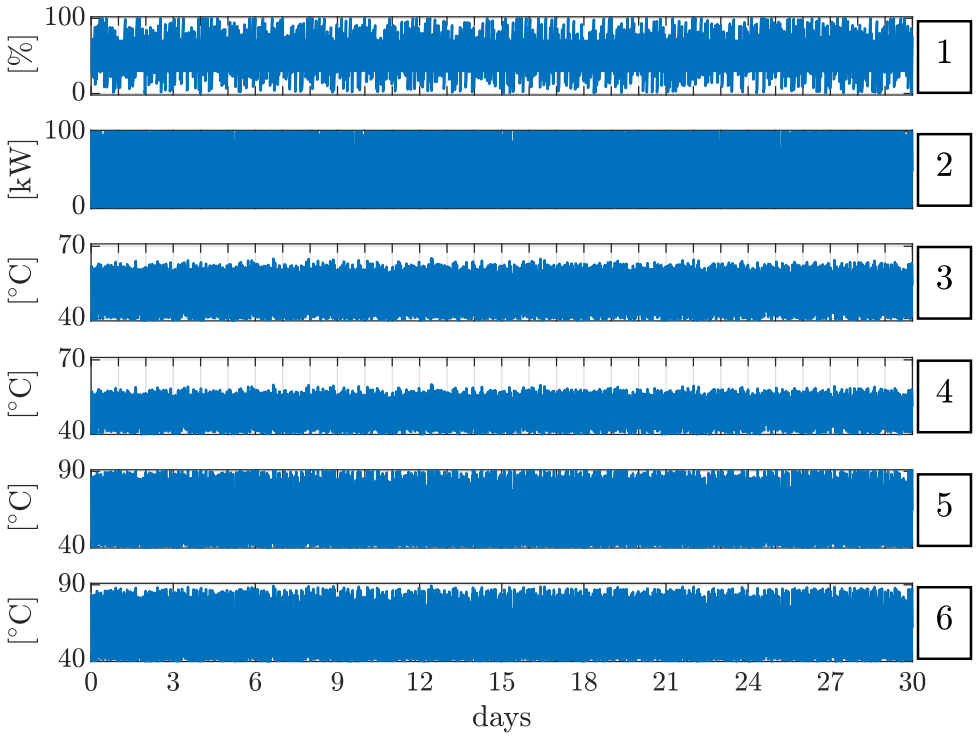

FIGURE 3.37: Results of the fast charger long time simulation: (1) battery SoC; (2) battery power; (3) buck IGBT temperature; (4) buck diode temperature; (5) rectifier IGBT temperature; (6) rectifier diode temperature.

the junction temperature and if compared to a potential PLECS simulation it results to be orders of magnitude faster. Nonetheless, the higher is the simulated time and the higher is the time and the amount of memory needed to calculate and store the final junction temperature vector: for this reason, the best practice would be to limit the temperature prediction to a certain period of time to avoid the necessity of a great amount of resources.

3.5 Discussion

The present chapter presented the thermal model of a power device for a two-level voltage source inverter (2L-VSI) aimed at the calculation of the cumulative damage in the device.

The main contribution of the proposed approach is the capability of performing accurate, long term simulations in a reduced time period, allowing a real-time estimation of the power devices cumulative damage and the remaining useful lifetime, opening up to the possibility of e.g. defining optimal maintenance strategies or adapting the converter operation to follow the optimal maintenance directives. The proposed model does not require additional characterizations of the power devices, just requiring the available parameters in the components datasheet/models which are provided by the manufacturer. The proposed thermal model is characterized by a significantly reduced computational cost without sacrificing the accuracy of the calculated junction temperatures. Moreover, the model is able to calculate the temperature ripple at the fundamental frequency, providing a useful tool for assessing the cumulative damage on the power semiconductors, since their degradation highly depends on the presence of thermal cycles corresponding to the converter power profile.

The thermal model was built by first calculating the average losses by considering two different modulation strategies: a Sinusoidal PWM (SPWM) strategy and a Sinusoidal PWM with Third Harmonic Injection (THISPWM) strategy. The analytical calculations were limited to one leg of the VSI and by distinctively analyzing a switch composed of a MOSFET with diode and an IGBT with diode. The MOSFET with diode model did not take into account the variation of the on-resistances with respect to the on-current. On the other hand, in the IGBT with diode, a modified model was proposed in order to take into account the dependency of the devices' on-voltages with respect to the on-currents. Finally, the junction temperature profile was calculated with the sum of two terms: an average temperature curve, obtained with a Simulink model, built by using the analytical formulations of the average losses, and a periodic ripple profile superimposed, obtained by means of a post-processing Matlab script.

The proposed approach was compared against a PLECS simulation by exploiting the thermal models provided by the manufacturers of a SiC MOSFET and an IGBT as a common test reference. The steady-state temperature profiles obtained with the analytical method showed a very good fit with the PLECS curves and also the IGBT analytical modified model produced a much more accurate result with respect to the simpler model featuring constant parameters. The reduced computational burden of the proposed approach resulted in a simulation time that was approximately one fiftieth of the simulation time required by PLECS. In fact, as shown in the thermal comparison section, the analytical model took approximately 5 s, including the temperature ripple calculation in post-processing against the 270 s needed by PLECS to carry out a 10 s simulation. This execution time allows to carry out real-time analysis of the power electronics device in order to take advantage of

the cumulative damage estimation to predict the behavior of the converter. As an additional test, experimental validation was carried out on a reduced-scale prototype based on a Semikron IGBT power module. The obtained temperature profile showed a very good agreement with the one calculated with the analytical approach.

The analytical thermal model for a bi-directional buck/boost converter was also presented in this chapter. The final aim was to analyze the thermal behavior of a vehicle fast charger, based on the ABB Terra HP150. In fact, by exploiting the 2L-VSI model and the Simulink built-in model of a battery pack, based on the Samsung SDI94 cells, different vehicles charging strategies were analyzed in order to find the most stressful in terms of damage in the power devices of the active rectifier connected to the AC grid. In order to speed up the simulations, the three-phase grid and the active rectifier were modeled in a dq reference frame thus avoiding the variation of the electrical variables at the grid frequency. It was found out that the strategies featuring a step power variation cause higher charging times, but also a much lower damage in the power devices. Moreover, by comparing the cumulative damage results with and without the temperature ripple, it was underlined the importance of considering the temperature ripple at the AC output current frequency in order to obtain a more accurate result in terms of device lifetime. In fact, the difference in terms of damage were noticeable, resulting in approximately a 20% difference. Also in this case, the execution time was measured and it was found out that to simulate one hour of the fast charger thermal behavior only 30 s were needed allowing the estimation of the active rectifier damage in a considerable amount of time for the predictive maintenance of the fast charging station.

Future developments of this work could include an assessment of the fast charger efficiency in different working points, along with the comparison of different charging architectures. This application could be also used as a financial tool, used to estimate the damage caused by a specific charging event, possibly including a corresponding share in the charging price.

Conclusion

This dissertation presented different case studies regarding the electrification of non-road mobile machinery (NRMM), discussing new electric drive topologies, the design and analysis of multi-three-phase electrical machines and the modeling of a vehicle fast charger to evaluate the cumulative damage in power electronics converters.

In Chapter 1, the work was focused on two different case studies. The first case was aimed at the design and analysis of a multi-three-phase machine intended for the hybridization of a 5-ton bucket-excavator. The main purpose of the hybrid power system was to downsize the internal combustion engine using the electric drive to supply the peak power demand during the machine operation. Finite element simulations considering different fault case scenarios were run in order to assess the fault operation capability and the unbalanced airgap radial force acting on the rotor. The simulations highlighted a particular fault configuration characterized by a peak radial force equal to 287 N: this condition happens when two adjacent sets are healthy and the other two are in fault. In the second case study, a comparison between a traditional architecture and a Multi-Functional Converter System (MFCS) was carried out. The analysis pointed out that the battery current is composed of two fundamental terms: an average term, which is responsible for the power flow from the battery to the inverter, and a ripple component, is limited only by the machine homopolar inductance, which is caused by the modulation. The analysis of the PWM spectrum showed that, by fixing the machine star point potential, the homopolar components of the pole voltages do not cancel out and this causes the circulation of very high homopolar currents in the machine with a significant ripple at the switching frequency. The analysis also showed that, if a proper poles/slots configuration is chosen, the homopolar components do not affect the machine magneto-motive force at the airgap, which contains the same spatial harmonics as a traditional machine and thus the machine performance is preserved. Moreover, a comparison with respect to a traditional architecture with a DC-DC boost converter placed between the battery and the DC bus was carried out. The results of the comparison showed that the traditional drive is more efficient by approximately 13% than the MFCS in the rated point, mainly because of the higher winding losses in the MFCS' machine due to the additional homopolar current. Nevertheless, considering the overload point, the two architectures showed a similar drive efficiency, even if the MFCS' machine was still less efficient, given the absence of the DC-DC boost converter losses in the MFCS.

In Chapter 2, two studies were carried out. In the first part of the chapter the design of a high power density electric motor for a rim-driven propulsor

was presented: the electric machine featured a thin radial section and a hair-pin winding construction. The electric machine was designed and simulated in order to analyze the machine performance and, secondly, to calculate the losses and estimate the machine efficiency and temperatures. Thanks to the particular application, the electric machine cooling was guaranteed by a submerged operation and a wet rotor construction. This particular, yet simple cooling method was the main condition which allowed to design a machine with a very high torque and power density, comparing favourably against a traditional internal combustion engine. In the second part of the chapter a reconfigurable multi-three-phase drive architecture for naval propulsion was presented. This architecture is capable of performing the machine winding reconfiguration (i.e. connecting them in series, in parallel or a mixing of the two) thanks to additional circuits named reconfiguration cells (RCs). The impact of the reconfiguration cells (RCs) was evaluated both in terms of additional losses as well as fault sensitivity of the reconfigurable drive. To overcome the conduction losses associated to full solid-state RCs (i.e. by employing SCR, IGBT and MOSFET) a hybrid relay topology was considered, in order to mitigate the impact of the conduction losses in the system efficiency, especially when dealing with large power sizes. It was found that when the electric machine operates at reduced speed and power, the reconfigurable drive allow to increase the system efficiency and reduce the phase current ripple (for the same switching frequency), by series connecting the machine winding (series-configured drive). The advantages in terms of efficiency and current ripple of the reconfigurable drive at low speed operation were also demonstrated experimentally on a reduced scale prototype, capable of "on the fly" reconfiguration of the machine's winding when operating under load, without stopping. Taking the standard multi-three-phase drive architecture as the reference and considering the Hybrid-Relay RCs reconfigurable architecture, the SC drive was able to reduce the converters losses by 75%. Nevertheless, even when taking into account the additional RCs losses, the total power converter losses reduction were approximately equal to 59%. The advantage mainly comes from the elimination of both conduction and switching losses associated with the other modular converters that are deactivated.

Chapter 3 presented the thermal model of a power device for a two-level voltage source inverter (2L-VSI) aimed at the calculation of the cumulative damage in the device. The main contribution of the proposed approach is the capability of performing accurate, long term simulations in a reduced time period, allowing a real-time estimation of the power devices cumulative damage and the remaining useful lifetime. The thermal model was built by first calculating the average losses by considering two different modulation strategies: a sinusoidal PWM strategy and a sinusoidal PWM with third harmonic injection strategy. The analytical calculations were limited to one leg of the VSI and by distinctively analyzing a switch composed of a MOSFET with diode and an IGBT with diode. From the simulations it was found that the steady-state temperature profiles obtained with the analytical method showed a very good fit with the PLECS curves. The IGBT analytical

modified model showed a much more accurate result with respect to the simple model with constant on-resistances with respect to the on-currents. The reduced computational burden of the proposed approach resulted in a simulation time that was approximately one hundredth of the simulation time required by PLECS. To complete the analysis, an experimental validation was carried out on a reduced-scale prototype based on a Semikron IGBT power module: the obtained temperature profile showed a very good agreement with the one calculated with the analytical approach. The final study of this chapter focused on analyzing the thermal behavior of a vehicle fast charger. Different vehicles charging strategies were analyzed in order to find the most stressful in terms of damage in the power devices of the active rectifier connected to the AC grid. It was found out that the strategies featuring a step power variation cause higher charging times, but also a much lower damage in the power devices. Moreover, it was underlined the importance of considering the temperature ripple at the AC output current frequency in order to obtain a more accurate result in terms of device lifetime.

Appendix A

Homopolar Current in a PMSM for a MFCS architecture

The equation (1.70) describes the evolution of the AC homopolar current in the Multi-Functional Converter System (MFCS):

$$\sum_{h=0}^{\infty}\sum_{n=0,3,6,\dots}^{\infty} V_{phn}\cos(h\omega_s t \pm n\theta_e + \phi'_{hn}) - v_{\mathrm{B}} = -\frac{R_s}{3}\tilde{i}_{\mathrm{B}} - \frac{L_0}{3}\frac{d\tilde{i}_{\mathrm{B}}}{dt} \tag{A.1}$$

where V_{phn} is the amplitude of the h,n-th harmonic of the homopolar component of the inverter's leg voltages, v_{B} is the battery voltage applied to the star point of the machine, $\tilde{i}_{\mathrm{B}}$ is the neutral current, R_s is the machine stator resistance, L_0 is the machine homopolar inductance, $\theta_e = \omega_e t$ is the electrical angle, ω_e is the electrical speed and n is the harmonic order. Since the battery voltage depends on the battery State of Charge (SoC) it can be considered constant, or a slowly varying function. The (A.1) can be re-written as:

$$\frac{d\tilde{i}_{\mathrm{B}}(t)}{dt} + \frac{R_s}{L_0}\tilde{i}_{\mathrm{B}}(t) = \frac{3v_{\mathrm{B}}}{L_0} - \sum_{h=0}^{\infty}\sum_{n=0,3,6,\dots}^{\infty}\frac{3V_{phn}}{L_0}\cos((h\omega_s \pm n\omega_e)t + \phi'_{hn}) \tag{A.2}$$

Since the $(A.2)$ is in the form:

$$y'(t) + a_0 y(t) = g(t) \tag{A.3}$$

where:

$$\begin{aligned} &y(t) = \tilde{i}_{\mathrm{B}}(t), \quad y'(t) = \frac{d\tilde{i}_{\mathrm{B}}(t))}{dt}, \quad a_0 = \frac{R_s}{L_0} \\ &g(t) = \frac{3v_{\mathrm{B}}}{L_0} - \sum_{h=0}^{\infty}\sum_{n=0,3,6,\dots}^{\infty}\frac{3V_{phn}}{L_0}\cos(\Omega_{hn}t + \phi'_{hn}) \end{aligned} \tag{A.4}$$

and $\Omega_{hn} = h\omega_s \pm n\omega_e$. The solution of the (A.2) can be obtained as:

$$y(t) = e^{-A(t)}\left(y_0 + \int_{t_0}^{t} g(s)e^{A(s)}ds\right) \tag{A.5}$$

where $y_0 = y(t_0)$ is the initial value. By imposing $t_0 = 0$ and $y(0) = 0$, the (A.5) becomes:

$$y(t) = e^{-A(t)} \int_0^t g(s) e^{A(s)} ds \tag{A.6}$$

The term $A(t)$ is equal to:

$$A(t) = \int_0^t a_0 \, ds = t \frac{R_s}{L_0} \tag{A.7}$$

therefore $\tilde{i}_{\mathrm{B}}(t)$ can be calculated as:

$$\begin{aligned}
&\tilde{i}_{\mathrm{B}}(t) \\
&= e^{-t\frac{R_s}{L_0}} \int_0^t \left[\frac{3v_{\mathrm{B}}}{L_0} - \sum_{h=0}^{\infty} \sum_{n=0,3,6,\ldots}^{\infty} \frac{3V_{phn}}{L_0} \cos(\Omega_{hn} s + \phi'_{hn}) \right] e^{s\frac{R_s}{L_0}} ds \\
&= -\frac{3v_{\mathrm{B}}}{R_s} e^{-t\frac{R_s}{L_0}} - \sum_{h=0}^{\infty} \sum_{n=0,3,6,\ldots}^{\infty} \frac{3V_{phn}}{L_0} e^{-t\frac{R_s}{L_0}} \int_0^t \cos(\Omega_{hn} s + \phi'_{hn}) e^{s\frac{R_s}{L_0}} ds
\end{aligned} \tag{A.8}$$

The quantity $\int \cos(\Omega_{hn} s + \phi'_n) e^{s\frac{R_s}{L_0}} ds$ can be integrated by parts:

$$\begin{aligned}
&\int \cos(\Omega_{hn} s + \phi'_n) e^{s\frac{R_s}{L_0}} ds \\
&= \frac{1}{\Omega_{hn}} \sin(\Omega_{hn} s + \phi'_n) e^{s\frac{R_s}{L_0}} - \frac{R_s}{\Omega_{hn} L_0} \int \sin(\Omega_{hn} s + \phi'_n) e^{s\frac{R_s}{L_0}} ds \\
&\int \cos(\Omega_{hn} s + \phi'_n) e^{\frac{s}{\tau_0}} ds \\
&= \frac{1}{\Omega_{hn}} \sin(\Omega_{hn} s + \phi'_n) e^{s\frac{R_s}{L_0}} - \frac{R_s}{\Omega_{hn} L_0} \left[-\frac{1}{\Omega_{hn}} \cos(\Omega_{hn} s + \phi'_n) e^{s\frac{R_s}{L_0}} \right. \\
&\left. + \frac{R_s}{\Omega_{hn} L_0} \int \cos(\Omega_{hn} s + \phi'_n) e^{s\frac{R_s}{L_0}} ds \right] \\
&\int \cos(\Omega_{hn} s + \phi'_n) e^{\frac{s}{\tau_0}} ds \\
&= \frac{1}{\Omega_{hn}} \sin(\Omega_{hn} s + \phi'_n) e^{s\frac{R_s}{L_0}} + \frac{R_s}{\Omega_{hn}^2 L_0} \cos(\Omega_{hn} s + \phi'_n) e^{s\frac{R_s}{L_0}} \\
&- \frac{R_s^2}{(\Omega_{hn} L_0)^2} \int \cos(\Omega_{hn} s + \phi'_n) e^{s\frac{R_s}{L_0}} ds \\
&\frac{R_s^2 + (\Omega_{hn} L_0)^2}{(\Omega_{hn} L_0)^2} \int \cos(\Omega_{hn} s + \phi'_n) e^{s\frac{R_s}{L_0}} ds \\
&= \frac{1}{\Omega_{hn}} \sin(\Omega_{hn} s + \phi'_n) e^{s\frac{R_s}{L_0}} + \frac{R_s}{\Omega_{hn}^2 L_0} \cos(\Omega_{hn} s + \phi'_n) e^{s\frac{R_s}{L_0}} \\
&\int \cos(\Omega_{hn} s + \phi'_n) e^{s\frac{R_s}{L_0}} ds \\
&= \frac{L_0}{R_s^2 + (\Omega_{hn} L_0)^2} \left[\Omega_{hn} L_0 \cos(\Omega_{hn} s + \phi'_n) + R_s \sin(\Omega_{hn} s + \phi'_n) \right] e^{s\frac{R_s}{L_0}}
\end{aligned} \tag{A.9}$$

the term between the brackets can be written in the form $Z_{0hn}\cos(\Omega_{hn}s + \phi'_n - \varphi_{0hn})$, where:

$$Z_{0hn} = \sqrt{R_s^2 + (\Omega_{hn}L_0)^2}, \quad \varphi_{0hn} = \arctan\left(\frac{\Omega_{hn}L_0}{R_s}\right) \tag{A.10}$$

where Z_{0n} is the n-th homopolar stator impedance. Thus the result of definite integral of eq. (A.9) is given by:

$$\begin{aligned}
&\int_0^t \cos(\Omega_{hn}s + \phi'_n)e^{s\frac{R_s}{L_0}}ds \\
&= \frac{L_0}{Z_{0hn}}\left[\cos(\Omega_{hn}s + \phi'_n - \varphi_{0hn})e^{s\frac{R_s}{L_0}}\right]_0^t \\
&= \frac{L_0}{Z_{0hn}}\left[\cos(\Omega_{hn}t + \phi'_n - \varphi_{0hn})e^{t\frac{R_s}{L_0}} - \cos(\phi'_n - \varphi_{0hn})\right]
\end{aligned} \tag{A.11}$$

By using the (A.11), the expression of eq. (A.8) becomes:

$$\begin{aligned}
\tilde{i}_B(t) &= -\frac{3v_B}{R_s}e^{-t\frac{R_s}{L_0}} - \sum_{h=0}^{\infty}\sum_{n=0,3,6,\ldots}^{\infty}\frac{3V_{phn}}{L_0}e^{-t\frac{R_s}{L_0}}\int_0^t \cos(\Omega_{hn}s + \phi'_n)e^{s\frac{R_s}{L_0}}ds \\
\tilde{i}_B(t) &= -\frac{3v_B}{R_s}e^{-t\frac{R_s}{L_0}} \\
&- \sum_{h=0}^{\infty}\sum_{n=0,3,6,\ldots}^{\infty}\frac{3V_{phn}}{Z_{0hn}}e^{-t\frac{R_s}{L_0}}\left[\cos(\Omega_{hn}t + \phi'_n - \varphi_{0n})e^{t\frac{R_s}{L_0}} - \cos(\phi'_n - \varphi_{0hn})\right] \\
\tilde{i}_B(t) &= -\frac{3v_B}{R_s}e^{-t\frac{R_s}{L_0}} \\
&- \sum_{h=0}^{\infty}\sum_{n=0,3,6,\ldots}^{\infty}\frac{3V_{phn}}{Z_{0hn}}\left[\cos(\Omega_{hn}t + \phi'_n - \varphi_{0hn}) - \cos(\phi'_n - \varphi_{0hn})e^{-t\frac{R_s}{L_0}}\right] \\
\tilde{i}_B(t) &= -\sum_{h=0}^{\infty}\sum_{n=0,3,6,\ldots}^{\infty}\frac{3V_{phn}}{Z_{0hn}}\cos(\Omega_{hn}t + \phi'_n - \varphi_{0hn}) \\
&+ \left[\sum_{h=0}^{\infty}\sum_{n=0,3,6,\ldots}^{\infty}\frac{3V_{phn}}{Z_{0hn}}\cos(\phi'_n - \varphi_{0hn}) - \frac{3v_B}{R_s}\right]e^{-t\frac{R_s}{L_0}}
\end{aligned} \tag{A.12}$$

therefore, the steady-state expression of the neutral current is equal to:

$$\tilde{i}_B(t) = -\sum_{h=0}^{\infty}\sum_{n=0,3,6,\ldots}^{\infty}3\tilde{I}_{Bhn}\cos(h\omega_s \pm n\theta_e + \phi'_n - \varphi_{0hn}) \tag{A.13}$$

where:

$$\tilde{I}_{Bhn} = \frac{V_{phn}}{Z_{0hn}} \tag{A.14}$$

is the amplitude of the n-th harmonic of the battery current and $\theta_e = \omega_e t$.

Appendix B

Average Conduction Loss Calculation for a Half-Bridge

B.1 MOSFET and Diode

The MOSFET average conduction losses over one fundamental period considering the forward conduction phase, ($P_{\mathrm{c}Q,f}$), and during the reverse phase ($P_{\mathrm{c}Q,r}$, $P_{\mathrm{c}D,r}$) are obtained as:

$$P_{\mathrm{c}Q,f} = \frac{1}{2\pi}\int_{-\beta}^{\pi+\beta} m_H(\alpha) R_{Q\mathrm{on}} i_{Q,f}^2(\alpha) d\alpha \tag{B.1}$$

$$P_{\mathrm{c}Q,r} = \frac{1}{2\pi}\int_{\pi+\beta}^{2\pi-\beta} m_H(\alpha) R_{Q\mathrm{on}} i_{Q,r}^2(\alpha) d\alpha \tag{B.2}$$

$$P_{\mathrm{c}D,r} = \frac{1}{2\pi}\int_{\pi+\beta}^{2\pi-\beta} m_H(\alpha) \left[R_{D\mathrm{on}} i_{D,r}^2(\alpha) + V_{D0} i_{D,r}(\alpha)\right] d\alpha \tag{B.3}$$

by introducing the (3.13),(3.14) into the (B.2),(B.3), and remembering that the MOSFET and diode on-resistances ($R_{Q\mathrm{on}} + R_{D\mathrm{on}}$) and the diode no-load voltage (V_{D0}) are independent from the current, yields to:

$$P_{\mathrm{c}Q,f} = \frac{R_{Q\mathrm{on}}}{2\pi}\int_{-\beta}^{\pi+\beta} m_H(\alpha) i_o^2(\alpha) d\alpha \tag{B.4}$$

$$\begin{aligned} P_{\mathrm{c}Q,r} = {} & \frac{R_{Q\mathrm{on}} R_{D\mathrm{on}}^2}{2\pi(R_{Q\mathrm{on}} + R_{D\mathrm{on}})^2}\int_{\pi+\beta}^{2\pi-\beta} m_H(\alpha) i_o^2(\alpha) d\alpha \\ & - \frac{2R_{Q\mathrm{on}} R_{D\mathrm{on}} V_{D0}}{2\pi(R_{Q\mathrm{on}} + R_{D\mathrm{on}})^2}\int_{\pi+\beta}^{2\pi-\beta} m_H(\alpha) i_o(\alpha) d\alpha \\ & + \frac{R_{Q\mathrm{on}} V_{D0}^2}{2\pi(R_{Q\mathrm{on}} + R_{D\mathrm{on}})^2}\int_{\pi+\beta}^{2\pi-\beta} m_H(\alpha) d\alpha \end{aligned} \tag{B.5}$$

$$\begin{aligned} P_{\mathrm{c}D,r} = {} & \frac{R_{Q\mathrm{on}}^2 R_{D\mathrm{on}}}{2\pi(R_{Q\mathrm{on}} + R_{D\mathrm{on}})^2}\int_{\pi+\beta}^{2\pi-\beta} m_H(\alpha) i_o^2(\alpha) d\alpha \\ & + \frac{R_{Q\mathrm{on}} V_{D0}(R_{D\mathrm{on}} - R_{Q\mathrm{on}})}{2\pi(R_{Q\mathrm{on}} + R_{D\mathrm{on}})^2}\int_{\pi+\beta}^{2\pi-\beta} m_H(\alpha) i_o(\alpha) d\alpha \\ & - \frac{R_{Q\mathrm{on}} V_{D0}^2}{2\pi(R_{Q\mathrm{on}} + R_{D\mathrm{on}})^2}\int_{\pi+\beta}^{2\pi-\beta} m_H(\alpha) d\alpha \end{aligned} \tag{B.6}$$

By considering a sinusoidal output current:

$$i_o(\alpha) = I_p \sin(\alpha) \tag{B.7}$$

and by introducing the (B.7) into the (B.4-B.6) yields to:

$$P_{cQ,f} = \frac{R_{Qon} I_p^2}{2\pi} \int_{-\beta}^{\pi+\beta} m_H(\alpha) \sin^2(\alpha) d\alpha \tag{B.8}$$

$$\begin{aligned} P_{cQ,r} = & \frac{R_{Qon} R_{Don}^2 I_p^2}{2\pi (R_{Qon} + R_{Don})^2} \int_{\pi+\beta}^{2\pi-\beta} m_H(\alpha) \sin^2(\alpha) d\alpha \\ & - \frac{2 R_{Qon} R_{Don} V_{D0} I_p}{2\pi (R_{Qon} + R_{Don})^2} \int_{\pi+\beta}^{2\pi-\beta} m_H(\alpha) \sin(\alpha) d\alpha \\ & + \frac{R_{Qon} V_{D0}^2}{2\pi (R_{Qon} + R_{Don})^2} \int_{\pi+\beta}^{2\pi-\beta} m_H(\alpha) d\alpha \end{aligned} \tag{B.9}$$

$$\begin{aligned} P_{cD,r} = & \frac{R_{Qon}^2 R_{Don} I_p^2}{2\pi (R_{Qon} + R_{Don})^2} \int_{\pi+\beta}^{2\pi-\beta} m_H(\alpha) \sin^2(\alpha) d\alpha \\ & + \frac{R_{Qon} V_{D0} I_p (R_{Don} - R_{Qon})}{2\pi (R_{Qon} + R_{Don})^2} \int_{\pi+\beta}^{2\pi-\beta} m_H(\alpha) \sin(\alpha) d\alpha \\ & - \frac{R_{Qon} V_{D0}^2}{2\pi (R_{Qon} + R_{Don})^2} \int_{\pi+\beta}^{2\pi-\beta} m_H(\alpha) d\alpha \end{aligned} \tag{B.10}$$

by defining the following constants:

$$a = \frac{R_{Qon}}{4\pi} \tag{B.11}$$

$$b = \frac{1}{(R_{Qon} + R_{Don})^2} \tag{B.12}$$

the (B.8-B.10) become:

$$P_{\mathrm{c}Q,f} = 2aI_p^2 \int_{-\beta}^{\pi+\beta} m_H(\alpha)\sin^2(\alpha)d\alpha \tag{B.13}$$

$$\begin{aligned} P_{\mathrm{c}Q,r} &= 2abR_{D\mathrm{on}}^2 I_p^2 \int_{\pi+\beta}^{2\pi-\beta} m_H(\alpha)\sin^2(\alpha)d\alpha \\ &\quad - 4abR_{D\mathrm{on}}V_{D0}I_p \int_{\pi+\beta}^{2\pi-\beta} m_H(\alpha)\sin(\alpha)d\alpha \\ &\quad + 2abV_{D0}^2 \int_{\pi+\beta}^{2\pi-\beta} m_H(\alpha)d\alpha \end{aligned} \tag{B.14}$$

$$\begin{aligned} P_{\mathrm{c}D,r} &= 2abR_{D\mathrm{on}}R_{Q\mathrm{on}}I_p^2 \int_{\pi+\beta}^{2\pi-\beta} m_H(\alpha)\sin^2(\alpha)d\alpha \\ &\quad + 2abV_{D0}(R_{D\mathrm{on}} - R_{Q\mathrm{on}})I_p \int_{\pi+\beta}^{2\pi-\beta} m_H(\alpha)\sin(\alpha)d\alpha \\ &\quad - 2abV_{D0}^2 \int_{\pi+\beta}^{2\pi-\beta} m_H(\alpha)d\alpha \end{aligned} \tag{B.15}$$

by defining the following variables:

$$\begin{aligned} K_1 &= aI_p^2 & K_2 &= abR_{D\mathrm{on}}^2 I_p^2 \\ K_3 &= 2abR_{D\mathrm{on}}V_{D0}I_p & K_4 &= abV_{D0}^2 \\ K_5 &= abR_{D\mathrm{on}}R_{Q\mathrm{on}}I_p^2 & K_6 &= abV_{D0}(R_{D\mathrm{on}} - R_{Q\mathrm{on}})I_p \end{aligned} \tag{B.16}$$

the expressions for the forward and reverse losses become:

$$P_{\mathrm{c}Q,f} = 2K_1 \int_{-\beta}^{\pi+\beta} m_H(\alpha)\sin^2(\alpha)d\alpha \tag{B.17}$$

$$\begin{aligned} P_{\mathrm{c}Q,r} &= 2K_2 \int_{\pi+\beta}^{2\pi-\beta} m_H(\alpha)\sin^2(\alpha)d\alpha \\ &\quad - 2K_3 \int_{\pi+\beta}^{2\pi-\beta} m_H(\alpha)\sin(\alpha)d\alpha \\ &\quad + 2K_4 \int_{\pi+\beta}^{2\pi-\beta} m_H(\alpha)d\alpha \end{aligned} \tag{B.18}$$

$$\begin{aligned} P_{\mathrm{c}D,r} &= 2K_5 \int_{\pi+\beta}^{2\pi-\beta} m_H(\alpha)\sin^2(\alpha)d\alpha \\ &\quad + 2K_6 \int_{\pi+\beta}^{2\pi-\beta} m_H(\alpha)\sin(\alpha)d\alpha \\ &\quad - 2K_4 \int_{\pi+\beta}^{2\pi-\beta} m_H(\alpha)d\alpha \end{aligned} \tag{B.19}$$

B.1.1 Sinusoidal PWM

By defining the upper switch duty-cycle for a sinusoidal PWM (SPWM) modulation strategy:

$$m_H^{\text{SPWM}}(\alpha) = \frac{1}{2}\left[1 + \widetilde{M}_{\text{A}} \sin(\alpha + \varphi)\right] \tag{B.20}$$

and by introducing the (B.20) into the (B.17-B.19) yields to:

$$P_{\text{cQ},f}^{\text{SPWM}} = K_1 \int_{-\beta}^{\pi+\beta} \left[1 + \widetilde{M}_{\text{A}} \sin(\alpha + \varphi)\right] \sin^2(\alpha) d\alpha \tag{B.21}$$

$$\begin{aligned} P_{\text{cQ},r}^{\text{SPWM}} &= K_2 \int_{\pi+\beta}^{2\pi-\beta} \left[1 + \widetilde{M}_{\text{A}} \sin(\alpha + \varphi)\right] \sin^2(\alpha) d\alpha \\ &\quad - K_3 \int_{\pi+\beta}^{2\pi-\beta} \left[1 + \widetilde{M}_{\text{A}} \sin(\alpha + \varphi)\right] \sin(\alpha) d\alpha \\ &\quad + K_4 \int_{\pi+\beta}^{2\pi-\beta} \left[1 + \widetilde{M}_{\text{A}} \sin(\alpha + \varphi)\right] d\alpha \end{aligned} \tag{B.22}$$

$$\begin{aligned} P_{\text{cD},r}^{\text{SPWM}} &= K_5 \int_{\pi+\beta}^{2\pi-\beta} \left[1 + \widetilde{M}_{\text{A}} \sin(\alpha + \varphi)\right] \sin^2(\alpha) d\alpha \\ &\quad + K_6 \int_{\pi+\beta}^{2\pi-\beta} \left[1 + \widetilde{M}_{\text{A}} \sin(\alpha + \varphi)\right] \sin(\alpha) d\alpha \\ &\quad - K_4 \int_{\pi+\beta}^{2\pi-\beta} \left[1 + \widetilde{M}_{\text{A}} \sin(\alpha + \varphi)\right] d\alpha \end{aligned} \tag{B.23}$$

The (B.21) can be written as:

$$\begin{aligned} P_{\text{cQ},f}^{\text{SPWM}} &= K_1 \int_{-\beta}^{\pi+\beta} \sin^2(\alpha) d\alpha + K_1 \widetilde{M}_{\text{A}} \int_{-\beta}^{\pi+\beta} \sin(\alpha + \varphi) \sin^2(\alpha) d\alpha \\ &= K_1 \left[\beta - \frac{1}{2}\sin(2\beta) + \frac{3}{2}\widetilde{M}_{\text{A}} \cos(\beta)\cos(\varphi)\right. \\ &\quad \left. - \frac{1}{6}\widetilde{M}_{\text{A}} \cos(3\beta)\cos(\varphi) + \frac{\pi}{2}\right] \end{aligned} \tag{B.24}$$

the (B.22) can be written as:

$$\begin{aligned}
P_{\mathrm{cQ},r}^{\mathrm{SPWM}} &= K_2 \int_{\pi+\beta}^{2\pi-\beta} \sin^2(\alpha) d\alpha + K_2 \widetilde{M}_{\mathrm{A}} \int_{\pi+\beta}^{2\pi-\beta} \sin^2(\alpha) d\alpha \\
&- K_3 \int_{\pi+\beta}^{2\pi-\beta} \sin(\alpha) d\alpha + K_3 \widetilde{M}_{\mathrm{A}} \int_{\pi+\beta}^{2\pi-\beta} \sin(\alpha) d\alpha \\
&+ K_4 \int_{\pi+\beta}^{2\pi-\beta} d\alpha + K_4 \widetilde{M}_{\mathrm{A}} \int_{\pi+\beta}^{2\pi-\beta} d\alpha \\
&= K_2 \Bigg[-\beta + \frac{1}{2}\sin(2\beta) - \frac{3}{2}\widetilde{M}_{\mathrm{A}} \cos(\beta)\cos(\varphi) \\
&+ \frac{1}{6}\widetilde{M}_{\mathrm{A}} \cos(3\beta)\cos(\varphi) + \frac{\pi}{2} \Bigg] \\
&- K_3 \Bigg[-2\cos(\beta) - \widetilde{M}_{\mathrm{A}} \beta \cos(\varphi) + \frac{1}{2}\widetilde{M}_{\mathrm{A}} \sin(2\beta)\cos(\varphi) \\
&+ \frac{\pi}{2}\widetilde{M}_{\mathrm{A}} \cos(\varphi) \Bigg] \\
&+ K_4 \Bigg[-2\beta - 2\widetilde{M}_{\mathrm{A}} \cos(\beta)\cos(\varphi) + \pi \Bigg]
\end{aligned} \tag{B.25}$$

the (B.23) can be written as:

$$\begin{aligned}
P_{\mathrm{cD},r}^{\mathrm{SPWM}} &= K_5 \int_{\pi+\beta}^{2\pi-\beta} \sin^2(\alpha) d\alpha + K_5 \widetilde{M}_{\mathrm{A}} \int_{\pi+\beta}^{2\pi-\beta} \sin^2(\alpha) d\alpha \\
&+ K_6 \int_{\pi+\beta}^{2\pi-\beta} \sin(\alpha) d\alpha + K_6 \widetilde{M}_{\mathrm{A}} \int_{\pi+\beta}^{2\pi-\beta} \sin(\alpha) d\alpha \\
&- K_4 \int_{\pi+\beta}^{2\pi-\beta} d\alpha + K_4 \widetilde{M}_{\mathrm{A}} \int_{\pi+\beta}^{2\pi-\beta} d\alpha \\
&= K_5 \Bigg[-\beta + \frac{1}{2}\sin(2\beta) - \frac{3}{2}\widetilde{M}_{\mathrm{A}} \cos(\beta)\cos(\varphi) \\
&+ \frac{1}{6}\widetilde{M}_{\mathrm{A}} \cos(3\beta)\cos(\varphi) + \frac{\pi}{2} \Bigg] \\
&+ K_6 \Bigg[-2\cos(\beta) - \widetilde{M}_{\mathrm{A}} \beta \cos(\varphi) + \frac{1}{2}\widetilde{M}_{\mathrm{A}} \sin(2\beta)\cos(\varphi) \\
&+ \frac{\pi}{2}\widetilde{M}_{\mathrm{A}} \cos(\varphi) \Bigg] \\
&- K_4 \Bigg[-2\beta - 2\widetilde{M}_{\mathrm{A}} \cos(\beta)\cos(\varphi) + \pi \Bigg]
\end{aligned} \tag{B.26}$$

B.1.2 Sinusoidal PWM with Third Harmonic Injection

If a sinusoidal PWM with third harmonic injection (THISPWM) is used, the upper switch duty-cycle is characterized by a third harmonic component

(THC) which is added to the sine PWM duty-cycle:

$$m_H^{\text{THISPWM}}(\alpha) = m_H^{\text{SPWM}}(\alpha) + m_H^{\text{THC}}(\alpha) \tag{B.27}$$

where:

$$m_H^{\text{THC}}(\alpha) = \frac{1}{12}\widetilde{M}_{\text{A}} \sin(3\alpha + 3\varphi) \tag{B.28}$$

by introducing the (B.28) into the (B.17-B.19) yields to:

$$P_{\text{cQ},f}^{\text{THC}} = K_1 \frac{1}{6}\widetilde{M}_{\text{A}} \int_{-\beta}^{\pi+\beta} \sin(3\alpha + 3\varphi)\sin^2(\alpha)d\alpha \tag{B.29}$$

$$\begin{aligned} P_{\text{cQ},r}^{\text{THC}} = {} & K_2 \frac{1}{6}\widetilde{M}_{\text{A}} \int_{\pi+\beta}^{2\pi-\beta} \sin(3\alpha + 3\varphi)\sin^2(\alpha)d\alpha \\ & - K_3 \frac{1}{6}\widetilde{M}_{\text{A}} \int_{\pi+\beta}^{2\pi-\beta} \sin(3\alpha + 3\varphi)\sin(\alpha)d\alpha \\ & + K_4 \frac{1}{6}\widetilde{M}_{\text{A}} \int_{\pi+\beta}^{2\pi-\beta} \sin(3\alpha + 3\varphi)d\alpha \end{aligned} \tag{B.30}$$

$$\begin{aligned} P_{\text{cD},r}^{\text{THC}} = {} & K_5 \frac{1}{6}\widetilde{M}_{\text{A}} \int_{\pi+\beta}^{2\pi-\beta} \sin(3\alpha + 3\varphi)\sin^2(\alpha)d\alpha \\ & + K_6 \frac{1}{6}\widetilde{M}_{\text{A}} \int_{\pi+\beta}^{2\pi-\beta} \sin(3\alpha + 3\varphi)\sin(\alpha)d\alpha \\ & - K_4 \frac{1}{6}\widetilde{M}_{\text{A}} \int_{\pi+\beta}^{2\pi-\beta} \sin(3\alpha + 3\varphi)d\alpha \end{aligned} \tag{B.31}$$

which become:

$$P_{\text{cQ},f}^{\text{THC}} = K_1 \left[\frac{1}{6}\widetilde{M}_{\text{A}} \cos(3\varphi)\right]\left[-\frac{1}{2}\cos(\beta) + \frac{1}{3}\cos(3\beta) - \frac{1}{10}\cos(5\beta)\right] \tag{B.32}$$

$$\begin{aligned} P_{\text{cQ},r}^{\text{THC}} = {} & K_2 \left[\frac{1}{6}\widetilde{M}_{\text{A}} \cos(3\varphi)\right]\left[\frac{1}{2}\cos(\beta) - \frac{1}{3}\cos(3\beta) + \frac{1}{10}\cos(5\beta)\right] \\ & - K_3 \left[\frac{1}{6}\widetilde{M}_{\text{A}} \cos(3\varphi)\right]\left[-2\cos(\beta)\sin^3(\beta)\right] \\ & + K_4 \left[\frac{1}{6}\widetilde{M}_{\text{A}} \cos(3\varphi)\right]\left[-\frac{2}{3}\cos(3\beta)\right] \end{aligned} \tag{B.33}$$

$$\begin{aligned} P_{\text{cD},r}^{\text{THC}} = {} & K_5 \left[\frac{1}{6}\widetilde{M}_{\text{A}} \cos(3\varphi)\right]\left[\frac{1}{2}\cos(\beta) - \frac{1}{3}\cos(3\beta) + \frac{1}{10}\cos(5\beta)\right] \\ & + K_6 \left[\frac{1}{6}\widetilde{M}_{\text{A}} \cos(3\varphi)\right]\left[-2\cos(\beta)\sin^3(\beta)\right] \\ & - K_4 \left[\frac{1}{6}\widetilde{M}_{\text{A}} \cos(3\varphi)\right]\left[-\frac{2}{3}\cos(3\beta)\right] \end{aligned} \tag{B.34}$$

B.2 IGBT and Diode

The analytical expression of the conduction power loss for a IGBT and diode contain the following terms:

$$I_{Q\text{avg}} = \frac{I_p}{2\pi}\int_0^{\pi} m_H(\alpha)\sin(\alpha)d\alpha \tag{B.35}$$

$$I^2_{Q\text{rms}} = \frac{I_p^2}{2\pi}\int_0^{\pi} m_H(\alpha)\sin^2(\alpha)d\alpha \tag{B.36}$$

$$I_{D\text{avg}} = \frac{I_p}{2\pi}\int_{\pi}^{2\pi} m_H(\alpha)\sin(\alpha)d\alpha \tag{B.37}$$

$$I^2_{D\text{rms}} = \frac{I_p^2}{2\pi}\int_{\pi}^{2\pi} m_H(\alpha)\sin^2(\alpha)d\alpha \tag{B.38}$$

B.2.1 Sinusoidal PWM

By defining the upper switch duty-cycle for a sinusoidal PWM (SPWM) modulation strategy:

$$m_H^{\text{SPWM}}(\alpha) = \frac{1}{2}\left[1 + \widetilde{M}_{\text{A}}\sin(\alpha+\varphi)\right] \tag{B.39}$$

by introducing the (B.39) into the (B.35-B.38) yields to:

$$\begin{aligned} I_{\text{Qavg}}^{\text{SPWM}} &= \frac{I_p}{4\pi}\int_0^{\pi}\left[1+\widetilde{M}_{\text{A}}\sin(\alpha+\varphi)\right]\sin(\alpha)d\alpha \\ &= \frac{I_p}{4\pi}\left(\int_0^{\pi}\sin(\alpha)d\alpha+\widetilde{M}_{\text{A}}\int_0^{\pi}\sin(\alpha+\varphi)\sin(\alpha)d\alpha\right) \\ &= I_p\left(\frac{1}{2\pi}+\frac{\widetilde{M}_{\text{A}}\cos(\varphi)}{8}\right) \end{aligned} \tag{B.40}$$

$$\begin{aligned} \left(I_{\text{Qrms}}^{\text{SPWM}}\right)^2 &= \frac{I_p^2}{4\pi}\int_0^{\pi}\left[1+\widetilde{M}_{\text{A}}\sin(\alpha+\varphi)\right]\sin^2(\alpha)d\alpha \\ &= \frac{I_p^2}{4\pi}\left(\int_0^{\pi}\sin^2(\alpha)d\alpha+\widetilde{M}_{\text{A}}\int_0^{\pi}\sin(\alpha+\varphi)\sin^2(\alpha)d\alpha\right) \\ &= I_p^2\left(\frac{1}{8}+\frac{\widetilde{M}_{\text{A}}\cos(\varphi)}{3\pi}\right) \end{aligned} \tag{B.41}$$

$$\begin{aligned} I_{\text{Davg}}^{\text{SPWM}} &= \frac{I_p}{4\pi}\int_{\pi}^{2\pi}\left[1+\widetilde{M}_{\text{A}}\sin(\alpha+\varphi)\right]\sin(\alpha)d\alpha \\ &= \frac{I_p}{4\pi}\left(\int_0^{\pi}\sin(\alpha)d\alpha+\widetilde{M}_{\text{A}}\int_0^{\pi}\sin(\alpha+\varphi)\sin(\alpha)d\alpha\right) \\ &= I_p\left(-\frac{1}{2\pi}+\frac{\widetilde{M}_{\text{A}}\cos(\varphi)}{8}\right) \end{aligned} \tag{B.42}$$

$$\begin{aligned} \left(I_{\text{Drms}}^{\text{SPWM}}\right)^2 &= \frac{I_p^2}{4\pi}\int_{\pi}^{2\pi}\left[1+\widetilde{M}_{\text{A}}\sin(\alpha+\varphi)\right]\sin^2(\alpha)d\alpha \\ &= \frac{I_p^2}{4\pi}\left(\int_0^{\pi}\sin^2(\alpha)d\alpha+\widetilde{M}_{\text{A}}\int_0^{\pi}\sin(\alpha+\varphi)\sin^2(\alpha)d\alpha\right) \\ &= I_p^2\left(\frac{1}{8}-\frac{\widetilde{M}_{\text{A}}\cos(\varphi)}{3\pi}\right) \end{aligned} \tag{B.43}$$

B.2.2 Sinusoidal PWM with Third Harmonic Injection

If a sinusoidal PWM with third harmonic injection (THISPWM) is used, the upper switch duty-cycle is characterized by a third harmonic component (THC) which is added to the sine PWM duty-cycle:

$$m_H^{\text{THISPWM}}(\alpha) = m_H^{\text{SPWM}}(\alpha) + m_H^{\text{THC}}(\alpha) \tag{B.44}$$

where:

$$m_H^{\text{THC}}(\alpha) = \frac{1}{12}\widetilde{M}_{\text{A}}\sin(3\alpha+3\varphi) \tag{B.45}$$

by introducing the (B.45) into the (B.35-B.38) yields to:

$$I_{Q\text{avg}}^{\text{THC}} = \frac{\widetilde{M}_{\text{A}} I_p}{24\pi} \int_0^{\pi} \sin(3\alpha + 3\varphi)\sin(\alpha)d\alpha = 0 \tag{B.46}$$

$$\left(I_{Q\text{rms}}^{\text{THC}}\right)^2 = \frac{\widetilde{M}_{\text{A}} I_p^2}{24\pi} \int_0^{\pi} \sin(3\alpha + 3\varphi)\sin^2(\alpha)d\alpha = -I_p^2 \frac{\widetilde{M}_{\text{A}}\cos(3\varphi)}{90\pi} \tag{B.47}$$

$$I_{D\text{avg}}^{\text{THC}} = \frac{\widetilde{M}_{\text{A}} I_p}{24\pi} \int_{\pi}^{2\pi} \sin(3\alpha + 3\varphi)\sin(\alpha)d\alpha = 0 \tag{B.48}$$

$$\left(I_{D\text{rms}}^{\text{THC}}\right)^2 = \frac{\widetilde{M}_{\text{A}} I_p^2}{24\pi} \int_{\pi}^{2\pi} \sin(3\alpha + 3\varphi)\sin^2(\alpha)d\alpha = I_p^2 \frac{\widetilde{M}_{\text{A}}\cos(3\varphi)}{90\pi} \tag{B.49}$$

Bibliography

[1] . EU Parliament, "Directive (ec) 97/68/ec of the european parliament and of the council of 16 december 1997 on the approximation of the laws of the member states relating to measures against the emission of gaseous and particulate pollutants from internal combustion engines to be installed in non-road mobile machinery," 1997.

[2] . EU Parliament, "Regulation (eu) 2016/1628 of the european parliament and of the council of 14 september 2016 on requirements relating to gaseous and particulate pollutant emission limits and type-approval for internal combustion engines for non-road mobile machinery, amending regulations (eu) no 1024/2012 and (eu) no 167/2013, and amending and repealing directive 97/68/ec," 2016.

[3] R. Bojoi, S. Rubino, A. Tenconi, and S. Vaschetto, "Multiphase electrical machines and drives: A viable solution for energy generation and transportation electrification," in *2016 International Conference and Exposition on Electrical and Power Engineering (EPE)*, Oct. 2016, pp. 632–639. DOI: 10.1109/ICEPE.2016.7781416.

[4] H. Nakai, K. Moriya, H. Ohtani, H. Fuma, and Y. Inaguma, "Overview of multi-functional converter systems," *R&D Review of Toyota Central R&D Labs*, vol. 39, no. 3, 2004.

[5] K. Moriya, H. Nakai, Y. Inaguma, H. Ohtani, and S. Sasaki, "A novel multi-functional converter system equipped with input voltage regulation and current ripple suppression," in *Fourtieth IAS Annual Meeting. Conference Record of the 2005 Industry Applications Conference, 2005.*, vol. 3, 2005, 1636–1642 Vol. 3. DOI: 10.1109/IAS.2005.1518666.

[6] D. Tschanz, H. Lovatt, A. Vezzini, and V. Perrenoud, "A multi-functional converter for a reduced cost, solar powered, water pump," in *2010 IEEE International Symposium on Industrial Electronics*, 2010, pp. 568–572. DOI: 10.1109/ISIE.2010.5637661.

[7] B. Ge, L. Chen, and F. Xu, "Single stage boost-inverter integrated electric drives for electric vehicles," in *2019 IEEE Transportation Electrification Conference and Expo (ITEC)*, 2019, pp. 1–5. DOI: 10.1109/ITEC.2019.8790599.

[8] T. Hackner and J. Pforr, "Comparison of topologies to drive the machine of an automotive electrical power steering with higher voltage levels," in *2009 IEEE Energy Conversion Congress and Exposition*, 2009, pp. 3493–3500. DOI: 10.1109/ECCE.2009.5316321.

[9] T. Hackner and J. Pforr, "Comparison of different winding schemes of an asynchronous machine driven by a multi-functional converter system," in *2010 IEEE Energy Conversion Congress and Exposition*, 2010, pp. 570–577. DOI: 10.1109/ECCE.2010.5617967.

[10] T. Hackner, J. Pforr, H. Polinder, and J. A. Ferreira, "Optimization of the winding arrangement to increase the zero-sequence inductance of a synchronous machine with multifunctional converter drive," *IEEE Transactions on Industry Applications*, vol. 48, no. 6, pp. 2277–2286, 2012. DOI: 10.1109/TIA.2012.2227052.

[11] M. Vukovic, R. Leifeld, and H. Murrenhoff, "Reducing fuel consumption in hydraulic excavators—a comprehensive analysis," *Energies*, vol. 10, no. 5, 2017, ISSN: 1996-1073. DOI: 10.3390/en10050687. [Online]. Available: https://www.mdpi.com/1996-1073/10/5/687.

[12] L. Martellucci and R. Capata, "High performance hybrid vehicle concept-preliminary study and vehicle packaging," *Energies*, vol. 15, no. 11, 2022, ISSN: 1996-1073. DOI: 10.3390/en15114025. [Online]. Available: https://www.mdpi.com/1996-1073/15/11/4025.

[13] E. Gold, "Combinations of clutches and motors for p2 hybrids," *ATZ worldwide*, vol. 120, no. 6, pp. 46–51, Jun. 2018, ISSN: 2192-9076. DOI: 10.1007/s38311-018-0054-3. [Online]. Available: https://doi.org/10.1007/s38311-018-0054-3.

[14] S. Rubino, R. Bojoi, E. Levi, and O. Dordevic, "Vector control of multiple three-phase permanent magnet motor drives," in *IECON 2018 - 44th Annual Conference of the IEEE Industrial Electronics Society*, Oct. 2018, pp. 5866–5871. DOI: 10.1109/IECON.2018.8591146.

[15] S. Rubino, R. Bojoi, D. Cittanti, and L. Zarri, "Decoupled and modular torque control of multi-three-phase induction motor drives," *IEEE Transactions on Industry Applications*, vol. 56, no. 4, pp. 3831–3845, 2020. DOI: 10.1109/TIA.2020.2991122.

[16] M. Barcaro, N. Bianchi, and F. Magnussen, "Analysis and tests of a dual three-phase 12-slot 10-pole permanent magnet motor," in *2009 IEEE Energy Conversion Congress and Exposition*, Sep. 2009, pp. 3587–3594. DOI: 10.1109/ECCE.2009.5316094.

[17] S Zarotti, R. Paoluzzi, G Ganassi, F Terenzi, P Dardani, and G Pietropaolo, "Analysis of hydraulic excavator working cycle," Oct. 2009.

[18] A. Fatemi, D. M. Ionel, M. Popescu, Y. C. Chong, and N. A. O. Demerdash, "Design optimization of a high torque density spoke-type pm motor for a formula e race drive cycle," *IEEE Transactions on Industry Applications*, vol. 54, no. 5, pp. 4343–4354, 2018. DOI: 10.1109/TIA.2018.2844804.

[19] K. Ludwinek, "Some aspects of representation of inductance distributions in dq0-axes in a salient pole synchronous generator," *environment*, vol. 12, p. 16, 2014.

[20] X. Zhang, J.-Y. Gauthier, X. Lin-Shi, R. Delpoux, and J.-F. Trégouët, "Modeling, control, and experimental evaluation of multifunctional converter system," *IEEE Transactions on Industrial Electronics*, vol. 68, no. 9, pp. 7747–7756, 2021. DOI: 10.1109/TIE.2020.3013779.

[21] G. R. Ainslie-Malik, "Mathematical analysis of pwm processes," Jul. 2013. [Online]. Available: http://eprints.nottingham.ac.uk/13021/.

[22] M. J. Brand, M. H. Hofmann, S. S. Schuster, P. Keil, and A. Jossen, "The influence of current ripples on the lifetime of lithium-ion batteries," *IEEE Transactions on Vehicular Technology*, vol. 67, no. 11, pp. 10 438–10 445, 2018. DOI: 10.1109/TVT.2018.2869982.

[23] E. Fornasiero, L. Alberti, N. Bianchi, and S. Bolognani, "Considerations on selecting fractional—slot windings," in *2010 IEEE Energy Conversion Congress and Exposition*, 2010, pp. 1376–1383. DOI: 10.1109/ECCE.2010.5618269.

[24] M. Hsieh, J. Chen, Y. Yeh, *et al.*, "Integrated design and realization of a hubless rim-driven thruster," in *IECON 2007 - 33rd Annual Conference of the IEEE Industrial Electronics Society*, Nov. 2007, pp. 3033–3038. DOI: 10.1109/IECON.2007.4460298.

[25] B. D. Varaticeanu, P. Minciunescu, C. Nicolescu, S. S. Matei, and M. G. Neacsu, "Design and validation of a 2.5 kw electric naval propulsion system with rim driven propeller," in *2017 Electric Vehicles International Conference (EV)*, 2017, pp. 1–5. DOI: 10.1109/EV.2017.8242096.

[26] G. Pan, B. Cheng, P. Zhang, and Y. Cao, "Coupling design and performance analysis of rim-driven integrated motor propulsor," in *OCEANS 2016 - Shanghai*, 2016, pp. 1–6. DOI: 10.1109/OCEANSAP.2016.7485456.

[27] RINA, "Are rim-driven propulsors the future?" *The Naval Architect*, Jul. 2017.

[28] F. Scuiller, J. Charpentier, and E. Semail, "Multi-star multi-phase winding for a high power naval propulsion machine with low ripple torques and high fault tolerant ability," in *2010 IEEE Vehicle Power and Propulsion Conference*, Sep. 2010, pp. 1–5. DOI: 10.1109/VPPC.2010.5729185.

[29] P. Van Dine, A. Franco, S. Forney, J. H. Chapman, and M. A. Quadrini, *Rim-driven propulsion pod arrangement*, U.S. Patent 6,837,757 B2, Jan. 4, 2005.

[30] B. Cheng, G. Pan, and Y. Cao, "Analytical design of the integrated motor used in a hubless rim-driven propulsor," *IET Electric Power Applications*, vol. 13, no. 9, pp. 1255–1262, 2019. DOI: https://doi.org/10.1049/iet-epa.2018.5303. eprint: https://ietresearch.onlinelibrary.wiley.com/doi/pdf/10.1049/iet-epa.2018.5303. [Online]. Available: https://ietresearch.onlinelibrary.wiley.com/doi/abs/10.1049/iet-epa.2018.5303.

[31] G. Sala, D. Gerada, C. Gerada, and A. Tani, "Radial force control for triple three-phase sectored spm machines. part i: Machine model," in *2017 IEEE Workshop on Electrical Machines Design, Control and Diagnosis (WEMDCD)*, 2017, pp. 193–198. DOI: 10.1109/WEMDCD.2017.7947746.

[32] G. Sala, D. Gerada, C. Gerada, and A. Tani, "Radial force control for triple three-phase sectored spm machines. part ii: Open winding fault tolerant control," in *2017 IEEE Workshop on Electrical Machines Design, Control and Diagnosis (WEMDCD)*, 2017, pp. 275–280. DOI: 10.1109/WEMDCD.2017.7947759.

[33] L. Tang, T. Burress, and J. Pries, "A reconfigurable-winding system for electric vehicle drive applications," in *2017 IEEE Transportation Electrification Conference and Expo (ITEC)*, Jun. 2017, pp. 656–661. DOI: 10.1109/ITEC.2017.7993347.

[34] T. Gerrits, C. G. E. Wijnands, J. J. H. Paulides, and J. L. Duarte, "Electrical gearbox equivalent by means of dynamic machine operation," in *Proceedings of the 2011 14th European Conference on Power Electronics and Applications*, Aug. 2011, pp. 1–10.

[35] B. Daniels, J. Gurung, H. Huisman, and E. A. Lomonova, "Feasibility study of multi-phase machine winding reconfiguration for fully electric vehicles," in *2019 Fourteenth International Conference on Ecological Vehicles and Renewable Energies (EVER)*, May 2019, pp. 1–6. DOI: 10.1109/EVER.2019.8813594.

[36] G. Berardi and N. Bianchi, "Design guideline of an ac hairpin winding," in *2018 XIII International Conference on Electrical Machines (ICEM)*, 2018, pp. 2444–2450. DOI: 10.1109/ICELMACH.2018.8506785.

[37] A. Arzillo, S. Nuzzo, P. Braglia, *et al.*, "An analytical approach for the design of innovative hairpin winding layouts," in *2020 International Conference on Electrical Machines (ICEM)*, vol. 1, 2020, pp. 1534–1539. DOI: 10.1109/ICEM49940.2020.9270927.

[38] M. Soltani, S. Nuzzo, D. Barater, and G. Franceschini, "Considerations on the preliminary sizing of electrical machines with hairpin windings," in *2021 IEEE Workshop on Electrical Machines Design, Control and Diagnosis (WEMDCD)*, 2021, pp. 46–51. DOI: 10.1109/WEMDCD51469.2021.9425645.

[39] T. Zou, D. Gerada, A. La Rocca, *et al.*, "A comprehensive design guideline of hairpin windings for high power density electric vehicle traction motors," *IEEE Transactions on Transportation Electrification*, pp. 1–1, 2022. DOI: 10.1109/TTE.2022.3149786.

[40] C. Du-Bar and O. Wallmark, "Eddy current losses in a hairpin winding for an automotive application," in *2018 XIII International Conference on Electrical Machines (ICEM)*, 2018, pp. 710–716. DOI: 10.1109/ICELMACH.2018.8507265.

[41] P. S. Ghahfarokhi, A. Podgornovs, A. J. Marques Cardoso, A. Kallaste, A. Belahcen, and T. Vaimann, "Hairpin windings manufacturing, design, and ac losses analysis approaches for electric vehicle motors," in *2021 11th International Electric Drives Production Conference (EDPC)*, 2021, pp. 1–7. DOI: 10.1109/EDPC53547.2021.9684208.

[42] A. Reinap, M. Andersson, F. J. Márquez-Fernández, P. Abrahamsson, and M. Alaküla, "Performance estimation of a traction machine with direct cooled hairpin winding," in *2019 IEEE Transportation Electrification Conference and Expo (ITEC)*, 2019, pp. 1–6. DOI: 10.1109/ITEC.2019.8790545.

[43] G. Venturini, G. Volpe, M. Villani, and M. Popescu, "Investigation of cooling solutions for hairpin winding in traction application," in *2020 International Conference on Electrical Machines (ICEM)*, vol. 1, 2020, pp. 1573–1578. DOI: 10.1109/ICEM49940.2020.9271026.

[44] P. S. Ghahfarokhi, A. Podgornovs, A. Kallaste, T. Vaimann, A. Belahcen, and A. J. Marques Cardoso, "Oil spray cooling with hairpin windings in high-performance electric vehicle motors," in *2021 28th International Workshop on Electric Drives: Improving Reliability of Electric Drives (IWED)*, 2021, pp. 1–5. DOI: 10.1109/IWED52055.2021.9376390.

[45] G. Venturini, G. Volpe, and M. Popescu, "Slot water jacket cooling system for traction electrical machines with hairpin windings: Analysis and comparison," in *2021 IEEE International Electric Machines & Drives Conference (IEMDC)*, 2021, pp. 1–6. DOI: 10.1109/IEMDC47953.2021.9449581.

[46] E. Preci, S. Nuzzo, G. Valente, *et al.*, "Segmented hairpin topology for reduced losses at high-frequency operations," *IEEE Transactions on Transportation Electrification*, vol. 8, no. 1, pp. 688–698, 2022. DOI: 10.1109/TTE.2021.3103821.

[47] D. P. Morisco, H. Rapp, I. L. Iepure, and A. Möckel, "Extended modelling approach of hairpin winding eddy current losses in high power density traction machines," in *2020 International Conference on Electrical Machines (ICEM)*, vol. 1, 2020, pp. 874–880. DOI: 10.1109/ICEM49940.2020.9270785.

[48] L. Di Leonardo, A. Credo, M. Tursini, and M. Villani, "Rapid analytical method to evaluate eddy current losses in hairpin wound im due to pwm," in *IECON 2021 – 47th Annual Conference of the IEEE Industrial Electronics Society*, 2021, pp. 1–6. DOI: 10.1109/IECON48115.2021.9589474.

[49] E. Preci, D. Gerada, M. Degano, *et al.*, "Hairpin windings: Sensitivity analysis and guidelines to reduce ac losses," in *2021 IEEE Workshop on Electrical Machines Design, Control and Diagnosis (WEMDCD)*, 2021, pp. 82–87. DOI: 10.1109/WEMDCD51469.2021.9425643.

[50] M. Pastura, D. Barater, S. Nuzzo, and G. Franceschini, "Investigation of resistivity impact on ac losses in hairpin conductors," in *IECON 2021 – 47th Annual Conference of the IEEE Industrial Electronics Society*, 2021, pp. 1–6. DOI: 10.1109/IECON48115.2021.9589047.

[51] A. Acquaviva, M. Diana, B. Raghuraman, L. Petersson, and S. Nategh, "Sustainability aspects of electrical machines for e-mobility applications part ii: Aluminium hairpin vs. copper hairpin," in *IECON 2021 – 47th Annual Conference of the IEEE Industrial Electronics Society*, 2021, pp. 1–6. DOI: 10.1109/IECON48115.2021.9589649.

[52] G. Berardi, S. Nategh, N. Bianchi, and Y. Thioliere, "A comparison between random and hairpin winding in e-mobility applications," in *IECON 2020 The 46th Annual Conference of the IEEE Industrial Electronics Society*, 2020, pp. 815–820. DOI: 10.1109/IECON43393.2020.9255269.

[53] C. Alosa, F. Immovilli, and E. Lorenzani, "Reconfigurable multi-three-phase propulsion system for naval rim-driven propeller," in *2020 International Symposium on Power Electronics, Electrical Drives, Automation and Motion (SPEEDAM)*, 2020, pp. 442–447. DOI: 10.1109/SPEEDAM48782.2020.9161936.

[54] G. Grandi and J. Loncarski, "Evaluation of current ripple amplitude in three-phase pwm voltage source inverters," in *2013 International Conference-Workshop Compatibility And Power Electronics*, Jun. 2013, pp. 156–161. DOI: 10.1109/CPE.2013.6601146.

[55] D. Graovac and M. Pürschel, "Igbt power losses calculation using the data-sheet parameters," *Infineon Application Note*, Jan. 2009.

[56] D. Graovac, M. Pürschel, and A. Kiep, "Mosfet power losses calculation using the data-sheet parameters," *Infineon Application Note*, Jan. 2006.

[57] T. Setz, M. Lüscher, and V. Kappatos, "Applying igcts," *ABB Application Note*, Jun. 2016.

[58] L. M. Moore and H. N. Post, "Five years of operating experience at a large, utility-scale photovoltaic generating plant," *Progress in Photovoltaics: Research and Applications*, vol. 16, no. 3, pp. 249–259, 2008. DOI: https://doi.org/10.1002/pip.800. eprint: https://onlinelibrary.wiley.com/doi/pdf/10.1002/pip.800. [Online]. Available: https://onlinelibrary.wiley.com/doi/abs/10.1002/pip.800.

[59] K. Ma, H. Wang, and F. Blaabjerg, "New approaches to reliability assessment: Using physics-of-failure for prediction and design in power electronics systems," *IEEE Power Electronics Magazine*, vol. 3, no. 4, pp. 28–41, 2016. DOI: 10.1109/MPEL.2016.2615277.

[60] S. Rahimpour, H. Tarzamni, N. V. Kurdkandi, O. Husev, D. Vinnikov, and F. Tahami, "An overview of lifetime management of power electronic converters," *IEEE Access*, vol. 10, pp. 109 688–109 711, 2022. DOI: 10.1109/ACCESS.2022.3214320.

[61] M. Liserre, G. Buticchi, J. I. Leon, *et al.*, "Power routing: A new paradigm for maintenance scheduling," *IEEE Industrial Electronics Magazine*, vol. 14, no. 3, pp. 33–45, 2020. DOI: 10.1109/MIE.2020.2975049.

[62] M. Xu, K. Ma, Q. Zhong, and M. Liserre, "Frequency-domain thermal modeling of power modules based on heat flow spectrum analysis," *IEEE Transactions on Power Electronics*, vol. 38, no. 2, pp. 2446–2455, 2023. DOI: 10.1109/TPEL.2022.3210505.

[63] S. Russo, G. Bazzano, D. Cavallaro, A. Sitta, and M. Calabretta, "Thermal analysis approach for predicting power device lifetime," *IEEE Transactions on Device and Materials Reliability*, vol. 19, no. 1, pp. 159–163, 2019. DOI: 10.1109/TDMR.2019.2892185.

[64] Z. Ni, X. Lyu, O. P. Yadav, B. N. Singh, S. Zheng, and D. Cao, "Overview of real-time lifetime prediction and extension for sic power converters," *IEEE Transactions on Power Electronics*, vol. 35, no. 8, pp. 7765–7794, 2020. DOI: 10.1109/TPEL.2019.2962503.

[65] H. Li, B. Zhou, R. Yao, *et al.*, "A thermal twin modeling method of press pack igbt based on power loss," *IEEE Transactions on Electron Devices*, vol. 69, no. 12, pp. 6922–6928, 2022. DOI: 10.1109/TED.2022.3217424.

[66] Y. Chen, P. Zhang, B. Hou, and H.-Z. Huang, "Study on lifetime model of power devices based on junction temperature," in *2019 International Conference on Quality, Reliability, Risk, Maintenance, and Safety Engineering (QR2MSE)*, 2019, pp. 84–89. DOI: 10.1109/QR2MSE46217.2019.9021225.

[67] B. Wang, J. Cai, X. Du, and L. Zhou, "Review of power semiconductor device reliability for power converters," *CPSS Transactions on Power Electronics and Applications*, vol. 2, no. 2, pp. 101–117, 2017. DOI: 10.24295/CPSSTPEA.2017.00011.

[68] Z. Zhou, P. Holland, and P. Igic, "Compact thermal model of a three-phase igbt inverter power module," in *2008 26th International Conference on Microelectronics*, 2008, pp. 167–170. DOI: 10.1109/ICMEL.2008.4559249.

[69] J. Rabkowski and T. Płatek, "Comparison of the power losses in 1700v si igbt and sic mosfet modules including reverse conduction," in *2015 17th European Conference on Power Electronics and Applications (EPE'15 ECCE-Europe)*, 2015, pp. 1–10. DOI: 10.1109/EPE.2015.7309444.

[70] G.-J. Su, "Loss modeling for sic mosfet inverters," in *2018 IEEE Vehicle Power and Propulsion Conference (VPPC)*, 2018, pp. 1–6. DOI: 10.1109/VPPC.2018.8604972.

[71] S. Amirpour, T. Thiringer, and D. Hagstedt, "Energy loss analysis in a sic/igbt propulsion inverter over drive cycles considering blanking time, mosfet's reverse conduction and the effect of thermal feedback," in *2020 IEEE Energy Conversion Congress and Exposition (ECCE)*, 2020, pp. 1505–1511. DOI: 10.1109/ECCE44975.2020.9236168.

[72] A. Acquaviva, A. Rodionov, A. Kersten, T. Thiringer, and Y. Liu, "Analytical conduction loss calculation of a mosfet three-phase inverter accounting for the reverse conduction and the blanking time," *IEEE Transactions on Industrial Electronics*, vol. 68, no. 8, pp. 6682–6691, 2021. DOI: 10.1109/TIE.2020.3003586.

[73] Y. Zhang, H. Wang, Z. Wang, Y. Yang, and F. Blaabjerg, "A simplification method for power device thermal modeling with quantitative error analysis," *IEEE Journal of Emerging and Selected Topics in Power Electronics*, vol. 7, no. 3, pp. 1649–1658, 2019. DOI: 10.1109/JESTPE.2019.2916575.

[74] Y. Zhang, H. Wang, Z. Wang, Y. Yang, and F. Blaabjerg, "Simplified thermal modeling for igbt modules with periodic power loss profiles in modular multilevel converters," *IEEE Transactions on Industrial Electronics*, vol. 66, no. 3, pp. 2323–2332, 2019. DOI: 10.1109/TIE.2018.2823664.

[75] M. Maerz and P. Nance, *Thermal modeling of power electronic systems*, Feb. 2000.

[76] M. Ikonen, "Power cycling lifetime estimation of igbt power modules based on chip temperature modeling," 2012.

[77] D. Carlucci, "Battery state of health and state of charge estimation: Comparison between classical and machine learning techniques," M.S. thesis, Politecnico di Torino, 2021.